Evaluation of Multiaxial Fatigue Behavior of Welded Construction Steel Pipes Considering Microstructural Transformations and Residual Stresses

Zur Erlangung des akademischen Grades einer

Doktorin der Ingenieurwissenschaften (Dr.-Ing.)

von der KIT-Fakultät für Maschinenbau des

Karlsruher Instituts für Technologie (KIT)

genehmigte

Dissertation

von

M.Sc. Kimiya Hemmesi

Tag der mündlichen Prüfung: 17.12.2024

Hauptreferent: Prof. Dr.-Ing. habil. Volker Schulze

Korreferent: Prof. Dr. Peter Gumbsch

Vorwort

Die vorliegende Arbeit entstand während meiner Tätigkeit als wissenschaftliche Mitarbeiterin am Karlsruher Institut für Technologie- Institut für Angewandte Materialien IAM-WK, und Fraunhofer Institut für Werkstoffmechanik IWM, Freiburg. Die Untersuchungsergebnisse wurden im Rahmen des DFG-Projekts mit dem Thema „Numerische Einführung der Schädigungswirkung von Eigenspannungen für mehrachsige Festigkeitskonzepte bei Schweißbauteilen und -Strukturen“ erarbeitet. Deshalb möchte ich der DFG an dieser Stelle für ihre Unterstützung danken.

Kimiya Hemmesi, August 2024

Abstract

The main objective of the current research is to better understand the combined effects of weld-induced microstructures, residual stresses and stress concentrations on the fatigue behavior of welds subjected to complex multiaxial cyclic loadings. As such, characterization of welding residual stresses, relaxation and redistribution of residual stresses under mechanical loading, microstructure-dependent material deformation behavior, fatigue damage quantification and notch effect were the key areas of investigation. Comprehensive experiments including deformation tests on round solid and tubular samples, and fatigue tests on tubular weld specimens made of S355J2H steel were conducted to support the analysis. To assess the role of residual stresses in fatigue damage, two groups of similar weld samples, with and without residual stresses, were compared.

In weld integrity assessment, accurately capturing the interaction between load and residual stresses is crucial. Traditionally, this has involved simplifications, such as assuming uniform residual stress distribution. While advanced experimental and numerical methods now allow for more precise determination of residual stress magnitude and distribution, integrating all influencing thermal, metallurgical, and mechanical factors remains challenging.

The reliability of predicted residual stresses strongly depends on the assumptions and simplifications made. Given the limitations of both experimental and numerical methods, a combined approach is essential. Recent software advances have improved computational weld mechanics, but a deep understanding of the underlying physics and theory remains crucial. This research addresses key welding phenomena, including temperature-dependent deformation and metallurgical phase transformations.

Residual stress relaxation can occur partially or fully under thermal or mechanical loads if the combined stresses exceed the material's yield strength. Beyond their magnitude and distribution, the relaxation and redistribution of residual stresses under operational loads are critical for accurate weld design and life prediction. If significant residual stresses remain after relaxation, they may combine with load stresses, affecting fatigue life. Ignoring relaxation can lead to inaccurate life estimates, reducing reliability and leading to overdesigned, cost-inefficient structures. Relaxation behavior varies with material type and loading conditions.

Numerous methods exist for fatigue assessment and lifetime estimation of components under multiaxial stress states. Some models extend classical static

material strength hypotheses, such as equivalent stress/strain quantities, to multiaxial conditions, assuming an equivalent uniaxial stress; these invariant approaches yield acceptable results under proportional or In-Phase (IP) loading but often overestimate fatigue life under non-proportional or Out-of-Phase (OP) conditions due to their inability to capture non-proportional hardening. Advanced analysis methods, offering insight into the physical background of fatigue failure under uniaxial and multiaxial loading, are therefore emphasized in this study. Another group of models calculates a damage parameter on specific planes where fatigue cracks initiate, with critical plane approaches focusing on a single preferred plane and being classified as stress, strain, or energy-based models. These approaches are well-suited for multiaxial stress states arising from external loading or inherent features like notches or weld toes, and can capture both Low Cycle Fatigue (LCF) and High Cycle Fatigue (HCF), including non-proportional loading effects.

In this research, the strain-based Fatemi-Socie (FS) damage parameter was used to quantify fatigue damage, providing improved life estimations over conventional methods and effectively correlating multiaxial fully reversed constant amplitude fatigue data of heat-treated (residual stress free) specimens. For as-welded samples with residual stresses, the modified FS parameter offered even higher accuracy in correlating data and predicting fatigue life.

To account for the notch effect on local deformation and stress gradient, a more robust approach called Theory of Critical Distance (TCD) was implemented together with a constitutive plasticity model which leads to a better correlation of multiaxial fatigue data in comparison to the conventional approaches such as the Neuber's rule with a fatigue notch factor.

Due to significant microstructural phase transformations caused by welding in the weld area and Heat Affected Zone (HAZ), a detailed study compared the material behavior of the Base Material (BM) and HAZ under various cyclic loading conditions. The HAZ microstructure near the weld was reproduced via specific heat treatment, followed by deformation tests on both BM and HAZ. Material characterization revealed notable differences between the base material (BM) and heat affected zone (HAZ) under monotonic and cyclic loading. Concurrently, the cyclic Chaboche plasticity model was implemented in a Finite Element (FE) model, with parameters calibrated using complex multiaxial tests. To incorporate Non-Proportional Hardening (NPH), Tanaka's constitutive model was coupled with the Chaboche model by modifying the isotropic hardening term.

In addition, both materials exhibited cyclic transient softening within a specific strain range. To account for this behavior, a damage-dependent cyclic stress-strain curve was incorporated into the lifetime assessments alongside the modified FS damage model. Since the FS damage parameter includes both stress and strain components, it effectively captures material hardening (or softening) effects in fatigue life predictions. This approach to modeling cyclic transient softening resulted in improved accuracy of life predictions in the LCF regime.

While this study focused on fatigue crack initiation in welded joints, it also briefly examined micro/macro crack propagation using a discrete crack growth approach. This method effectively predicts both crack initiation and propagation, implicitly accounting for the notch effect in a more realistic way. The greatest improvement in fatigue life prediction was observed in pure axial tests, while pure torsion tests showed minimal impact due to a weaker stress/strain gradient at the notch—making crack propagation life negligible compared to initiation. The approach also captures microstructural influences on cracking through both plasticity behavior and cracking mechanisms.

To my loving parents, for their unwavering support, encouragement, and sacrifices that made this journey possible. Your belief in me never faltered, and your constant love and guidance propelled me forward, even in the face of challenges. This dissertation stands as a testament to your enduring faith in my abilities.

And to all those who selflessly contribute to the world of science without seeking recognition, and who generously share the wealth of their knowledge. This dissertation is dedicated to your noble spirit and invaluable contributions.

Acknowledgements

I extend my sincere gratitude to all those who have contributed in various capacities to the completion of this dissertation.

I am deeply grateful to my supervisors, Prof. Dr. Volker Schulze from the Karlsruhe Institute of Technology (KIT), and Prof. Dr. Peter Gumbsch from the Karlsruhe Institute of Technology (KIT) and the Fraunhofer Institute for Mechanics of Materials (IWM). Their profound scientific expertise has provided invaluable insights into my research.

Special recognition is reserved for Dr. Michael Luke from the Fraunhofer Institute for Mechanics of Materials (IWM) for his constant support. Beyond his professional guidance, his empathy and encouragement have been particularly valuable to me.

I am also indebted to Dr. Dieter Siegele from the Fraunhofer Institute for Mechanics of Materials (IWM) and Prof. Dr. Ali Fatemi from the University of Memphis for their generous support, significantly enriching my research endeavors.

My deepest gratitude goes to my parents, family, and friends for their unwavering support. Their encouragement and understanding, especially during difficult moments, have been indispensable to my journey.

Finally, I express my thanks to all those who have contributed, regardless of the scale, to this academic venture. Your support has been immensely important to me.

Table of Contents

List of Figures

List of Tables

List of Symbols

Symbol	Description
Chapter 2	
α	Thermal expansion coefficient
E	Modulus of elasticity/Young's modulus
σ_{th}	Thermal stress
P	Metallurgical phase fraction
$\bar{P}$	Phase fraction at equilibrium
τ	Delay time associated with the reaction
F	Adjusting parameter in the Leblond model
T	Temperature
P_M	Martensite phase fraction
P_A	Austenite phase fraction
M_S	Start temperature for the martensite transformation
k	Experimental parameter in the Koistinen-Marburger model
$\dot{\varepsilon}$	Total strain rate
$\dot{\varepsilon^e}$	Elastic strain rate
$\dot{\varepsilon^p}$	Plastic strain rate
$\dot{\varepsilon^{th}}$	Thermal strain rate
$\dot{\varepsilon^v}$	Strain rate due to volume change
$\dot{\varepsilon^{tp}}$	Transformation plastic strain rate
$\varepsilon_i^{th}(T)$	Thermal strain of phase i at temperature T
k	Transformation plasticity coefficient
P_α	Phase fraction of the ferritic (harder) phase
S	Deviatoric stress
h	Non-linear function for the applied stress
$\bar{\sigma}$	Equivalent stress
σ_y	0.2% Yield strength
$\varepsilon_{\alpha\to\gamma}^{th}$	Difference of thermal strain between phase α and γ
ε_γ^{eff}	Average cumulated plastic strain in the austenitic phase
θ	Strain hardening recovery factor
σ^L	Sum of load stresses
σ^{RS}	Residual stress
N	Number of cycles
$\sigma_{m,1}$	Mean stress at the first cycle
$\sigma_m(N)$	Mean stress at N_{th} cycle
A, M	Constants which incorporate the influence of material yield strength, stress and strain amplitudes

r	Stress relaxation exponent
$\Delta\varepsilon$	Total strain range
$\Delta\varepsilon_{th}$	Threshold strain range required for the occurrence of relaxation
x	Current position of a material point
x_0	Reference position of a material point
u	Displacement
D^e	Fourth-rank tensor
λ, μ	Lame's constants
$\dot{p}$	Accumulated plastic strain increment
b, Q	General temperature-dependent isotropic parameters
S	Nominal stress
K_t	Elastic stress concentration factor
σ^e	Local pseudo stress
ε^e	Local pseudo strain
σ	Actual local stress
ε	Actual local strain
K_{tq}	Ratio of the pseudo elastic von Mises notch stress to the nominal stress
σ_q	Elastic-plastic von Mises stress value at the notch
ε_q	Elastic-plastic von Mises strain value at the notch
K_f	Fatigue notch factor
ρ	Material characteristic length
r	Radius of the notch root
σ_u	Ultimate tensile strength
L	Critical distance
ΔK_{th}	Mode I threshold stress intensity factor range
$\Delta\sigma_o$	Fatigue limit stress range
τ_a	Shear stress amplitude
τ_m	Mean shear stress
$\sigma_{n,a}$	Normal stress amplitude
$\sigma_{n,m}$	Normal mean stress
k	Parameter related to the normal stress sensitivity of the material
τ_f'	Shear fatigue strength coefficient
b_0	Shear fatigue strength exponent
N_f	Number of cycles to failure
$\frac{\Delta\tau_{max}}{2}$	Shear stress amplitude in the critical plane
$t_{A,B}$	Shear fatigue strength for case A or B cracking
S	Parameter related to the normal strain sensitivity of the material
σ_f'	Axial fatigue strength coefficient
b	Axial fatigue strength exponent
ε_f'	Axial fatigue ductility coefficient
c	Axial fatigue ductility exponent

ν_e	Elastic Poisson's ratio
ν_p	Poisson's ratio for fully plastic conditions

Chapter 3

A	Percentage of elongation at onset of necking
Z	Percentage of elongation at failure
d	Lattice spacing
θ	Diffraction angle
λ	Wavelength
n	Number of wavelengths
S_{ii}	Residual stress components
ε_{ii}	Strain components
$\bar{\sigma}_a$	Equivalent stress amplitude
$\bar{\varepsilon}_a$	Equivalent strain amplitude
$\bar{K}'$	Equivalent cyclic strength coefficient
$\bar{n}'$	Equivalent cyclic strength exponent
C_M	Machine stiffness
C_P	Sample stiffness
u_{tot}	Total displacement
l	Specimen effective gauge length
$\tau_0{}^*$	Surface shear stress
T^*	Torque at the last data point of the previous half cycle
θ^*	Angle at the last data point of the previous half cycle
r_1	Inner radius of the tube
$\varepsilon'_{xy,max}$	Maximum shear strain values over one cycle on a desired plane
$\varepsilon'_{xy,min}$	Minimum shear strain values over one cycle on a desired plane
φ	Coordinate rotation angle
ψ	Load phase shift
τ'_f	Shear fatigue strength coefficient
b_0	Shear fatigue strength exponent
γ'_f	Shear fatigue ductility coefficient
c_0	Shear fatigue ductility exponent

Chapter 5

Φ	Material parameter accounting for isotropic non-proportional effects
$\tilde{b}$	Modified isotropic hardening rate constant

Chapter 6

d	Average grain size
n	Total number of measurements

n_i	Number of measurements corresponding to the grain size d_i
V_T	Total material volume
V_i	Volume of the i^{th} grain
d_i	Size of the i^{th} grain

Chapter 7

$\frac{1}{{N_f}^i}$	Contribution of each cycle into the total damage
${N_f}^i$	Number of cycles corresponding to a damage value
σ_e	Effective stress
ε_e	Effective strain

List of Abbreviations

AW	As-Welded
BM	Base Material
CCT	Continuous Cooling Transformation
CPFEM	Crystal Plasticity Finite Element Method
CSSC	Cyclic Stress-Strain Curve
EDM	Electrical Discharge Machining
EESH	Effective Equivalent Stress Hypothesis
ESED	Equivalent Strain Energy Density
FEM	Finite Element Method
FS	Fatemi-Socie
GNN	Graph Neural Network
HAZ	Heat Affected Zone
HCF	High Cycle Fatigue
HT	Heat-Treated
IP	In-Phase
IST	Incremental Step Test
LCF	Low Cycle Fatigue
MAG	Metal Active Gas
Mod-FS	Modified Fatemi-Socie
ND	Neutron Diffraction
NPH	Non-Proportional Hardening
NSIF	Notch Stress Intensity Factor
OP	Out-of-Phase
SED	Strain Energy Density
SFE	Stacking Fault Energy
SIF	Stress Intensity Factor
SWT	Smith-Watson-Topper
S-N	Stress-Life
TCD	Theory of Critical Distance
VSE	Virtual Strain Energy
WM	Weld Material

Chapter 1 Introduction

1.1 Introduction to Research Topics

The term fatigue describes the degradation and failure of structures under cyclic loading conditions. The cyclic loading conditions originate in various reasons such as varying loads during service conditions, vibrations, or fluctuating stresses that, for instance, appear at the start of a machine. Therefore, the frequencies of the repetitive loads may also vary in a large range. This has to be considered in design, where the dimensioning of components has to be in accordance with the expected number of cycles within the component's lifetime. The importance of fatigue is underpinned by the fact that it is, with a share of approximately 90%, the largest cause of failure in metals. Usually, failure occurs at load levels lower than the ones observed in static strength tests. Moreover, fatigue failure is critical since it appears spontaneously without any prior plastic deformation, even in ductile materials.

The fracture surface of fatigue cracks has a characteristic pattern that reveals information about the history of the failed component. Fatigue cracks typically initiate due to overloads, or at stress concentrations that may stem from constructional notches or microscopic features such as micropores or precipitates. Another mechanism that is observed in cyclically loaded parts is the formation of dislocation structures that lead to roughening of the surface. These so-called intrusions and extrusions are additional micro-notches which could initiate a crack, particularly in torsion or bending, where the maximum stress can be found at the surface. Several of those micro cracks might evolve in the whole volume but eventually only one will form a macro crack with its surface perpendicular to the maximum principal stress direction. The area of the crack surface where the fatigue crack propagates appears to be smooth. However, there is a macroscopic pattern that stems from load changes or

load intermittence during service. The so-called beach mark patterns are represented by concentric lines on the fatigue crack surface. On a microscopic scale the progress of the crack tip with every cycle can be observed by the so-called striations. In other words, each striation represents an increment of crack growth during each cycle. Once the remaining cross-section is too small to withstand the applied load, final rupture of the part happens, leaving a rough crack surface behind. These experimental findings together with the concepts of fracture mechanics motivate the development of damage models to predict fatigue lifetime. Parameters that influence crack initiation and crack growth have to be considered to represent the underlying physical mechanisms. Once a sufficient correlation with experimental data is found, these damage parameters can be applied in numerical models as well, allowing for a fully virtual lifetime estimation that can be transferred to real engineering parts in application.

For engineering structures with simple geometries exposed to simple uniaxial loads, there is a wide range of well-established approaches to predict fatigue life. In this regard fatigue life curves based on stress or strain can be referred to. Using these curves, which are generated experimentally for the desired materials, the stress and strain state of the material in a component can be related to its respective lifetimes.

The level of complexity is increased by allowing realistic load cases present in application, e.g., a combination of axial and torsional cycles resulting in multiaxial stress and strain states. It would be straightforward to replace the uniaxial stresses and strains with an equivalent description like the ones given in von Mises framework. However, this is only valid for the special case of a proportional load path, where normal and shear components reach their minimum and maximum values at the same time. Therefore, the need for more robust approaches that can cover general conditions of geometry and loading is felt. Geometrical complexities such as grooves, fillets and notches known as stress concentrators are normally the fatigue crack prone sites where local plastic deformation occurs as a result of elevated stress.

The subject of reliable fatigue assessment becomes even more important when it comes to the load-bearing welded components. In this respect, material inhomogeneity, weld induced notches and welding residual stresses are three important factors affecting the structural integrity of welded structures subjected to multiaxial loading. Among these factors, specifically the influence of residual stresses on fatigue behavior is not yet quantified for use in design codes and guidelines. The evidence for this fact is that in most research works it is assumed that the residual

stresses are equal to the mean stresses, while it cannot be ignored that the residual stresses, compared to the mean stresses, show uneven distributions on one hand and may relax or redistribute under external loading on the other hand. It is now clear that in many cases the welding residual stresses can influence crack formation and crack growth behavior as well as the crack orientation. The uncertainties in determining the exact magnitude and distribution of residual stresses within the material and their real effect on fatigue behavior have led to many conservative assumptions in design codes and regulations. Thus, there is still room for developing accurate techniques for determining residual stresses and finding further development approaches to combine the realistic effect of residual stresses in structural integrity assessment.

For the durability analysis of a weldment, it is first important to understand the metallurgical and mechanical evolution of the material during welding and then to evaluate the influence of microstructural evolutions on the static and cyclic properties of the material. For the accurate fatigue analysis of welds, besides selecting a proper damage parameter, a comprehensive description of the constitutive behavior of material and its variation over different areas of weld, namely weld metal, heat affected zone and base material, is essential to determine the exact stress-strain state in the likely crack initiation sites. In particular, if considerable weld notches are present, local plastic deformation is more likely, which is not negligible in an advanced lifetime analysis.

Each condition mentioned so far adds to the complexity of exact lifetime estimation. This is especially true when realistic operating conditions are present, which are inherent even in the simplest cases. Although several research papers in the literature have individually focused on these aspects, few studies address the synergistic effect of all these factors. In line with the above discussion, there is a clear need for advanced studies on the fatigue behavior of welded components under multiaxial loading. To keep pace with the rapid growth of technology, optimal designs are required for critical industries such as energy, automotive and aerospace, where catastrophic failure is unacceptable. To achieve such safe and reliable structures, it is inevitable to describe different levels of fatigue in a welded structure, while taking all influencing parameters into account as much as possible. Such an approach not only benefits new designs but can also support the assessment of the durability for the structures in use in the framework of life extension. In summary, in addition to providing durable and weight-efficient components and structures, the precise fatigue design concept substantially reduces costs in various phases of manufacture, maintenance and repair.

1.2 Research Motivation and Objectives

The main objective of the current research was to better understand the combined effects of weld-induced microstructures, residual stresses and stress concentrations on the fatigue behavior of welds subjected to complex multiaxial cyclic loadings. In this context, the emphasis was on finding the best techniques for describing different aspects of fatigue failure in welds and combining all these techniques into a single fatigue analysis guideline that can be used for welds in a logical and practical way. In order to maintain the general applicability of this procedure, an attempt has been made to base the fatigue analysis methodology on the physical aspects at different stages of the phenomena, the formation and relaxation of residual stresses and fatigue damage mechanisms. This approach, in comparison with the purely empirical fatigue analysis techniques, provides more robust and reliable fatigue assessment results.

To achieve these goals, a wide range of different experimental work including advanced residual stress measurements, material deformation and fatigue tests along with advanced computational analyses has been applied to support the three main objectives of this research, namely, accurate determination of welding residual stresses, description of the residual stress behavior under cyclic loading and finally understanding the mechanism of fatigue damage under operating conditions. In order to cover a relatively realistic condition, a variety of load designs with and without residual stresses were considered.

The different phases of the analysis procedure that were investigated in the project are summarized in a flow chart given in Figure 1.1. Areas of important contributions are highlighted with different colors.

1.3 Outline of Dissertation

This dissertation begins with a comprehensive literature survey, which is given in Chapter 2 and specifies theories, different modelling techniques and experimental results that have already been published in various scientific sources. The order of different topics in this chapter is associated with the sequence of different phases in the current project: Welding residual stresses, their nature and origin, residual stress measurement and simulation techniques, residual stress relaxation mechanism and prediction methods, material deformation behavior under multiaxial loading,

including various aspects such as notch deformation, non-proportional hardening, etc. and finally fatigue crack initiation, physics and theories behind, and fatigue damage quantification techniques.

Chapter 3 presents the experimental program conducted in this study. To support various aspects of accurate computational analyses, a series of tests and measurements were carried out as part of this program. Material selection, specimen design and fabrication, residual stress measurements, microstructure analyses and hardness measurements, test equipment, crack monitoring techniques and the test program itself, including deformation behavior tests on smooth round specimens and uniaxial and multiaxial fatigue tests on welded specimens are the main topics covered in this chapter. A summary of tests results is provided in Chapter 4. This chapter specifically presents the fatigue baselines for the desired damage parameters derived from the fundamental test results.

Given the importance of defining accurate stress-strain states in the material as a prerequisite for accurate fatigue life estimations, it is especially important to identify and characterize the exact static and cyclic material behavior. Due to the inhomogeneity of the welded materials, all deformation tests including static and cyclic tests were performed for two materials, the BM and the HAZ. Chapter 5, a cyclic plasticity model was implemented to describe the material's constitutive deformation behavior under complex loading conditions. The main focus was on incorporating a non-proportionality term into the conventional constitutive equations.

Before entering the fatigue analysis of a welded component, a precise insight into the residual stress state of the material is essential. The role of residual stresses in the structural behavior of the material can be critical, so advanced experimental and computational tools must be applied to accurately determine both the magnitude and distribution of residual stresses. Chapter 6 outlines a comprehensive investigation on the applicability of computational methods to predict the three-dimensional welding residual stress field. Advanced residual stress measurements described in Chapter 3 have been used to support the validity of the predictions. One of the most important differences between residual stresses and mean stresses is that residual stresses can relax or redistribute under mechanical load. Therefore, it is necessary to know the stable fraction of residual stresses after loading cycles. In the continuation of Chapter 6, the relaxation behavior of residual stresses under uniaxial and multiaxial loading was investigated by means of numerical method along with in-situ residual stress measurements.

Finally, Chapter 7 is devoted to the material crack initiation behavior of the welded parts under the constant amplitude uniaxial and multiaxial fatigue loadings. The main areas of discussion in this chapter are the welding-induced microstructural changes, residual stresses and notch effects with regards to the fatigue damage of welds. The fatigue life prediction results are primarily presented based on the conventional equivalent stress and equivalent strain approaches. These analyses were performed for the welded specimens in as-welded and stress-relieved conditions to be able to distinguish the influence of residual stresses on the fatigue damage. Similarly, fatigue analysis methods based on the critical plane concept were applied and their results were compared with the results of conventional equivalent approaches. The original strain-based Fatemi-Socie (FS) model and the modified FS model were selected for the mentioned analyses. In fact, the ability of the critical plane damage parameter to include the synergistic effect of all influencing parameters in the assessment of multiaxial fatigue of welds was the main concern. In the following, the effect of incorporating transient softening on the improvement of the predicted fatigue lives in the LCF regime was investigated. The issue of micro/macro crack propagation was addressed at the end of Chapter 7 by describing the discrete fatigue crack growth approach. This method assesses different aspects namely stress gradient effect, crack nucleation and micro/macro crack propagation inherently.

Chapter 8 provides a comprehensive summary of the key findings and contributions of the research presented in the earlier chapters. It summarizes the findings from the experimental work, computational analyses and theoretical studies and provides a holistic view of the research findings. Furthermore, Chapter 8 highlights the limitations of the current study and makes suggestions for future research, emphasizing areas where further investigation could improve the understanding and application of the phenomena studied in relation to welded structures.

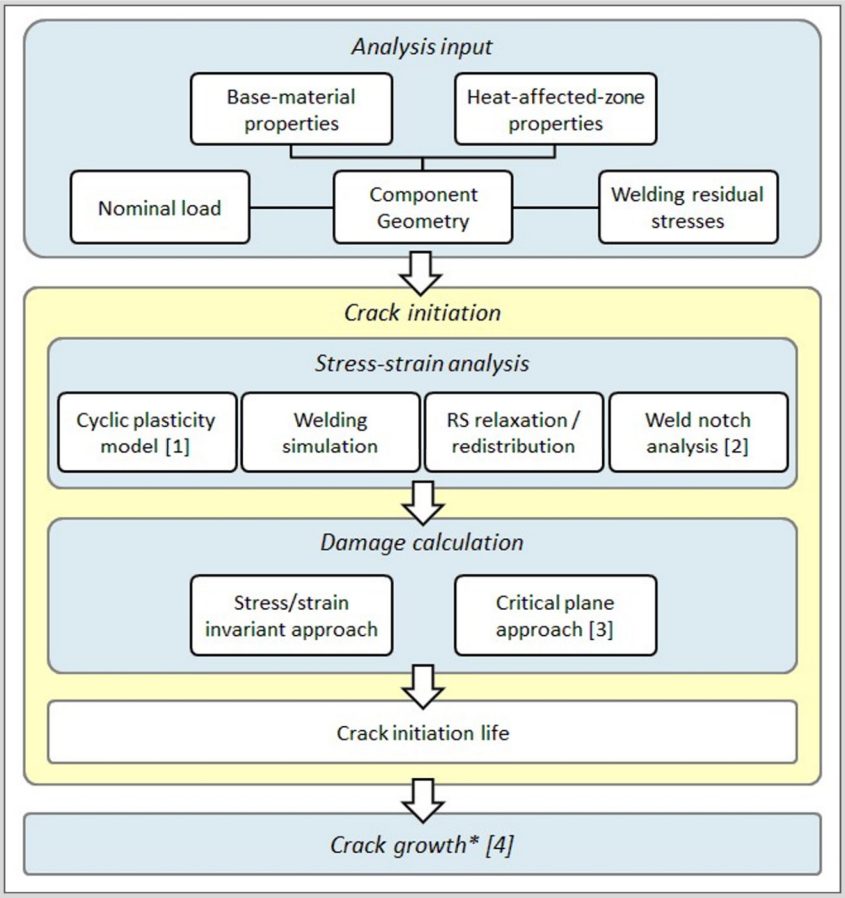

[1] Comparison of the material plastic response for the as-received and heat-treated (Gleeble) materials under simple uniaxial and complex multiaxial loading conditions:

- Application of a unified set of material parameters to describe the cyclic hardening and softening

[2] Theory of Critical Distance (TCD)

- Application of the TCD for the **welds**

[3] Application of the critical plane approach for the multiaxial fatigue assessment of **welds**

- Influence of weld-induced local material phase transformations on fatigue damage (Base Material (BM) vs. Heat Affected Zone (HAZ))
- Implementation of a non-proportionality factor into the calculation of fatigue damage under non-proportional loads
- Interactive effect of geometrical notch (weld notch) and local material properties on the fatigue damage of weld
- Evaluation of the welding residual stress effects on the fatigue damage of welds
- Application/evaluation of the Fatemi-Socie (FS) damage parameter with regard to the incorporation of the welding residual stress into the fatigue damage evaluations
- Incorporation of the transient cyclic softening into the multiaxial fatigue damage evaluations

[4] Constant amplitude crack growth and prediction (complementary*)

Figure 1.1. Areas of key contribution (Fatigue analysis only).

Chapter 2 Literature Review

There are different methods for predicting the fatigue life of welded components under multiaxial loading, which are of varying accuracy depending on the number of influencing factors included in this approach. Regardless of the method chosen, there are several steps that have to be taken before the very last step, the damage estimation. Welding residual stresses and their behavior under mechanical load, solid state phase transformations, notch effect and local plastic deformation, load non-proportionality effect and non-proportional hardening are some of these aspects. The flow chart shown in Figure 1.1 represents these different steps required for the fatigue crack initiation analysis of welds. With respect to fatigue crack initiation, there are several parameters that can relate the multiaxial fatigue damage to the stress-strain state in the material. Approaches for evaluating multiaxial fatigue, whether stress-based, strain-based or energy-based, are categorized into two main groups of invariant approaches and critical plane approaches. Regardless of which approach is used, a precise knowledge of the stress-strain field under the applied load is essential. However, this stress-strain state is not only generated by external mechanical load, but also by the weld induced residual stresses. The uneven three-dimensional residual stress distribution in the material, which may change under the forthcoming external loads, can make the condition even more complex.

A suitable damage model should normally contain both stress and strain terms and be capable of including the influence of mean stress and residual stresses in the fatigue damage evaluations. For this purpose, the constitutive behavior of the material must be described in sufficient detail to establish a good relationship between the stresses and strains, especially when plastic deformation is present. An appropriate plasticity model that incorporates the concept of non-proportional hardening can be helpful in this respect.

Since welded components usually contain weld notches, knowledge of the local stress-strain state at the notch, where fatigue cracks are more likely to occur, is now important and information on the nominal stress-strain field is not sufficient. Therefore, appropriate models are required to convert the nominal stresses and strains at the notches with respect to the local deformations.

An extensive literature review was conducted on different aspects of multiaxial fatigue of welds to obtain a sound understanding of the current state of the research communities in this area of research. A summary of these studies is given in the following sections, while attempting to maintain comprehensiveness, brevity, and ease of reading. The most popular methods used in every aspect of complex fatigue analysis for welds are presented.

2.1 Welding Residual Stresses

Welding residual stresses and methods for determining the magnitude and distribution of residual stresses in welded components in view of the potential impact of residual stresses on the structural integrity of the component have been the concern of many research councils over the last decades. Tensile residual stresses superimposed with load stresses can assist in initiating fatigue cracks or accelerate the propagation of existing cracks. In contrast, compressive residual stresses can potentially improve the material resistance against cyclic deterioration by inducing crack closure. With the aim of including the residual stress effect in the integrity assessments, a number of conservative approaches have been proposed in the design codes and guidelines [1]. For failure analyses, for instance, it is assumed that the residual stresses are uniform and stable over the entire cross-section, much the same as mean stresses. However, for an advanced and robust fatigue assessment, it is essential to determine the actual state of residual stresses within the component, especially in areas prone to cracking. To achieve this goal, a wide range of research activities, in both experimental and numerical frameworks, has been devoted to the characterization of welding residual stresses. Thanks to advanced measurement- and calculation tools, considerable progress has been accomplished in this area. Nevertheless, there is still room for improvement due to the numerous complex interrelationships between thermal, metallurgical and mechanical aspects. In other

words, quantifying all these aspects and their interactions is not an easy task and requires a deep understanding of the underlying theory.

Concerning predictive approaches, the level of accuracy and reliability of the analyses strongly depends on the number of variables involved and the degree of simplifications that can be imposed on the different aspects such as definition of the heat source, temperature-dependent material properties, solid-state phase transformations and constitutive material behavior.

Experimental methods would have to be applied to substantiate the validity of the predictions. However, due to their uncertainties, a combination of different experimental techniques may need to be employed to overcome these uncertainties. Advanced nonlinear computational approaches are known as a powerful prediction tool for simulating welding thermal cycles and the resulting residual stresses. In the context of computational mechanics of welds, the modern software infrastructure, i.e., physics, mechanics, materials science, mathematics, and numerical algorithms, has been sufficiently enriched to enable complex calculations for welded structures [2].

The first and most important step towards an accurate description of the welding residual stresses is to gain a deep insight into the nature and origin of such residual stresses. A sound physical analysis can lead to a better understanding of the role of welding residual stresses in supporting or suppressing fatigue failure. Early research into welding residual stresses date back to the 1930s, when strain gauges were the most practical technique for measuring residual stresses and more advanced diffraction-based techniques were still in their infancy. But today, thanks to the advancement of measurement techniques and computational infrastructures, a unique platform is available for understanding the formation of residual stress and its association with the material properties.

In the following sections a theoretical description of the nature and development of welding residual stresses is given.

2.1.1 Nature and Origins

In the course of welding the heat source induces a thermal cycle into the material, whereby local thermal expansions and contractions end in a thermal stress field. The following equation expresses the relationship between the thermal stress and the

temperature gradient given by the product of the material's thermal expansion coefficient, α, and the modulus of elasticity, E:

$$\sigma_{th} = \alpha . E . \Delta T \quad (2\text{-}1)$$

During welding, the material in the weld bead and adjacent areas expand due to local increase of the temperature, but this expansion is inhibited by the cold-elastic material of the surrounding area. This causes thermal compressive stresses. If the stress is high enough to exceed the yield strength of the material at the given temperature, local plastic deformation occurs. As it cools, the already permanently shortened material shrinks, and this shrinkage induces tensile stresses that end in tensile residual stress at room temperature. A schematic representation of the tensile welding residual stress formation is shown in Figure 2.1 with an example of welding a pair of single plates. Since internal stresses are self-equilibrating, compressive residual stresses would evolve in the longitudinal direction away from the weld bead, as seen in Figure 2.1 (b). If one were to assume that the plates are cut at the weld seam after welding, there would have to be a displacement at the plate edges due to the local shrinkage of the weld seam as shown in Figure 2.1 (b and c).

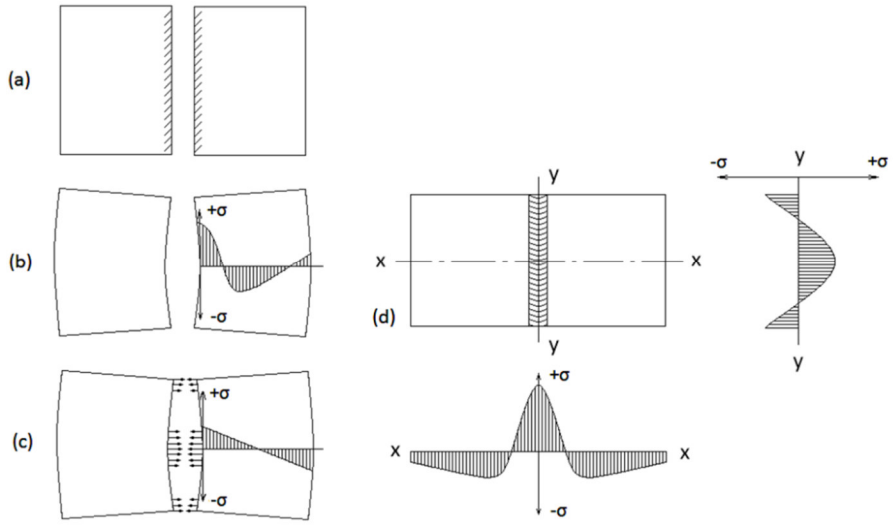

Figure 2.1 Schematic display of welding residual stress evolution in a two-plates weld model [3].

In reality, however, the plates are joined at the weld seam, so transverse residual stresses are created in the plates to maintain geometric compatibility, although there is no restriction in the transverse direction for the plates. Transverse residual stresses, similar to axial stresses, are also self-equilibrating [4].

As explained, hindered shrinkage during cooling plays an essential role in the formation of welding residual stresses. It has long been assumed that this is the only factor that determines the distribution and magnitude of residual stresses. However, thanks to the strain measurement techniques, especially x-ray diffraction, it has been shown that in some cases welding residual stresses are compressive in the weld centerline [5][6][7]. For some materials that undergo solid state phase transformation during thermal processes, the developed residual stress may deviate from this general description depending on whether ferritic, bainitic or martensitic phase transformations are present.

In steels, body-centered cubic (bcc) crystals such as ferrite, bainite, and martensite have a larger volume compared to face-centered cubic (fcc) crystals like austenite. As the crystal volume increases during cooling, compressive stress is induced in the weld bead. If this compressive stress is sufficiently large, it can counteract the tensile thermal stresses caused by shrinkage, potentially resulting in compressive residual stress in the weld bead and its vicinity. A complete welding thermal cycle, including expansions and contractions induced by both temperature gradients and phase transformations, is illustrated by a dilatometry measurement on pressure vessel steel, as shown in Figure 2.2 [8]. Initially, the material expands with the temperature increase until it exceeds the austenitizing temperature. Due to the volume reduction from the $\alpha \rightarrow \gamma$ transformation, the material contracts until the transformation is complete and then expands again at a higher rate, attributable to the higher thermal expansion coefficient of austenite compared to ferrite. During cooling, the material shrinks as the temperature decreases until reaching the $\gamma \rightarrow \alpha$ transformation temperature. Upon transformation, the material's volume increases and continues expanding until the transformation ends, after which natural contraction resumes as the temperature drops back to the initial level.

Jones and Alberry [9][10] examined how microstructural changes affect welding residual stresses in three types of steel samples: austenitic, bainitic, and martensitic. In austenitic steel, as depicted in Figure 2.3, axial thermal stress increases continuously due to hindered shrinkage, resulting in relatively high tensile residual stress dependent on material yield strength. Conversely, bainitic and martensitic steels undergo phase transformations (e.g., $\gamma \rightarrow \alpha$ during cooling), causing thermal stresses to initially decrease during transformation due to volume expansion, followed by a subsequent increase until ambient temperature is reached. Residual stresses in these steels are influenced not only by yield strength but also by

transformation temperature. For martensitic steel, if the transformation temperature is sufficiently low to prevent further post-transformation expansion, residual stresses remain low, as shown in Figure 2.3. In contrast, materials with higher transformation temperatures can continue to expand even after the transformation is complete. One such example is the bainitic steel which exhibits continued material expansion after transformation, as shown in Figure 2.3. This expansion is further accelerated by the material's higher thermal expansion coefficient, resulting in higher tensile residual stress compared to austenite.

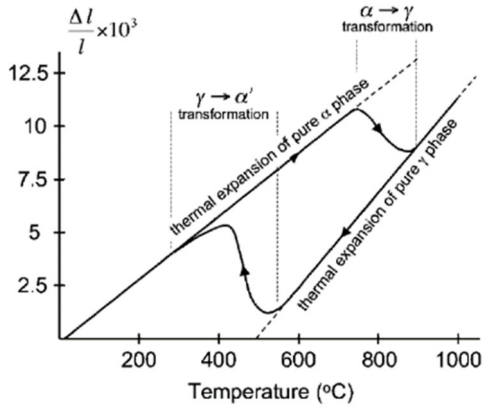

Figure 2.2 Dilatometry diagram for heating and cooling of A508 class 3 reactor pressure vessel steel at the rates of 30 K/s and 2 K/s respectively [11].

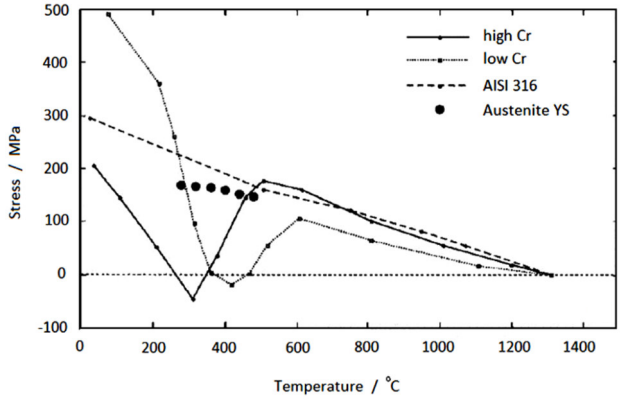

Figure 2.3 Evolution of axial thermal stresses in the specimens made of Austenitic (AISI 316), bainitic (low Cr) and martensitic (high Cr) steel specimens [9][10].

The influence of $\gamma \rightarrow \alpha$ phase transformations on the evolution of welding residual stresses is shown in more detail in a schematic model by Wohlfahrt [12] as shown in Figure 2.4. For simplicity, this model assumes that the modulus of elasticity and the

thermal expansion coefficient of the materials are independent of temperature. However, the influence of the material yield strength is included. The transformation induced compressive residual stresses developed during ferritic-pearlitic transformation comply with the temperature-dependent yield strength of the material. Once the transformation is complete, tensile thermal stresses induced by hindered shrinkage accumulate again and reach the yield strength of ferritic-pearlitic steel at room temperature. Although the thermal expansion coefficient of the austenitic phase is larger than that of ferrite-pearlite, the increase rate of thermal stress in the ferritic-pearlitic phase (after the $\gamma \rightarrow \alpha$ transformation) is higher. This effect is related to the temperature-dependent material yield strength. At lower temperatures, the rate of increase in yield strength with temperature decrease is greater for the ferritic-pearlitic phase compared to the austenitic phase.

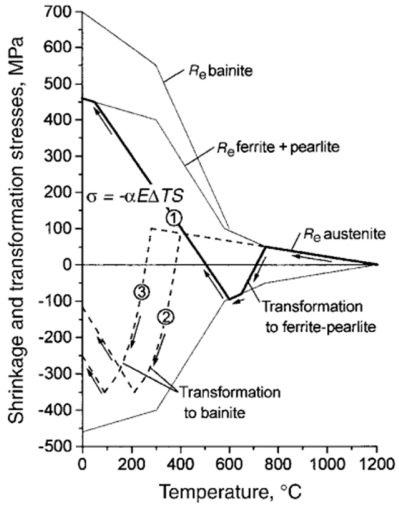

Figure 2.4 Schematic representation of residual stress evolution depending on the shrinkage and phase transformation [12].

2.1.2 Residual Stress Measurement

The residual stress measurement techniques can be categorized into destructive (or partially destructive) and non-destructive methods. One of the best-known destructive techniques is the hole-drilling method in which the residual stress at a certain point can be determined with regards to the change of local deformation due to a controlled material removal at the respective point. However, this method has a few limitations; the hole-drilling equipment, namely the strain gauge rosette, needs a flat surface to be able to measure the local strains. Therefore, on top of the weld

reinforcement or in the weld-notch there would be geometrical limitations for the strain measurements. In addition to that, the distance between measurement points cannot be shorter than the size of the rosettes which limit the possibility to capture with a high resolution the whole residual stress profile on a desired direction.

Diffraction measurement techniques, as the non-destructive methods, made a revolution in the residual stress evaluation methodologies. For the surface residual stresses for instance, the x-ray diffraction technique can provide very accurate results. The methodology and principles are given with details in [13]. A comprehensive survey on the evolution of x-ray diffraction technique since 1934 for the measurement of welding residual stresses is performed by Wohlfahrt [14]. X-ray diffraction, however, is a time-consuming method if the residual stress state in the bulk of the material is supposed to be measured by this method. Indeed, application of x-ray for the measurement of in-depth residual stresses requires the gradual material removal from the surface by means of electrochemical processes which would not be non-destructive anymore. Regardless of the difficulties in removing thin layers at the geometrical complexities e.g., weld notch, this material removal can alter the state of residual stress in the material which cannot be necessarily quantified. Appropriate alternative methods are the intensified x-ray diffraction or synchrotron and neutron diffraction techniques. While the x-ray measurements are applicable down to a depth of approximately 10 microns, the synchrotron and neutron diffraction methods let the residual stresses to be determined in deeper layers down to 100 microns and a few millimeters respectively. The methodology and principles of each method are given elsewhere [13][15].

Besides experimental approaches, advanced numerical methods can be used as a strong tool to describe the evolution of residual stresses during the welding process. The combination of experimental and numerical methods can provide a deep understanding of the effects of process-dependent factors and material characteristics on the resulting welding residual stress field in the material.

2.1.3 Welding Simulation

Residual stress distribution and its behavior under mechanical loading play a major part in the correct assessment of structural integrity in welded joints, particularly

where the fatigue performance of the structures is concerned. Welding as a complicated joining process is not easy to model, mainly because of the large number of parameters and their interaction that have to be considered. On the other hand, the effect of each parameter cannot be quantitatively defined by pure experimental residual stress measurement techniques, along with being costly or inapplicable in certain situations, such as large or complicated structures.

For an accurate welding simulation, various assumptions and simplifications must be taken into account as far as possible. These include the representation of the heat source, solid-state phase transformations, single-phase material properties (that are particularly temperature-dependent) and material hardening behavior.

2.1.3.1 Thermal-metallurgical analysis

The heat flux Q is given by ηUI for the gas metal arc welding where η is the arc efficiency, U is the arc voltage, and I is the welding current. The volumetric heat source represented by a double ellipsoid proposed by Goldak et al. [16] is very common for modeling the heat input to the body.

Some materials such as the construction steels undergo both diffusive and non-diffusive form of metallurgical solid-state phase transformations during cooling. Several models and possibilities for explaining the material's metallurgical history are available. The Leblond [17] and Koistinen-Marburger [18] models are widely used for the diffusion type and displacive reactions during welding, respectively. These two models are formulated by Equation 2-2 and Equation 2-3:

$$\dot{P} = \frac{\bar{P}(T) - P}{\tau(T)} F(\dot{T}) \tag{2-2}$$

Where P is metallurgical phase fraction, $\bar{P}$ is phase fraction at equilibrium, τ is the delay time associated with the reaction, F is adjusting parameter and T is temperature. The second is:

$$P_M(T) = P_A\big(1 - exp\big(-k(M_S - T)\big)\big), \qquad T < M_S \tag{2-3}$$

Where P_M and P_A are martensite and austenite phase fractions, M_S is the start temperature for the martensite transformation and k is an experimental parameter.

The prerequisite for the above methods is to define the Continuous Cooling Transformation (CCT) diagrams experimentally. The CCT diagram of the material can be replicated based on a phenomenological approach using the Leblond model [19].

2.1.3.2 Mechanical analysis

At the end of the thermo-metallurgical stage, both thermal and metallurgical histories are available which include temperature and phase fractions at each element. These results are then used as the input information for mechanical calculations.

In mechanical simulation of welding processes, the total strain rate is decomposed as shown in Equation 2-4:

$$\dot{\varepsilon} = \dot{\varepsilon}^{e} + \dot{\varepsilon}^{p} + \dot{\varepsilon}^{tp} + \dot{\varepsilon}^{th} + \dot{\varepsilon}^{v} \tag{2-4}$$

Besides the elastic strain rate $\dot{\varepsilon}^{e}$, the ordinary plastic strain rate $\dot{\varepsilon}^{p}$ and the thermal strain rate $\dot{\varepsilon}^{th}$, two other terms called strain rate due to volume change $\dot{\varepsilon}^{v}$ and transformation plastic strain rate $\dot{\varepsilon}^{tp}$ are also included.

In general, four solid-state phase transition related considerations that have to be taken into account in welding residual stress calculations are the volume changes due to phase transformation, microstructure-dependent mechanical properties, transformation-induced plasticity and recovery of strain hardening during transformation. Regarding thermal and metallurgical factors ε^{th} and ε^{v}, the combined strain term is briefly referred to as thermal strain and represented as follows [20]:

$$\varepsilon^{th}(P,T) = \sum P_i \varepsilon_i^{th}(T) \tag{2-5}$$

Where $\varepsilon_i^{th}(T)$ is the thermal strain of phase i at temperature T. The formula contains simultaneously thermal and metallurgical expansion and contraction and varies according to the temperature and phase changes. In order to determine $\varepsilon_i^{th}(T)$, an experimental dilatometer curve is required. Dilatometry allows dimension changes in a specimen to be read as a function of temperature. Using a dilatometer, various material parameters, in particular thermal expansion, could be determined.

It is necessary to separately identify the temperature-dependent properties of each phase in order to explain the effect of the microstructure on the mechanical properties

of the material; in particular for yield strength and strain hardening properties that dramatically change as austenite transforms into martensite.

The third transformation related factor during welding is transformation plasticity which is an additional plasticity appearing when a harder phase grows within a softer base phase. Even at stresses much lower than the yield strength, this plastic flow exists. The plastic strain caused by a $\gamma \rightarrow \alpha$ transformation can be determined by Equation 2-6 [11]:

$$\dot{\varepsilon^{tp}} = -\,{}^{3}/_{2}\, k.h\left(\frac{\bar{\sigma}}{\sigma_y}\right).S.lnP_\alpha.\dot{P_\alpha} \tag{2-6}$$

Where k is the transformation plasticity coefficient, P_α is the phase fraction of the harder (ferritic) phase, S is deviatoric stress, h is non-linear function for the applied stress, $\bar{\sigma}$ is equivalent stress and σ_y is yield stress of the material. The coefficient k can be measured experimentally from combined dilatometric tests. The other possibility is to compute the value of k using Equation 2-7:

$$k = \frac{2\varepsilon_{\gamma\rightarrow\alpha}^{th}}{\sigma_y^{\gamma}} \tag{2-7}$$

$\varepsilon_{\gamma\rightarrow\alpha}^{th}$ is the difference of thermal strain between γ and α phases and σ_y^{γ} is yield stress of phase γ.

The last metallurgy-related factor is hardening recovery, where the material's strain hardening partially or completely disappears due to structural changes. In SYSWELD, this phenomenon is defined by using two strain hardening parameters for the original and product phases, unlike the usual strain hardening law that uses one general parameter. During transformation, the strain hardening history may be retained or restored, depending on whether the α-phase inherits all or part of the strain hardening of the γ-phase [11]:

$$\dot{\varepsilon}_\alpha^{eff} = -\frac{\dot{P}_\alpha}{P_\alpha}\varepsilon_\alpha^{eff} + \theta\,\frac{\dot{P}_\alpha}{P_\alpha}\,\varepsilon_\gamma^{eff} \tag{2-8}$$

Where ε_γ^{eff} is the average cumulated plastic strain in the austenitic phase and θ is a transformation-dependent parameter, ranging from 0 to 1. It is generally assumed that strain memory disappears in diffusional transformations, i.e., austenitic, ferritic, and bainitic transformations (θ = 0), while it can be preserved in martensitic transformations.

2.2 Welding Residual Stress Relaxation

When subjected to external thermal or mechanical loads, either static or cyclic, residual stresses can superimpose the load stresses. If the resulting stresses exceed the material's yield strength, plastic deformation occurs, leading to partial or complete relaxation of residual stresses. Local relaxations may cause the residual stress field to redistribute to maintain internal stress equilibrium. Welding residual stresses can compromise the integrity of welded components if the stable fraction of these stresses significantly influences the material's overall stress state. Depending on material properties and applied loads, residual stresses may remain stable or stabilize after a few load cycles. Under sufficient mechanical or thermal loads, dislocation movement through mechanisms such as dislocation slip, grain boundary slip, or creep [21] can convert elastic residual deformations into permanent microstrain [22].

As previously described, the inhomogeneous thermal cycle during welding induces local expansion and shrinkage in the weld seam and its vicinity, hindered by the surrounding non-heat affected materials. This causes local plastic deformations and internal stresses in the material [23]. The extent to which external stresses can alter this internal stress field has been a research focus since the 1950s. One of the most representative models is the 3-bars model [3] proposed by Erker in 1954. In this model, three parallel steel bars are connected with both ends constrained. The middle bar, representing the weld, has a cross-section twice as large as the lateral bars, which represent the base material. When the middle bar is heated, it expands, but the lateral bars restrict this expansion, inducing thermal compressive stress in the middle bar and tensile stress in the lateral bars. If the thermal stress causes yielding, the middle bar shortens permanently, resulting in tensile residual stress in the middle bar and compressive residual stress in the lateral bars. When external tensile stress is applied, the combined tensile load-stress and tensile residual stress in the middle bar may exceed the material's yield strength, leading to plastic flow and permanent elongation of the middle bar. The lateral bars absorb the tensile load elastically until their compressive residual stresses are overcome. This load-induced elongation partially or fully compensates for the initial weld-induced shortening, reducing inhomogeneous plastic deformation and relaxing residual stresses. The entire relaxation theory can be summarized by the following relationship:

$$\sigma^{L} + \sigma^{RS} > R_e \tag{2-9}$$

Namely relaxation can occur when the sum of load stresses σ^L, and residual stresses σ^{RS}, exceeds the yield strength of the material R_e. In real conditions, residual and load stresses have a three-dimensional nature, making the situation more complex than described in Relation 2-9. Since yielding criteria are typically defined using equivalent stresses (e.g., principal stresses), Relation 2-9 can be generalized as follows:

$$f((\sigma_1 - \sigma_2),(\sigma_2 - \sigma_3),(\sigma_3 - \sigma_1)) > g(R_e) \tag{2-10}$$

Assuming a von Mises criterion and a plane stress condition, the Relation 2-10 can be simplified as follows:

$$\sigma_1^2 + \sigma_3^2 - \sigma_1.\sigma_3 > R_e^2 \tag{2-11}$$

This relationship represents an ellipse where the minor and major axes are $2\sqrt{2/3}\,R_e$ and $2\sqrt{2}R_e$. Therefore, it can be stated that relaxation occurs as soon as the point representing the stress state in the principal stress space protrudes from the von Mises ellipse.

Despite the critical role of welding residual stresses in failure analyses, few studies have quantified their behavior under uniaxial and multiaxial loading conditions. According to McClung in 2007 [24], nearly half of the approximately 250 research papers on residual stress focus on relaxation or stability, but most pertain to manufacturing processes other than welding, such as machining and mechanical surface treatment. While inhomogeneous plastic deformation forms residual stresses in all manufacturing processes, welding residual stresses are less controlled and more uneven due to the complexity of the welding process. Additionally, the geometric complexities and non-uniform microstructure of welds make understanding the relaxation behavior of welding residual stresses more challenging compared to other production-related residual stresses. Most research has focused on the beneficial compressive residual stresses from surface treatments, neglecting the potentially harmful tensile residual stresses from welding that can compromise structural integrity. A deeper understanding of residual stress behavior under external loading leads to more accurate lifetime evaluations. The mechanisms of relaxation are briefly outlined in the following sections.

2.2.1 Mechanisms of Relaxation

The relaxation phenomenon can be categorized into quasi-static, cyclic, and crack-induced relaxation. During the initial cycles, quasi-static relaxation occurs due to macroscopic yielding, where the combined residual and load stresses exceed the material's monotonic yield strength. Even if this sum remains below the yield strength during cyclic loading, microscopic plastic deformation can induce further relaxation, depending on the material's microstructure [25]. This process involves dislocation movement influenced by dislocation density and microstructural barriers such as grain and precipitate boundaries [26][27]. Additionally, the rate of relaxation can increase during the final stages of loading due to crack initiation and propagation.

Farajian et al. conducted an extensive experimental study on the behavior of welding residual stresses in components made of different steel under quasi-static and cyclic loading conditions [28]. It was shown that the von Mises yield criterion, combined with the monotonic yield strength, effectively describes the relaxation of welding residual stresses under cyclic loading. In the HCF regime, relaxation was insignificant, with only a slight decrease in the first cycle. This stability was especially evident in high-strength steel components with less pronounced weld notches until the onset of failure, after which the relaxation rate increased with fatigue crack growth. In the LCF regime, significant relaxation occurred during the first half of the stress cycle, interpreted as quasi-static relaxation. Subsequently, residual stresses either remained stable or relaxed gradually at a lower rate until failure. The relaxation rate during cyclic loading varied depending on whether the material was cyclically softened or hardened, and is therefore related to the cyclic yield strength of the material, $R_{e,cycl}$.

2.2.2 Prediction Approaches to the Residual Stress Relaxation

Owing to the multitude of affecting parameters such as the complexity of the initial field of residual stress, load type, load amplitude and material property also at room temperatures, it is difficult to precisely assess the relaxation of welding residual stresses [29]. One approach is to experimentally quantify residual stress variations using various measurement techniques, which is very costly and time-consuming and often even inapplicable. There are two common methods for the prediction of residual

stress relief in addition to measurements, namely empirical [30][31][32] and numerical methods. The empirical approach is simpler to use but less capable of considering all the parameters of control, but the latter has demonstrated a high promise for reliable results [25][29][32].

As for the empirical approach first, the proposed relaxation equations for mean stresses were also extended to the case of residual stresses by equating the residual stresses with the mean stresses, where the degradation of the mean stresses or residual stresses in these relations is represented as a function of the number of cycles, e.g., as a linear logarithmic function [33][34]:

$$\sigma_m(N) = A + M\sigma_{m,1}\, log(N) \tag{2-12}$$

where N is the number of cycles, $\sigma_{m,1}$ is the mean stress at the first cycle, $\sigma_m(N)$ is the mean stress at N_{th} cycle and A and M are constants which incorporate the influence of material yield strength, stress and strain amplitudes. It has been shown that such relationships are applicable only after the first cycle.

Beside the logarithmic function, the relationship between the mean stress relaxation and number of cycles could also be expressed in the form of a power function [35][36]:

$$\sigma_m(N) = \sigma_{m,1}N^r \tag{2-13}$$

where r is the stress relaxation exponent which depends on the applied strain amplitude. As noted by Landgraf and Chernenkoff [36] the rate of relaxation increases with the increase of the strain amplitude:

$$r = 8.5 \times 10^{-2}\left(1 - \frac{\Delta\varepsilon}{\Delta\varepsilon_{th}}\right) \tag{2-14}$$

where $\Delta\varepsilon$ is the total strain range and $\Delta\varepsilon_{th}$ is the threshold strain range required for the occurrence of relaxation which has been proposed to be determined according to the material Brinell hardness:

$$\frac{\Delta\varepsilon_{th}}{2} = exp[-8.41 + 5.36 \times 10^{-3}(HB)] \tag{2-15}$$

It is worth noting that the stress ratio effect is found in none of these models. Furthermore, in order to predict the dramatic quasi-static relaxation of residual stress in the early cycles, the models listed are not valid. To solve this problem, Lindgren and Lepistö [37] suggested that the exponent of stress relaxation can be divided into terms of quasi-static and cyclic relaxation with the latter defining the rate of cycle-dependent relaxation and is independent of the mean stress, while the former

depends on the mean stress. That is because quasi-static relaxation typically happens when the amplitude of the strain is sufficiently high for yielding to occur.

$$r = r_{quasi-static} + r_{cyclic} \quad (2\text{-}16)$$

If the strain magnitude is less than the threshold, there would be no significant stress relaxation. Once the strain amplitude reaches the threshold, cycle-dependent mean stress relaxation begins. If the strain amplitude is large enough to cause yielding, plastic deformation and quasi-static relaxation occur in the initial cycles, followed by cyclic relaxation of the residual mean stress. Ultimately, in the case of significant yield, without additional cyclic relaxation, quasi-static relaxation may occur independently. Residual stress relaxation is akin to the creep mechanism, involving time-dependent stress-strain evolution due to dislocation motion under mechanical loading [38]. Qian et al. [39] proposed a phenomenological model similar to the creep method to estimate residual stress relaxation by considering dislocation motion during cyclic loading. This model showed high agreement with experimental results for AISI 1008 and AISI 4140 steels under various applied stresses and load cycles.

In addition to mathematical models, which are essentially based on the interpolation or extrapolation of experimental data on residual stress relaxation, finite element techniques are increasingly used to incorporate more influencing variables. The FE approach can generally predict both quasi-static and cyclic residual stress relaxation, but the accuracy depends heavily on the applied constitutive model of plasticity [40][41][42]. FE-based studies indicate that most residual stress relaxation occurs in the first cycle or within the first few cycles, depending on the material model used. However, to validate these simulation methods, more complex loading conditions and advanced experimental techniques are needed.

2.3 Material Deformation Modelling

The following sections provide a summary on the constitutive description of plasticity, focusing on von Mises plasticity, the most widely used model for metals. A significant development in plasticity theory was the formulation of associated plasticity around 1950, with key contributions from Hill [43], Drucker [44] and Prager [45]. Prager proposed the linear kinematic hardening rule to describe the Bauschinger

effect, altering the elastic limit in cyclically loaded specimens [46]. Armstrong and Frederick [47] introduced a dynamic recovery term for back stress evolution. Later, Chaboche [48] independently applied the nonlinear kinematic hardening equation in unified viscoplasticity theory. Chaboche and Rousselier [49][50] further modified the Armstrong-Frederick law by decomposing the back stress additively, improving the hardening behavior approximation.

Under non-proportional loading, certain materials undergo additional cyclic hardening depending on strain amplitude and path [51][52][53]. Taira et al. [51] first observed non-proportional hardening in 1968, later explained by Lamba and Sidebottom [54] and Kanazawa et al. [55] as resulting from interactions among multiple slip systems creating complex immobile dislocation structures. Doong et al. [56] studied the microstructure's effect on non-proportional hardening, finding an inverse relationship with Stacking Fault Energy (SFE): materials like aluminum (high SFE), copper (medium SFE), and stainless steel (low SFE) exhibited differing degrees of non-proportional hardening. The prediction of non-proportional hardening has been approached through constitutive theories and empirical models. Tanaka [57] introduced an internal variable tensor to account for the directional characteristics of dislocation structures, successfully applying it in cyclic plasticity models for various steels and polycrystalline copper, as reported in [58] and [59].

2.3.1 Constitutive Relations

To describe the kinematics of a body in Euclidean space, the position of a material point x is given as a function:

$$x = \chi(x_0, t) \tag{2-17}$$

where x_0 is the reference position and t is time. The displacement u is then defined as:

$$u(x_0, t) = \chi(x_0, t) - x_0 \tag{2-18}$$

This is known as a Lagrangian description, which is used in structural mechanics. Provided that χ is invertible, a field variable can be converted into a function of the current position x, which is known as the Euler description and is often used in fluid mechanics. From now on, the Lagrangian description is used without further writing the subscript indicating the reference position.

Due to the application to cyclic loading conditions, the deformation is assumed to be small, i.e., a linearized strain measure can be used. Therefore, the strain tensor is defined as a symmetric gradient of the displacement vector:

$$\varepsilon = \nabla^S u = \frac{1}{2}\left(\frac{\partial u_i}{\partial x_j} + \frac{\partial u_j}{\partial x_i}\right) \tag{2-19}$$

and can be decomposed additively into an elastic and a plastic strain:

$$\varepsilon = \varepsilon^e + \varepsilon^p \tag{2-20}$$

For the elastic range, a linear relationship between stress and elastic strain is given by Hooke's law:

$$\sigma = D^e : (\varepsilon - \varepsilon^p) \tag{2-21}$$

where D^e is a fourth-rank tensor, representing the material's stiffness. In isotropic materials, the elastic stress response can be described using just two parameters. Thus, Equation 2-21 simplifies to:

$$\sigma = \lambda tr(\varepsilon^e)\mathbf{I} + 2\mu\varepsilon^e \tag{2-22}$$

using Lame's constants λ and μ. Since plastic deformations conserve volume, it is logical to subtract the hydrostatic component from the stress tensor to obtain the deviatoric stress tensor:

$$\sigma' = \sigma - \frac{1}{3} tr(\sigma)\mathbf{I} \tag{2-23}$$

from which von Mises equivalent stress can be calculated.

$$\bar{\sigma} = \sqrt{\frac{3}{2}} \|\sigma'\| \tag{2-24}$$

Similar to Equation 2-23, the plastic strain tensor is deviatoric, meaning $tr(\varepsilon^p) = 0$, which is referred to as plastic incompressibility.

In a tensile test, a uniaxial stress state can be established, and the specimen's response is recorded in a stress-strain curve. For metallic materials, the curve typically shows an initial linear segment representing the elastic response. Beyond a certain stress value, the material behavior deviates from linearity. The yield surface $f = 0$ in its most general form is expressed as:

$$f = \|\sigma\|_{\mathrm{H}} - \sigma_y \tag{2-25}$$

with σ_y defining the yield surface size and a quadratic norm:

$$\|\sigma\|_{\mathrm{H}} = \sqrt{\sigma : \mathbb{H} : \sigma} \tag{2-26}$$

where $\mathbb{H}$ is a fourth-rank tensor. In the case of von Mises plasticity, commonly used for isotropic metals, $\mathbb{H}$ is proportional to the deviatoric projector I^{d},

$$\mathbb{H} = \frac{3}{2}\mathrm{I}^{\mathrm{d}} = \frac{3}{2}\left(\mathrm{I} - \frac{1}{3}\mathbf{I} \otimes \mathbf{I}\right) \tag{2-27}$$

Thus, Equation 2-25 can be rewritten as:

$$f = \sqrt{\frac{3}{2}}\|\sigma'\| - \sigma_y \tag{2-28}$$

Figure 2.5 depicts the von Mises yield surface in three-dimensional principal stress space as a cylinder with its axis along the hydrostatic line, where $\sigma_1 = \sigma_2 = \sigma_3$. The radius of the cylinder is proportional to the yield stress, and the plane $\sigma_1 + \sigma_2 + \sigma_3 = 0$ is called the deviatoric plane.

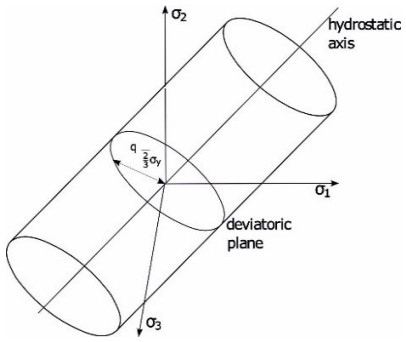

Figure 2.5 Three-dimensional representation of von Mises yield surface in principal stress space.

So far, the yield surface describes perfect plasticity, where stress remains constant with increasing strain. To include hardening or softening, the yield surface depends on the accumulated plastic strain p. Introducing the back-stress tensor α translates the yield surface, modifying Equation 2-28 to:

$$f = \sqrt{\frac{3}{2}}\left\|\sigma' - \alpha'\right\| - \sigma_y \tag{2-29}$$

where α' is the deviatoric back-stress tensor. Both hardening contributions will be detailed further. In associated plasticity theory, the plastic strain evolution follows a potential relation where the yield surface matches the flow potential:

$$\dot{\varepsilon}^p \propto \frac{\partial f}{\partial \sigma} \tag{2-30}$$

The proportionality constant is determined using the consistency condition $f = \dot{f} = 0$. For von Mises plasticity, inserting Equation 2-29 in Equation 2-30 gives the flow rule:

$$\dot{\varepsilon}^p = \dot{p}\frac{3}{2}\frac{\sigma' - \alpha'}{\|\sigma' - \alpha'\|} = \sqrt{\frac{3}{2}}\dot{p}\mathrm{N} \tag{2-31}$$

with $\dot{p}$ as the accumulated plastic strain increment:

$$\dot{p} = \sqrt{\frac{2}{3}}\|\dot{\varepsilon}^p\| \tag{2-32}$$

and the direction of the plastic strain rate:

$$\mathrm{N} = \frac{\dot{\varepsilon}^p}{\|\dot{\varepsilon}^p\|} \tag{2-33}$$

2.3.1.1 Isotropic hardening

The change in yield surface size is described by an isotropic hardening law. The special case where the yield surface size remains constant is known as perfect plasticity. The yield stress, which defines the size of the yield surface, is assumed to depend on the accumulated plastic strain. Its evolution is typically described by a rate equation:

$$\dot{\sigma}_y = b(Q - \sigma_y)\dot{p} \tag{2-34}$$

where b and Q are in general temperature-dependent material parameters. Integrating Equation 2-34 with the initial yield stress $\sigma_{y,0}$ gives an exponential expression for the yield stress:

$$\sigma_y(p) = \sigma_{y,0} + Q(1 - \exp(-bp)) \tag{2-35}$$

Here, Q represents the saturated yield surface size, and b defines the rate of isotropic hardening. Figure 2.6 shows isotropic hardening for a von Mises yield surface in principal stress space, illustrated by the expansion of the initial yield surface.

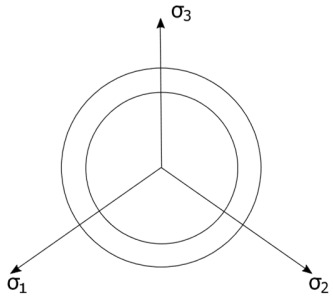

Figure 2.6 Graphical representation of isotropic hardening for a von Mises yield surface in principal stress space.

2.3.1.2 Kinematic hardening

Under cyclic loading, hardening effects are primarily dominated by kinematic hardening. While isotropic hardening involves a change in the yield surface size, kinematic hardening is characterized by a shift of the yield surface, described by the back-stress tensor α. Figure 2.7 illustrates this for a von Mises yield surface in principal stress space. Prager [60] suggested a back-stress evolution collinear with the plastic strain rate, but this linearity is rarely seen in engineering materials. Armstrong and Frederick [47] proposed a more accurate model by introducing a recall term, known as dynamic recovery:

$$\dot{\alpha} = \frac{2}{3} C \dot{\varepsilon}_p - \gamma \alpha \dot{p} \tag{2-36}$$

which is collinear with α and proportional to the norm of the plastic strain rate. This yields an exponential evolution of back-stress instead of a linear one for monotonic uniaxial loading conditions. A better approximation can be achieved by summing multiple back-stress components of the form of Equation 2-36:

$$\alpha = \sum_{k=1}^{M} \alpha^{(k)} \tag{2-37}$$

$$\dot{\alpha}^{(k)} = \frac{2}{3} C^{(k)} \dot{\varepsilon}_p - \gamma^{(k)} \alpha^{(k)} \dot{p} \tag{2-38}$$

This approach extends the strain domain and better describes the elastic-plastic transition. The parameters $\{C^{(k)}, \gamma^{(k)}\}$ are not material constants but a series decomposition that simplifies the expression for the cyclic tensile curve. A nonlinear kinematic hardening model with a decomposed back-stress tensor enables the modeling of effects that occur in cyclically loaded parts, namely the Bauschinger effect, the effect of plastic shakedown, cyclic ratchetting and mean stress relaxation.

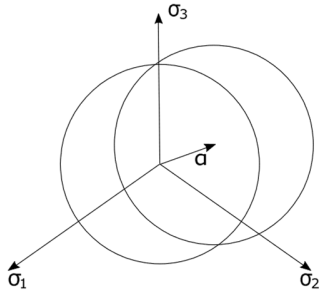

Figure 2.7 Graphical representation of kinematic hardening for a von Mises yield surface in principal stress space.

2.3.1.3 Non-proportional hardening

Multiaxial cyclic loading conditions necessitate the consideration of non-proportional hardening effects, introduced by the shape of load paths. Proportional loading occurs when various loading types reach their maximum and minimum value simultaneously. In contrast, non-proportional loading occurs when different loading types, such as normal and shear components, have different frequencies and/or are out-of-phase. This causes constant changes in the principal axes with respect to time and rotation of the maximum shear plane. Many approaches to modeling non-proportional hardening are empirical. There are constitutive theories, e.g., by Chaboche [49] or Ohno [61], but they fail to account for cyclic softening under proportional cycles following non-proportional cycles. This section presents Tanaka's approach [57], which uses an internal variable to reflect the internal dislocation structure responsible for non-proportional hardening in cyclically loaded metals.

The internal variable should represent the directional character of the dislocation structure. Therefore, the variable denoted with $\mathbb{C}$ is chosen as a fourth-rank tensor [57]. This rank ensures that during axial cycling, the dislocation structure evolves similarly under both tensile and compressive loads. The gradual change of $\mathbb{C}$ during cyclic loading is described by a rate-type equation, as small plastic deformations cannot drastically alter the dislocation structure. A target value, corresponding to the deformation process, is included in the evolution equation. For pure axial or torsional cycles, $\mathbb{C}$ should match this target value and remain constant for proportional cycles. Thus, the evolution equation is formulated as:

$$\dot{\mathbb{C}} = c_c(\mathrm{N} \otimes \mathrm{N} - \mathbb{C})\dot{p} \tag{2-39}$$

where c_c is a material constant and N is the direction of plastic flow defining the target value of $\mathbb{C}$ by a dyadic product. The non-proportionality parameter is defined as:

$$A = \sqrt{1 - \frac{\mathrm{N}:\mathbb{C}^{\mathrm{T}}:\mathbb{C}:\mathrm{N}}{\mathbb{C}:\mathbb{C}}} \tag{2-40}$$

$$A = \sqrt{1 - \frac{N_{kl}C_{ijkl}C_{ijmn}N_{mn}}{C_{opqr}C_{opqr}}} \tag{2-41}$$

with $i, \dots, r \in [1,3]$ and $0 \leq A \leq 1$. The non-proportionality parameter can be incorporated into evolution equations for both kinematic and isotropic hardening by establishing target values for the material parameters. Modeling transient hardening

or softening effects under both proportional and non-proportional load paths requires suitable experimental data to calibrate the evolution equations.

2.3.2 Notch Stress/Strain Concept

The methods for calculating elastic-plastic stresses and strains were described in the previous section can be directly applied only if the values of stresses or strains are known at the desired locations. For those components containing geometric discontinuities or notches, some complementary approaches are required to convert the nominal stresses to the local ones depending on the material property, the load type and the notch geometry. With sufficient computational resources, the nonlinear Finite Element Method (FEM) almost always predicts the most accurate stress and strain results, provided that the constitutive relations of cyclic plasticity are adequately defined. For complex component geometries, however, attention must be paid to the high computational costs of FEM. Other analytical approaches have been proposed which can predict local stresses and strains at the notch roots with reasonable accuracy and considerably lower costs. These approaches function by relating the local stress and strain to pseudo stress and strain at the notch root, as if the material behavior remains linearly elastic beyond the material yield strength. The linear elastic stress-strain analyses offer the advantage of low calculation costs. The theoretical pseudo-stress and pseudo-strain are identified by σ^e and ε^e. The two best known and most popular methods for estimating local stress and local strain were those proposed by Neuber [62] and Glinka [63]. Neuber's rule assumes that, under elastic-plastic conditions, the product of the local elastic stress and strain at a notch remains equal to the product of the nominal elastic stress and strain:

$$\frac{(K_t S)^2}{E} = \sigma^e \varepsilon^e = \sigma\varepsilon \tag{2-42}$$

where S is the nominal stress, E is Young's modulus, K_t is the elastic stress concentration factor, σ^e and ε^e are local pseudo stress and strain respectively, and σ and ε are actual local stress and strain at the notch, respectively.

The Glinka's rule is based on the ESED (Equivalent Strain Energy Density) concept and states that the value of ESED at the notch is the same for the linear elastic and elastic-plastic state, provided that the plastic zone at the notch tip is local and surrounded by elastic material. It has been shown that the Neuber's rule matches the plane stress state and the Glinka's rule the plane strain state better [64]. In addition to

the models by Neuber and Glinka, several other models have been proposed to provide a general model for application to all notch geometries. However, these methods are relatively new and require more evaluation. The Neuber's rule has proven to be the most popular and simplest method to derive the actual stress and strain values at the notch root. In fact, this model better satisfies the tendency to be conservative in the assessment of fatigue damage. For this reason, considerable efforts have been made to modify and adapt the Neuber's rule for more complex multiaxial loading conditions.

In 1998 Hoffmann and Seeger [65] extended the Neuber's rule to the general case of multiaxial loading. They replaced the axial local stress and strain terms in the Neuber's equation by the equivalent local stress and strain terms:

$$\frac{(K_{tq}S)^2}{E} = \sigma_q \varepsilon_q \tag{2-43}$$

where K_{tq} is the ratio of the pseudo elastic von Mises notch stress to the nominal stress. σ_q and ε_q are the elastic-plastic von Mises stress and strain values at the notch. Then, the principal stress and strain at the notch root were correlated with the equivalent notch stress and strain using Hencky's flow rule, taking into account two assumptions; first, it was assumed that the principal directions are always constant and are identical for both elastic and elastic-plastic states. Additionally, the ratio of local surface strains remains constant for both elastic and elastic-plastic conditions. These assumptions are presented as follows:

$$\theta_p^e = \theta_p = A \tag{2-44}$$

$$\frac{\varepsilon_2^e}{\varepsilon_1^e} = \frac{\varepsilon_2}{\varepsilon_1} = B \tag{2-45}$$

Where A and B are constant values. By replacing the stress and strain terms in the respective equation with the stress and strain range terms and by applying the cyclic stress-strain curve of the material, the models can be extended to the cyclic loading state. However, after reducing the equation to a simple uniaxial case, the assumptions of Hoffmann and Seeger contradict Neuber's rule. Furthermore, the assumption that the local surface strain ratio is constant only holds for the circumferential notches. To overcome this problem, it was suggested by Moftakhar et al. [66] that the ratio of the largest principal stress and strain components at the notch root to the total strain energy density should be applied:

$$\frac{\sigma_1^e \varepsilon_1^e}{\sigma_{ij}^e \varepsilon_{ij}^e} = \frac{\sigma_1 \varepsilon_1}{\sigma_{ij} \varepsilon_{ij}} \tag{2-46}$$

Although this extended Neuber rule provided a good correlation with experimental results, it could not accurately estimate the local stress and strain values under non-proportional loading conditions due to the assumption of constant principal directions. It should be noted that regardless of whether the external load is proportional or non-proportional, the condition at the notch tip is almost always non-proportional.

The method developed by Barkey et al. [67] is another outstanding method by which the actual notch stresses and strains for general, proportional and non-proportional multiaxial loading conditions can be predicted by relating the pseudo-stress to the local strains. A structural yield surface and a load-notch strain curve are the prerequisites for this method. To find the relationship between the nominal load and the notch strain, either a direct strain measurement at the notch or estimation methods such as uniaxial Neuber's rule or nonlinear FEM can be used to determine the local notch strain. Next, using a suitable cyclic plasticity model such as the multi-surface model by Mroz [68] the notch strain can be determined directly from the nominal load. The pseudo stress-pseudo strain and pseudo stress-local strain approaches are schematically illustrated in Figure 2.8.

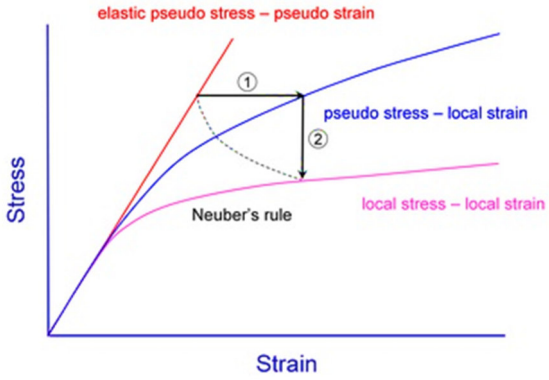

Figure 2.8 Schematic illustration showing the evolution of the pseudo stress approach in terms of elastic (pseudo stress-pseudo strain), structural (pseudo stress-local strain), and material (local stress-local strain) curves.

2.3.3 Stress and Strain Gradient Effects

For an accurate analysis of fatigue damage, it is necessary not only to know the exact values for stress and strain at the notch root but also to determine the stress and strain gradient. The stress concentration factor defines the greatest stress and strain at the notch root. However, a steep gradient from the point of maximum concentration away from the notch root is always present. Fatigue process zone is not a single point, but a finite volume of the material, so neglecting the gradient effect can result in excessively conservative life predictions [69].

The fatigue notch factor K_f is one of the simplest and most widespread methods that could be applied in conjunction with local stress and strain estimation methods such as the Neuber's rule to incorporate the gradient effect into the fatigue life estimation [70]. Fatigue notch factor is derived by comparing the fatigue strength of notched and un-notched specimens at a given fatigue life and depends on the notch geometry, material properties and load type. The K_f value for lifetimes beyond 1e6 cycles can be approximated by Equation 2-47 [71]:

$$K_f = 1 + \frac{K_t - 1}{1 + \sqrt{\rho / r}} \tag{2-47}$$

ρ is the material characteristic length and r is the radius of the notch root. Where the material characteristic length is not available, it is possible to estimate this value by means of empirical methods; for steel alloys, for instance, it is given as follows [72]:

$$\log \rho = -\frac{\sigma_u - 134}{586} \tag{2-48}$$

where σ_u is the ultimate tensile strength of the material in MPa and ρ is in mm. According to Topper et al. [70] better estimates of fatigue life can be obtained if K_f is used in place of K_t together with the Neuber's rule. For example, finding K_t in the fatigue notch factor formula requires the stress concentration factor of that particular notch, which is defined by the ratio of maximum stress to nominal stress, but it is not always easy to determine the nominal stress in complex components. Another limitation is that the material characteristic length may not be always available and eventually the fatigue notch factor formula would be undefined if the notch root radius is zero. In addition, the implementation of this method for non-proportional multiaxial loading, where the stress concentration factor varies continuously over a cycle, could be a challenge. To overcome the limits of the fatigue notch factor, another

method called theory of critical distance (TCD) has been proposed, based on the fracture mechanics concept, to include the gradient effect [73][74]. The critical distance L is a material dependent characteristic length identified by the crack transition length from the state controlled by the fatigue limit to the state controlled by the threshold stress intensity factor for the particular material.

This transition length can be determined according to the Kitagawa-Takahashi diagram (Figure 2.9). The critical distance L is given by Equation 2-49:

$$L = \frac{1}{\pi}\left(\frac{\Delta K_{th}}{\Delta\sigma_0}\right)^2 \tag{2-49}$$

where ΔK_{th} is the mode I threshold stress intensity factor range and $\Delta\sigma_o$ is the fatigue limit stress range both at the same load ratio.

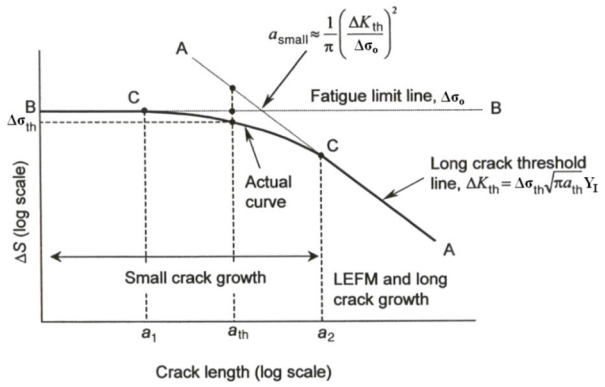

Figure 2.9 Schematic illustration of the Kitagawa-Takahashi diagram for small crack growth [75].

A number of TCD methods exist, namely the point method (PM), the line method (LM), the area method (AM) and the volume method (VM). Among these methods, the first two are more common. In the PM method, the gradient effect is incorporated into the fatigue analysis by considering the stress and strain values at a distance of $L/2$ from the point of maximum stress or strain at the notch root along a path perpendicular to the notch curvature. For LM, the analyses use the mean value of the stress or strain profile over a length of $2L$ starting from the point of maximum stress or strain at the notch root along a path perpendicular to the notch curvature (Figure 2.10).

The TCD method has been extended to multiaxial loading conditions. If the linear-elastic concept is used for fatigue analysis, the value of L would depend on the fatigue life so that a reduction in fatigue life would increase the value of L [76]; however, this is not the case if the elastic-plastic behavior is included in the analyses [77]. It is known

that the value of L is generally greater for pure torsion than for pure axial load. However, it has been shown by Susmel and Taylor [78] that assuming a constant value of L under torsion equal to that of the axial load leads to an error of ±25% in predicting fatigue life. Moreover, such an assumption leads to a more conservative prediction for pure torsion. Therefore, it is concluded that a constant L-value from uniaxial loading can reasonably be applied to pure torsion and other loading conditions. With this assumption the TCD method can be extended to the constant amplitude multiaxial loading condition. In order to apply the TCD method to general multiaxial loading conditions where non-proportional load or mean stress exist, it is proposed that instead of the stress and strain values individually, the mean value of the desired damage parameter itself be specified by the TCD method.

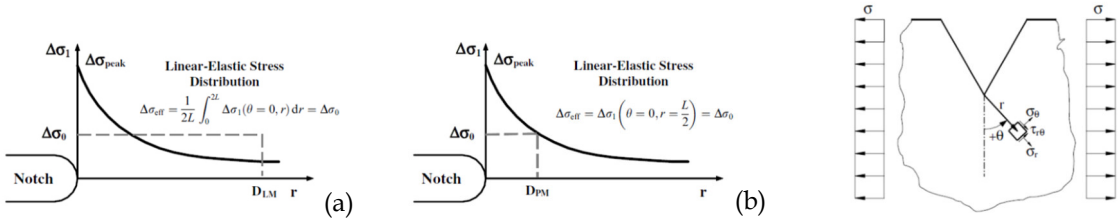

Figure 2.10 Schematic illustration of the TCD formulation of (a) the Line Method, (b) the Point Method [75].

2.4 Multiaxial Fatigue Damage Parameters

2.4.1 Overview of Parameters

After determining the correct magnitude and distribution of stresses and strains at the critical areas of a component, the next key step is to develop a methodology to quantify the multiaxial fatigue damage based on the stress-strain state and its variation. To date, a variety of different damage parameters have been proposed to estimate fatigue damage under multiaxial loading based on different combinations of stress or strain terms or even both. Nevertheless, none of these approaches has succeeded in fully covering all materials and loading conditions in terms of fatigue damage estimation.

A series of conventional damage models, namely the invariant approaches [79][80], are based on the extension of the classical static material strength hypothesis, to the multiaxial loading conditions. In a stress-based invariant approach, by setting the equivalent stress equal to the uniaxial stress of the same magnitude, experimental uniaxial fatigue life curve could be used as a fatigue baseline for the lifetime predictions. Methods such as von Mises stress and maximum shear stress for ductile materials and maximum principal stress can be used for brittle materials.

Strain-based invariant approaches such as von Mises strain, maximum shear strain and maximum principal strain can be used in a similar way to relate the multiaxial strain state to an equivalent axial strain state, especially when significant plastic deformation is present. It should be noted that invariant approaches do not include directly the mean stress effect into the damage evaluations but require additional considerations.

These invariant approaches [79][80] are straightforward and could provide acceptable results in proportional loading conditions. However, for complex conditions such as non-proportional loading cases the invariant approaches often overestimate the fatigue life. One reason is that non-proportional hardening effect which typically shortens the fatigue life cannot be incorporated precisely by these approaches [81][82]. In particular, the fatigue data of multiaxial tests with different ratios of axial and shear stresses cannot be adequately correlated [81]. In addition, these methods are generally based on the correlation of experimental fatigue data and do not reflect the mechanism of the damage.

In 1995, Sonsino [83] proposed a modified invariant approach known as the Effective Equivalent Stress Hypothesis (EESH). This approach is based on the assumption that crack initiation is driven by local shear stress components and their interaction on various interference planes. The interaction of shear stresses is accounted for by developing an effective shear stress, which is subsequently used to determine the effective equivalent stress.

The limitation of Sonsino's approach is the need for some information such as the stress concentration factor or phase shift of load signals that are not always available in practice. Furthermore, this approach does not take into account the phase shift variations during operation. Lee et al. [80] applied a non-proportionality factor and a non-proportional strain hardening coefficient to the equivalent stress amplitude to account for the damaging effect of the non-proportional load.

Energy-based approaches have also been introduced to quantify fatigue damage in components under uniaxial and multiaxial loads by utilizing the product of stress and strain [84][85]. Having both stress and strain terms, energy-based damage parameters could take the material constitutive behavior into account when evaluating fatigue damage. However, due to their scalar nature, the energy-based approaches cannot represent the mechanism of fatigue failure which is attributed to the activation of slip planes within the polycrystalline grains. Therefore, the orientation of crack plane cannot be predicted by energy-based approaches.

To overcome the weak points and limitations of conventional invariant approaches, attempts have been made in recent decades to develop more advanced approaches that take into account the physical background of fatigue failure in damage assessment [86][87]. In a given set of approaches, damage parameters relate the fatigue-induced local damage in the material to the stresses and strains acting on a specific plane. The concepts of specific planes can be divided basically into two groups of 'Integral Approaches' and 'Critical Plane Approaches'. In the case of integral approach [88], the damage parameter is obtained by integrating the stress or strain terms over the entire interference planes passing through a volume element. Critical plane approaches, on the other hand consider only one specific critical plane as the preferred plane for the fatigue crack nucleation. Critical plane approaches which are classified as stress, strain or energy-based models could appropriately describe the damage behavior, particularly when multiaxial stress states exist due to multiaxial loading condition (external), or geometric constraints at notches. Critical plane models could cover both low cycle fatigue (LCF) and high cycle fatigue (HCF) regimes and are also capable of capturing the material constitutive behavior under non-proportional loading conditions. The applicability of each approach depends mostly on the material related failure mechanism. A pervasive critical plane model often consists of a combination of different loading parameters such as pure shear, pure normal or even mixed-mode parameters. In other words, a critical plane model can describe the fatigue damage mechanism along either shear or tensile planes, by incorporating different stress or strain terms governing crack initiation [89]. Although the implementation of the critical plane approaches is more complicated, they are known to be the most appropriate for describing actual fatigue failure mechanisms and for estimating both the fatigue crack initiation life and the initial crack orientation.

The general form of the critical plane damage models for the fatigue crack initiation is as follows [90]:

$$G\ (\max \tau_a, \tau_m, \sigma_{n,a}, \sigma_{n,m}, N) = 1 \quad (2\text{-}50)$$

where τ_a is the shear stress amplitude, τ_m the mean shear stress, $\sigma_{n,a}$ the normal stress amplitude and $\sigma_{n,m}$ the normal mean stress acting on the critical plane. It is generally postulated that for ductile materials the fatigue cracks initiate in shear-mode and then branch into mode-I of cracking. The first shear stress-based critical plane model was proposed by Findley in the1950s [91]:

$$\left(\frac{\Delta\tau}{2} + k\sigma_n\right)_{max} = \sqrt{1+k^2}\,\tau_f'(2N_f)^{b_0} \quad (2\text{-}51)$$

where k is a parameter related to the normal stress sensitivity of the material, τ_f' is the shear fatigue strength coefficient, b_0 is shear fatigue strength exponent and N_f is the number of cycles to failure. Based on Findley's model, alternative shear stress is the driving force for crack nucleation, whereas normal stress promotes the growth of microscopic fatigue cracks. Stress-based critical plane approaches fit better the HCF regime, where local stresses and strains remain mainly elastic.

Similarly, the shear stress-based damage parameter by McDiarmid [92] assumes that the fatigue damage occurs on the plane with the maximum shear stress range and is related to the maximum normal stress acting on this plane:

$$\frac{\Delta\tau_{max}}{2} + \frac{t_{A,B}}{2\sigma_u}\sigma_{n,max} = \tau_f'\left(2N_f\right)^{b_0} \quad (2\text{-}52)$$

Where $\frac{\Delta\tau_{max}}{2}$ is the maximum shear stress amplitude in the critical plane, $\sigma_{n,max}$ is the maximum normal stress acting on the critical plane and σ_u is the ultimate tensile strength. $t_{A,B}$ is the shear fatigue strength for case A or B cracking, where case A and case B refer to cracks growing along the surface and into the surface, respectively.

Once the deformation becomes significantly elastic-plastic, strain-based critical plane models can better correlate the fatigue data. Brown and Miller in 1973 [93] proposed that both the cyclic shear strain and normal strain on the plane of maximum shear must be considered. According to this model the cyclic shear strain causes the crack nucleation, and the normal strain assists the crack growth:

$$\frac{\Delta\gamma_{max}}{2} + S\Delta\varepsilon_n = A\frac{\sigma_f'}{E}\left(2N_f\right)^b + B\varepsilon_f'(2N_f)^c \quad (2\text{-}53)$$

where S is a parameter related to the normal strain sensitivity of the material, σ_f' is axial fatigue strength coefficient, b is fatigue strength exponent, ε_f' is axial fatigue

ductility coefficient, c is fatigue ductility exponent and N_f is the number of cycles to failure. A and B constants are presented as follows:

$$A = 1 + \nu_e + S(1 - \nu_e) \tag{2-54}$$

$$B = 1 + \nu_p + S(1 - \nu_p) \tag{2-55}$$

where ν_e is elastic Poisson's ratio and ν_p is Poisson's ratio for fully plastic conditions.

The disadvantage of such strain based critical plane models is that the possible non-proportional hardening and its damaging effect cannot be considered. The reason is that the damage is described only in terms of strain components and cannot reflect the changes in material constitutive behavior. Therefore, critical plane approaches containing both stress and strain terms became attractive. In 1988 Fatemi and Socie [94] proposed to replace the normal strain by the normal stress term. This model is interpreted as the cyclic shear strain model modified by normal stress.

$$\frac{\Delta\gamma_{max}}{2}\left(1 + k\frac{\sigma_{n,max}}{\sigma_y}\right) = \frac{\tau_f'}{G}\left(2N_f\right)^{b_0} + \gamma_f'(2N_f)^{c_0} \tag{2-56}$$

In this model the parameters that govern fatigue damage are the maximum shear strain amplitude $\frac{\Delta\gamma_{max}}{2}$ and the maximum normal stress $\sigma_{n,max}$ acting on the plane of the maximum shear strain. The right side of the equation corresponds to the shear strain-lifetime curve of the respective material. In the absence of experimental data, some approximation methods based on axial fatigue properties have been proposed as follows [95]:

$$P_{FS} = \left[(1 + \nu_e)\frac{\sigma_f'}{E}(2N_f)^b + (1 + \nu_p)\varepsilon_f'(2N_f)^c\right]\left[1 + k\frac{\sigma_f'}{2\sigma_y}(2N_f)^b\right] \tag{2-57}$$

Based on the FS parameter, similar to the previously mentioned models, cyclic shear strain is the main cause of fatigue crack initiation, and the maximum normal stress on the crack plane may assist or resist crack formation and small crack propagation due to the friction and interlocking effects between opposite crack surfaces. This concept was investigated through a number of studies by evaluating the initiation and propagation of fatigue cracks for different materials and geometries subjected to various biaxial and multiaxial load paths. It was found that under similar normal and shear strain amplitudes, increasing the tensile mean stress normal to the maximum shear strain plane increases the fatigue crack growth rate and decreases the fatigue life as a result. Similarly, the application of compressive normal stress to the shear

plane reduces the growth rate of fatigue cracks, which can be described by the increase in friction between the opposite crack surfaces and the resulting interlocking effect. This hypothesis was proven by observing the fracture surface profiles and the fatigue crack front. Accordingly, the other advantage of the FS damage parameter is that thanks to the maximum normal stress term of the parameter, not only the non-proportional hardening damaging effect but also the mean stress effect can be included in the fatigue damage evaluations [96][97][98]. Another major difference between the FS damage model and the previously mentioned models, e.g., Findley, is that the normal stress term in FS model is multiplied by the shear strain amplitude, meaning that without cyclic shear strain the damage value would be zero, whereas the earlier models were built on the summation of shear and maximum normal stress terms. This allows a non-zero fatigue damage to be predicted on a plane where only static normal stress exists.

Gates and Fatemi [75] proposed a modified version of FS damage parameter by replacing the yield strength term with the product of shear strain range on the maximum shear plane and shear modulus, namely the shear stress range ($G\Delta\gamma$). An improvement in the prediction of fatigue life has been achieved with the modified FS model, while retaining all the advantages and physical significance of the FS model. In other words, the interaction between the normal and shear stress/strain components which varies with the load level can be incorporated through the modified FS parameter. In the meantime, no additional empirical fitting constants are required. As with the original FS parameter, the right-hand side of the model equation linking the values of the damage parameter to the fatigue life based on the shear strain life properties could also be formulated based on the axial strain life properties:

$$\frac{\Delta\gamma_{max}}{2}\left(1+k\frac{\sigma_{n,max}}{G\Delta\gamma}\right)=\left[(1+\nu_e)\frac{\sigma_f'}{E}(2N_f)^b+(1+\nu_p)\varepsilon_f'(2N_f)^c\right]+k\frac{\sigma_f'}{4G}(2N_f)^b \qquad (2\text{-}58)$$

For more brittle materials, where cracks tend to start and grow on maximum principal plane, the Smith-Watson-Topper (SWT) parameter [99] has proved to be reasonably successful in quantifying the fatigue damage under a variety of multiaxial loading conditions [100][101]. The SWT parameter, which is based on the product of maximum principal strain amplitude, $\frac{\Delta\varepsilon_1}{2}$, and maximum normal stress on the principal plane, $\sigma_{n,max}$, is expressed in Equation 2-59:

$$\frac{\Delta\varepsilon_1}{2}\sigma_{n,max}=\frac{\sigma_f'^{\,2}}{E}(2N_f)^{2b}+\sigma_f'\varepsilon_f'(2N_f)^{b+c} \qquad (2\text{-}59)$$

whereby the maximum normal stress term, similar to the FS parameter, can include the mean stress effect. In the event that large mean compressive stresses are present, the SWT parameter may lead to non-conservative prediction results despite its acceptance. To overcome this problem Kujawski in 2014 proposed a deviatoric SWT parameter that functions only based on the distortion energy. This improved the correlation of experimental and predicted fatigue lives where large compressive mean stresses exist [102].

Energy-based approaches define the normal and shear work on a critical plane. As such, the model proposed by Liu in 1993 is the extension of Virtual Strain Energy (VSE) parameter [103]. Based on this model, either maximum tensile work plane or maximum shear work plane can be potentially the critical plane. Therefore, the amount of VSE must be determined on both planes and the plane with the maximum VSE would be known as the critical plane. The following equation presents the VSE parameter where tensile failure mode is of concern:

$$\Delta W_I = (\Delta\sigma_n \Delta\varepsilon_n)_{max} + (\Delta\tau\Delta\gamma) = \frac{4\sigma'^2_f}{E}(2N_f)^{2b} + 4\sigma'_f\varepsilon'_f(2N_f)^{b+c} \quad (2\text{-}60)$$

Similarly, the amount VSE can be defined assuming shear failure mode. As seen this model consists of both elastic and plastic work components. VSE, however, does not directly include the mean stress effect into the damage evaluation. To overcome this drawback Chu [104] and Glinka et al. [105] added the maximum normal and shear stress terms on a certain plane into the energy-based damage models. The model by Chu is expressed as follows:

$$\Delta W^* = (\sigma_{n,max}\frac{\Delta\varepsilon}{2} + \tau_{n,max}\frac{\Delta\gamma}{2})_{max} \quad (2\text{-}61)$$

and here is the one by Glinka:

$$\Delta W^* = \frac{\Delta\tau}{2}\frac{\Delta\gamma}{2}\left(\frac{\sigma'_f}{\sigma'_f - \sigma_{n,max}} + \frac{\tau'_f}{\tau'_f - \tau_{n,max}}\right) \quad (2\text{-}62)$$

Models by Chu and Glinka, unlike Liu's model do not account for the axial and shear modes separately but a combining effect of normal and shear work, in terms of single damage parameter, on a specific plane.

The performance of multiaxial fatigue damage parameters depends on the variety of aspects that can be considered by the damage parameter and the resulting accuracy in the correlation of experimental results and predictions. These aspects include

material type, changes in material constitution behavior, mean stress effect, various complex multiaxial load combinations including different load paths, with and without non-proportionality. A damage model must have such characteristics that fatigue life of components under different conditions can be reliably predicted.

As discussed, the FS model is known for its general applicability to a wide range of materials such as different steels, aluminum alloys and super alloys under proportional or non-proportional multiaxial loading conditions. The other advantage of the FS model is the ability to account for the influence of mean stresses in the damage assessments [98][100][101][106][107][82][108][85].

Nevertheless, it must be acknowledged that critical plane approaches such as FS model, although effective for predicting multiaxial fatigue, have inherent limitations. These models are phenomenological and rely on macroscopic stress-strain data, without 'explicitly' accounting for microstructural features like grain orientation, phase distribution, or local heterogeneities—factors especially important in welded joints with sharp microstructural gradients and residual stress fields. To address this, recent research has explored microstructure-sensitive methods using machine learning and micromechanical modeling. As such, Thomas et al. [109] demonstrate the potential of Graph Neural Networks (GNNs) to predict fatigue life by learning directly from microstructural data. By representing grains and grain boundaries as nodes and edges, GNNs capture the topological and spatial features of microstructures. Similarly, the work by Durmaz et al. [110] highlights the importance of experimentally validating microstructure-sensitive fatigue simulations through micromechanical testing. These simulations, typically based on Crystal Plasticity Finite Element Methods (CPFEM), offer a physics-based alternative to conventional models by explicitly capturing slip system activation, localized plasticity, and hardening behavior at the grain scale.

2.4.2 Current Trends in Fatigue Assessments of Welds

In most studies to date, the real effect of welding residual stresses on the high-cycle fatigue strength of welded joints is often overlooked—either by treating them as mean stresses or by making overly conservative assumptions. Typically, their influence is only reflected in experimentally determined fatigue reference curves. Recently, however, local approaches have begun to account for residual stress fields under axial

loading, particularly through Notch Stress Intensity Factors (NSIFs) and local Strain Energy Density (SED) averaged over a control volume. This has been enabled by novel numerical models that compute residual NSIFs and their evolution under fatigue loading [111][112][113]. However, these methods typically assume that the weld toe or weld root are the most critical sites for fatigue crack initiation due to high stress concentrations. In reality, the HAZ can also be a potential initiation site, depending on the loading conditions. The first study demonstrating the asymptotic nature of residual stresses near the weld toe dates back to 2006 [113]. It was shown that both thermal and residual stress fields near a V-notch tip are singular. Accordingly, fatigue damage near weld notches is governed by the intensity of both load-induced and residual stresses. This method is the extension of the more conventional NSIFs initially proposed by Lazzarin et al. [114] that were linked to the external mechanical loads. This approach has some limitations regarding the complexity of real structures under multiaxial loading conditions. First, the dependency of NSIF to the notch opening angle and second the complication of defining an equivalent NSIF for multiaxial stress states.

Wang et al. [115] investigated the effect of welding residual stresses on fatigue strength and initial crack orientation in welded T-joints under axial loading by coupling stress and energy-based fracture mechanics criteria. Residual stresses were first calculated numerically, and fatigue strength was then assessed using the material's ‘fatigue threshold’ and ‘fatigue limit’. Results of this work showed good agreement with the IIW recommendations [116] suggesting that the influence of residual stresses depends on the applied stress ratio (R). Accordingly, for stress ratios above 0.5, the effect of residual stresses is minor, though not entirely negligible. However, for stress ratios below 0.5, their influence becomes more significant. It was also concluded that residual stresses may affect the orientation of fatigue cracks. Experimental validation of this finding has been deferred to future studies.

In the field of critical plane approaches, it is commonly known that the tensile residual stress component normal to the critical damage plane is mostly detrimental. Because it increases the probability of fatigue crack nucleation as well as the rate of fatigue crack growth. Thus, in multiaxial fatigue assessment of welds, the direction of the mean and residual stresses with respect to the damage plane is important to be taken into account [86].

Bäckström and Marquis studied the applicability of three damage parameters including maximum principal stress range, maximum shear stress range, and a modified critical plane model over a significant number of biaxial fatigue test data from welded joints based on hot spot stresses. The critical plane model proved most effective. However, actual welding residual stresses were not calculated; instead, normal stresses up to the base material's yield strength were assumed on the critical damage planes to account for their effect [117].

To the best of the author's knowledge, the only study in the literature that applies the critical plane approach while explicitly accounting for the actual welding residual stress field is the work by Lopez-Jauregi [118]. This work studied the influence of residual stresses in butt welds under uniaxial fatigue loading. Using the nominal stress-based critical plane approach by Papadopoulos [90] and Carpinteri et al. [119], relatively good results were reported. This approach determines the critical plane orientation based on the averaged direction of the principal stresses over the loading history. However, the calculated welding residual stress field was not experimentally validated, and uncertainties in crack orientation estimation were not addressed.

The comparison of the Fatemi-Socie as a critical plane damage model with the von Mises equivalent strain parameter as an invariant model is shown in Figure 2.11. In this study, notched and un-notched metallic specimens under multiaxial constant amplitude fatigue loading are investigated by Gates et al. [75]. The resulting life predictions, for both notched and un-notched specimens by the critical plane damage model showed clear improvement in the scatter band for axial, torsional, in-phase and out-of-phase loading conditions [75].

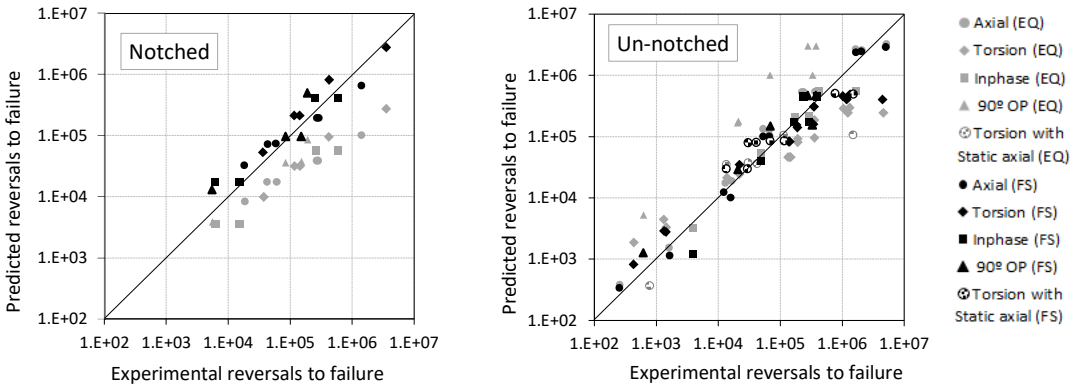

Figure 2.11 Predicted versus experimental lives for the notched and un-notched specimens [75] based on the equivalent von Mises strain and Fatemi-Socie critical plane parameters.

Chapter 3 Experimental Program

3.1 Material Selection

The material under investigation is constructional steel S355J2H. According to the reference normative EN 10210-2:2016, this steel contains a weight amount of carbon smaller than 0.22%, and an equivalent amount of carbon smaller than 0.45%. At room temperature (20°C) the yield strength is higher than 355 MPa, the tensile strength is in the range 510 to 680 MPa, and the elongation at failure is greater than 22% [120]. This material, which is extensively used in the manufacture of technical components and structures, is characterized by a ferritic-pearlitic microstructure and an average hardness of 180 HV10. The chemical composition of the material was determined by spectrometry, and the average values of the measurements are given in Table 3.1.

The main objective of this study was to investigate the influence of different welding aspects on the multiaxial fatigue behavior of welds for general applications. One of these key aspects is the microstructural evolution during welding that may arise in a variety of materials. The main motivation for the choice of this material, apart from its broad application, was above all its significant phase transformations during terms of heating and cooling in the weld seam and the adjacent area.

Three batches of tubular material were delivered with different dimensions to be used in different stages of the project, namely characterization of welding residual stresses [121], relaxation of welding residual stresses [122] and the multiaxial fatigue assessments. All batches had the same nominal chemical composition; however, the mechanical properties of the different batches were not the same. The reason for procuring tubes with different dimensions at different stages of the project was the size limitation of the available equipment, e.g., for residual stress measurements and

fatigue testing. It was therefore not possible to use an identical geometry and material for the entire project, although this would have been desirable.

Table 3.1 Chemical composition (%) of the welded sample in the base material.

C	Si	Mn	P	S	Mg	Cu	Cr	Ni	Mo
0.141	0.154	1.352	0.001	<0.001	<0.001	0.103	0.096	0.046	0.014
Ti	**Al**	**Sn**	**Co**	**Ta**	**V**	**Nb**	**B**	**W**	
0.011	0.008	0.001	0.003	<0.01	0.097	0.001	<0.001	<0.01	

3.2 Specimen Design and Fabrication

Two different types of specimens were fabricated for use in this study: welded tubular specimens and material characterization samples. Welded specimens used for residual stress studies and fatigue lifetime evaluations had three sizes, as mentioned in Section 3.1. Although variations in the size of weld specimens were necessary due to equipment limitations, all specimens shared the same essential geometric and metallurgical characteristics. Each specimen was machined from raw seamless tubing, and single-pass bead-on-tube welds were applied at the mid-length using fusion-welding techniques. Temperature profiles were recorded on some specimens using thermocouples at various locations on the material near the weld. Of the weld specimens, only details of the fatigue specimens are given in this section and are shown in Figure 3.1. Detailed information on the residual stress specimens is given in [120] and [122]. For the welding of the fatigue specimens shown in Figure 3.1, the Metal Active Gas (MAG) welding process was used, with the welding current was set to 150 Amperes, the voltage was 18.0 Volts, and the welding speed was 50.6 centimeters per minute. The arrangement of thermocouples for temperature measurements during welding of the fatigue specimens and the measurement results on some thermocouples are shown in Figure 3.2. Of all fatigue test specimens, half were preserved in the As-Welded condition (AW), and the rest were Heat-Treated (HT) to release the welding residual stresses for further comparisons. The corresponding heat treatment was carried out in a vacuum furnace at 560°C for 30 minutes.

The material characterization samples, on the other hand, were mostly full round samples in addition to a few tubular ones made from the same tubular raw material. Manufacturing these samples out of the tube-wall imposed a size restriction in the

design of the samples, so that the (outside) diameter could not be larger than the wall thickness of the raw material. Since the shear stress under torsion in the elastic-plastic state has a non-linear distribution over the cross-section, it is recommended to use thin-walled specimens for torsion tests in order to ensure an almost uniform stress distribution along the tube thickness. However, with such small diameters, it was complicated and expensive to produce true thin-walled tubular samples. This size limitation caused another problem in conducting strain-controlled torsion and tension-torsion tests, as there was no possibility of using axial-torsion extensometer that can fit such small sample size. Of all samples for material characterization, only half were made from the material in the delivery condition (BM samples). For the remainder, the material was previously heat-treated with Gleeble to simulate the microstructure of the HAZ in the crack-prone area, namely HAZ near-field (HAZ samples). The geometries of the solid and tubular specimens for material characterization are given in Figure 3.3.

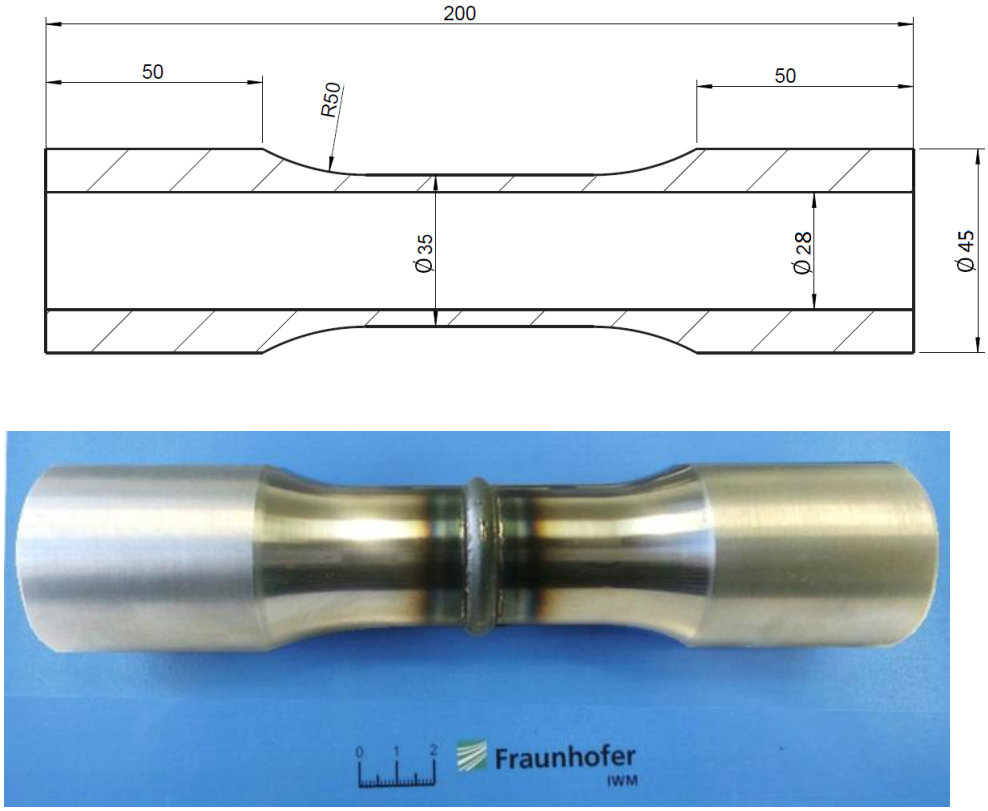

Figure 3.1 Geometry of fatigue weld specimens.

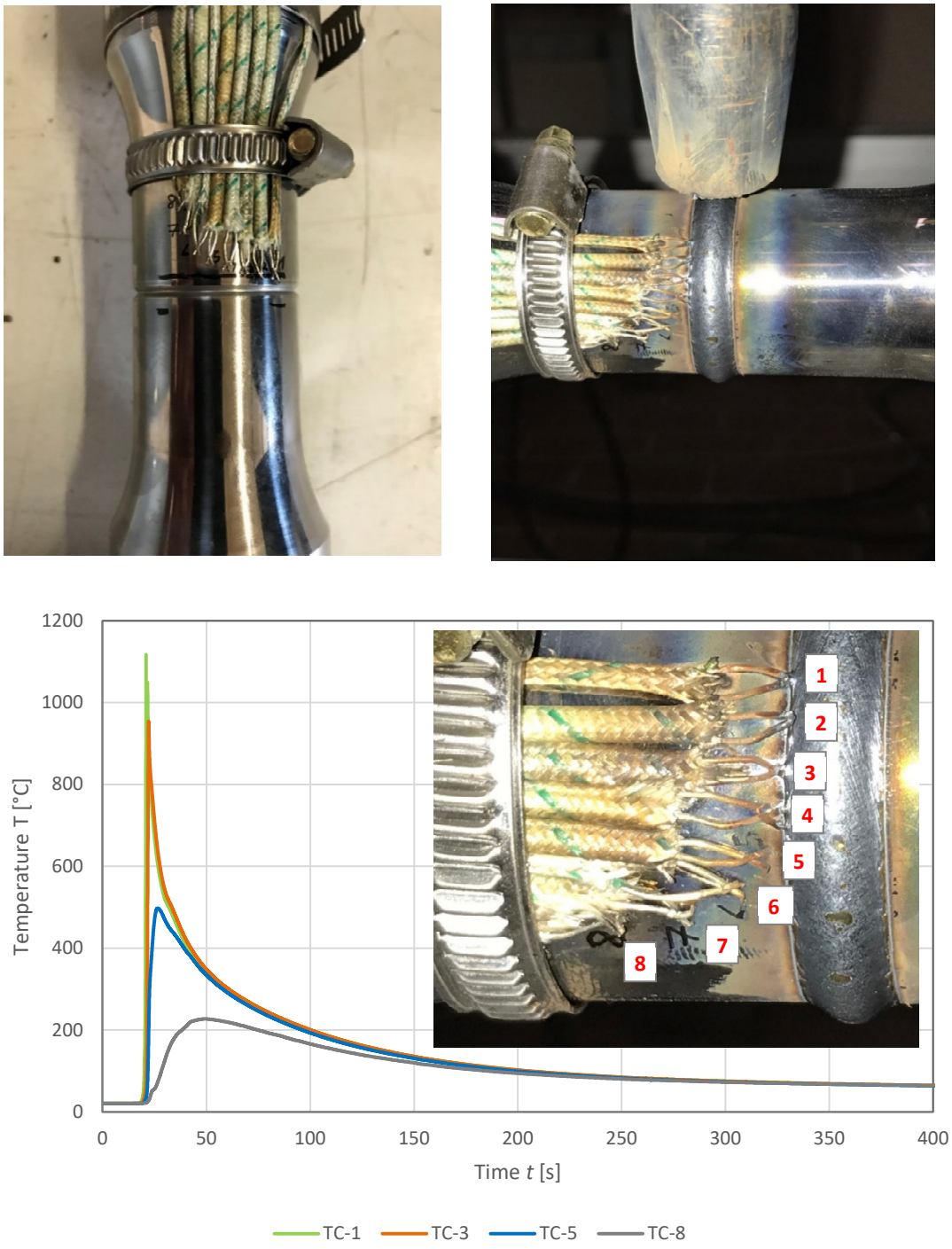

Figure 3.2 Temperature measurement during welding; position of thermo-elements and the measurement results for thermocouples 1, 3, 5 and 8 (TC-1, TC-3, TC-5 and TC-8).

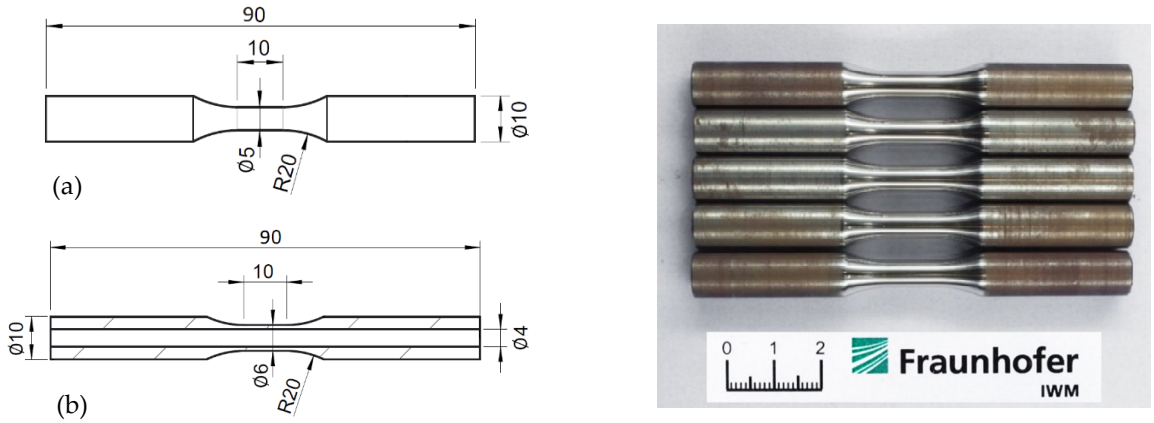

Figure 3.3 Geomerty of material characterization samples; (a) full solid smooth specimen and (b) tubular smooth specimen.

3.3 Welding Residual Stress Measurement

In order to get a profound insight into the distribution of residual stresses over the entire cross-section, advanced methods of x-ray and neutron diffraction were used alongside each other. These accurate measurements were later used as a powerful tool for the verification of the simulation results.

3.3.1 Surface Residual Stresses

The surface welding residual stresses were measured in each of the four quadrants of the weld specimen using x-ray diffraction technique. Measurements were conducted at the Institute of Joining and Welding (ifs) in TU-Braunschweig. The experimental setup for x-ray diffraction is shown in Figure 3.4 (a). To generate *Cr-Kα* x-rays, a middle point free 8-axis diffractometer with a voltage of 35 kV and an exposure of 30 mA was used along with a collimator of 2 mm diameter. For the diffraction angle (θ) between 74.5° and 81.5°, the tilt angle of {211} ferrite lattice plane (Ψ) was set to 0°, 13°, 18°, 30°, 39°, 42°, and 45° in order to record the interference lines. Peak position of the interference lines was defined based on the center of gravity. The residual stresses were finally determined using the method $sin^2\psi$ [123], with elasticity constants set to E = 206 (GPa), $\frac{1}{2}S_2 = 6.08\ \mathrm{E}^{-6}$ (MPa^{-1}) and ν = 0.28.

Any deformation in the crystal lattice can alter the inter-planar lattice spacing. By quantifying the alteration of lattice spacing along with the Bragg's theory, the residual stresses in the material can be determined [124][125]. Bragg's equation is given as follows:

$$n\lambda = 2d \sin\theta \tag{3-1}$$

where d is the lattice spacing, θ is the diffraction angle, λ is wavelength and n is the number of wavelengths. Once the lattice spacing of the deformed material and the stress-free reference lattice spacing d_0 are known, then the elastic strain would be straightforward to be calculated using Equation 3-2:

$$\varepsilon = \frac{d-d_0}{d_0} \tag{3-2}$$

Residual stress components, σ_{ii}, can be then calculated according to Hooke's law and by using the measured strain components, ε_{ii}, and the elastic constants E and ν:

$$\sigma_{ii} = \frac{E}{1+\nu}\varepsilon_{ii} + \frac{\nu E}{(1+\nu)(1-2\nu)}\sum \varepsilon_{jj} \tag{3-3}$$

3.3.2 In-depth Residual Stresses

To measure the depth profile of residual stresses in the material, neutron diffraction method (ND) was applied using the neutron strain scanner instrument E3 at the Helmholtz Center for Materials and Energy (HZB) in Berlin, utilizing the neutron flux provided by the Berlin Experimental Reactor II (BER II). The experimental setup for neutron diffraction is shown in Figure 3.4 (b). These measurements were performed only over a longitudinal section at 180° from the weld start point.

The lattice spacing was measured along the intersection line between the incident and scattered beams. {211} ferritic peak and a measurement volume of 2×2×2 mm^3 were chosen for the measurements. The attempt was made to keep the measurement points far enough away from the surface so that the entire measurement volume remains within the material and the surface effect is reduced. Similar to x-rays, for the neutron diffraction method the reference stress-free lattice spacing d_0 must be defined. A comb specimen was produced by Electrical Discharge Machining (EDM) out of a weld specimen containing all material regions, consisting of weld area, HAZ and base material. The dimensions of the comb specimen were chosen so as to ensure that the entire gauge volume is completely within the material and that in the meantime all stress components are relieved in all directions.

The elastic strains were measured in three orthonormal directions to allow all stress and strain components to be determined. For this purpose, the position of the specimen with respect to the measuring device was changed so that the residual stresses could be specified in the main directions, namely along the specimen axis, along the weld circumference and perpendicular to the surface. Alignment of the sample in all directions of movement was made using theodolite and by scanning the neutron intensity. The neutron diffraction measurements were performed according to the guidelines given in [126].

(a)

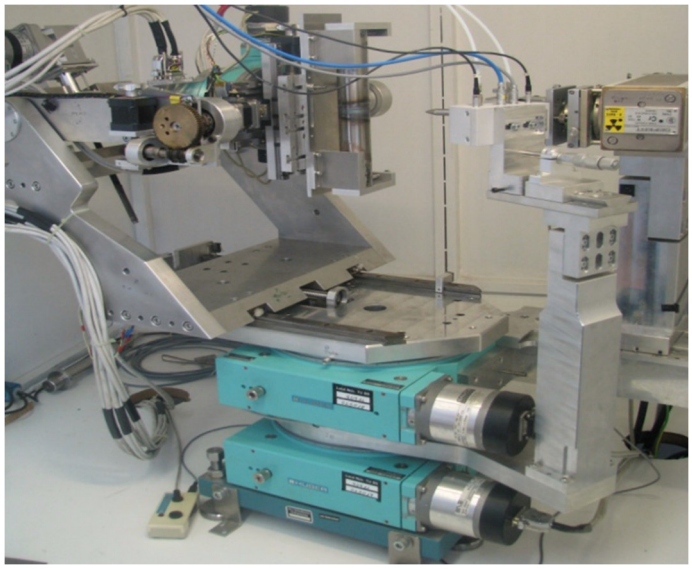

(b)

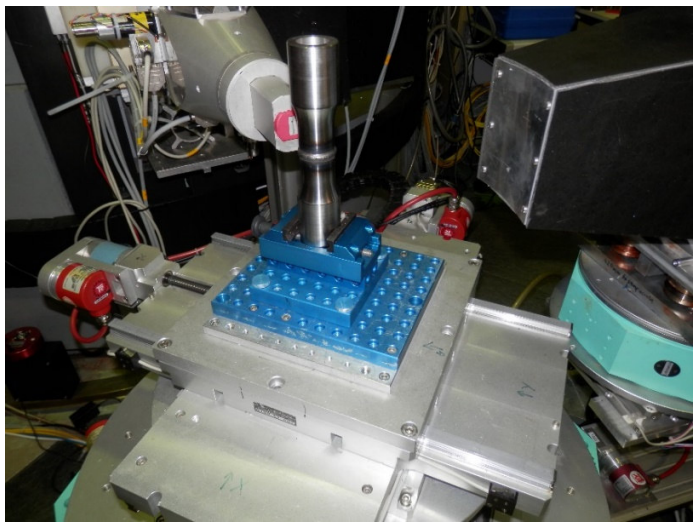

Figure 3.4 Diffraction measurement equipment; (a) x-ray, (b) Neutron.

3.4 Microstructure Analysis and Hardness Measurement

One of the weld specimens was cut to allow cross-sectional examinations. The position of the examined cross-section is 180° away from the starting point of the weld. This was to avoid the influence of reheating on the microstructural features. The cut surface was ground and polished in a certain number of steps. In the first step, the surface was leveled using a Struers LaboPol-6 semi-automatic grinder with a 320 μm grit grinding wheel, removing most of the deformations caused by the cutting process. In the next step, the Buehler AutoMet 300 automatic polishing machine was used with a sequence of papers of different grit sizes. The 9-micron polishing step aimed to refine the scratch pattern and reduce the deformation zone. The following 3-micron step served to eliminate the deformation caused by the previous polishing step and to reduce the size of the scratches. The final polishing step was performed using OPS (Oxide Polishing Suspension), intended to result in a mirror-like and deformation-free specimen surface. After polishing, metallographic etching was performed to visualize grain boundaries, alloy features, etc. For this purpose, the surface was immersed in a 2% Nital solution for 8 seconds. After the preparations, the metallographic microstructure was visualized under an Aristomet light microscope, which allows magnifications up to 1000x.

In addition to the microstructural investigations, a field hardness test was also carried out. Hardness is defined as the resistance of a material to localized plastic deformation by a standard source. It is not considered a fundamental property of a material, but is related to yield strength, tensile strength, and other factors [127]. The Vickers hardness test was chosen for the specimen studied because it has the widest scale among hardness tests and is applicable to all metals. The hardness measurement was performed using a Qness Q30a+ micro hardness tester (ATM Qness GmbH, Mammelzen, Germany), with data analysis performed by Qpix Control2 software, and the procedure respects the HV1 standards. This test is suggested by DIN EN ISO 6507-1 for S355 group of construction steels, and a first attempt with this load showed its suitability. The prescribed force was 1 kgf, i.e., 9.807 N, and was maintained for a duration of 10 seconds. Each impression was then measured with the microscope, with 10x magnification. A matrix of points has been created in order to see the hardness difference between BM, HAZ and Weld Material (WM). The measurement

distances were set at 0.3 mm in the axial direction and 0.2 mm in the thickness direction, resulting in a total of more than one thousand measurements.

3.5 Testing Equipment

As previously mentioned, the cyclic tests performed in the current study are classified into two main groups, namely material characterization tests on smooth specimens and fatigue tests on weld specimens. The material characterization alone comprises deformation tests and reference fatigue tests. Within the scope of material characterization, mechanical testing was carried out on the smooth specimens under uniaxial and combined axial-torsional loads, including planning, preparation and execution of fatigue and deformation tests. At KIT-IAM WK, a Zwick/Roell machine with a maximum capacity of 200 kN was used for the static tensile testing and a hydraulic machine of type Schenck PC 63N/44 (Figure 3.5) with a capacity of 60 kN was used for the uniaxial cyclic tests.

Constant amplitude cyclic torsion and tension-torsion tests were performed at Fraunhofer IWM by an Instron 8800 (servo-hydraulic) with a maximum capacity of 100 kN axial and 1 kN.m (Figure 3.6). In this machine the axial and torsional movements are controlled by two separate valves, so they can be driven independently from each other. For the performance of the material tests, the Instron software “WaveMatrix” was used. It allows for simple setup with block programs, specifying the desired control mode, wave shape, amplitude and frequency for the axial and torsional channel in each step. A summary of mechanical tests performed on the BM and HAZ is given in the following sections.

The servo-hydraulic testing machine from the manufacturer Schenk PC 1.0N/So (Figure 3.7) was used at KIT-IAM WK for the uniaxial and multiaxial constant amplitude fatigue testing of the welded specimens. This machine has two servohydraulic pistons with a maximum axial force of 400 kN, a maximum torque of 4 kN.m and is controlled by the "MTS FlexTest40" program. The specimens were clamped between two hydraulic clamping jaws, of which the upper one was rigidly connected to the machine frame and the lower one with the pistons located below, which apply forces and moments.

In all tests, the alignment of the machine was controlled in accordance with ASTM Standard E1012 (2009) to be within a maximum bending strain of 5% at an axial strain of 1000 microstrains. A reference specimen with two arrays of four strain gauges (eight gauges total) placed circumferentially around its upper- and lower-gauge section, was used for the alignment measurements.

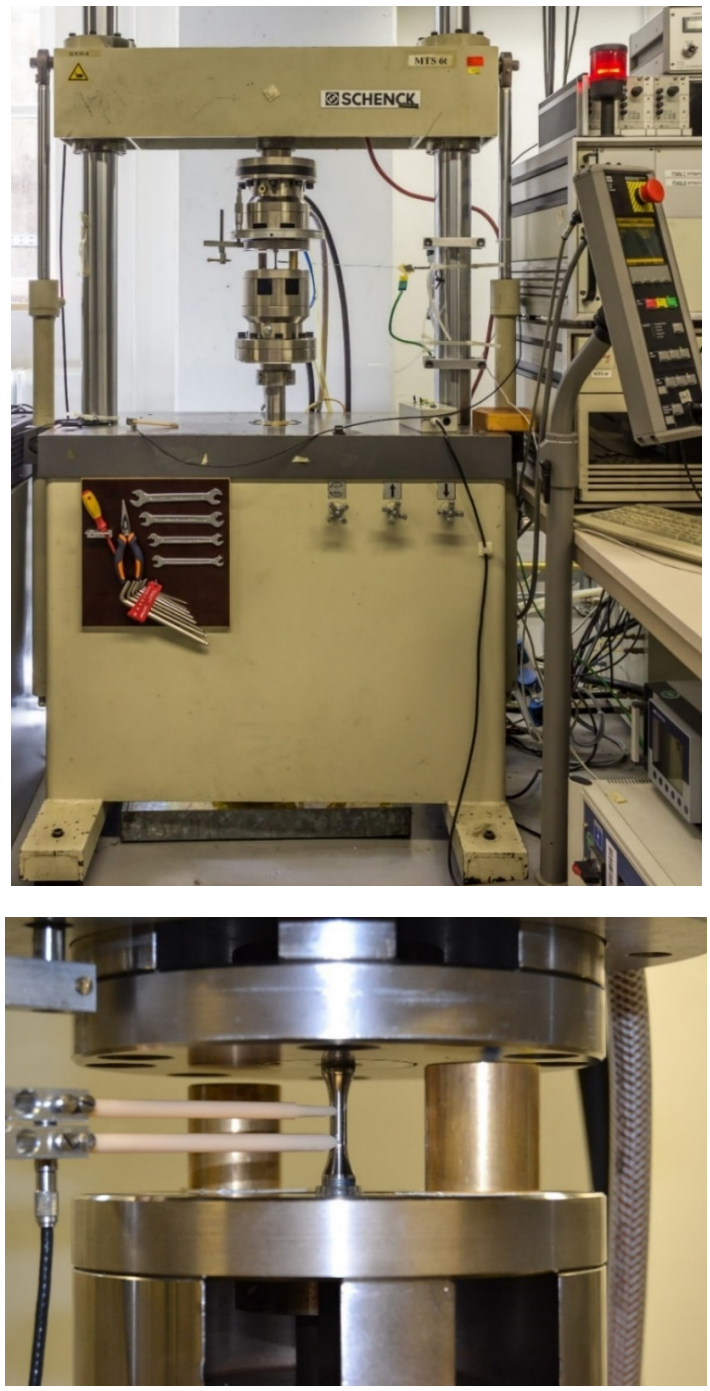

Figure 3.5 Schenck PC 63N/44 tension-compression machine at KIT-IAM WK.

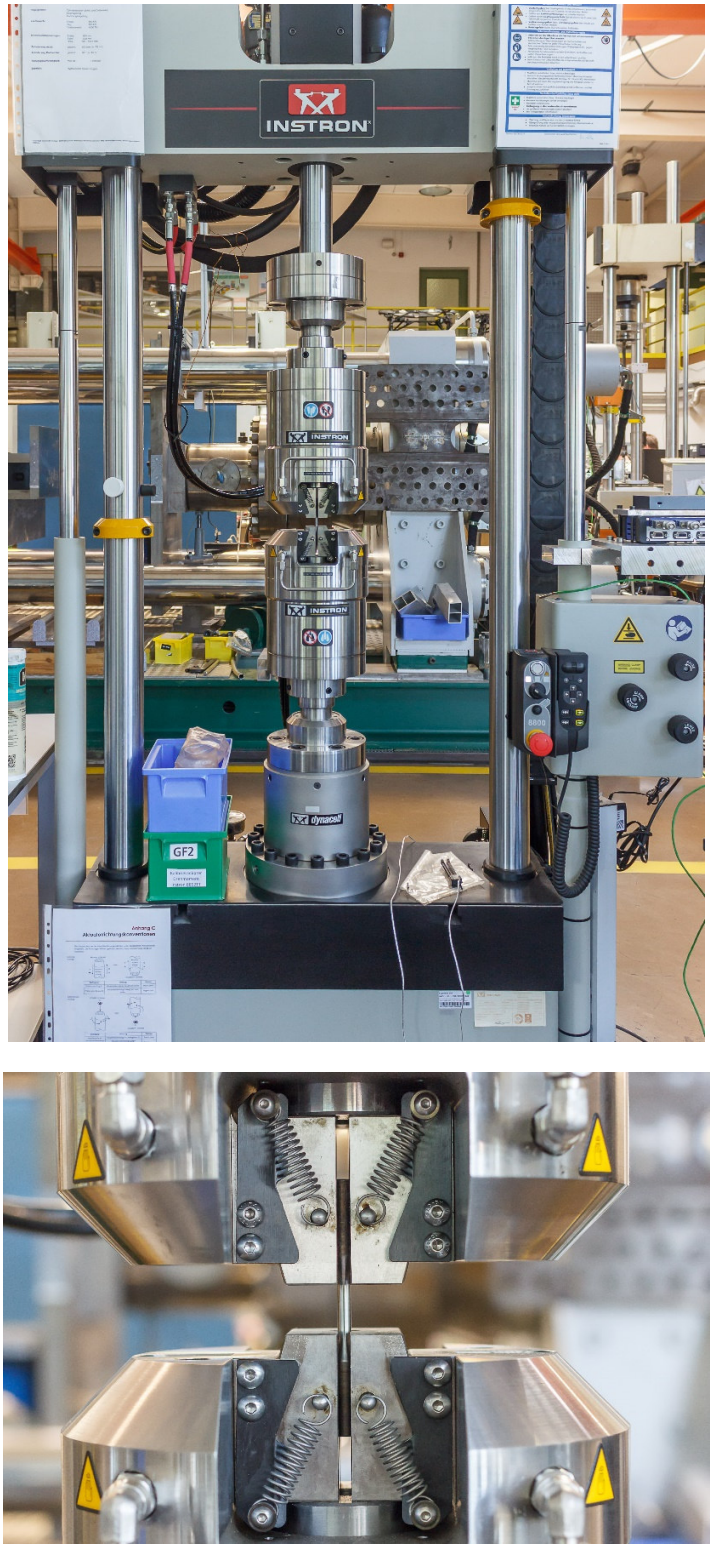

Figure 3.6 Instron 8800 tension-torsion machine at Fraunhofer IWM.

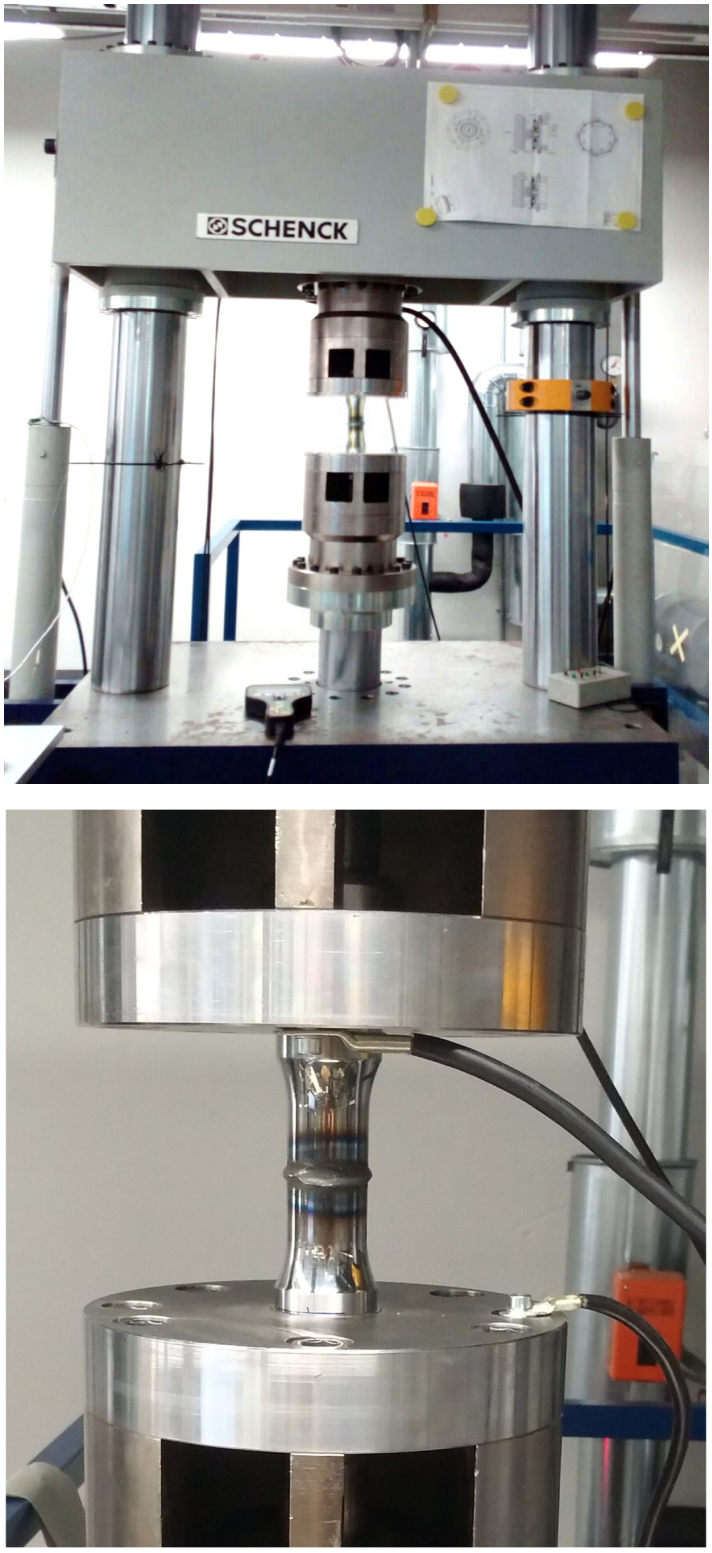

Figure 3.7 Schenck PC 1.0N/So tension-torsion machine at KIT-IAM WK.

3.6 Crack Monitoring Techniques

The direct replica technique was used to reproduce the surface topography of a sample that cannot be observed directly with the microscope. The resulting replica gives an inverted topography image. This technique is employed in general when the direct examination of the sample is not possible. In this case, a reproduction of the surface was required to record the initiation and growth of small cracks in the fatigue test. The replica technique allows the detection of short surface cracks in smooth specimens. In both LCF and HCF regimes, tests were interrupted after increments of 5% steps of the estimated lifetime. Acetate foils of 30μm thickness were dissolved in acetone solution and placed on the specimen surface. After drying, the foil contains the negative pattern of the crack on the surface of the specimen. The foils were then investigated by light microscope in reverse order. The first step to take replica is cleaning the specimen surface with paper soaked in acetone. A piece of acetate foil of appropriate size was cut and immersed in the acetone CH3COCH3 solution for a duration of approximately one second and put immediately on the specimen. If the immersion duration is longer, the acetate foil tends to melt, while if the duration is shorter, the foil is not softened enough to adhere to the specimen. If the procedure is carried out properly, the foil adheres perfectly and autonomously to the specimen. Then, it is necessary to wait until the acetone has evaporated and the foil is completely dry (approximately three minutes). At this point it is possible to remove slowly the foil from the specimen. The replicas were then located on the glass slides. Each glass corresponds to a determined percentage of the estimated lifetime of the specimen, i.e., a specified number of cycles. As already pointed out, in this investigation it is important to run the fatigue test until the final failure. Only in this way can the main crack that leads to the final fracture be identified, allowing its initiation and propagation to be examined. The replica taken before the beginning of the test can show if a scratch or other element on the specimen surface acted as stress concentrator for the nucleation of the crack. Usually approximately 20 replicas were taken for each specimen. This corresponds to 5% of the predicted lifetime. In order to obtain reliable lifetime data, it may be useful to perform a fatigue test using the same parameters. This way the association between lifetime percentage and number of cycles is more precise. In order to investigate the development of the crack, the replicas were analyzed backwards, i.e., starting from the replica closer to the final failure until the

one taken before the test (N = 0 cycles). They were analyzed by means of the microscope, and the crack length was measured linearly. The microscope used for the investigation was the Light Microscope Leica Aristomet, while the software was Olympus Stream Enterprise. The magnification was 50x.

3.7 Testing Program

In the course of this investigation, several different tests were carried out to substantiate the analytical investigations. Material characterization tests and weld specimen fatigue tests were the most important categories in this context. A prerequisite for an accurate analytical evaluation of fatigue is a thorough knowledge of the various aspects of the fatigue phenomenon and the properties of the material under investigation. Especially in high temperature processes, such as welds, microstructural development of the materials should be considered. Beside material characterization tests, fatigue tests on the welded specimens were performed to validate the approaches to multiaxial fatigue assessment implemented in this study.

An overview of the loading conditions applied, and the information obtained from the individual test types is given in the following sections. Table 3.2 outlines the objectives of the test program in more detail. Experimental results are summarized in Chapter 4. In addition, Chapter 6 and Chapter 7 offer an interactive overview of the experimental and analytical results.

Table 3.2 Summary of the objectives for the tests included in the experimental program.

		Specimen type			
		Solid cylindrical 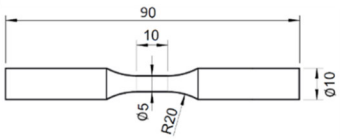	Un-notched tubular 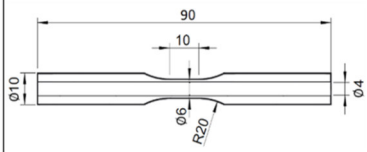	Welded tubular 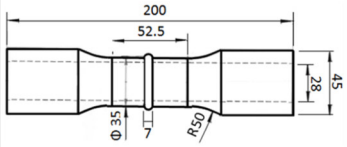	
		S355J2H-Base / S355J2H-Gleeble	S355J2H-Base	As welded	Stress relieved
Test/Loading type	**Deformation**	**Load type:** - Pure tension (strain-controlled) - Pure torsion (deformation-controlled) - IP and OP tension-torsion (deformation-controlled) **Obtain:** - Monotonic and cyclic material property - Non-proportional hardening - Stable and transient constitutive behavior - Differences in deformation properties of base material and HAZ **Evaluate** - Yield criteria - Cyclic plasticity models	**Load type:** - Pure torsion (deformation -controlled) - IP and OP tension-torsion (deformation -controlled) **Goal:** - Validation of the deformation test results from solid cylindrical samples, using semi-thin-walled samples. **Evaluate** - Cyclic plasticity models	N/A	
	Constant amplitude fatigue	**Load type:** - Pure tension (strain/load-controlled) - Pure torsion (load-controlled) - IP and OP tension-torsion (load-controlled) **Obtain:** - S-N fatigue properties - ε-N fatigue properties **Evaluate:** - Multiaxial fatigue damage parameter - Proportion of crack initiation vs crack propagation lifetimes	N/A	**Load type:** - Pure tension (load-controlled) - Pure torsion (load-controlled) - IP and OP tension-torsion (load-controlled) **Obtain:** - S-N fatigue curves for weld specimens **Evaluate:** - Applicability of the fatigue damage parameter for welded joints - Contribution of the welding residual stresses into the damage - Crack path/branching	

3.7.1 Material Characterization Testing

The experimental program for material characterization consisted of two main components: deformation tests and fatigue tests. Smooth specimens were utilized throughout all material characterization tests. Deformation tests encompassed monotonic tensile tests and uniaxial as well as multiaxial Incremental Step Tests (IST), aiming to characterize the plastic behavior of the materials under complex loading conditions [128]. Concurrently, LCF and HCF tests were conducted to establish fatigue baselines for each material. These baselines, in the form of stress or strain-life curves, were subsequently used for lifetime estimations. Given that the investigated material undergoes metallurgical phase transformations in the weld and its vicinity, the test program was tailored for two distinct material zones, namely the BM and HAZ, as detailed in Section 3.2. This approach involved executing all deformation and fatigue tests separately for each material. IST and fatigue tests were conducted under constant amplitude cyclic loading conditions, encompassing pure axial, pure torsional, and multiaxial axial-torsional loading. The load ratio R was consistently set to -1 (fully reversed) for all tests, with both proportional and non-proportional loading conditions considered for multiaxial loading.

3.7.1.1 Deformation Behavior Testing

Monotonic tensile tests, conducted in accordance with DIN EN ISO 6892-1:2017-02, were fundamental in determining key mechanical properties including Young's modulus, E, yield strength, σ_y, ultimate strength, σ_u, elongation at the onset of necking, A, and elongation at failure, Z. Additionally, cyclic deformation tests, specifically incremental step tests (IST), were performed to characterize the stress-strain relationship under dynamic loading conditions. The cyclic stress-strain curve can be described using a Ramberg-Osgood relationship:

$$\bar{\varepsilon}_a = \frac{\bar{\sigma}_a}{E} + \left(\frac{\bar{\sigma}_a}{\bar{K}'}\right)^{1/\bar{n}'} \tag{3-4}$$

where $\bar{K}'$ and $\bar{n}'$ are the equivalent cyclic strength coefficient and exponent respectively.

Various types of loading, including axial, torsional and multiaxial loading, were considered for testing. Multiaxial loading included both in-phase and 90° out-of-phase conditions to assess and quantify any non-proportional hardening effects in the

material. Given the high strain levels in the incremental step tests (IST), pure axial ISTs were conducted under strain-controlled conditions. However, due to the absence of a device capable of direct strain-controlled testing for pure torsional and axial-torsional loads, these tests were instead conducted using machine displacement and angular control modes. The ratio between the angular displacement and axial displacement amplitudes was selected to ensure that the ratio of calculated strains remained within the elastic range as:

$$\frac{\Delta\gamma}{2} = \sqrt{3}\frac{\Delta\varepsilon}{2} \tag{3-5}$$

The primary goal of this comprehensive deformation testing program is to evaluate the effectiveness of the applied material constitutive equations in describing the plasticity behavior of the materials under complex loading conditions. A summary of the deformation tests on smooth specimens is provided in Table 3.3 to Table 3.10.

Table 3.3 Smooth specimen: BM-Axial incremental step test matrix.

Strain-controlled				
Specimen ID	**Frequency [1/s]**	**Axial strain amplitude [%]**	**R-ratio**	**Number of Cycles (per Step)**
BM-A-01	0.05	0.05/0.1/0.2/0.3/…/1.0	-1	5
BM-A-02	0.05	0.3/0.5/0.6/1.0/1.5/2.0	-1	20

Table 3.4 Smooth specimen: BM-Torsion incremental step test matrix (Frequency: 0.1 Hz, R-ratio: -1).

Deformation-controlled			
Step number	**Angular displacement amplitude [°]**	**Torque amplitude [N.m]**	**Number of Cycles**
1	1.0	6.86	10
2	1.5	8.64	10
3	2.0	8.70	10
4	3.0	9.17	10
5	4.5	9.88	10
6	6.0	10.42	10
7	8.0	11.01	10
8	10.0	11.50	10
9	15.0	12.34	10

Table 3.5 Smooth specimen: BM-IP incremental step test matrix (Frequency: 0.1 Hz, R-ratio: -1).

Deformation-controlled					
Step number	**Axial displacement amplitude [mm]**	**Angular displacement amplitude [°]**	**Force amplitude [kN]**	**Torque amplitude [N.m]**	**Number of Cycles**
1	0.045	0.74	3.07	4.82	10
2	0.068	1.11	4.47	5.65	10
3	0.089	1.47	4.95	5.82	10
4	0.134	2.21	5.94	6.29	10
5	0.178	2.94	6.66	6.96	10
6	0.223	3.67	7.12	7.48	10
7	0.336	5.51	7.98	8.36	10

Table 3.6 Smooth specimen: BM-OP incremental step test matrix (Frequency: 0.1 Hz, R-ratio: -1).

Deformation-controlled					
Step number	**Axial displacement amplitude [mm]**	**Angular displacement amplitude [°]**	**Force amplitude [kN]**	**Torque amplitude [N.m]**	**Number of Cycles**
1	0.089	1.47	5.89	8.17	10
2	0.157	2.57	7.51	10.35	10
3	0.223	3.68	8.15	11.29	10
4	0.334	5.51	8.77	12.12	10

Table 3.7 Smooth specimen: HAZ-Axial incremental step test matrix.

Strain-controlled				
Specimen ID	**Frequency [1/s]**	**Axial strain amplitude [%]**	**R-ratio**	**Number of Cycles (per Step)**
HAZ-A-01	0.05	0.2/0.4/0.6/0.8/1/1.5/2	-1	100
HAZ-A-02	0.05	0.2/0.4/0.6/0.8/1	0.1	100

Table 3.8 Smooth specimen: HAZ-Torsion incremental step test matrix (Frequency: 0.1 Hz, R-ratio: -1).

Deformation-controlled			
Step number	**Angular displacement amplitude [°]**	**Torque amplitude [N.m]**	**Number of Cycles**
1	1.0	4.20	10
2	1.5	6.23	10
3	2.0	8.27	10
4	3.0	10.33	10
5	4.5	11.35	10
6	6.0	11.93	10
7	8.0	12.36	10
8	10.0	12.56	10
9	15.0	12.84	10
10	20.0	13.03	10

Table 3.9 Smooth specimen: HAZ-IP incremental step test matrix (Frequency: 0.1 Hz, R-ratio: -1).

Deformation-controlled					
Step number	**Axial displacement amplitude [mm]**	**Angular displacement amplitude [°]**	**Force amplitude [kN]**	**Torque amplitude [N.m]**	**Number of Cycles**
1	0.121	0.80	4.54	3.05	12
2	0.183	1.20	6.72	4.58	12
3	0.264	1.61	8.85	5.65	12
4	0.310	2.01	10.36	5.22	12
5	0.372	2.41	11.57	5.74	12
6	0.363	2.41	11.24	5.89	12
7	0.432	2.81	12.27	6.68	12
8	0.498	3.21	12.73	7.22	12
9	0.557	3.61	12.80	7.44	12

Table 3.10 Smooth specimen: HAZ-OP incremental step test matrix (Frequency: 0.1 Hz, R-ratio: -1).

Deformation-controlled					
Step number	**Axial displacement amplitude [mm]**	**Angular displacement amplitude [°]**	**Force amplitude [kN]**	**Torque amplitude [N.m]**	**Number of Cycles**
1	0.120	0.80	4.52	3.27	12
2	0.182	1.20	6.73	4.90	12
3	0.244	1.60	8.93	6.53	12
4	0.358	2.41	11.65	8.77	12
5	0.428	2.80	12.55	9.66	12
6	0.492	3.21	12.91	10.19	12
7	0.562	3.61	13.10	10.57	12
8	0.618	4.02	13.20	10.84	12
9	0.683	4.42	13.25	11.00	12

In pure axial cyclic testing, determining stresses from the testing machine and strains from the extensometer was straightforward. However, in torsional and biaxial cyclic testing, a workaround was required to obtain the desired quantities [128]. Since direct strain measurement was not possible during torsional and biaxial fatigue tests, a calibration model was used to establish a relationship between the machine actuator's angle and displacement and the specimen's shear and tensile strain. The model assumes that the machine deforms linearly and elastically with a constant stiffness, while the specimen has a constant stiffness in the elastic range but a variable stiffness when plastic flow occurs. In this model, the specimen and the machine are treated as two serial springs (Figure 3.8).

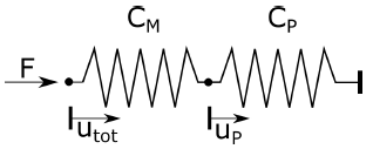

Figure 3.8 Serial springs model for calculating machine stiffness.

For serial springs, the force is the same for all springs, but the total displacement is the sum of the displacements of the individual springs. This results in an equivalent spring constant, which is expressed as follows:

$$\frac{1}{C_{eq}} = \frac{1}{C_M} + \frac{1}{C_P} \tag{3-6}$$

where C_M and C_P represent the machine stiffness and the sample stiffness in the axial direction, respectively. Given that the machine records the total displacement u_{tot}, the equivalent spring constant C_{eq} can be determined as:

$$C_{eq} = \frac{F}{u_{tot}} \tag{3-7}$$

and C_P is known as:

$$C_P = \frac{F}{u_P} \tag{3-8}$$

where u_P is the sample displacement. In an elastic mode, the stiffness of the sample can be easily calculated as follows:

$$C_P = \frac{EA}{l} \tag{3-9}$$

where l is the sample effective gauge length. This calculation uses the results from a monotonic elastic test. Knowing C_{eq} and C_P, the machine stiffness, C_M, can be estimated, assuming it remains nearly constant across the load ranges tested in this study. With C_M known, the normal strain in the sample can be calculated as follows:

$$\varepsilon = \frac{1}{l}\left(u_{tot} - \frac{F}{C_M}\right) \tag{3-10}$$

To determine the relationship between the shear load acting on the specimen and the total twist angle, a similar method was applied using the torsional stiffness, C_M^{tor}:

$$\gamma = \frac{r}{l}\left(\theta_{tot} - \frac{M}{C_M^{tor}}\right) \tag{3-11}$$

where r is the radius of the gauge section. For both axial and torsional loads, the spring model incorporating the calculated machine stiffness was employed to predict the strain during an elastic-plastic monotonic test. These tests were controlled by displacement and angle, respectively. Additionally, the strains in the samples were measured with the Aramis system, as described in Section 3.7.1.3, to validate this approach.

While calculating normal stress is straightforward, it is important to account for the non-uniform distribution of shear stress across the cross-section under torsional loading. The normal stress can be calculated using Equation 3-12:

$$\sigma = \frac{F}{\pi r^2} \tag{3-12}$$

Under torsional loading, the distribution of shear stress remains linear as long as the material is within the elastic limits. However, once plastic deformation occurs, especially near the surface, the calculation of maximum shear stress requires different equations. Cyclic torsional tests typically use thin-walled tubular specimens to maintain a constant stress profile across the thickness of the wall. Due to the uneven distribution of strains during these tests, some sections of the material undergo plastic deformation while others remain elastic. This discrepancy leads to residual stresses after unloading, influenced by the material's self-restraint properties. As discussed in Section 3.2, there were limited tubular samples available for incremental step testing of BM. Even among these samples, with an outer diameter of 6 mm and a wall thickness of 1 mm, they often do not meet the thin-walled criterion. According to Nadai [129], determining shear stress requires not only the torque value but also the slope of the torque-twist angle curve. Equation 3-13 describes Nadai's formula:

$$\tau_0 = \frac{1}{2\pi {r_0}^3}\left(3T + \theta \frac{\mathrm{d}T}{\mathrm{d}\theta}\right) \tag{3-13}$$

The formula is developed for monotonic tests and is thus applicable only to the initial quarter cycle of a hysteresis loop. It has been shown that this method can also be applied to the subsequent unloading and to any sequence of cyclic torsion tests. According to Wu et al. [130], the stress-strain relationship can be established as follows:

$$\tau_0 - {\tau_0}^* = \frac{1}{2\pi {r_0}^3}\left(3(T - T^*) + (\theta - \theta^*)\frac{\mathrm{d}T}{\mathrm{d}\theta}\right) \tag{3-14}$$

where ${\tau_0}^*$ represents the surface shear stress, T^* is the torque, and θ^* denotes the angle at the last data point of the preceding half cycle. One significant limitation of Equation 3-13 and Equation 3-14 is the need to calculate the torque's derivative with respect to the twist angle, given that the data is discrete and potentially noisy. To address this issue, the torque-twist angle loops were divided into two curves: one for increasing torque values and one for decreasing, as depicted in Figure 3.9. Each curve was then fitted with a polynomial using linear regression analysis, and subsequently, the modified Nadai Equation 3-14 was applied incrementally with the analytic derivative $\frac{\mathrm{d}T}{\mathrm{d}\theta}$.

This approach is preferred over calculating the derivative discretely, such as through central differences, due to the data's noise. The polynomial degree is adjusted based on the shape of the torque-twist angle response. For the available test data, polynomial degrees ranging from two to ten were selected.

A polynomial degree of one is adequate when computing only the peak stresses, as demonstrated in Equation 3-14. Figure 3.9 illustrates an example of the fitting process. The smoothing effect is noticeable in the unloading section near the minimum torque.

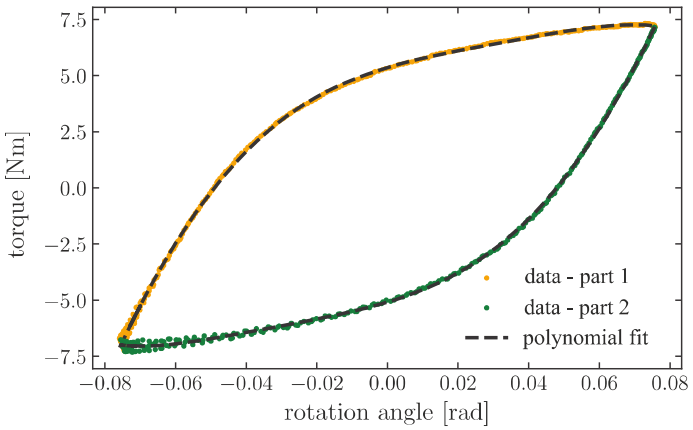

Figure 3.9 Example of the fitting process for a torsional LCF test (polynomial degree d = 5) [128].

With a diameter-to-wall thickness ratio of $d/t = 6$, as already mentioned, there is doubt whether the thin-wall assumption still applies. Therefore, a non-uniform stress profile is assumed where the shear stress τ_0 on the outer surface is related to τ_1 on the inner surface using Brown's extension of Nadai's equation [131]:

$$\tau_0 = \frac{1}{2\pi {r_0}^3}\left(3T + \theta\frac{\mathrm{d}T}{\mathrm{d}\theta}\right) + \left(\frac{r_1}{r_o}\right)^3 \tau_1 \tag{3-15}$$

Here, r_1 represents the inner radius. Since τ_1 is unknown, an approximation is given by:

$$\tau_0 = \frac{1}{2\pi}\left[\frac{3T}{{r_0}^3 - {r_1}^3} + \left(\frac{4r_0}{{r_0}^4 - {r_1}^4} - \frac{3}{{r_0}^3 - {r_1}^3}\right)\theta\frac{\mathrm{d}T}{\mathrm{d}\theta}\right] \tag{3-16}$$

This approximation holds true for the elastic and perfectly plastic scenarios. It can be confirmed that the latter equation equals Equation 3-13 when the inner radius is zero.

The stress responses derived at different strain levels in an incremental step test enable the creation of cyclic stress-strain curves. These curves can be evaluated against monotonic test results or those from other cyclic loading conditions, ensuring comparability through equivalent stress and strain measures.

3.7.1.2 Fatigue Testing under Multiaxial Loading

Fatigue tests with constant amplitude in the form of LCF and HCF axial and torsional tests were carried out on smooth specimens to provide the fatigue baselines for the subsequent lifetime assessments. Fatigue baselines, either stress-life or strain-life curves, can be converted to any other damage parameter baselines. Multiaxial in-phase and 90° out-of-phase fatigue tests were also performed to characterize the multiaxial fatigue behavior of materials, such as the dependence on multiaxial cyclic strain paths. Moreover, the establishment of this wide range of fatigue tests enables the evaluation of each damage model's ability to correlate different fatigue data and to incorporate a broad set of influencing factors e.g., varying degrees of non-proportionality and strain-path dependency, into the damage calculations. For all fatigue tests, fully reversed loading state (R = -1) and a sinus wave signal were selected.

The criterion for failure was assumed to be a stiffness drop to 90% of the mid-time stiffness. Nevertheless, all tests were conducted until final failure. Automatic amplitude and phase control were used for both channels.

Under axial load, for HCF tests where a linear elastic material response is expected, experiments were carried out load-controlled along with strain measurement. This allows the highest possible testing frequency to be used. In all HCF tests, the ratio between the torque and force amplitudes was chosen so that the contribution of normal and shear stresses based on the von Mises equivalent stress are equal:

$$\frac{\Delta\sigma}{2} = \sqrt{3}\frac{\Delta\tau}{2} \tag{3-17}$$

At higher loads where non-linear plastic deformation is likely to occur, such as LCF or IST tests, a strain-controlled set up was employed. To align these fatigue tests with the local deformation of the specimens, a uniaxial extensometer was used. Since no specific axial-torsion extensometer that could fit such small specimens was available, all HCF and LCF test under pure torsion and axial-torsional loading conditions were run load, respectively force and torque controlled. For such tests, Aramis system [132] was used to measure the local strain field on the specimen. Details on strain measurement are given in Section 3.7.1.3. However, this was a blessing in disguise as it allowed the effect of stress and strain control modes on fatigue damage to be examined. As a matter of fact, in real operating conditions the nominal load is typically load-controlled, though at the stress concentrators the strain field generally

governs the local deformation. Summary of the fatigue tests on the smooth specimens is given in Table 3.11 to Table 3.18.

Low cycle fatigue is usually described by the Coffin-Manson equation, which relates plastic strain to the fatigue life [133][134]. Morrow [135] combined the elastic strain and plastic strain into a total strain and integrated the Basquin [136] relation, which describes the high-cycle behavior at low strain in the elastic state, into the Coffin-Manson equation:

$$\frac{\Delta\varepsilon}{2} = \frac{\Delta\varepsilon_e}{2} + \frac{\Delta\varepsilon_p}{2} = \frac{\sigma_f'}{E}\left(2N_f\right)^b + \varepsilon_f'\left(2N_f\right)^c \tag{3-18}$$

where $\frac{\Delta\varepsilon}{2}$ is the total strain amplitude and $\frac{\Delta\varepsilon_e}{2}$ and $\frac{\Delta\varepsilon_p}{2}$ are elastic and plastic strain amplitudes respectively. Similarly, strain-life curves can be presented in terms of shear strain amplitude as follows:

$$\frac{\Delta\gamma}{2} = \frac{\Delta\gamma_e}{2} + \frac{\Delta\gamma_p}{2} = \frac{\tau_f'}{G}\left(2N_f\right)^{b_0} + \gamma_f'\left(2N_f\right)^{c_0} \tag{3-19}$$

where $\frac{\Delta\gamma}{2}$ is the total shear strain amplitude associated with a fatigue life of N_f, τ_f' is the shear fatigue strength coefficients, b_0 is the shear fatigue strength exponent, γ_f' is the shear fatigue ductility coefficient, and c_0 is the shear fatigue ductility exponent.

The well-established Fatemi-Socie (FS) parameter was employed to fit a critical plane damage model. To reproduce the Wöhler curve in terms of the FS parameter versus fatigue life, each stress or strain term of the parameter for a given slip plane must be defined as a function of the applied stresses and strains. A fully analytical script was developed in Python 3.7 to directly transform the stresses and strains obtained from tests on any arbitrary plane in the crystal structure. Since in the case of biaxial tension-torsion load, only one tensile and one shear stress and strain exist, the transformation equations simplify to a two-dimensional case with y and x being axial and transverse directions of the samples in the non-rotated coordinate system. Using these equations, the FS parameter can be built on any arbitrary plane. The FS parameter and the respective transformation equations are given below:

$$\mathrm{FS} = \left(\varepsilon_{xy,max}' - \varepsilon_{xy,min}'\right)\left(1 + k\frac{\sigma_{y_{max}}'}{\sigma_F}\right) \tag{3-20}$$

$$\sigma_y' = \frac{1}{2}\sigma_y + \frac{1}{2}\sigma_y\cos(2\varphi) - \tau_{xy}\sin(2\varphi) \tag{3-21}$$

$$\varepsilon'_{xy} = \frac{1}{2}\varepsilon_y \sin(2\varphi) + \varepsilon_{xy}\cos(2\varphi) \quad (3\text{-}22)$$

where $\varepsilon'_{xy,max}$ and $\varepsilon'_{xy,min}$ are the maximum and minimum values of the shear strain within one cycle on the desired plane and φ denotes the coordinate rotation angle. The values of damage parameter were calculated iteratively over every 1° plane to find the plane with maximum damage. The global stress and strain terms were input in the form of sine wave functions to simulate a loading cycle. Normal stress (σ_y) and normal strain (ε_y) were in the form of $A\sin(\omega t)$ and shear stress (τ_{xy}) and shear strain (ε_{xy}) were in the form of $A\sin(\omega t + \psi)$. A represents the stress or strain amplitude, ω is the angular frequency, t is the time and ψ is the load phase shift which is 90° in the case of out-of-phase loading.

Table 3.11 Smooth specimen: BM-Axial fatigue test matrix.

Strain-controlled						
Specimen ID	**Outer diameter [mm]**	**Frequency [1/s]**	**Force amplitude [kN]**	**Axial stress amplitude [MPa]**	**Axial strain amplitude [%]**	**Cycles to Failure (N_f)**
BM-A-01	5.06	0.125	7.70	382.0	0.4	4.24E+03
BM-A-02	4.96	0.100	7.30	377.7	0.5	5.98E+03
BM-A-03	5.05	0.083	8.30	413.7	0.6	1.54E+03
BM-A-04	4.98	0.083	8.25	423.5	0.6	2.61E+03
BM-A-05	5.03	0.0625	8.70	438.0	0.8	8.00E+02
BM-A-06	5.00	0.050	8.90	453.3	1.0	6.33E+02
Force-controlled						
Specimen ID	**Outer diameter [mm]**	**Frequency [1/s]**	**Force amplitude [kN]**	**Axial stress amplitude [MPa]**	**Axial strain amplitude [%]**	**Cycles to Failure (N_f)**
BM-A-07	4.93	20	5.85	306	0.178	3.27E+05
BM-A-08	4.94	20	5.87	306	0.178	3.24E+05
BM-A-09	4,98	20	5.90	303	0.154	3.49E+06
BM-A-10	4.98	15	6.00	308	0.181	3.31E+05
BM-A-11	5.02	20	6.02	304	0.171	4.46E+05
BM-A-12	5.01	15	6.10	310	0.191	1.66E+05
BM-A-13	5.00	15	6.10	311	0.200	1.53E+05
BM-A-14	5.05	15	6.20	309	0.175	4.61E+05
BM-A-15	4.97	15	6.20	320	0.188	8.57E+04
BM-A-16	5.02	15	7.20	364	0.300	1.27E+04

Table 3.12 Smooth specimen: BM-Torsion fatigue test matrix.

Torque-controlled						
Specimen ID	Outer diameter [mm]	Frequency [1/s]	Torque amplitude [N.m]	Shear stress amplitude [MPa]	Shear strain amplitude [%]	Cycles to Failure (N_f)
BM-T-01	4.97	5	4.81	199.6	0.331	2.33E+06
BM-T-02	5.01	5	5.17	209.5	0.315	1.18E+06
BM-T-03	5.01	5	5.37	217.7	0.348	4.43E+05
BM-T-04	5.01	5	5.62	227.7	0.383	2.12E+05
BM-T-05	4.97	1	5.79	240.4	0.502	7.84E+04
BM-T-06	5.02	3	6.12	246.8	0.552	4.25E+04
BM-T-07	5.05	2	6.33	258.2	0.608	2.72E+04
BM-T-08	4.99	1	6.53	267.7	0.861	9.10E+03
BM-T-09	5.01	1	6.85	277.0	0.809	1.08E+04
BM-T-10	5.02	1	7.32	295.3	1.110	4.80E+03
BM-T-11	5.00	2	7.40	301.5	1.010	4.45E+03

Table 3.13 Smooth specimen: BM-IP fatigue test matrix.

Force/torque controlled								
Specimen ID	Outer diameter [mm]	Frequency [1/s]	Force amplitude [kN]	Torque amplitude [N.m]	Axial stress amplitude [MPa]	Shear stress amplitude [MPa]	Von Mises stress [MPa]	Cycles to Failure (N_f)
BM-IP-01	5.00	5	4.21	3.02	213.9	122.8	301.6	3.40E+06
BM-IP-02	5.01	5	4.43	3.17	224.7	128.5	355.6	7.67E+05
BM-IP-03	5.00	5	4.76	3.39	241.9	138.1	340.1	2.38E+05
BM-IP-04	5.00	5	4.92	3.53	250.8	143.7	353.3	1.29E+05
BM-IP-05	5.01	5	5.10	3.65	259.3	147.9	364.4	6.65E+04
BM-IP-06	5.01	5	5.28	3.76	268.1	152.5	376.3	2.54E+04
BM-IP-07	5.01	3	5.46	3.89	277.4	158.0	389.6	2.26E+04
BM-IP-08	5.00	2	5.78	4.12	294.6	167.9	413.9	7.60E+03
BM-IP-09	5.03	1	6.18	4.39	311.4	176.2	436.0	5.50E+03
BM-IP-10	4.99	0.5	6.57	4.70	336.3	192.8	473.9	2.90E+03

Table 3.14 Smooth specimen: BM-OP fatigue test matrix.

Force/torque controlled								
Specimen ID	**Outer diameter [mm]**	**Frequency [1/s]**	**Force amplitude [kN]**	**Torque amplitude [N.m]**	**Axial stress amplitude [MPa]**	**Shear stress amplitude [MPa]**	**Von Mises stress [MPa]**	**Cycles to Failure (N_f)**
BM-OP-01	5.02	5	4.93	3.56	250.8	142.6	352.0	3.74E+05
BM-OP-02	5.00	5	5.26	3.76	268.2	152.5	376.4	2.25E+05
BM-OP-03	5.01	5	5.28	3.78	268.2	153.3	377.4	7.57E+04
BM-OP-04	5.01	5	5.65	4.03	285.7	162.6	401.1	1.16E+05
BM-OP-05	5.02	5	6.19	4.42	312.1	177.3	437.8	3.27E+04
BM-OP-06	5.01	3	6.47	4.63	328.1	186.1	459.9	1.78E+04
BM-OP-07	5.06	1	7.14	4.92	355.1	193.2	487.9	4.64 E+03

Table 3.15 Smooth specimen: HAZ-Axial fatigue test matrix.

Strain-controlled						
Specimen ID	**Outer diameter [mm]**	**Frequency [1/s]**	**Force amplitude [kN]**	**Axial stress amplitude [MPa]**	**Axial strain amplitude [%]**	**Cycles to Failure (N_f)**
HAZ-A-01	5.03	0.167	8.70	437.9	0.3	2.74E+04
HAZ-A-02	5.03	0.125	9.30	468.3	0.4	8.92E+03
HAZ-A-03	5.03	0.100	9.68	487.5	0.5	5.18E+03
HAZ-A-04	4.99	0.0625	10.43	533.6	0.8	1.20E+03
Force-controlled						
Specimen ID	**Outer diameter [mm]**	**Frequency [1/s]**	**Force amplitude [kN]**	**Axial stress amplitude [MPa]**	**Axial strain amplitude [%]**	**Cycles to Failure (N_f)**
HAZ-A-05	5.00	25	7.58	385.9	0.195	3.09E+06
HAZ-A-06	5.04	15	7.78	390.0	0.190	5.99E+05
HAZ-A-07	5.04	15	7.94	398.2	0.200	3.31E+05
HAZ-A-08	5.03	15	8.25	415.0	0.210	2.93E+05
HAZ-A-09	5.03	25	8.57	431.8	0.230	1.41E+05

Table 3.16 Smooth specimen: HAZ-Torsion fatigue test matrix.

Torque-controlled						
Specimen ID	**Outer diameter [mm]**	**Frequency [1/s]**	**Torque amplitude [N.m]**	**Shear stress amplitude [MPa]**	**Shear strain amplitude [%]**	**Cycles to Failure (N_f)**
HAZ-T-01	5.00	10	6.19	251.6	0.308	2.00E+06
HAZ-T-02	5.07	25	6.69	260.6	0.352	5.90E+05
HAZ-T-03	5.09	20	6.93	267.9	0.374	2.18E+05
HAZ-T-04	5.00	5	8.00	325.7	0.462	4.40E+04
HAZ-T-05	5.00	2	8.49	345.8	0.510	1.80E+04
HAZ-T-06	5.00	1	8.99	365.8	0.610	7.00E+03

Table 3.17 Smooth specimen: HAZ-IP fatigue test matrix.

Force/torque controlled								
Specimen ID	Outer diameter [mm]	Frequency [1/s]	Force amplitude [kN]	Torque amplitude [N.m]	Axial stress amplitude [MPa]	Shear stress amplitude [MPa]	Von Mises stress [MPa]	Cycles to Failure (N_f)
HAZ-IP-01	4.98	10	5.70	4.21	292.7	173.4	419.3	6.88E+05
HAZ-IP-02	5.00	5	5.96	4.30	303.7	175.7	429.9	6.57E+05
HAZ-IP-03	5.00	20	5.97	4.33	304.1	262.1	546.4	2.69E+05
HAZ-IP-04	4.95	10	6.39	4.99	332.0	210.2	492.7	1.85E+05
HAZ-IP-05	5.00	2	7.07	5.09	360.1	207.8	509.1	1.30E+05
HAZ-IP-06	5.00	1	7.64	5.50	389.3	218.5	542.9	1.55E+04
HAZ-IP-07	5.01	0.5	8.48	6.12	430.2	247.9	607.8	2.58E+03
HAZ-IP-08	4.99	0.5	8.71	6.29	445.4	257.8	630.7	1.40E+03

Table 3.18 Smooth specimen: HAZ-OP fatigue test matrix.

Force/torque controlled								
Specimen ID	Outer diameter [mm]	Frequency [1/s]	Force amplitude [kN]	Torque amplitude [N.m]	Axial stress amplitude [MPa]	Shear stress amplitude [MPa]	Von Mises stress [MPa]	Cycles to Failure (N_f)
HAZ-OP-01	5.00	5	6.08	4.39	310.1	178.8	438.3	2.61E+06
HAZ-OP-02	5.00	2	6.52	4.67	332.1	190.3	467.9	1.83E+06
HAZ-OP-03	5.00	3	6.63	4.78	337.7	194.7	477.2	3.04E+05
HAZ-OP-04	4.99	2	7.11	5.15	363.6	211.1	515.6	2.64E+05
HAZ-OP-05	5.00	2	7.74	5.57	394.3	226.9	556.7	6.06E+04
HAZ-OP-06	5.01	0.5	8.00	5.89	405.8	238.5	579.1	3.86E+04
HAZ-OP-07	5.00	1	8.75	6.34	445.6	258.3	631.4	1.65E+04
HAZ-OP-08	4.99	0.5	9.49	6.78	483.6	277.9	682.3	7.70E+03
HAZ-OP-09	5.00	0.05	9.81	7.08	499.6	288.5	706.6	4.20E+03
HAZ-OP-10	5.00	0.5	10.62	7.86	540.4	319.8	773.9	2.50E+03

3.7.1.3 Strain Measurement

During the tests, the machine measures displacement and twist angle at its upper end, which differs significantly from the actual values on the specimens due to the machine's elastic components. To accurately calculate strain responses, displacement must be directly measured on the specimens. Various techniques can achieve this, such as clip-on extensometers, strain gauges, and optical methods. Real-time strain

measurements are crucial for strain-controlled testing, integrating directly into the machine control loop.

Clip-on extensometers were effectively employed for pure axial tests to ensure reliable strain measurements. However, for torsion and axial-torsional tests, finding a suitable axial-torsional extensometer with a sufficiently short measuring span proved challenging due to specimen size limitations. Strain gauges could serve as an alternative to clip-on extensometers, but drawbacks such as lack of reusability, long preparation times, and potential adhesive bond durability issues at higher load levels or cycles were considered. In light of these factors, the decision was made to utilize the optical Aramis strain measurement system [132]. Aramis employs digital image correlation to track a pattern on the specimen surface, providing detailed three-dimensional geometry and distortion data captured by two cameras, as depicted in Figure 3.10.

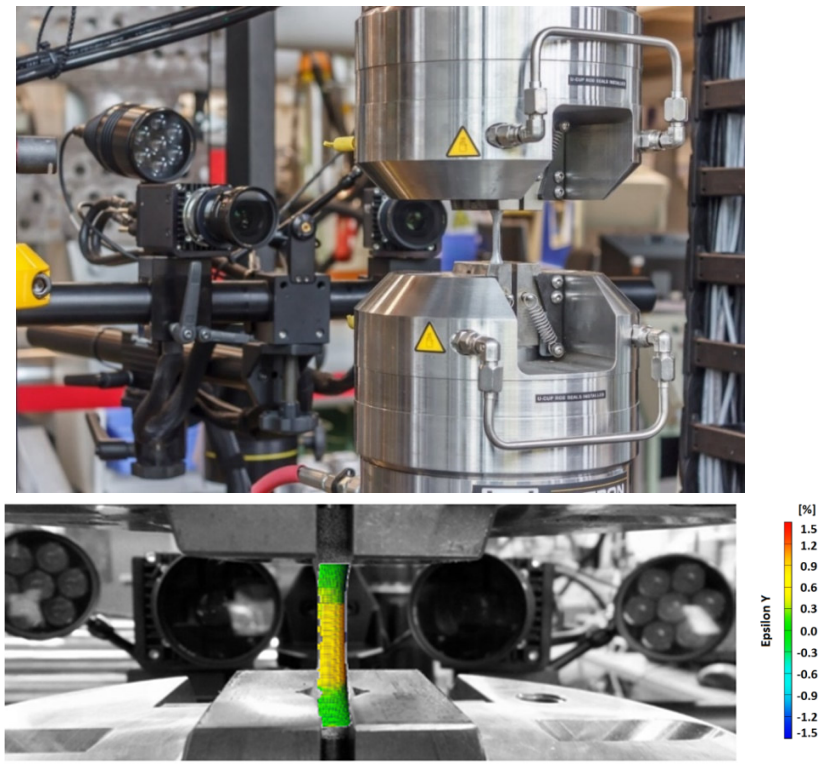

Figure 3.10 Three-dimensional Aramis setup and the calculated strain field under axial cyclic loading (ε_a = 0.7%).

In post-processing, the sample surface is automatically segmented into facets of predefined size (Figure 3.11 (a)). Pixel movements are tracked in each captured frame, allowing the calculation of deformation in the facets relative to a reference image (Figure 3.11 (b)). This process yields the strain field across the surface. Once the system is set up and calibrated, it operates straightforwardly. However, it is important to note that due to its extensive data processing requirements, the Aramis system is not suitable for real-time strain measurements during strain-controlled tests. Figure 3.10 illustrates the strain field results from an axial cyclic test obtained using the Aramis system.

(a) 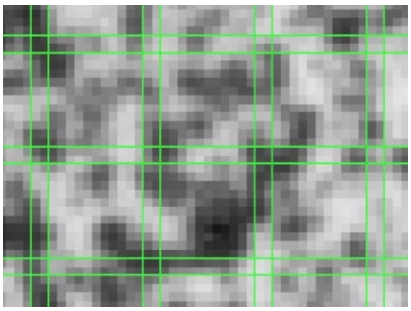 (b) 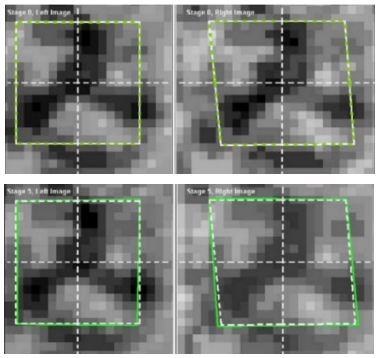

Figure 3.11 Facets on sample surface (a) and facet tracking (b) in Aramis [132].

3.7.2 Fatigue Testing of Weld-Specimens under Multiaxial Loading

Aside from material characterization tests, fatigue testing of the welded specimens was also conducted under constant amplitude uniaxial and multiaxial loading conditions in the Institute for Applied Materials IAM-WK (KIT). As for fatigue testing of smooth specimens, pure axial, pure torsion and in-phase and out-of-phase multiaxial tension-torsion tests were considered for lifetime evaluations of the welded specimens. All these tests were conducted in load-control mode and with a nominal load ratio of R=-1 with a sinus wave signal. Same as for material characterization tests, the ratio between the nominal torque and force amplitudes was chosen so that the contribution of normal and shear stresses based on the von Mises equivalent stress are equal:

$$\frac{\Delta\sigma}{2} = \sqrt{3}\frac{\Delta\tau}{2} \tag{3-23}$$

Two groups of identical samples, one with and one without residual stresses were considered for these tests. For this purpose, 90 tubular specimens were welded, half of them were heat-treated as explained in Section 3.2. Summary of the fatigue tests is given in Table 3.19 to Table 3.26. The main goals of these tests were to study the effects of the weld notch, microstructural phase transformations and welding residual stresses on the multiaxial fatigue damage and crack initiation life. As such, the experimental data from these tests allowed for the evaluation of notch stress-strain estimation models, stress gradient models, and local life prediction techniques under uniaxial and multiaxial loading conditions. The obtained stress-life curves for as-welded and stress-relieved conditions were compared together in order to understand the influence of welding residual stresses on the uniaxial and multiaxial fatigue behavior of welds.

Table 3.19 Welded specimen: HT Axial fatigue test matrix.

Specimen ID	R_o [mm]	R_i [mm]	A [mm^2]	Freq [1/s]	Force amplitude [kN]	Axial stress amplitude [MPa]	Cycles to Failure (N_f)
HT-A-01	17.42	14.00	337.5	15	63.41	187.8	3.64E+05
HT-A-02	17.42	14.01	336.7	15	57.10	169.5	1.13E+06
HT-A-03	17.42	14.00	337.5	15	64.14	189.9	3.34E+05
HT-A-04	17.42	14.01	336.1	5	76.32	227.0	1.67E+05
HT-A-05	17.40	14.01	334.5	5	73.60	220.0	2.35E+05
HT-A-06	17.40	13.99	336.7	5	54.15	160.8	5.42E+06
HT-A-07	17.42	14.01	336.1	5	90.76	269.9	9.88E+04
HT-A-09	17.42	14.01	337.1	10	57.32	170.0	5.65E+06
HT-A-10	17.44	13.98	341.4	15	54.60	159.9	5.25E+06

Table 3.20 Welded specimen: HT Torsion test matrix.

Specimen ID	R_o [mm]	R_i [mm]	J [mm^4]	Freq [1/s]	Torque amplitude [N.m]	Shear stress amplitude [MPa]	Von Mises stress [MPa]	Cycles to Failure (N_f)
HT-T-11	17.46	14.10	83978.4	3	1000	207.9	360.1	2.30E+04
HT-T-12	17.50	14.00	86979.8	3	900	181.0	313.6	3.65E+04
HT-T-13	17.47	14.13	83733.9	3	800	166.9	289.1	2.20E+06
HT-T-14	17.52	14.08	86410.3	3	820	166.3	288.0	1.36E+06
HT-T-15	17.50	14.10	85237.1	3	894	183.5	317.9	1.35E+05
HT-T-16	17.50	14.08	85457.0	3	861	176.3	305.3	1.89E+05
HT-T-17	17.53	14.07	86943.1	3	910	183.5	317.9	7.65E+04
HT-T-18	17.48	14.11	84385.9	3	827	171.3	296.7	2.96E+05
HT-T-19	17.46	14.00	85721.0	3	820	167.0	289.3	4.68E+05
HT-T-20	17.51	14.10	85658.5	3	803	164.2	284.5	1.84E+05

Table 3.21 Welded specimen: HT IP test matrix.

Specimen ID	R_o [mm]	R_i [mm]	A [mm^2]	J [mm^4]	Freq [1/s]	Force amplitude [kN]	Torque amplitude [N.m]	Axial stress amplitude [MPa]	Shear stress amplitude [MPa]	Von Mises stress [MPa]	Cycles to Failure (N_f)
HT-IP-21	17.44	14.11	330.0	83050.7	3	71.0	588.5	215.1	123.5	303.4	8.15E+04
HT-IP-22	17.47	14.13	331.4	83733.9	3	83.3	690.0	251.3	144.0	354.0	3.19E+04
HT-IP-23	17.49	14.08	338.2	85252.1	3	58.8	487.0	173.8	99.9	245.3	1.35E+05
HT-IP-24	17.50	14.00	346.3	86979.8	3	39.2	324.7	113.1	65.3	160.0	3.27E+06
HT-IP-25	17.50	14.01	345.2	86764.0	3	49.0	405.8	141.9	81.8	200.5	5.69E+05
HT-IP-27	17.50	14.00	346.3	86979.8	3	49.0	405.8	141.4	81.6	200.0	3.93E+05
HT-IP-28	17.42	14.03	334.8	83821.3	3	85.7	710.2	255.9	147.6	361.8	2.15E+04
HT-IP-29	17.52	13.98	350.6	88112.2	3	41.0	360.0	116.9	71.5	170.4	1.61E+06
HT-IP-30	17.47	13.99	344.4	86311.9	3	51.2	446.0	148.6	90.2	215.7	1.68E+05

Table 3.22 Welded specimen: HT OP test matrix.

Specimen ID	R_o [mm]	R_i [mm]	A [mm^2]	J [mm^4]	Freq [1/s]	Force amplitude [kN]	Torque amplitude [N.m]	Axial stress amplitude [MPa]	Shear stress amplitude [MPa]	Von Mises stress [MPa]	Cycles to Failure (N_f)
HT-OP-31	17.51	14.00	348.4	87612.2	3	73.5	608.7	210.9	121.7	298.2	1.42E+04
HT-OP-32	17.46	14.11	332.9	83967.1	3	44.1	365.2	132.4	75.9	186.6	1.28E+05
HT-OP-33	17.55	14.10	342.4	86817.9	3	34.3	284.1	100.1	57.4	141.1	1.01E+06
HT-OP-34	17.48	14.06	339.4	85474.5	3	58.8	487.0	173.0	99.6	244.5	4.11E+04
HT-OP-35	17.43	14.12	328.4	82702.2	3	39.2	324.7	119.3	68.4	168.2	3.86E+05
HT-OP-36	17.48	14.09	337.2	85036.5	3	51.4	426.1	152.4	87.6	215.0	7.31E+04
HT-OP-37	17.50	14.00	346.3	86979.8	3	34.3	284.1	99.0	57.1	140.0	1.01E+06
HT-OP-38	17.50	14.00	346.3	86979.8	3	33.1	280.0	95.4	56.3	136.4	3.14E+06
HT-OP-39	17.50	14.00	346.3	86979.8	3	36.4	300.0	105.0	60.3	148.2	3.23E+06

Table 3.23 Welded specimen: AW Axial test matrix.

Specimen ID	R_o [mm]	R_i [mm]	A [mm^2]	Freq [1/s]	Force amplitude [kN]	Axial stress amplitude [MPa]	Cycles to Failure (N_f)
AW-A-02	17.50	14.00	346.3	3	80.0	230.9	2.98E+05
AW-A-03	17.40	14.02	333.1	3	69.7	209.1	2.43E+05
AW-A-05	17.43	14.23	318.8	3	63.8	200.1	1.27E+06
AW-A-06	17.44	13.92	346.3	3	86.6	250.0	1.80E+05
AW-A-07	17.42	14.00	337.5	3	62.5	185.1	1.25E+06
AW-A-08	17.43	14.23	318.8	3	92.4	289.8	9.80E+04
AW-A-09	17.42	13.97	339.7	3	88.3	259.8	1.29E+05
AW-A-11	17.47	13.96	347.1	15	72.9	210.0	3.84E+05

Table 3.24 Welded specimen: AW Torsion test matrix.

Specimen ID	R_o [mm]	R_i [mm]	J [mm^4]	Freq [1/s]	Torque amplitude [N.m]	Shear stress amplitude [MPa]	Von Mises stress [MPa]	Cycles to Failure (N_f)
AW-T-11	17.50	14.02	86547.6	3	1000	202.2	350.2	3.87E+04
AW-T-12	17.50	13.96	87623.7	3	900	179.7	311.3	7.89E+05
AW-T-13	17.50	14.03	86330.6	3.5	800	162.1	280.8	5.00E+06
AW-T-14	17.50	14.05	86113.1	3	960	195.0	337.9	6.90E+04
AW-T-15	17.50	14.00	86979.8	3	870	175.0	303.1	5.83E+05
AW-T-16	17.48	14.03	85490.6	3	933	190.6	330.2	1.15E+05
AW-T-17	17.50	13.97	87409.6	3	1033	206.8	358.3	2.21E+04
AW-T-18	17.50	14.05	86113.1	3	930	188.9	327.3	2.09E+05
AW-T-19	17.50	14.05	86113.1	3	860	174.7	302.7	3.38E+06
AW-T-21	17.50	14.05	86113.1	3	1085	220.4	381.9	1.37E+04

Table 3.25 Welded specimen: AW IP test matrix.

Specimen ID	R_o [mm]	R_i [mm]	A [mm^2]	J [mm^4]	Freq [1/s]	Force amplitude [kN]	Torque amplitude [N.m]	Axial stress amplitude [MPa]	Shear stress amplitude [MPa]	Von Mises stress [MPa]	Cycles to Failure (N_f)
AW-IP-21	17.50	14.00	346.4	86979.8	3	65.00	538.50	187.7	108.3	265.4	1.99E+05
AW-IP-22	17.50	14.05	342.0	86113.1	3	60.00	497.00	175.5	101.0	247.8	1.91E+05
AW-IP-23	17.50	14.14	334.2	84574.0	3	71.50	592.30	213.9	122.6	301.4	8.25E+04
AW-IP-24	17.50	14.00	346.4	86979.8	3	55.40	459.00	159.9	92.3	226.2	3.59E+05
AW-IP-25	17.41	14.00	336.8	84055.4	3	85.70	710.00	254.5	147.1	360.1	1.29E+04
AW-IP-26	17.45	14.06	335.4	84218.5	3	41.60	344.90	124.0	71.5	175.2	1.73E+06
AW-IP-27	17.45	13.95	345.3	86160.8	3	49.00	405.80	141.9	82.2	201.0	4.66E+05
AW-IP-30	17.45	14.09	333.1	83780.5	3	44.20	375.38	132.7	78.2	189.6	9.66E+05
AW-IP-31	17.50	14.00	346.4	86979.8	3	80.00	675.00	231.0	135.8	329.7	3.32E+04
AW-IP-32	17.50	14.00	346.4	86979.8	3	49.23	407.85	142.1	82.1	201.0	1.50E+06
AW-IP-33	17.50	14.00	346.4	86979.8	3	80.00	675.00	231.0	135.8	329.7	2.95E+04
AW-IP-34	17.50	14.00	346.4	86979.8	3	60.68	502.75	175.2	101.2	247.8	1.00E+06
AW-IP-35	17.50	14.00	346.4	86979.8	3	60.68	502.75	175.2	101.2	247.8	6.76E+05

Table 3.26 Welded specimen: AW OP test matrix.

Specimen ID	R_o [mm]	R_i [mm]	A [mm^2]	J [mm^4]	Freq [1/s]	Force amplitude [kN]	Torque amplitude [N.m]	Axial stress amplitude [MPa]	Shear stress amplitude [MPa]	Von Mises stress [MPa]	Cycles to Failure (N_f)
AW-OP-31	17.5	14.0	346.4	86979.8	3	65.00	538.50	187.7	108.3	265.4	2.54E+04
AW-OP-32	17.5	14.0	346.4	86979.8	3	50.00	415.00	144.4	83.5	204.3	7.67E+04
AW-OP-33	17.5	14.0	346.4	86979.8	3	56.50	468.00	163.1	94.2	230.7	3.60E+04
AW-OP-35	17.5	14.0	346.4	86979.8	3	31.80	263.80	91.8	53.1	129.9	9.30E+05
AW-OP-36	17.5	14.0	346.4	86979.8	3	42.90	355.10	123.9	71.4	175.1	1.52E+05
AW-OP-37	17.5	14.0	346.4	86979.8	3	14.70	121.70	42.4	24.5	60.0	5.00E+06
AW-OP-39	17.5	14.0	346.4	86979.8	3	28.00	255.00	80.8	51.3	120.1	2.83E+06
AW-OP-41	17.5	14.0	346.4	86979.8	3	37.96	314.51	109.6	63.3	155.0	1.47E+06
AW-OP-42	17.5	14.0	346.4	86979.8	3	31.59	261.75	91.2	52.7	129.0	2.50E+06

Chapter 4 Test Results

The present study focuses on two main aspects, first the welding residual stresses and their behavior under multiaxial cyclic loading, and second the multiaxial fatigue behavior and damage estimation of welds. To achieve this, a large number of experiments were conducted, as detailed in Chapter 3, including residual stress measurements, material characterizations, and fatigue testing of welded specimens. This chapter provides an overview of the examination results for the fatigue weld specimens, whose geometry was given in Figure 3.1. Due to equipment limitations, the tubular weld specimens used for residual stress investigations had different geometries than the fatigue weld specimens, which will be discussed in Chapter 6.

Section 4.1 summarizes the results of the full-field residual stress measurements on the single-pass bead-on-tube specimens obtained using both x-ray and neutron diffraction techniques.

Section 4.2 provides detailed discussions on the microstructural analysis of a selected cross-section of the specimen using metallography, offering further insight into the characteristics of the weld and the adjacent regions. Additionally, the measured hardness field on the same cross-section is presented in this section, which is used to assess the microstructure in the welded area and its surroundings.

A short overview of the deformation tests results for both BM and HAZ in the frame of static (tensile) and cyclic (IST) tests is given in Section 4.3. These results will be used later in the FE analysis to describe the constitutive behavior of the materials.

The transient softening behavior of the BM and HAZ is discussed in Section 4.4. Understanding this behavior, which occurs within certain strain ranges, helps to incorporate this effect into more accurate fatigue damage assessments.

Finally, the results of fatigue tests on smooth and welded specimens are presented in Section 4.5 in the form of fatigue baselines and nominal S-N curves of the weld. Reference baselines are used for further damage calculations of weld specimens. The

results of experimental fatigue tests on weld specimens are used to validate the accuracy of fatigue damage evaluations.

4.1 Welding Residual Stress Measurement

The residual stress field in the initial state and after redistribution under cyclic loading was determined experimentally for the welded specimens described in Section 3.2 using diffraction techniques.

X-ray measurements on the specimen surface were made at 41 measurement points on both sides of the weld centerline, lying on a perpendicular line to the weld direction, as shown in Figure 4.1 (a). Neutron measurements were made at 305 measurement points on both sides of the weld centerline. The location of the measurement points across the weld cross-section is shown in Figure 4.1 (b). As a result, the full-field of residual stresses was determined for the three orthogonal directions axial, hoop and radial.

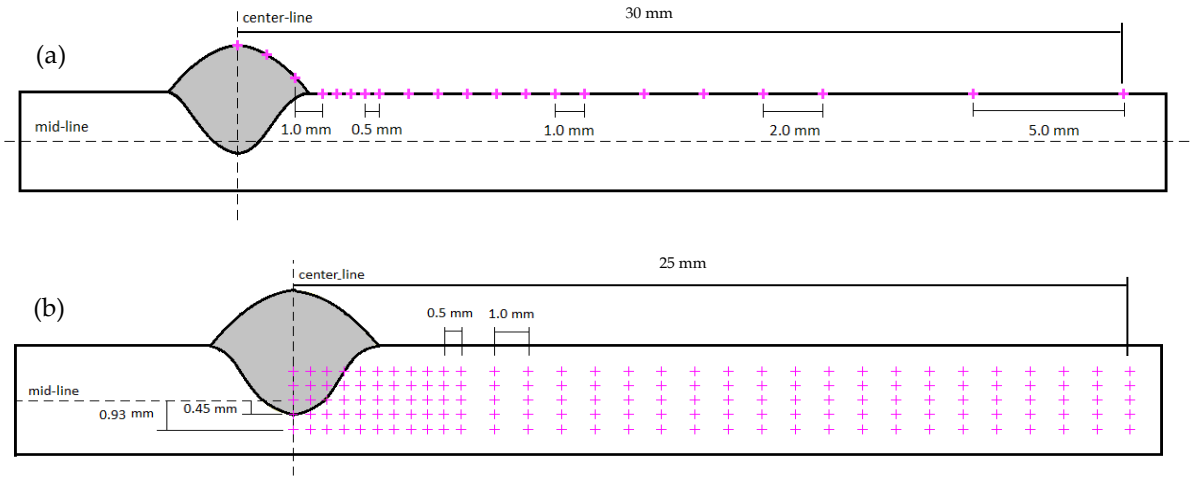

Figure 4.1 Location of residual stress measurement points on one side of the weld centerline in the fatigue specimen for the (a) x-ray and (b) neutron diffraction techniques.

To determine the reference stress-free lattice spacing, d_0, in different welding zones, comb specimens with 3×3×10 (+/-) teeth were made by EDM (Figure 4.2). The diameter of the wire was chosen to be 0.2 mm to minimize the superficial thermal influence.

For these reference measurements, the same instrument set-up was used as for the main residual stress measurements (Figure 4.3).

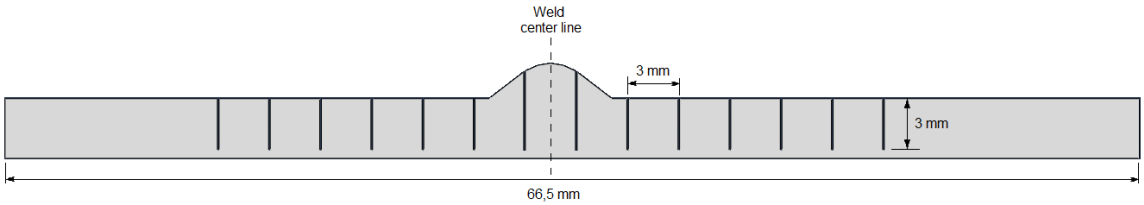

Figure 4.2 The comb specimen for the reference d_0 measurements in the fatigue specimen.

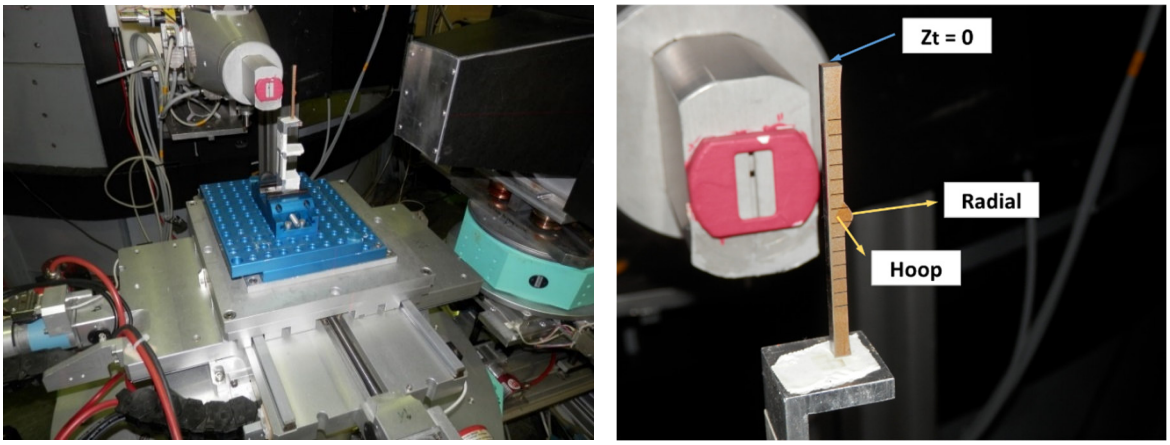

Figure 4.3 Neutron diffraction set-up for measuring the reference d_0.

The measured axial and hoop residual stresses on the surface and in the midline of the cross-section (at 180° from the start of welding) are shown in Figure 4.4. As can be seen in Figure 4.4 (a), tensile residual stresses are present on the specimen surface in the weld area in both axial and circumferential directions, whereas they are highly compressive in the HAZ. Considering the self-equilibrating character of the residual stresses, it is expected that the residual stresses will approach zero with increasing distance from the weld centerline. However, the compressive residual stresses have, contrary to expectations, expanded to both sides. These residual stresses are the initial compressive residual stresses induced by the manufacturing process and are not related to the weld. This is due to the fact that the pipes were not subjected to stress-relieving heat treatment prior to welding. Since these manufacturing residual stresses, which extend over a very small depth (less than 10 microns), are reduced in the heated area due to the heat cycle, they would not affect the subsequent welding residual stresses.

In the bulk of the material, however, the residual stresses are compressive in all directions in the weld zone and tend to go into tension in the HAZ and to become compressive again with increasing distance in the axial direction from the weld centerline (Figure 4.4 (b)).

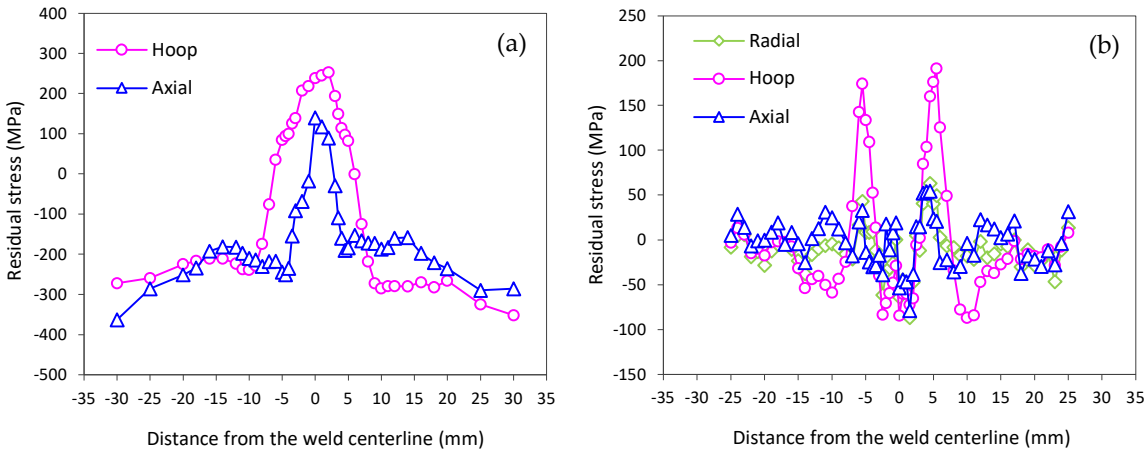

Figure 4.4 Measured residual stresses on the top surface (a) and at the cross-section midline (b) at 180° from weld start point in fatigue specimen.

4.2 Microstructure Analysis and Hardness

In the cross-section of the weld, three distinct zones can be clearly identified: the base material (BM), where the metallographic structure remains unaffected by the heat; the weld material (WM) or fusion zone, where the temperature was sufficient to cause melting; and the heat affected zone (HAZ), where the heat input altered the crystallographic structure of the material without causing it to melt [137].

According to the Continuous Cooling Transformation (CCT) diagrams, a wide range of transformations can occur depending on the cooling rate. These diagrams illustrate the sequence in which different austenite decomposition products form and the corresponding temperature ranges for their formation. Heat input and cooling conditions significantly influence the cooling rate of the metal, which in turn affects the size, morphology, volume fraction, and distribution of the microstructure. The differences between these regions can be clearly observed in the sample visualization as shown in Figure 4.5.

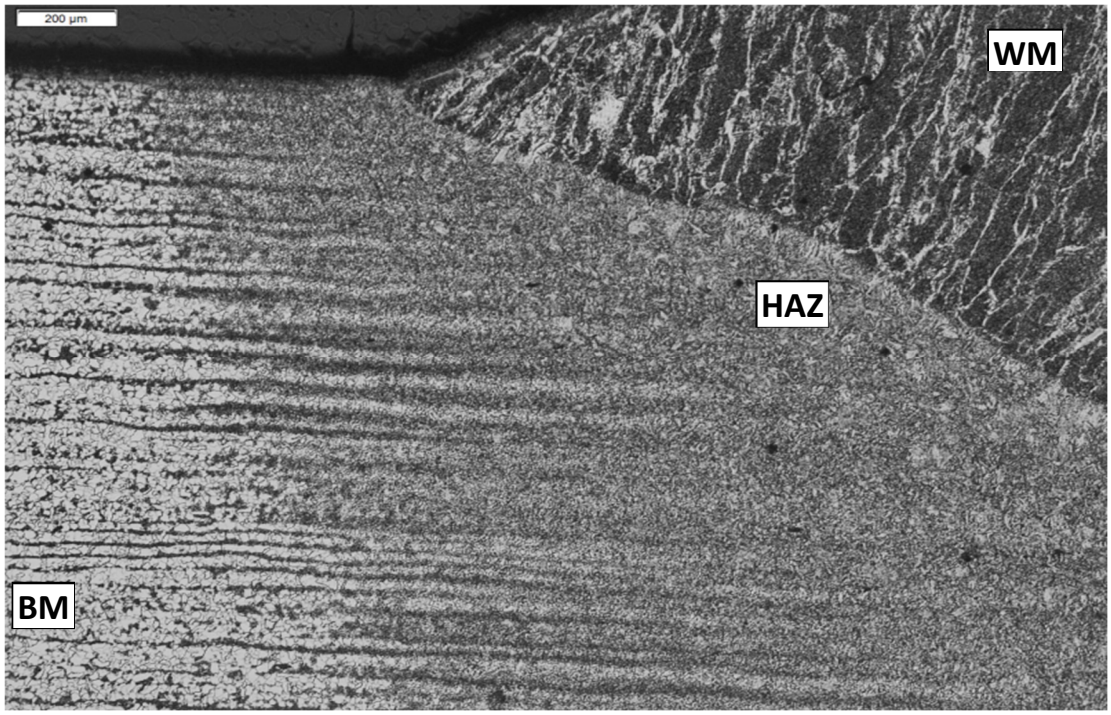

Figure 4.5 Longitudinal cross-section of the weld specimen with weld material (WM), heat affected zone (HAZ) and base material (BM).

The analyzed steel, containing less than 0.8 wt.% carbon (≈ 0.14%), is a hypo-eutectoid alloy with ferrite and pearlite as its primary constituents [137], as shown in Figure 4.6.

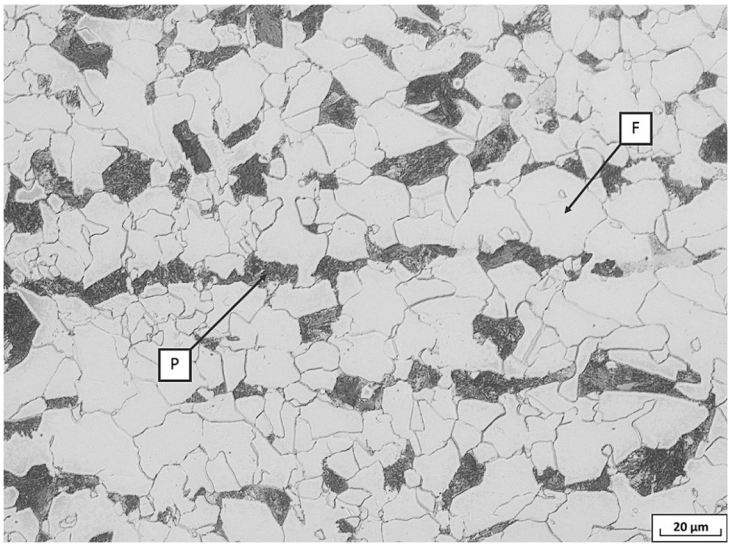

Figure 4.6 Base material microstructure with Ferrite (F) and Pearlite (P) (Magnification 500x).

4.2.1 The Fusion Zone

The fusion zone comprises both the deposited metal and the base material that was melted during welding. The extreme heat causes the metal to melt, leading to a solidification microstructure upon cooling. As the temperature decreases, δ-ferrite transforms into austenite, which nucleates at δ-δ grain boundaries, forming a columnar austenite grain structure similar to the original δ-grains. The microstructure that develops as the weld cools to ambient temperature is known as the as-deposited or primary microstructure (Figure 4.7). This microstructure primarily consists of allotriomorphic ferrite, Widmanstätten ferrite, acicular ferrite, and bainite, with potential traces of martensite, retained austenite, or degenerate pearlite [137]. The grains are approximately 100 μm wide and 5000 μm long, differing from equiaxed grains, which results in greater hardenability compared to a wrought alloy.

Optical microscopy alone cannot distinguish bainite from acicular ferrite, so this study uses the CCT diagram, along with hardness evaluations and temperature measurements.

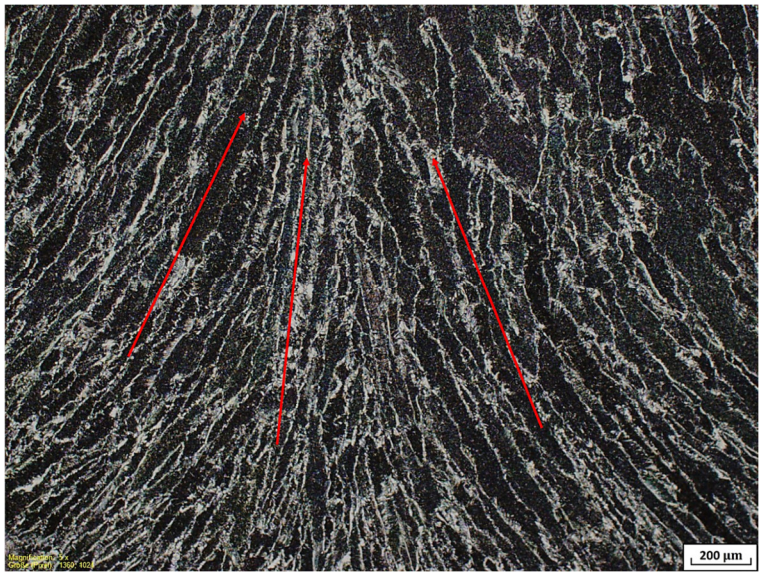

Figure 4.7 Fusion zone: columnar grains grown in the heat flow direction as indicated by the arrows.

The CCT diagram in Figure 4.8 shows the percentages of the different phases that form depending on the hardness and on the cooling rate, referred to as the time needed to cool down from the temperature of 850°C until 500°C. Since the diagram's steel composition differs from the analyzed steel, some values may vary slightly.

Temperature variations over time were measured during welding at different circumferential locations on the surface, at the boundary between the weld and the HAZ (Figure 3.2). The cooling time from 850°C to 500°C was approximately 25 seconds. The cooling times measured at the surface are shorter than at the points that are not directly exposed to the air flow. Additionally, uncertainties may arise because the measurements were taken from a section that does not precisely correspond to the one under investigation. Considering the uncertainties and approximations in temperature measurements and CCT diagrams, hardness measurements are more reliable as they are conducted precisely at various locations within the same sample. The measured hardness across the WM is approximately HV 205, a value that will be discussed in detail in Section 4.2.3. Multiple measurements on the same sample yield consistent results, allowing for a preliminary use of the CCT diagram for rough microstructural estimations, despite some inherent inaccuracies. Given the hardness value of around HV 205, the CCT curve in Figure 4.8 suggests a microstructure consisting of 78% upper bainite (indicated as Zw) and 22% ferrite, aligning with findings from Abson's research [138]. This supports the conclusion that the microstructure previously identified as acicular ferrite likely includes bainite.

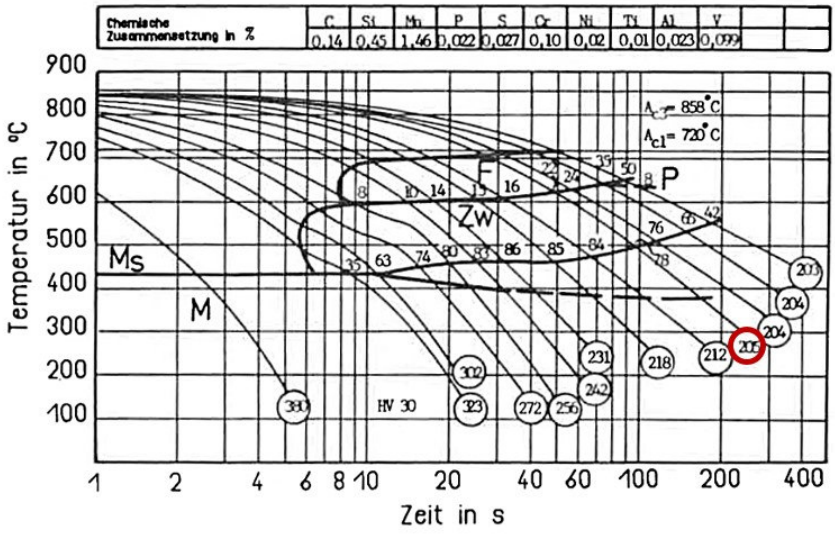

Figure 4.8 CCT diagram for S355 steel with the indicated chemical composition. The relevant curve is highlighted in red [19].

Taking the cooling time into account, the CCT curve indicates a cooling time of 100 seconds, whereas the measurement shown in Figure 3.2 shows a cooling time of 25 seconds. Since bainite formation is favored by higher cooling rates compared to ferrite, it is likely that the microstructure contains a higher proportion of bainite.

Figure 4.9 shows the WM microstructure. Allotriomorphic ferrite (α) initially forms as the austenite grains cool below the Ac3 temperature (910°C for pure iron, 858°C for the analyzed steel), nucleating at the columnar austenite grain boundaries. These boundaries facilitate ferrite formation through diffusion, resulting in thin, continuous ferrite layers. Below approximately 600°C, ferrite growth slows and reaches a limiting thickness. Widmanstätten ferrite then forms, as it grows without needing substitutional solute diffusion, even at lower temperatures. Widmanstätten and acicular ferrite formation are competitive, with acicular ferrite—prevalent in the fusion zone—nucleating on small non-metallic inclusions and growing in various directions, creating a complex microstructure.

A significant amount of bainite is present in the WM. Bainite forms when cooling rates are too fast for pearlite but not rapid enough for martensite. There are two types: upper and lower bainite. According to the CCT diagram in Figure 4.8, the weld primarily contains upper bainite, characterized by fine plates of ferrite about 0.2 μm thick and 10 μm long. Lower bainite, in contrast, has a similar structure but includes additional cementite particles within the ferrite plates. These cementite particles are extremely fine, only a few nanometers thick and approximately 500 nm long.

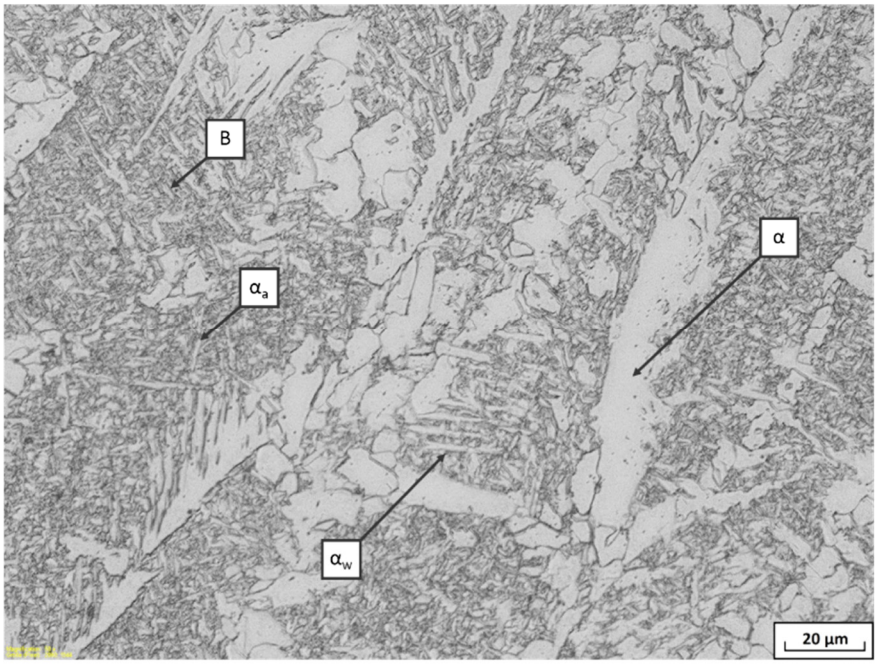

Figure 4.9 Allotriomorphic ferrite (α), acicular ferrite (α_a), Widmanstätten ferrite (α_w) and bainite in the fusion zone (Magnification 500x).

4.2.2 The Heat Affected Zone

During welding, heat diffuses from the fusion zone into the adjacent solid regions, creating a heating and cooling cycle that varies in intensity depending on the proximity to the fusion boundary. The peak temperature, as well as the heating and cooling rates, vary with distance from the fusion boundary. As a result, the heat affected zone (HAZ) exhibits a gradient in microstructure: regions close to the fusion boundary are heated to high temperatures and transform entirely to austenite, which then forms bainite as it cools to room temperature (Figure 4.10).

In addition to bainite, a small amount of martensite is likely to form due to the rapid cooling rate in this region. Martensite is a very hard phase where carbon, previously dissolved in austenite, remains trapped in the new phase. When martensite forms under constrained conditions, it appears as thin plates or laths to minimize strain energy from deformation. Near the fusion boundary, as depicted in Figure 4.10, the peak temperature exceeds the Ac3 temperature, leading to the formation of a coarse-grained austenite zone. The austenite grain size decreases sharply with increasing distance from the fusion boundary.

Figure 4.10 Microstructure including bainite and martensite in the HAZ close to the weld (Magnification 500x).

The HAZ regions that are farther away from the fusion boundary (Figure 4.11) reach lower peak temperatures, and only partially transform into austenite during the heating phase. The austenite that forms in these areas tends to have a higher carbon concentration, which is due to the increased solubility of carbon in γ at lower

temperatures. The parts of the material that do not transform into austenite are tempered.

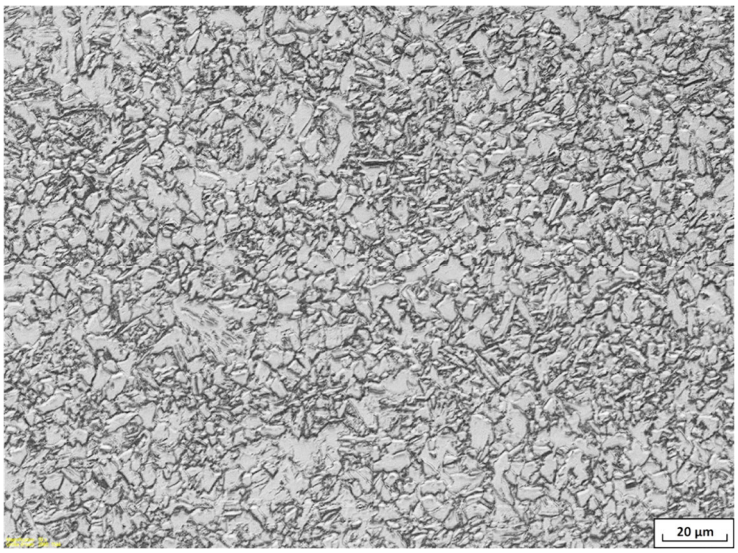

Figure 4.11 Microstructure of the HAZ farther from the welding boundary (Magnification 500x).

Where the peak temperature falls below the Ac1 temperature (Figure 4.12), the heat input primarily results in tempering of the microstructure. The extent of tempering decreases with increasing distance from the fusion boundary [137].

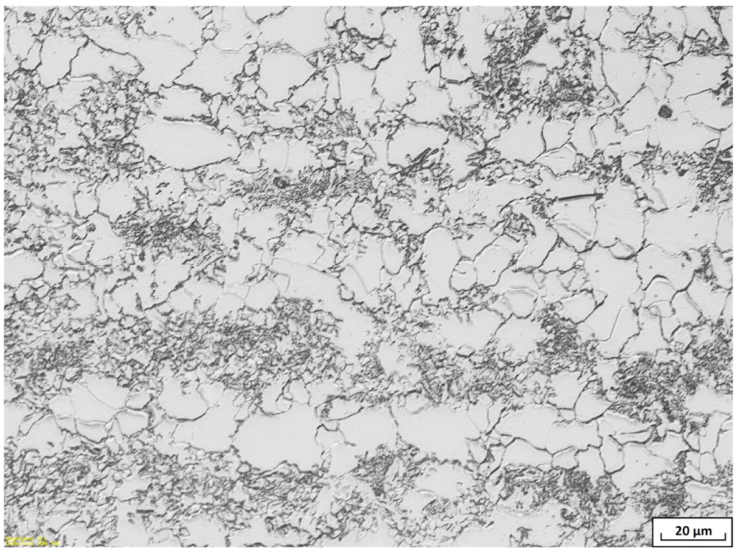

Figure 4.12 Microstructure of the HAZ close to the base material (Magnification 500x).

4.2.3 Hardness Measurement

As depicted in Figure 4.13, the hardness distribution is significantly impacted by the welding process. In the base material, hardness measurements vary slightly, ranging from HV 150 to HV 170. This variability correlates with the microstructure: Locations dominated by pearlite exhibit higher hardness values compared to areas with a higher proportion of ferrite, which generally has lower hardness.

In the HAZ, the hardness generally ranges between HV 190 and HV 210, with higher values nearer to the fusion boundary. This variation is attributed to the microstructure, which becomes finer closer to the weld zone. The peak hardness occurs near the weld boundaries, indicating the presence of predominantly bainitic microstructures with a probable small amount of martensite. According to the CCT diagram (Figure 4.8), hardness values in this range are consistent with a predominantly bainitic microstructure. Close to the weld, hardness values exceed HV 230.

In the welded zone, the hardness is approximately constant, with values around HV 200. Despite the presence of bainite, various phases of ferrite, and grains oriented according to the heat flow, the hardness remains relatively consistent. Near the free surface, the hardness slightly increases due to the higher cooling rate, which results from enhanced heat exchange with the surrounding air. This increased cooling rate promotes the formation of bainite, which is inherently harder than ferrite.

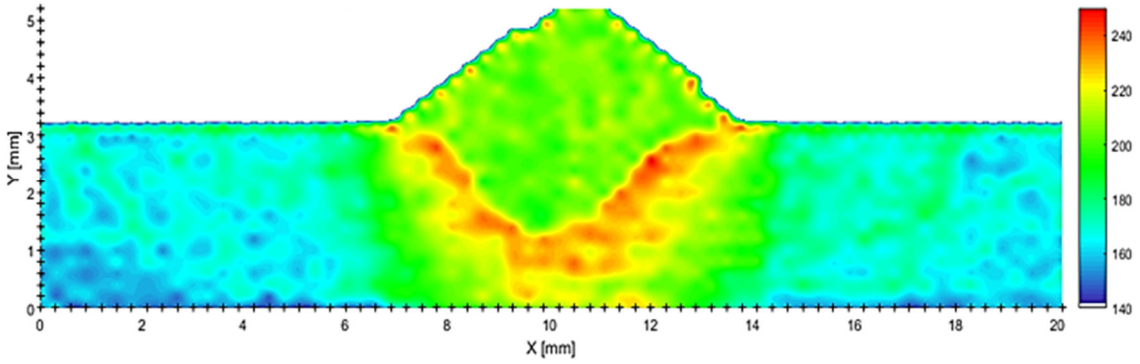

Figure 4.13 Hardness measurement of the whole cross-section (HV1) in fatigue specimen.

4.3 Deformation Test Results (Un-Welded Samples)

As detailed in Section 3.7.1, deformation test results are utilized to characterize the plastic deformation of materials under static and cyclic loads under specific conditions. Key aspects include strain range and strain rate dependence, non-proportional strain hardening, and transient softening. Since the loading conditions in this study are predominantly symmetric, ratcheting, and mean stress relaxation were not considered in the material characterization. The results are summarized in the following sections.

4.3.1 Static Testing of Base Material and HAZ

Figure 4.14 presents the tensile test results in terms of monotonic stress-strain curves for both BM and HAZ. While the Young's modulus, *E*, is nearly identical for both BM and HAZ, the HAZ exhibits significantly higher yield strength due to its bainitic-ferritic microstructure. Additionally, the HAZ material has a lower ductility, with a uniform elongation of 8.3%, compared to 16.4% for the BM. Both BM and HAZ demonstrate the formation and propagation of Lüders' bands immediately after yielding.

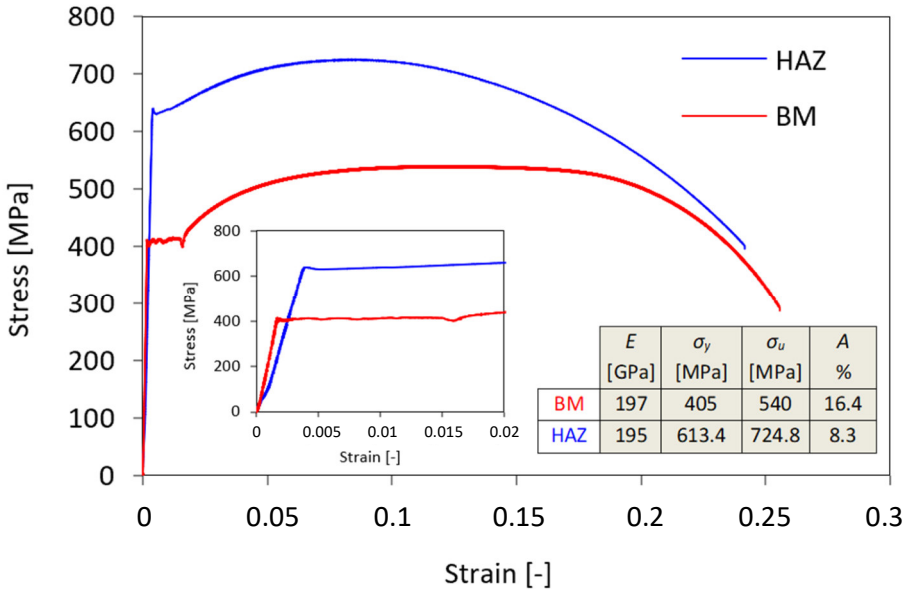

Figure 4.14 Monotonic stress-strain curves of BM and HAZ [128].

According to Hill [43], the von Mises criterion effectively determines the elastic limit of most metals that deform homogeneously under biaxial and multiaxial stress states. This criterion predicts yielding based on the distortion energy in the material and is widely used for its accuracy in homogeneous deformation scenarios. However, certain materials, such as annealed construction steel, may soften after yielding due to the formation of Lüders' bands, which leads to non-uniform deformation. For these materials, a maximum shear stress criterion, such as the Tresca criterion, may provide higher accuracy than the von Mises criterion. Strain hardening can also be accounted for in multiaxial stress states with reasonable accuracy. The Tresca criterion, which considers the maximum shear stress in the material, can be more relevant in scenarios involving non-uniform deformation.

4.3.2 Cyclic Testing of Base Material and HAZ

The experimental Cyclic Stress-Strain Curves (CSSCs) from uniaxial, proportional, and non-proportional multiaxial loading for both BM and HAZ are compared in Figure 4.15. The curves generally align well over a wide strain range. However, the proportional curves diverge from the non-proportional ones shortly after the onset of plasticity, with a constant stress difference of approximately 90 MPa for BM and over 200 MPa for the HAZ. For the BM, the slopes of the curves in the plastic region are similar across all loading conditions, whereas for the HAZ, the slope of the non-proportional curve deviates from the others. In conclusion, both the BM with its ferritic-pearlitic microstructure and the HAZ with its bainitic-ferritic (including some martensite) microstructure exhibited significant non-proportional hardening, which is a critical factor that cannot be ignored.

Table 4.1 and Table 4.2 provide an overview of the cyclic strength coefficients and exponents for all loading cases. The uniaxial and multiaxial cyclic deformation results for both BM and HAZ offer comprehensive insights into the material behavior under various loading conditions. By using the final set of material parameters for BM and HAZ, it is possible to compare the material states in the vicinity of the weld accurately. These comparisons highlight the necessity of considering different loading scenarios in the design and analysis of welded structures, ensuring their durability and performance under real conditions.

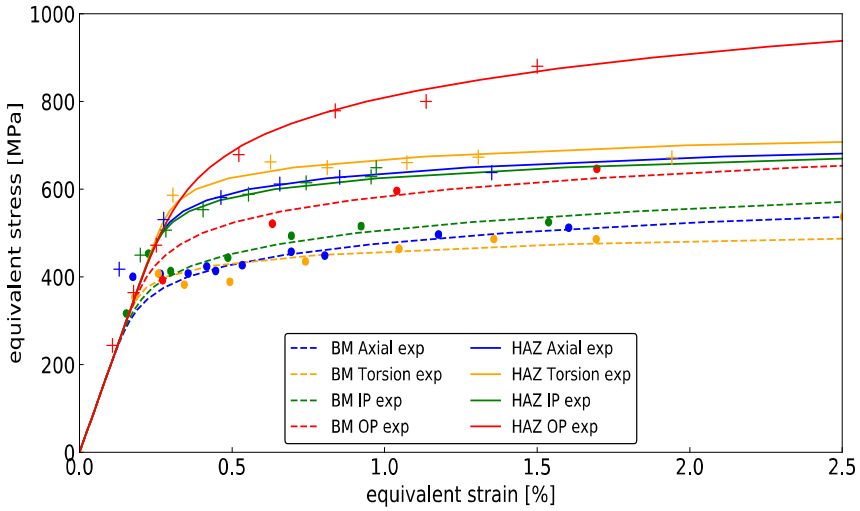

Figure 4.15 Comparison of CSSCs for BM and HAZ; Ramberg-Osgood fit is represented by dashed and solid lines [128]; IP and OP stand for in-phase and out-of-phase and 'exp' for experimental test.

Table 4.1 Monotonic and cyclic properties for S355J2H-BM (IP and OP stand for in-phase and out-of-phase).

Property	Symbol	Value	Unit
Monotonic Properties			
0.2% Yield Strength	σ_y	405	MPa
Ultimate Tensile Strength	σ_u	540	MPa
Modulus of Elasticity	E	197	GPa
Elongation at fracture	Z	26	%
Cyclic Properties			
0.2% Axial Yield Strength	σ_y'	390	MPa
Cyclic Axial Strength Coefficient	K'	730	MPa
Cyclic Axial Strain Hardening Exponent	n'	0.09	
Cyclic Shear Strength Coefficient	K_o'	615	MPa
Cyclic Shear Strain Hardening Exponent	n_o'	0.06	
Cyclic In-Phase Strength Coefficient	K_{IP}'	870	MPa
Cyclic In-Phase Strain Hardening Exponent	n_{IP}'	0.11	
Cyclic 90° OP Strength Coefficient	K_{NP}'	960	MPa
Cyclic 90° OP Strain Hardening Exponent	n_{NP}'	0.10	

Table 4.2 Monotonic and cyclic properties for S355J2H-HAZ (IP and OP stand for in-phase and out-of-phase).

Property	Symbol	Value	Unit
Monotonic Properties			
0.2% Yield Strength	σ_y	613	MPa
Ultimate Tensile Strength	σ_u	725	MPa
Modulus of Elasticity	E	195	GPa
Elongation at fracture	Z	24	%
Cyclic Properties			
0.2% Axial Yield Strength	σ_y'	570	MPa
Cyclic Axial Strength Coefficient	K'	860	MPa
Cyclic Axial Strain Hardening Exponent	n'	0.06	
Cyclic Shear Strength Coefficient	K_o'	860	MPa
Cyclic Shear Strain Hardening Exponent	n_o'	0.05	
Cyclic In-Phase Strength Coefficient	K_{IP}'	845	MPa
Cyclic In-Phase Strain Hardening Exponent	n_{IP}'	0.06	
Cyclic 90° OP Strength Coefficient	K_{NP}'	1500	MPa
Cyclic 90° OP Strain Hardening Exponent	n_{NP}'	0.12	

4.4 Transient Softening

When calibrating strain hardening constants using IST or LCF tests, it is common practice to focus on the initial cycles. However, a more thorough understanding of material behavior can be obtained by analyzing the complete history of an LCF test. The following section reviews the available test data for BM and HAZ, covering axial and torsional conditions. While the axial tests were performed under strain-controlled conditions, the torsional tests used a force-controlled setup.

To characterize the transient deformation behavior, the unconstrained variable—whether stress or strain—is plotted against the cycle number on a logarithmic scale. In strain-controlled tests, cyclic hardening is identified by an increase in stress amplitude, while cyclic softening is indicated by a decrease in stress amplitude. Conversely, in stress-controlled tests, cyclic hardening is observed as a decrease in strain, while cyclic softening is seen as an increase in strain.

The uniaxial fatigue test results for the BM are presented in Figure 4.16. This analysis includes four axial LCF tests with strain amplitudes ranging from 0.4% to 1.0% and three torsional LCF tests with stress amplitudes between 220 MPa and 270 MPa. In Figure 4.16 (a), the two tests with the highest strain amplitudes demonstrate rapid stabilization of stress amplitudes. LCF 6 shows a similar stabilization at a lower stress level after an initial drop in the first three cycles. For the lowest strain amplitude (LCF 8), transient softening occurs, with stress amplitude stabilizing after approximately 100 cycles. Figure 4.16 (b) depicts the torsional LCF test results. Notably, all stress-controlled tests used a ramp profile to apply stress amplitude, reaching the target within 200 to 300 cycles, which masks the material's initial response. Consequently, only cycles beyond 300 are analyzed. Despite this, transient softening effects are evident in all torsional LCF tests, with the cycle count required to achieve stable strain amplitude decreasing as stress levels increase.

Similar test program performed on the BM specimens, was applied to the HAZ. Symmetric axial LCF tests were performed under strain-controlled conditions, while torsional tests were stress-controlled, with stress amplitude gradually ramped up during the initial 300 cycles. The results are shown in Figure 4.17. The axial LCF tests had strain amplitudes between 0.3% and 0.8%, while the torsional tests were conducted with stress amplitudes ranging from 279 MPa to 346 MPa.

Figure 4.17 (a) presents the results from tension-compression tests. The test with the lowest strain amplitude demonstrates stable stress amplitude after ten cycles, which persists until failure without any transient behavior. In contrast, the other two tests show a continuous decrease in stress amplitude indicative of cyclic softening, similar to the BM behavior. For the test with the highest strain amplitude, an initial hardening phase is observed, lasting approximately 20 cycles before softening begins. Figure 4.17 (b) displays the stress-controlled torsional tests. The strain response in these tests confirms cyclic softening, with the degree of softening increasing as stress amplitudes rise. Unlike the BM, the strain amplitude does not stabilize but continues to increase until specimen failure.

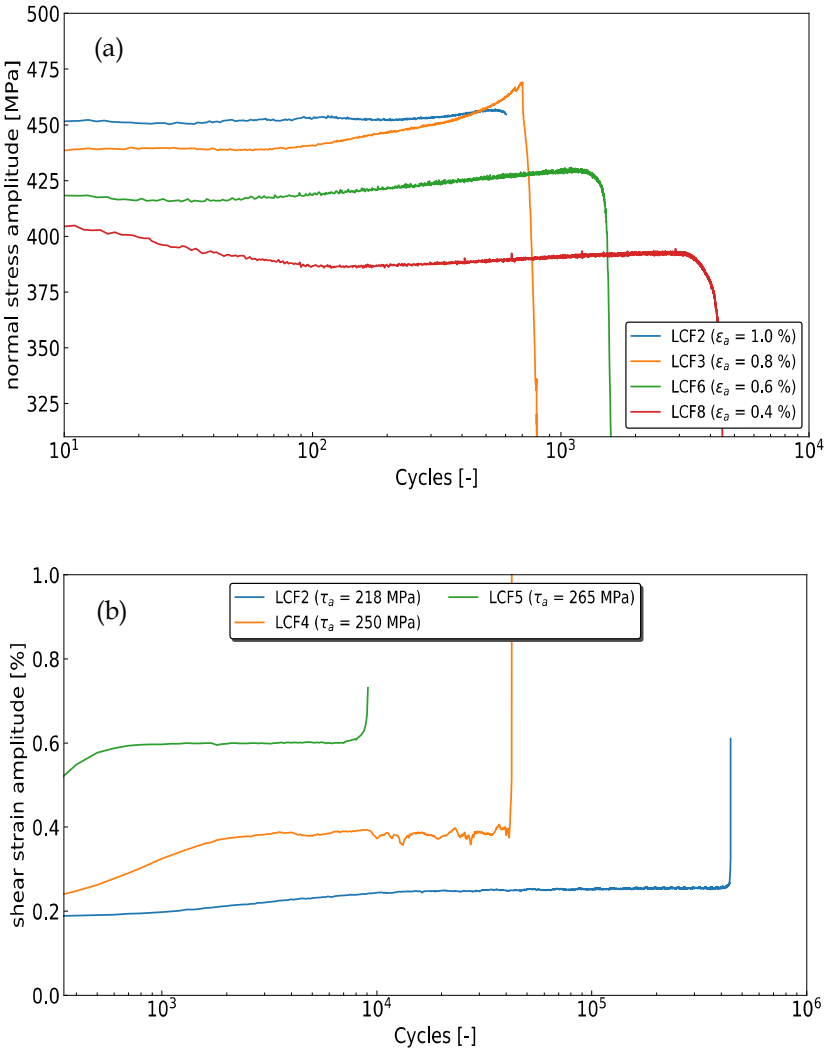

Figure 4.16 Uniaxial low-cycle fatigue test results for BM; (a) axial strain-controlled and (b) torsional stress-controlled [128].

From the discussions in this section, it is clear that both BM and HAZ exhibit transient softening at lower strain ranges within the elastic-plastic region. For BM under strain-controlled conditions, finite cyclic softening occurs within an equivalent strain range of 0.15% to 0.4% (normal strain in pure axial loading). The softening duration until stabilization ranges from 300 to 3000 cycles, inversely related to the strain range. In contrast, HAZ shows continuous softening until failure within an equivalent strain range of 0.4% to ≤0.8%.

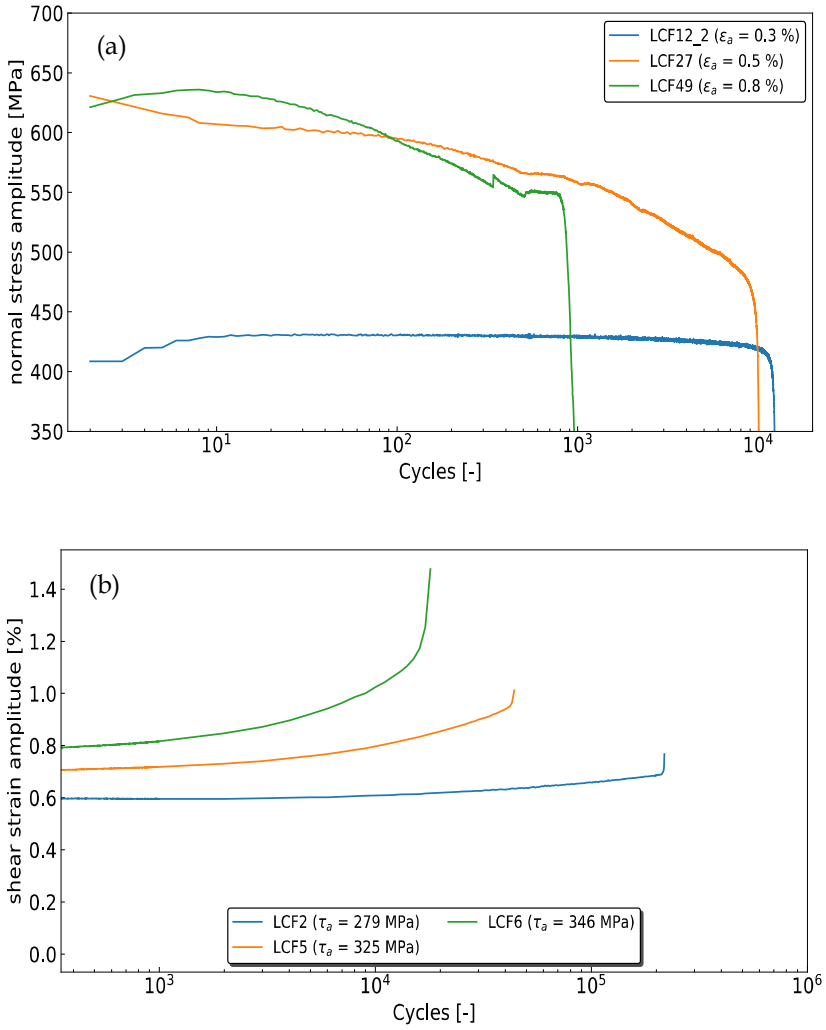

Figure 4.17 Uniaxial low-cycle fatigue test results for HAZ; (a) axial strain-controlled and (b) torsional stress-controlled [128].

4.5 Fatigue Test Results

In the present work, two groups of fatigue tests were performed, as described in Section 3.2. The first group involved fatigue tests on smooth specimens to establish the fatigue baselines necessary for the subsequent life predictions. The second group focused on welded specimens to examine the fatigue behavior of welds under both uniaxial and multiaxial loading conditions. The results of these fatigue tests are presented in the following sections.

4.5.1 Baseline Fatigue Life Curves of Base Material and HAZ (Un-Welded Samples)

Strain life curves for uniaxial strain amplitude and shear strain amplitude as a function of cycles to failure were generated based on the fatigue life data. When evaluating the Wöhler curve, it is essential to distinguish between the elastic and plastic components of the strain. The total strain was derived from the test data. The elastic component corresponds to the linear behavior according to Young's modulus, while the remaining portion represents the plastic strain. Subsequently, both components were plotted against the number of cycles (N_f) on a double-logarithmic scale.

For uniaxial loading, the applied strain was directly referred to as the total strain, since the test was strain-controlled. The elastic strain amplitude, ε_a^e, was calculated as $\frac{\sigma_a}{E}$, and the plastic strain amplitude, ε_a^p, was determined by subtracting the elastic strain amplitude from the total applied strain amplitude. However, for shear loading, the tests were conducted under load control, and the strain response was not directly measured. In this case, the applied shear strain amplitude was estimated using the serial springs approach described in Section 3.7.1.1. Additionally, to calculate the elastic shear strain amplitude, γ_a^e, based on $\frac{\tau_a}{G}$, the shear stress amplitude was first estimated using the Nadai approach [129] outlined in Section 3.7.1.1.

The four parameters of the Manson-Coffin and Morrow relationships were determined from the respective slopes and y-axis intercepts of the axial and shear strain-life curves. A summary of the baseline fatigue properties for the BM and HAZ

is provided in Table 4.1 and Table 4.2. Polynomial plots of the total strain amplitude for the BM and HAZ are shown in Figure 4.18 to Figure 4.21.

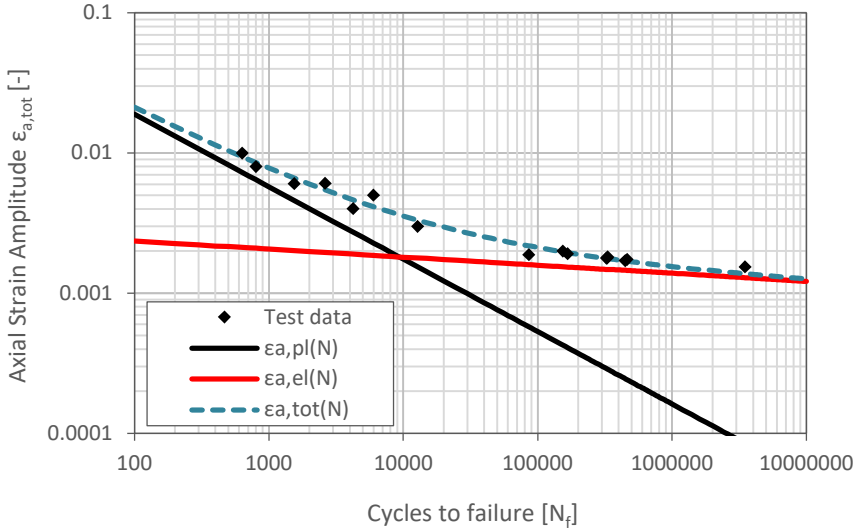

Figure 4.18 Normal strain-life curve for BM; $\varepsilon_{a,pl}$ and $\varepsilon_{a,el}$ stand for plastic and elastic axial strain amplitudes respectively.

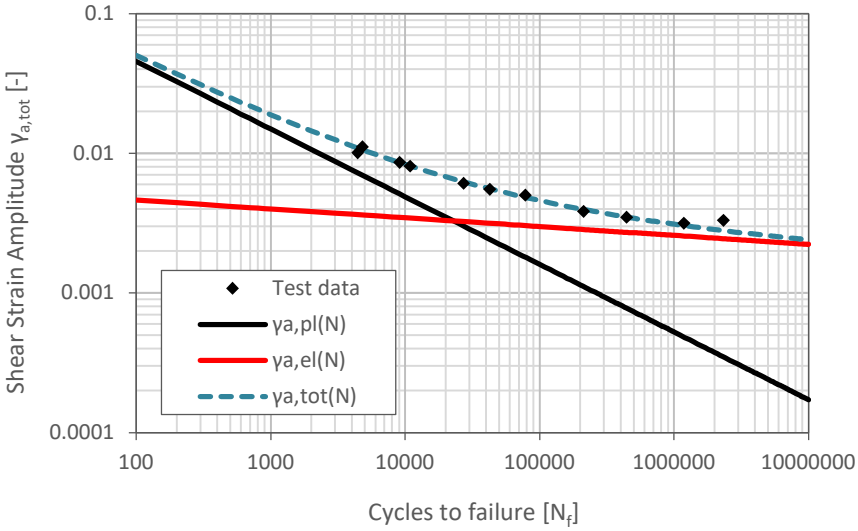

Figure 4.19 Shear strain-life curve for BM; $\gamma_{a,pl}$ and $\gamma_{a,el}$ stand for plastic and elastic shear strain amplitudes respectively.

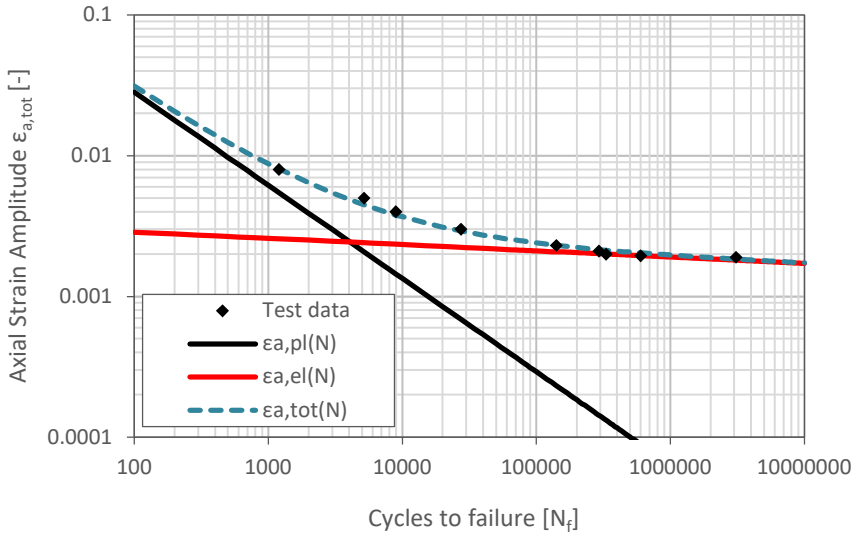

Figure 4.20 Normal strain-life curve for HAZ; $\varepsilon_{a,pl}$ and $\varepsilon_{a,el}$ stand for plastic and elastic axial strain amplitudes respectively.

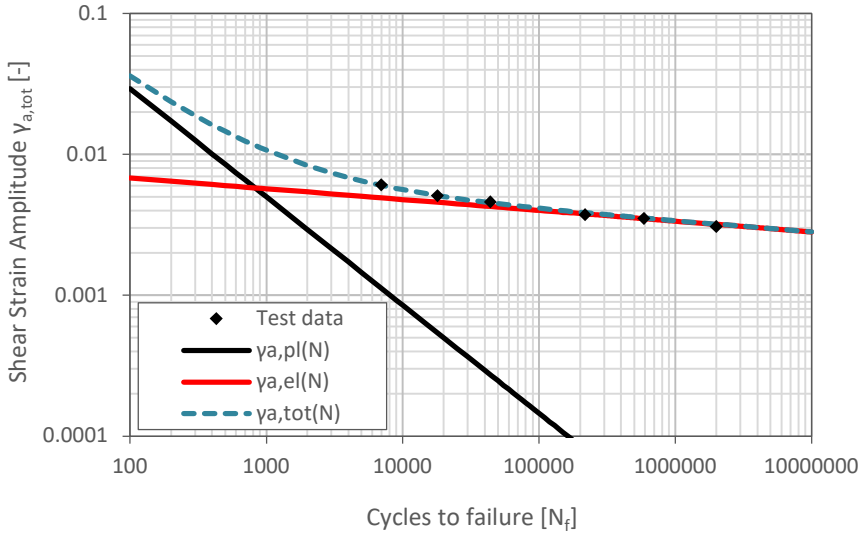

Figure 4.21 Shear strain-life curve for HAZ; $\gamma_{a,pl}$ and $\gamma_{a,el}$ stand for plastic and elastic shear strain amplitudes respectively.

The strain-life curves were reproduced for both the FS critical plane damage parameter and the modified FS (mod-FS) parameter. The damage parameters were calculated for all fatigue data from the test, i.e., axial, torsional and multiaxial in-phase and out-of-phase, using the Python script described in Section 3.7.1.2. The *k* value used to calculate the FS parameter is determined by comparing the calculated damage parameters under pure axial and pure torsional conditions at equal lifetime values.

Based on this, the values of k were set to 1.0 for the BM and 0.6 for the HAZ. The same values were used with the mod-FS parameter. Since the value of k theoretically varies with fatigue life, an effort was made to select a k value that would provide an acceptable fit across a relevant range of fatigue data, using a single value.

Fatigue analysis based on pure axial strain-life properties has been shown to yield more accurate results than using pure shear properties, as the axial strain-life baseline depends on the value of k [75]. Accordingly, using the right-hand sides of Equation 2-56 and Equation 2-58 and the axial strain-life properties of the BM, the FS and mod-FS fatigue life baselines for the BM were determined, as shown in Figure 4.22 and Figure 4.23, respectively. The fatigue life baselines for the HAZ were derived similarly and are presented in Figure 4.24 and Figure 4.25. All fatigue test data are also included in these graphs as FS and mod-FS damage values versus the recorded number of cycles to failure. The correlation of test data under different loading conditions is quite reasonable when using the FS parameter, indicating its ability to capture shear-based damage mechanisms in the material. The use of the mod-FS parameter further improved the correlation, particularly for non-proportional loading conditions. For instance, the coefficient of determination (R^2) for the out-of-phase loading case in the BM increased significantly from 0.13 with the original FS model to 0.65 using the mod-FS approach. In the HAZ, the R^2 value improved from 0.62 with the FS model to 0.67 with the mod-FS model.

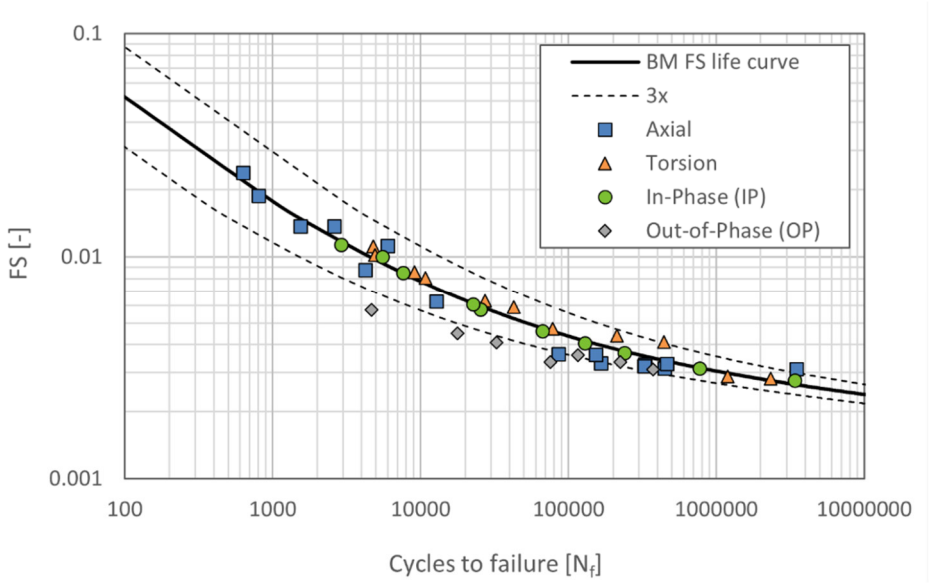

Figure 4.22 Fatigue baseline based on the FS critical plane parameter for BM.

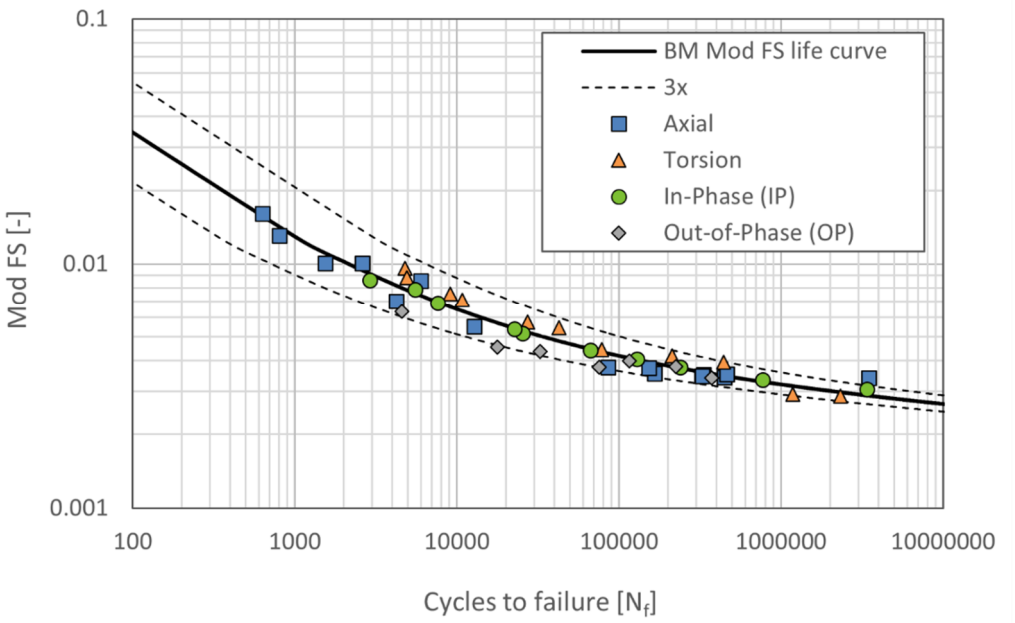

Figure 4.23 Fatigue baseline based on the mod-FS critical plane parameter for BM.

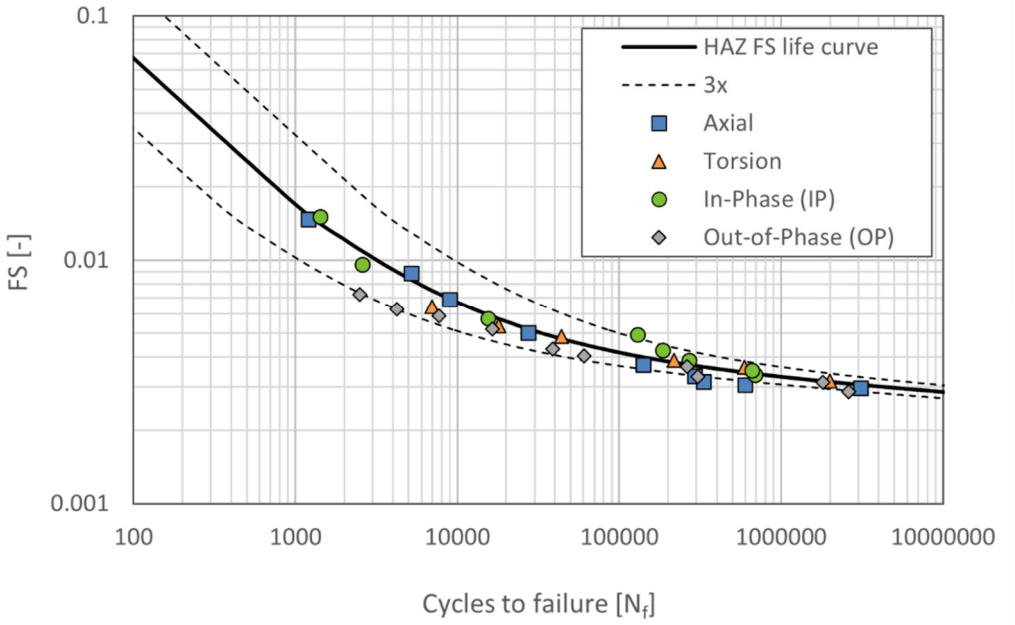

Figure 4.24 Fatigue baseline based on the FS critical plane parameter for HAZ.

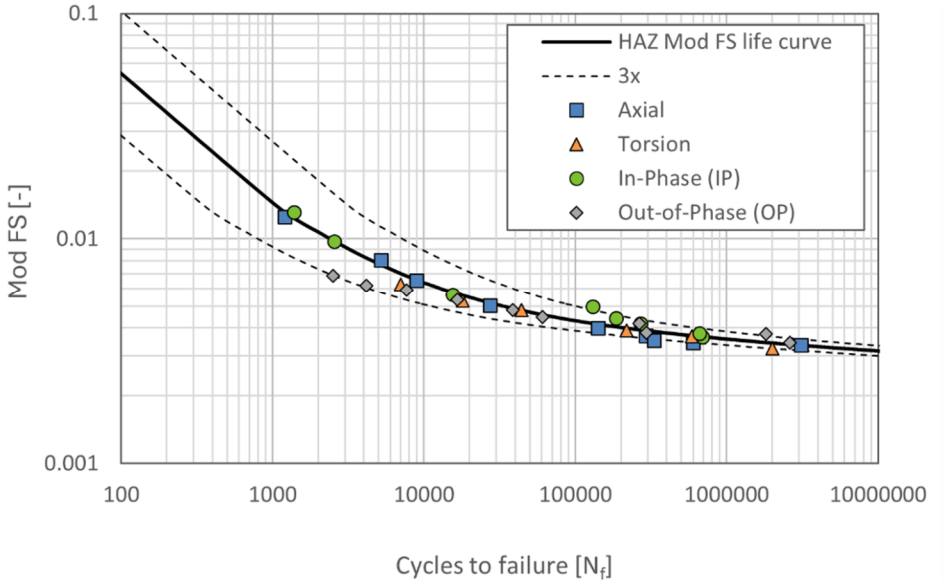

Figure 4.25 Fatigue baseline based on the mod-FS critical plane parameter for HAZ.

4.5.1.1 Effect of Load Non-Proportionality

During a non-proportional multiaxial course of stress, in contrast to the proportional stress state, the directions of the principal stresses and strains alter constantly with time, which causes a different cyclic behavior depending on the mechanical characteristics of that material. Under such conditions, several crystal planes passing through a material point experience a significant amplitude of shear strain, which could be comparable to that of the maximum shear plane. In terms of damage, there would consequently be additional planes, besides the plane experiencing the maximum damage, that also undergo a significant proportion of this maximum damage. This could result in a shear shift between the crystal planes. Figure 4.26 compares the states of fatigue damage in the smooth specimens under proportional and non-proportional tensile-torsional loads of the same magnitude, in terms of normalized mod-FS damage values versus the angle of slip planes (θ) with 1° intervals in a two-dimensional space. In both cases, the magnitude of the applied axial and shear stresses are equal, unless there is a 90° phase shift between the axial and shear components for the non-proportional event. It can be clearly seen that for the proportional stress state by rotating the axes from the axis normal to the maximum damage plane, the value of the damage parameter decreases significantly, while the

rate of decrease is much lower under the non-proportional state. In other words, the damage distribution versus plane orientation under non-proportional loading is much smoother than under proportional loading. However, such a fact is an unfavorable problem in the numerical sense, because under non-proportional cyclic load conditions there are a number of planes that undergo the maximum damage or a high percentage of it. This raises the question whether the fatigue crack preferably nucleates and propagates in the largest damage plane, while there are a number of other planes where the amount of damage is only slightly less than the maximum value. To better account for this effect, a so-called integral approach has been proposed, which is based on the integration of the damage values over the entire interference planes passing through a volume element.

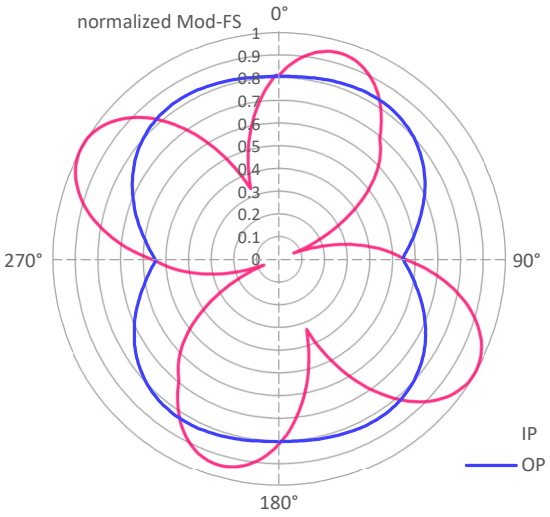

Figure 4.26 Non-proportionality effect in terms of the mod-FS damage vs. angle of the slip plane in a two-dimensional space for in-phase (IP) and out-of-phase (OP) load conditions.

The FS damage parameter corresponds to the shear strain-life curve of the respective material, as indicated below:

$$P_{FS} = \frac{\tau_f'}{G}\left(2N_f\right)^{b_0} + \gamma_f'(2N_f)^{c_0} \tag{4-1}$$

To simplify the life estimation based on the FS damage relationship, an inverse equation was derived by assuming a power law relationship as follows:

$$P_{FS} = \alpha\left(2N_f\right)^{b_0+c_0} + \beta \tag{4-2}$$

Assuming that the value and slope of the strain-life curve from Equation 4-2 at the transition life, $2N_t$, are equal to the corresponding values from Equation 4-1, the

constants α and β can be effectively calibrated. The transition life, which represents the intersection point between the elastic and plastic curves, is calculated as:

$$2N_t = (\frac{\tau_f'}{G\gamma_f'})^{\frac{1}{c_0-b_0}} \tag{4-3}$$

The constants α and β are then determined as:

$$\alpha = \left(\frac{\tau_f'}{G}\right)^{\frac{-b_0}{c_0-b_0}} \left(\frac{1}{\gamma_f'}\right)^{\frac{-c_0}{c_0-b_0}} \tag{4-4}$$

$$\beta = \left(\frac{\tau_f'}{G}\right)^{\frac{c_0}{c_0-b_0}} \left(\frac{1}{\gamma_f'}\right)^{\frac{b_0}{c_0-b_0}} \tag{4-5}$$

Based on the assumption that the total damage of a material element is equal to the sum of the damage over all slip planes running through that element, Equation 4-6 can represent this cumulative damage:

$$\sum_{i=1}^{n} \frac{1}{N_i} = \frac{1}{N_f} \tag{4-6}$$

here $\frac{1}{N_i}$ and $\frac{1}{N_f}$ represent the fatigue damage on each slip plane and the total damage in a material element respectively, where i is the plane number. With this understanding, the relationship to express the FS parameter for each individual slip plane could be as follows:

$$P_{FS,i} = \alpha'(2N_i)^{b_0'+c_0'} + \beta' \tag{4-7}$$

This equation describes a hypothetical strain-life baseline that characterizes the fatigue behavior of the material on each slip plane. It is assumed that all properties of this baseline are related to those of the macro-material. Then, the coefficients α' and β' could remain unchanged, denoted as $\alpha' = \alpha$ and $\beta' = \beta$, while the exponents b_0' and c_0' could differ through an identical linear relationship, expressed as $b_0' = n.\,b_0$ and $c_0' = n.\,c_0$, where n stands as a constant factor. By rearranging Equation 4-2 and Equation 4-7 and dividing the former by the latter, Equation 4-8 is obtained:

$$\frac{1}{(2N_f)^{1/n}} \cdot \frac{1}{(P_{FS,i}-\beta)^{1/n(b_0+c_0)}} = \frac{1}{2N_i} \cdot \frac{1}{(P_{FS}-\beta)^{1/n(b_0+c_0)}} \tag{4-8}$$

By summing over both sides of this equation with respect to the slip plane number i, and then exploiting Equation 4-6, the following equation will be obtained:

$$(2N_f)^{\frac{n-1}{n}}.\sum_{i=1}^{n}\frac{1}{(P_{FS,i}-\beta)^{1/n(b_0+c_0)}}=\frac{1}{(P_{FS}-\beta)^{1/n(b_0+c_0)}} \tag{4-9}$$

If the term $2N_f$ is substituted with its equivalent from Equation 4-2, Equation 4-9 simplifies as follows:

$$\alpha^{\frac{1-n}{n(b_0+c_0)}}.\sum_{i=1}^{n}\frac{1}{(P_{FS,i}-\beta)^{1/n(b_0+c_0)}}=\frac{1}{(P_{FS}-\beta)^{1/(b_0+c_0)}} \tag{4-10}$$

Assuming that for uniaxial and in-phase multiaxial loading conditions, the critical plane approach and the integral approach provide nearly similar results, the factor n can be calibrated for the respective material. In this study, the factor n was calibrated based on the pure axial fatigue test data by equating P_{FS} with $P_{FS,max}$. Then the validity of the calibrated n for the pure torsion and in-phase tension-torsion loading conditions was verified. After determining the correct value for the factor, the total damage (P_{FS_OP}) that occurred under the out-of-phase load could be estimated. Figure 4.27 presents the correlation of all fatigue data from smooth HAZ specimens using the proposed integral approach in combination with the mod-FS damage parameter. This approach demonstrates a significant improvement in the correlation of out-of-phase test data compared to the standalone critical plane method. In particular, the coefficient of determination (R^2) for the HAZ increases from 0.67 with the standalone mod-FS model (Figure 4.25) to 0.92 in combination with the integral approach.

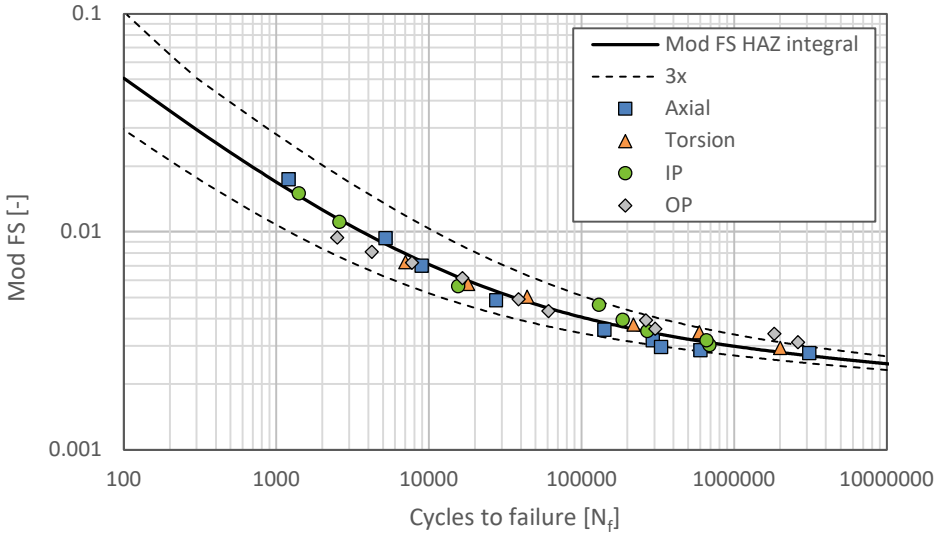

Figure 4.27 Fatigue baseline based on the integral approach and mod-FS damage parameter for HAZ.

4.5.1.2 Fatigue Crack Initiation/Propagation

To be able to differentiate between the crack initiation and crack growth, the formation and evolution of the fatigue cracks were monitored for a few constant amplitude pure axial fatigue tests on smooth BM and HAZ samples using the replica technique. Table 4.3 and Table 4.4 list the fatigue tests that were subjected to replica crack monitoring. Applying this method was also useful for gaining insight into the cracking mechanisms within the testing material. By observing the crack length in different stages of fatigue life, the significance of the crack growth phase for the overall life of the desired material could be determined. This allows the formulation of a correlation between fatigue baselines based on the total fatigue life and the fatigue initiation life. Since many damage models are designed to predict only the crack initiation life, it is important to differentiate between the various stages of the material's life. Only by understanding these differences, fatigue life predictions can be made more accurately.

Table 4.3 Smooth specimen: BM-Axial fatigue tests with replica technique.

Specimen ID	Frequency [1/s]	R-ratio	Axial stress amplitude [MPa]	Axial strain amplitude [%]	Cycles to Failure (N_f)
BM_LCF_0.5	0.5	-1	-	0.5	1.63E+04
BM_HCF_310	30	-1	310	0.186	7.08E+05

Table 4.4 Smooth specimen: HAZ-Axial fatigue tests with replica technique.

Specimen ID	Frequency [1/s]	R-ratio	Axial stress amplitude [MPa]	Axial strain amplitude [%]	Cycles to Failure (N_f)
HAZ_LCF_0.4	0.125	-1	-	0.4	6.53E+04
HAZ_HCF_390	15	-1	390	0.195	5.50E+05
HAZ_HCF_415	15	-1	415	0.210	2.90E+05

Figure 4.28 and Figure 4.29 show the results of crack monitoring using the replica technique at various stages of the growth on smooth BM samples under pure axial loads. Figure 4.28 represents the HCF test (BM_HCF_310), while Figure 4.29 represents the LCF test (BM_LCF_0.5), as listed in Table 4.3. As shown in Figure 4.28, during the HCF test in the BM, a dominant fatigue crack nucleated and propagated to the final fracture. However, during the LCF test (Figure 4.29), a network of micro-

cracks coalesced, spreading throughout the uniformly stressed gauge section of the specimen. Similarly, the results of crack monitoring applied to the smooth HAZ samples are shown in Figure 4.30 for the HCF test (HAZ_HCF_415) and Figure 4.31 for the LCF test (HAZ_LCF_0.4), as listed in Table 4.4. For the HAZ samples however, it was observed that the mechanism of cracking in both HCF and LCF loads is nucleation and growth of a dominant crack which reflects a more brittle material behavior of the HAZ compared to BM.

The plots in Figure 4.32 quantify crack behavior in terms of crack length relative to the lifetime fraction for BM and HAZ. It is evident from Figure 4.32 that the fatigue crack length increases and enters the unstable stage much faster in BM with a ferrite-pearlite structure than in HAZ with a predominantly bainitic microstructure. The figure also shows that the crack initiation stage (defined as a 0.1 mm crack) accounts for approximately 17% of the total life in the LCF test and about 6% in the HCF test for the BM. In contrast, these values are around 75% and 80% of the total life for the HAZ in the LCF and HCF tests, respectively. It can be observed that the crack growth rate increases rapidly after reaching a certain crack length, leading quickly to final fracture. These plots suggest that the crack propagation phase, as a proportion of the total lifetime for the HAZ samples—characterized by their higher brittleness—is minimal and even negligible compared to the BM. Based on this, efforts were made to generate crack initiation fatigue baselines using the existing replica investigation results (Figure 4.33). Due to the absence of replica-based fatigue tests suitable for establishing a strain-life baseline, it was assumed that the exponents of the curve equation would remain unchanged from the original baseline, with only the coefficients calibrated to achieve a good fit with the crack initiation test data. These diagrams clearly show that, for the HAZ, the difference between the crack initiation and the original baseline is negligible compared to the BM.

4.5.2 Fatigue Life Curves (Welded Specimens)

In this section the results of the fatigue tests on the welded specimens are presented. The test results of the uniaxial and multiaxial cyclic fatigue tests are shown in the form of Wöhler diagrams in double-logarithmic representation on the basis of the nominal stress versus the number of cycles. The runouts are marked with arrows.

Figure 4.34 shows the S-N diagrams of all load types for the HT and AW conditions. While the scatter of the data is reasonably good, the fatigue data for different load types do not correlate well with each other, and the slope of each fitted curve is different from the others. This is due to the existence of the weld notch, which introduces a local stress/strain that cannot be described by a nominal stress fatigue measure. Different slopes are attributed to different normal and shear stress concentration factors. Later in Chapter 7, local approaches are presented to find a better correlation of all fatigue data.

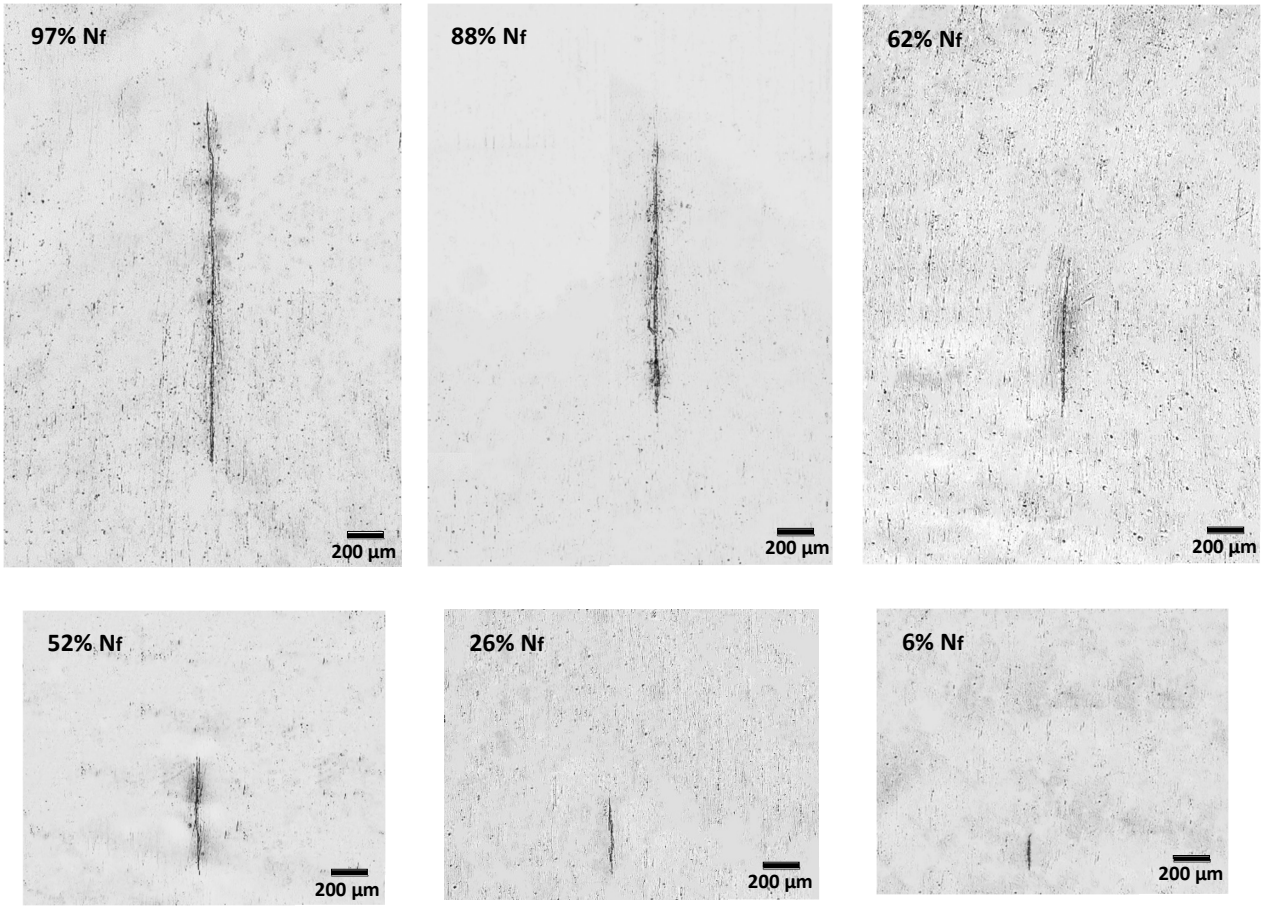

Figure 4.28 Stages of fatigue crack evolution recorded by the replica technique: BM_HCF_310, σ_a = 310 MPa.

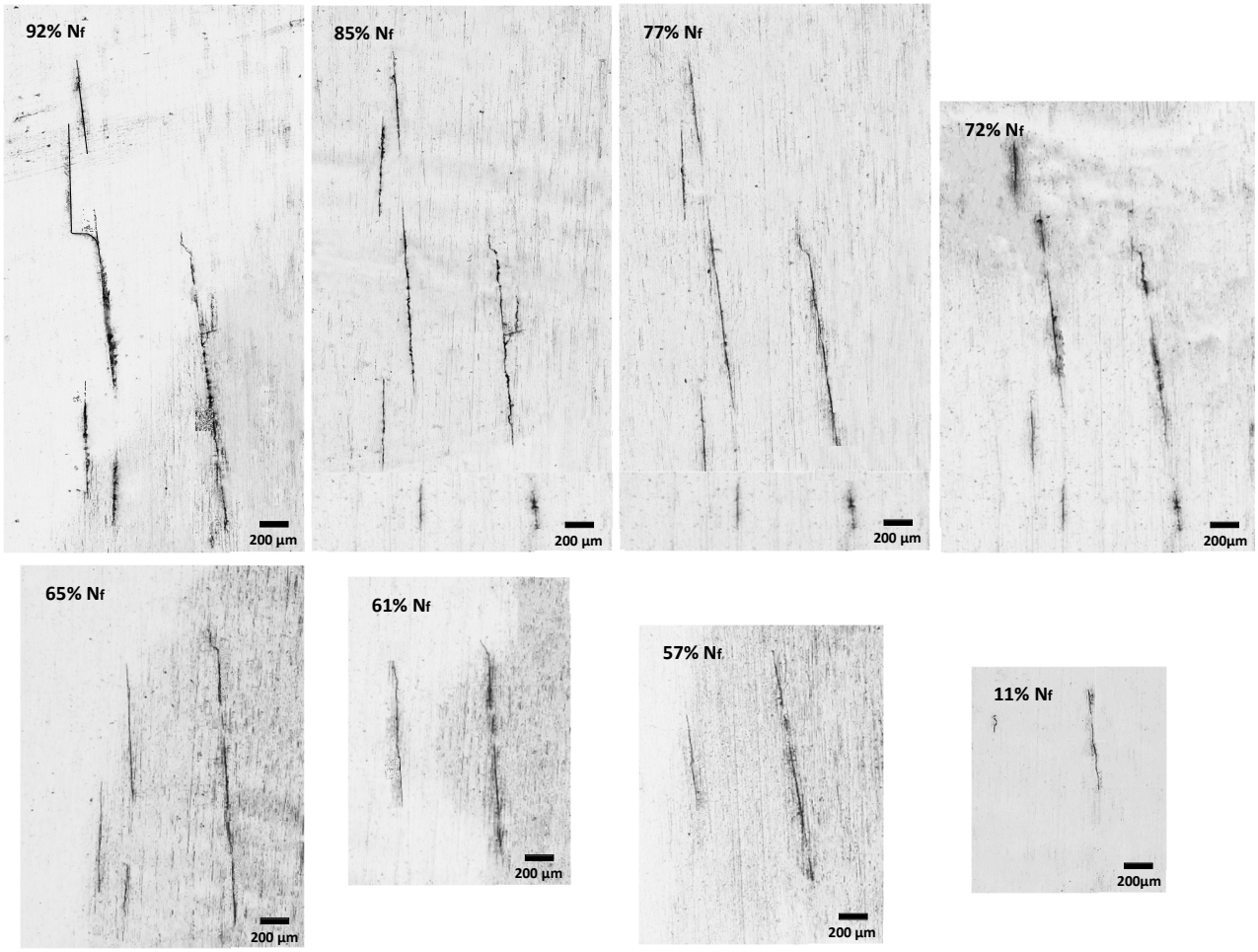

Figure 4.29 Stages of fatigue crack evolution recorded by the replica technique: BM_LCF_0.5, ε_a = 0.5%.

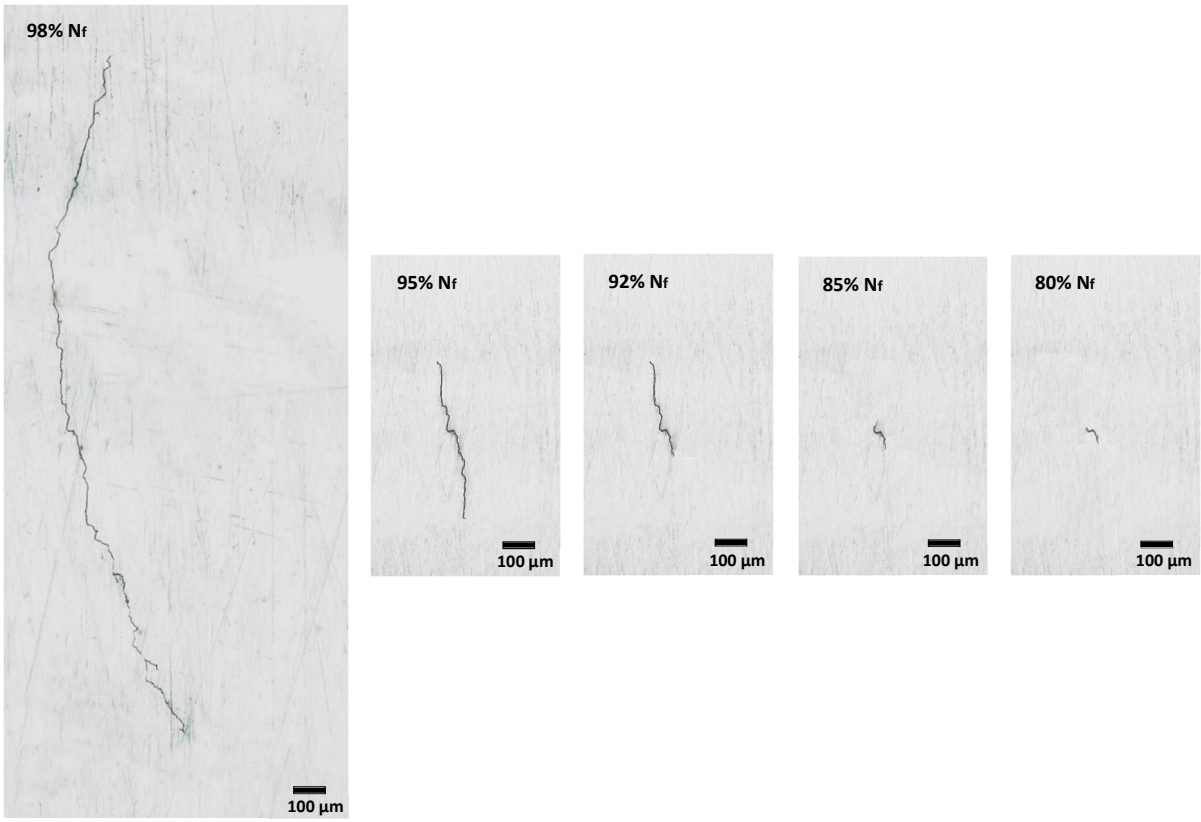

Figure 4.30 Stages of fatigue crack evolution recorded by the replica technique: HAZ_HCF_415, σ_a = 415 MPa.

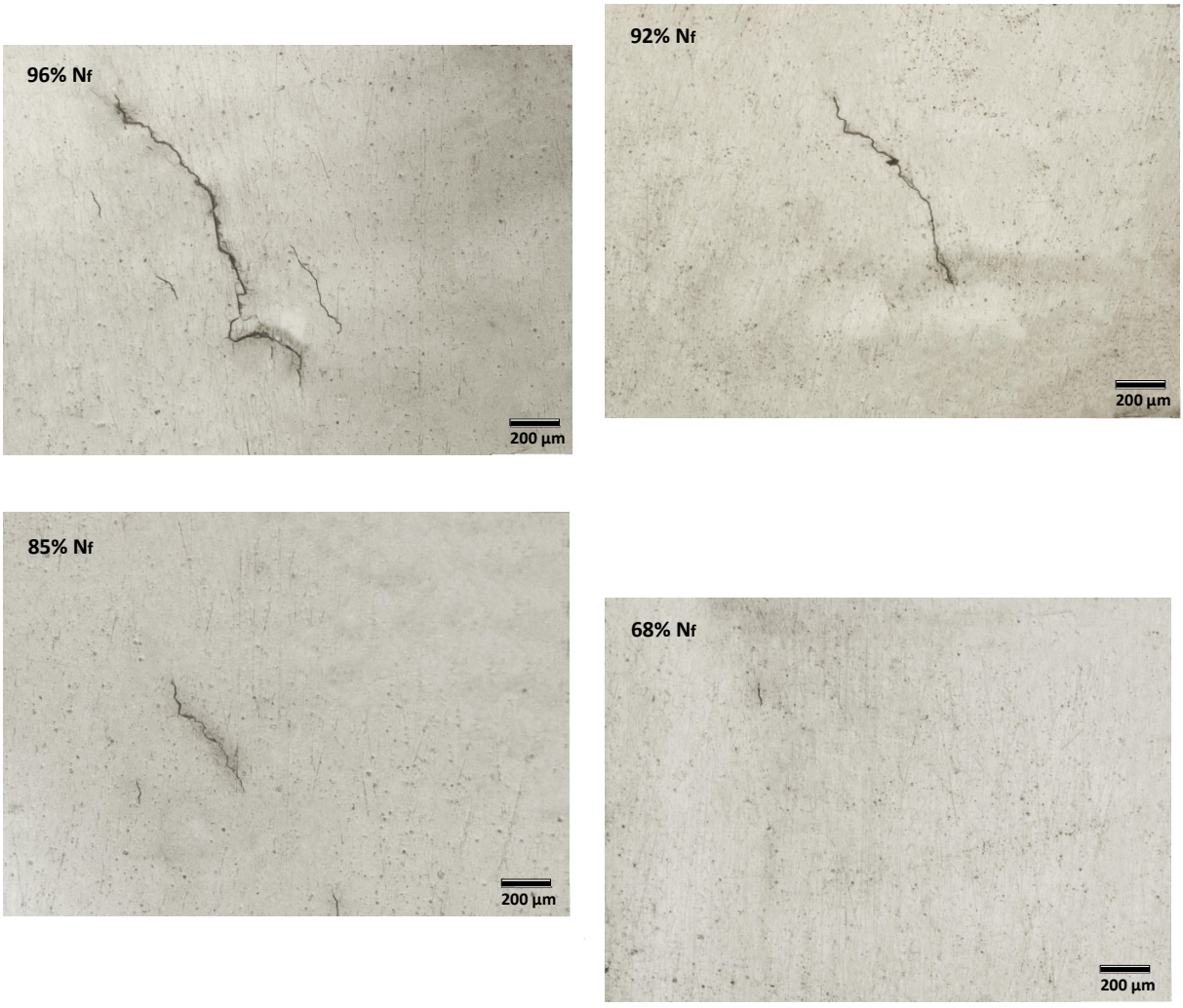

Figure 4.31 Stages of fatigue crack evolution recorded by the replica technique: HAZ_LCF_0.4, ε_a = 0.4 %.

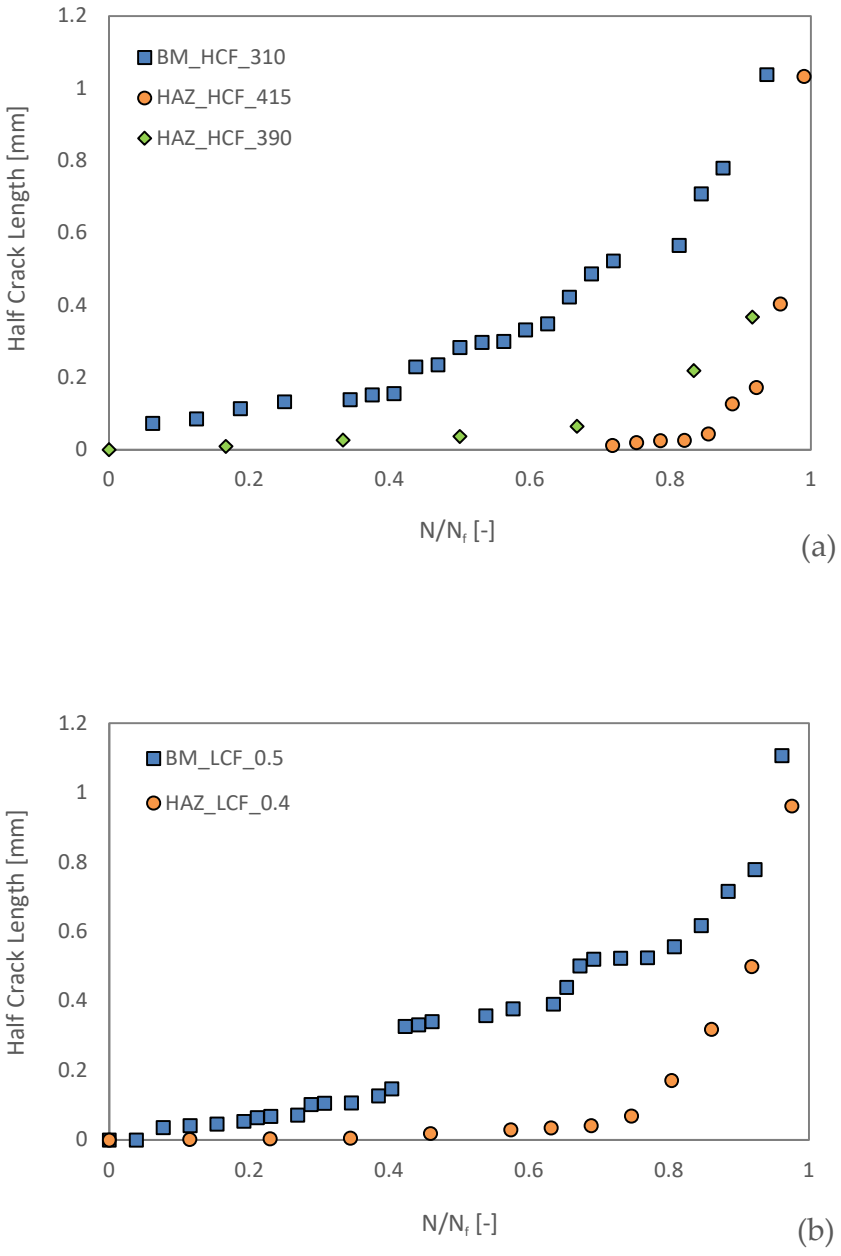

Figure 4.32 Fatigue crack initiation and growth behavior recorded by the replica technique for the BM and HAZ in the (a) HCF and (b) LCF regimes.

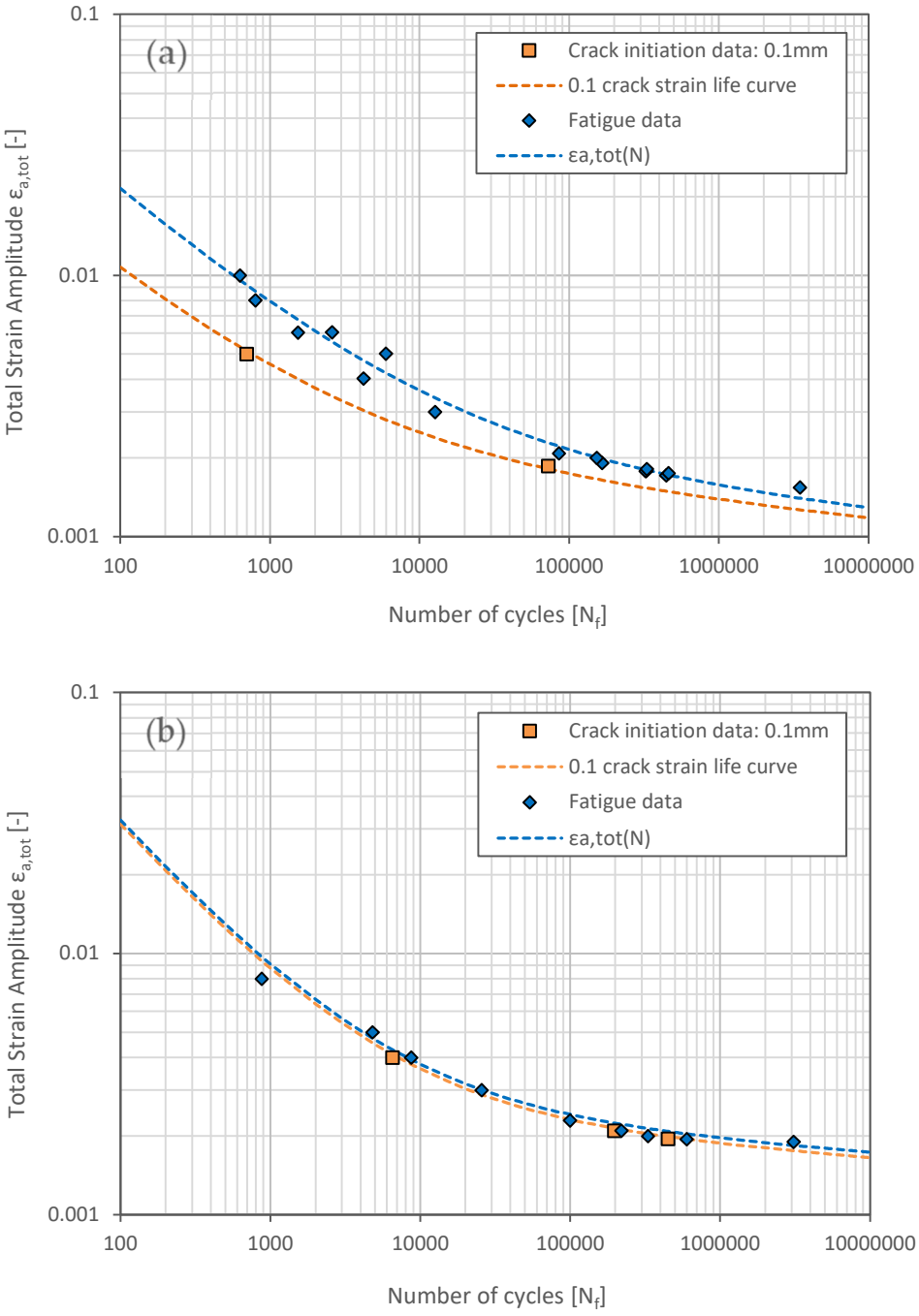

Figure 4.33 Comparison of crack initiation life vs. failure life for (a) BM (b) HAZ.

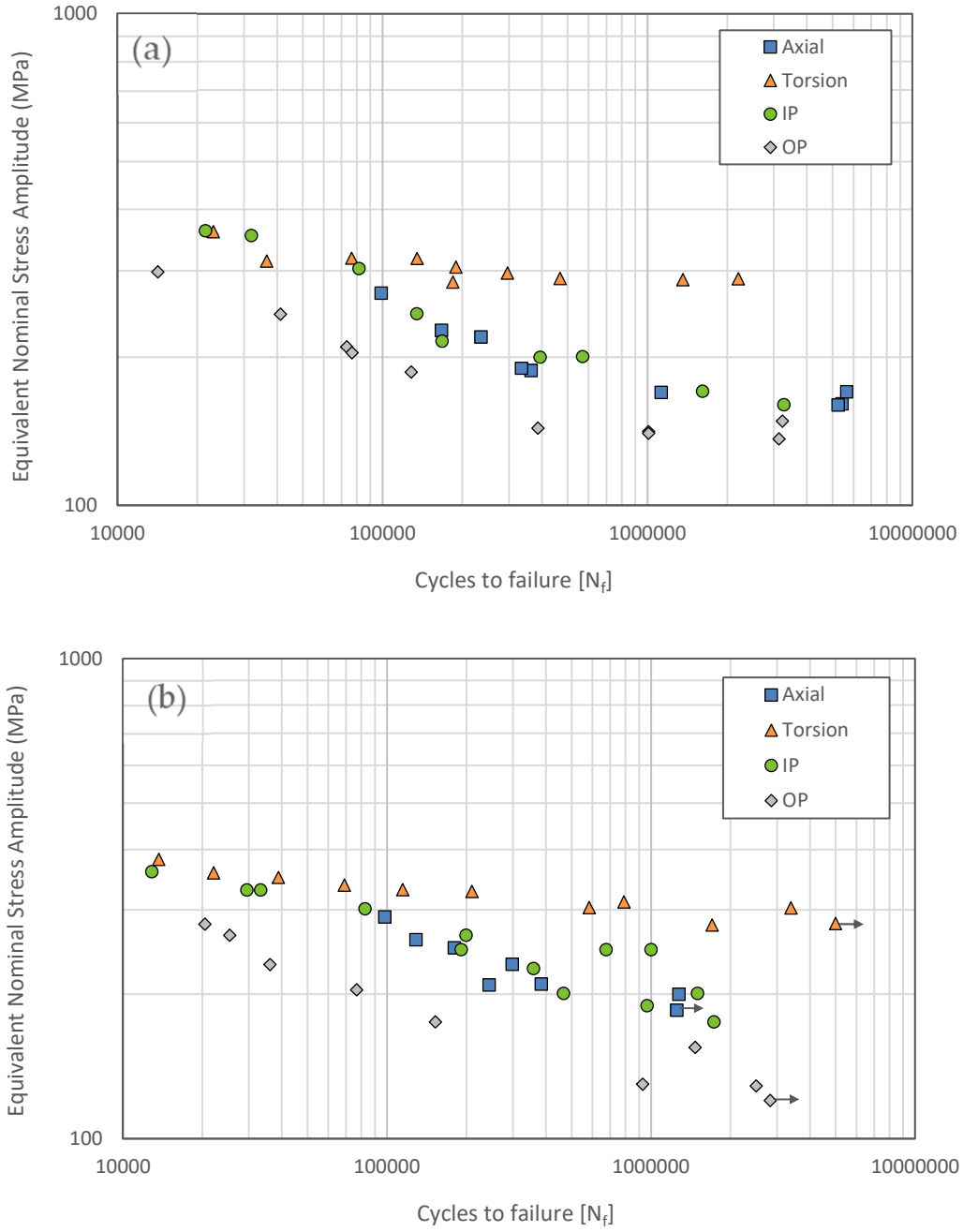

Figure 4.34 Fatigue life correlations for the (a) HT and (b) AW specimens in terms of equivalent nominal stress amplitude vs. cycles to failure and based on von Mises equivalent stress-life approach (→ Run-out).

4.6 Summary and Conclusions

Chapter 4 summarized the results of the experimental contributions in the present work, along with the respective assessment methodologies.

Full-field residual stress measurements of the fatigue weld specimens indicated that tensile axial and circumferential residual stresses exist on the specimen surface in the weld area, while the HAZ exhibits highly compressive residual stresses. However, in the bulk of the material, the residual stresses are compressive in all directions within the weld zone and tend to become tensile in the HAZ.

Detailed discussions on the microstructural analysis of a selected cross-section revealed that the base material, originally composed of ferrite and pearlite, undergoes a severe phase transformation during welding, resulting in a highly bainitic microstructure in the HAZ. The hardness of the base material, with an average of HV 160, increased to as high as HV 230 in the HAZ near the weld boundaries.

The material deformation test results for both the base material and HAZ were primarily reported in terms of static and cyclic stress-strain curves. According to the results, the HAZ exhibited significantly higher static strength and lower ductility compared to the base material. Under cyclic loading, the HAZ also showed higher strength, characterized by a higher cyclic strength coefficient and a lower cyclic strain hardening exponent, indicating increased brittleness. Both the base material and HAZ demonstrated significant non-proportional hardening.

The evaluation of transient softening behavior under axial and torsional cyclic loading revealed that for the base material, transient softening tends to stabilize after a certain number of cycles, depending on the strain amplitude. In contrast, for the HAZ, transient softening persists until final failure.

The results of fatigue tests on smooth specimens were presented as fatigue baselines. Initial reference baselines were established using strain-life curves and were further refined using Fatemi-Socie and modified Fatemi-Socie critical plane damage parameters for assessing the fatigue life of the weld specimens. Although the critical damage models provided reasonable correlations for various types of fatigue data, the non-proportional fatigue data generally exhibited a poorer correlation, suggesting that the models tended to underestimate fatigue damage under such loading conditions. This issue was subsequently addressed by employing an integral

approach, which considered damage values across multiple slip planes at the critical material point, rather than relying solely on the maximum damage value from a single plane.

A crack visualization technique using replica foils was implemented to monitor the progression of fatigue cracks from initiation to final fracture. It was observed that in the base material, crack propagation accounts for a relatively significant portion of the total fatigue life, whereas in the HAZ, this phase is minimal and nearly negligible compared to the base material.

The results of fatigue tests on welded specimens under different loading conditions were presented in the form of nominal S-N plots. While the scatter of the data was reasonable, the significant effect of weld notch as a stress raiser was emphasized, highlighting the need for local stress or strain-based fatigue assessments.

Chapter 5 Deformation Behavior Modelling

5.1 Cyclic Plasticity Model for Welding Simulation

The constitutive material model, particularly with regard to the hardening behavior, is crucial for the accuracy of residual stress calculations. By comparing the computed responses of a single element FE model subjected to symmetric strain-controlled cyclic loading with the recorded stress-strain behavior of the corresponding material [121] in isothermal constant amplitude LCF tests under strain-controlled conditions, the overall impact of the employed hardening model was evaluated. LCF tests were carried out at three comparatively high strain amplitudes of 3%, 5% and 7%, which were chosen to correspond to the strain ranges that the material is likely to experience during the welding process.

The proportion of isotropic hardening in SYSWLED can be quantified using a coefficient that ranges from zero to one. Additionally, the conventional hardening model can be adapted to accommodate nonlinear hardening behavior. Specifically, the combined hardening model of Armstrong-Frederick [47], which addresses nonlinear kinematic hardening under isothermal and monophasic conditions, is expressed as follows:

$$\bar{\sigma}\left(\varepsilon_{eq}^{p}\right) = \bar{\sigma}_0\left(\varepsilon_{eq}^{p}\right) + \frac{\mathrm{C}}{\gamma}\left(1 - \mathrm{e}^{-\gamma\varepsilon_{eq}^{p}}\right) \tag{5-1}$$

where $\bar{\sigma}$ represents $\sigma - \sigma_0$ and σ_0 is the yield stress at zero plastic strain, ε_{eq}^{p} is the equivalent plastic strain and C and γ are material kinematic hardening parameters which are only supported as a single pair in this model. In this equation, $\bar{\sigma}_0$ refers to the isotropic strain hardening component, which characterises the expansion of the yield surface size in relation to the accumulated plastic strain. SYSWELD uses stress-

strain data series to describe this parameter. The kinematic hardening term, which is determined by the evolution of the back stress tensor, controls the translation of the yield surface. SYSWELD also provides the facility to extend the model to multiphase and non-isothermal conditions. Nevertheless, none of the parameters can be expressed as a function of strain range. When calibrating material parameters, especially for S355, where even cyclic softening occurs at strain ranges below a certain level, it is therefore imperative to consider the strain range of the actual structure.

When using non-isotropic hardening models, the required parameters can be characterized in different ways by matching the models with either monotonic or cyclic uniaxial mechanical test results. Two scenarios were investigated in this study: in Case-1, pure linear kinematic or combined isotropic-linear kinematic models were implemented. The monotonic response in terms of true stress versus plastic strain was specified up to 100% of the maximum plastic strain. In Case-2, pure non-linear kinematic or combined isotropic-nonlinear kinematic hardening models were used. The parameters were determined by fitting to the first cycle of the material response in the cyclic test with a total strain range of 14%. Additional cyclic hardening was neglected in this case. As the weld is a single pass dummy bead-on-tube, monotonic tensile properties of the base material and cyclic properties from the first load reversal were introduced for the model.

For simple isotropic, pure kinematic and combined isotropic-kinematic hardening models, Figure 5.1 displays the calculated responses in all three strain ranges. The measured and calculated responses are plotted respectively in red and blue in this diagram. The dashed and solid blue lines show the results of Case-1 and Case-2 of the above scenarios. According to this figure, the overall agreement of the predicted responses with the cyclic test data is satisfactory for the simple isotropic model in all three strain ranges. This is also true when the Bauschinger effect is omitted, except for the sharper yield points observed in the cyclic response. The model performs particularly well in predicting the initial monotonic responses and the peak stresses.

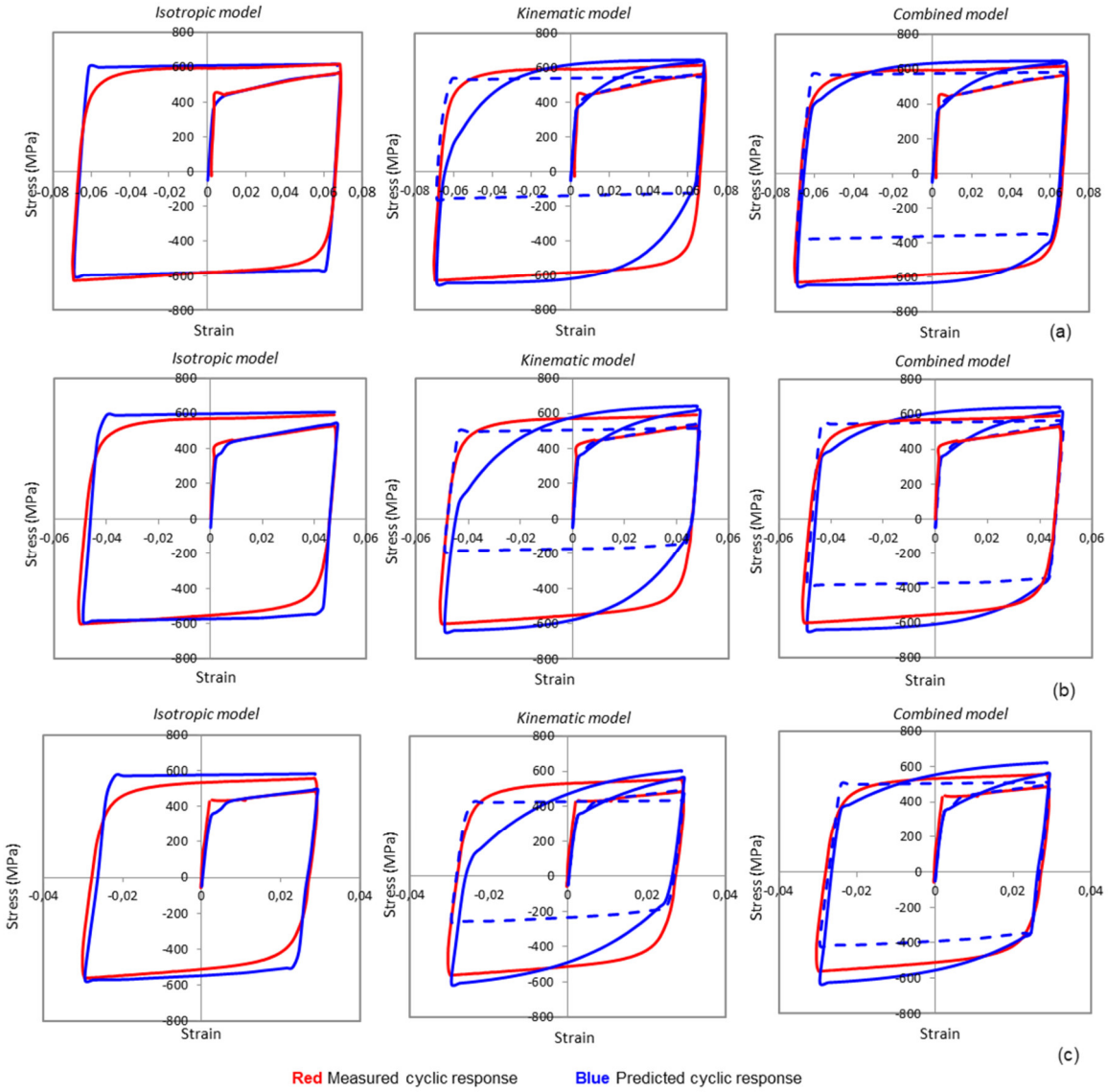

Figure 5.1 Predicted responses after first load reversal for S355J2H based on different material constitutive models at room temperature; (a) $\Delta\varepsilon$ = 0.14, (b) $\Delta\varepsilon$ = 0.1 and (c) $\Delta\varepsilon$ = 0.06. For Kinematic and Combined hardening models: Dashed line represents Case-1 with a linear fit where ε_{max} = 1.0 and solid line represents Case-2 with a nonlinear fit where $\Delta\varepsilon$ = 0.14 [121].

When using the kinematic model, which incorporates the Bauschinger effect, reversed yielding appears at significantly lower stress levels compared to tests, especially in higher strain ranges. The linear kinematic model performs significantly worse than the nonlinear model in estimating both the shape of the hysteresis loop and the magnitude of the peak stresses. To improve the peak values, the maximum plastic strain is reduced when defining the monotonic stress-strain curve in the model and adapted to the maximum strain amplitude used in cyclic tests. The selected maximum

plastic strain must actually cover all possible strain ranges during welding, as several strain cycles with different strain ranges are likely during welding. Whilst the non-linear kinematic model proves superior in predicting the shape of the hysteresis loop, it is inadequate for accurately predicting the initial monotonic response.

The incorporation of the nonlinear hardening behavior and the Bauschinger effect into the combined isotropic-nonlinear kinematic model with a 50% isotropic component improves the calculated shape of the hysteresis loop and the peak stresses. Nevertheless, similar to pure nonlinear kinematic model, this model shows limitations in effectively matching the initial load response. Despite the inherent challenge of fitting both monotonic and cyclic responses, a better fit can be achieved by optimizing the interaction between kinematic parameters and monotonic stress-strain data.

Although the parameters of the strain hardening model can be adequately calibrated using simple uniaxial and isothermal cyclic test results, the complexity increases when welding is considered as a thermo-mechanical cyclic loading process. This complexity increases further when dealing with materials such as S355J2H steel, which undergoes phase transformations in the solid state. It is technically possible to define kinematic parameters as a function of temperature and metallurgical phases, however achieving convergence within a realistic calculation time for welding simulations can be difficult. In this study, the isotropic strain hardening model was used for welding simulation as it shows relatively satisfactory agreement with cyclic test results within the specified strain ranges despite its inherent simplicity.

5.2 Cyclic Plasticity Model for Fatigue Simulation

The non-uniform heating during welding can lead to heterogeneous mechanical properties both in the weld metal and in the adjacent areas. This leads to additional complexity in the evaluation of local stress-strain behavior, especially under fatigue conditions. Therefore, it is essential to thoroughly characterize the variation of mechanical properties in the vicinity of weld notches, with a focus on cyclic properties. An accurate fatigue assessment requires not only appropriate fatigue damage parameters, but also a thorough understanding of material behavior with a particular focus on non-proportional hardening. This understanding is crucial for the

realistic representation of the stress-strain state of the material in a weld, especially in areas with weld notches, where plastic deformation is more likely to occur. For cyclically stabilized materials subjected to uniaxial or pure torsional loading, the accurate description of material constitutive behavior could be obtained by fitting the appropriate plasticity model to the stress-strain responses obtained from IST or LCF tests. However, for more complicated loading conditions such as multiaxial, non-proportional and variable amplitude loads, it is essential to consider not only the Bauschinger effect but also other material-dependent phenomena. These include transient hardening or softening, memory effect and non-proportional hardening.

5.2.1 Modelling Strategy

In order to describe the material deformation behavior from the raw experimental data and to calibrate the parameters of the material model, finite element simulations with single element models were performed for both tubular and solid specimens as described in Section 3.2. The commercial finite element software ABAQUS was used for pre-processing, solution, and post-processing. The use of single element models served the purpose of initially validating the developed user subroutines under simple loading conditions. This subsequently facilitated the extensive calibration process under more complicated loading conditions within a reasonable computing time.

Multiaxial single element tests were performed on a beam element PIPE31, which is a one-dimensional approximation of a continuum element and is based on the slenderness assumption. This element has two nodes and contains a hollow, thin-walled circular cross-section in three-dimensional space. A material model with the von Mises yield criterion was used, in which the effects of the deformation rate were neglected, so that a rate-independent theory could be chosen. As a basis, two different types of strain hardening were considered: isotropic and kinematic strain hardening. The latter was characterized by the Chaboche strain hardening model [48]. A material model provides a series of parameters that describe the plastic behavior of the materials under investigation. In general, the accuracy of the model increases with the number of parameters. However, as the number of parameters increases, the complexity of the model also grows. This complexity was evident in a complex calibration process aimed at determining an optimal set of material constants that could accurately represent the desired response of the material. The strain hardening

parameters were calibrated using experimental data from uniaxial tests. ABAQUS provides a built-in plasticity model that includes both kinematic hardening with a variable number of back stress components and isotropic hardening. To maintain simplicity, this model and its calibration algorithm were used as the basis. The validity of the calibrated model was then checked for the multiaxial loading conditions. However, since the hardening model built into ABAQUS does not account for non-proportional hardening, it was necessary to implement such a model. This was achieved by incorporating a UMAT subroutine to integrate the corresponding constitutive law by successive substitution together with the constitutive non-proportionality parameter of Tanaka [57].

Within this study, the focus was solely on adjusting the isotropic hardening parameters (Equation 2-34). To address isotropic non-proportional effects, the material parameter Φ was introduced. This parameter delineates the equivalent stress difference between load paths that are in-phase and those at a 90° out-of-phase angle:

$$\Phi = \bar{\sigma}_{\mathrm{OP}} - \bar{\sigma}_{\mathrm{IP}} \tag{5-2}$$

The modified isotropic hardening parameter contains Φ and assumes the maximum value of A for the non-proportional case.

$$\tilde{Q} = Q + \sqrt{2}A\Phi \tag{5-3}$$

The revision of the evolution equation for isotropic hardening leads to:

$$\dot{\sigma}_y = \tilde{b}(\tilde{Q} - \sigma_y)\dot{p} \tag{5-4}$$

where $\tilde{b}$ denotes the modified isotropic hardening rate constant.

5.2.2 Calibration of Hardening Parameters

In this section, the results of the calibration process for the BM and HAZ are presented [128]. The isotropic and kinematic strain hardening parameters were derived from uniaxial tests using either constant (LCF) or piecewise constant (IST) strain amplitudes. The validation focused exclusively on relevant stages of a complete IST response, namely those in the middle section. These stages include strains that are significant enough to cause plastic deformation but are kept minimal to ensure consistency within the applicable range of the calibrated model.

Calibration was performed using the built-in combined kinematic and isotropic hardening model in the ABAQUS software, comprising three back stress components. Isotropic strain hardening parameters were derived from strain-controlled LCF tests. For the calibration of the isotropic constants, the tests with the highest strain amplitudes were selected, namely 1.0 % for the BM and 0.8 % for the HAZ. The findings suggest that stabilization occurs around the tenth cycle. Peak stress versus cycle data was fitted with an exponential function described in Equation 2-35. This enabled the extraction of the hardening parameters Q and b, as detailed in Table 5.1.

Table 5.1 Isotropic hardening parameters for S355J2H - BM and HAZ [128].

Material	$\sigma_{y,0}$ [MPa]	Q [MPa]	b [-]
BM	243.43	13.37	26.81
HAZ	415.33	8.95	32.20

In a symmetric strain-controlled experiment, the shape of the hysteresis loop is determined by the kinematic strain hardening as it characterizes the evolution of the back stress. Therefore, it is necessary to use complete cycles to calibrate the corresponding parameters instead of relying on peak values over the entire strain history. The kinematic hardening model was calibrated using complete hysteresis loops obtained from IST and LCF tests. ABAQUS not only provides the kinematic hardening parameters, $C^{(k)}$ and $\gamma^{(k)}$, but also returns the size of the stabilized yield surface as part of the calibration output. To ensure the validity of the calibration, this quantity can be compared with the stabilized yield strength determined by the isotropic strain hardening calibration. The comparison shows a remarkable agreement between the values derived from different calibration procedures, indicating a precise calibration process. The resulting kinematic hardening parameters are presented in Table 5.2.

Table 5.2 Kinematic hardening parameters for S355J2H - BM and HAZ [128].

Material	$C^{(k)}$ [MPa]			$\gamma^{(k)}$ [-]		
	1	2	3	1	2	3
BM	16268	635071	116551	168.9	10850	1343.6
HAZ	78105	84330	34798	12808	1487.7	228.60

To verify the determined parameters, single element simulations were performed with strain amplitudes corresponding to the different steps of the incremental step test. The number of load cycles applied in the simulations were carefully selected to ensure that stable hysteresis was achieved. Figure 5.2 shows the hysteresis loops of selected steps of the IST and the corresponding simulated loops.

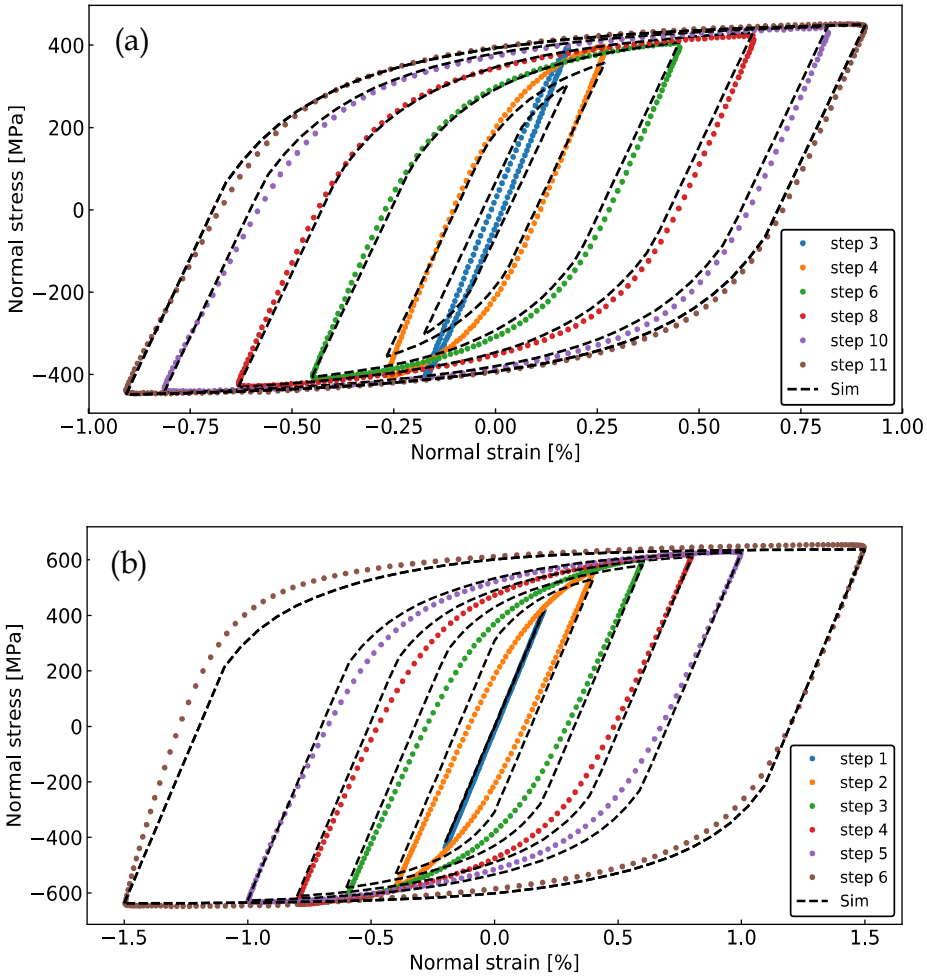

Figure 5.2 Axial hysteresis loops for the BM (a) and HAZ (b) - experimental loops from IST are represented in colored symbols and simulated loops in dashed blacklines [128].

For the BM, the axial hysteresis loops from experimental and simulated data closely align for steps 6 to 11. However, for smaller strain amplitudes in steps 4 and 3, the simulated loops exhibit notable deviations from the experimental ones before reaching the peak tensile and compressive stresses. Steps with similar behavior or

with linear behavior (step no. < 3) were excluded from the display in order to improve the graphical clarity.

In HAZ, the simulation accurately predicts the maximum and minimum axial stresses for all steps of the IST, with the exception of the lower strain range in step 2, where the peak stresses are underestimated. A comparison of the shape of the hysteresis loops shows a common trend of slightly over predicted stresses in the elastic-plastic transition for steps 2 to 5. In contrast to the stabilized loops, step 6, which was an unstable loop that ended in failure, has a more pronounced "knee" and agrees better with the simulation. This is particularly evident in the pressure part of the hysteresis.

The accuracy of the calibrated parameters was evaluated for more complicated loading conditions, i.e., pure torsion, as well as for multiaxial proportional and non-proportional loading conditions. The derivation of stresses and strains from axial experiments is a straightforward process and the decision to use single element tests instead of full specimen simulations is easily justifiable. In contrast, torsional tests require some preliminary considerations before applying the calibrated material parameters. Section 3.7.1.1 discussed in detail the process of generating stress and strain data from the torques and angles recorded by the testing machine. Following these considerations, the isotropic and kinematic hardening parameters derived from the axial tests were integrated into simulations corresponding to torsional, proportional, and non-proportional ISTs. For these simulations, a single element model was used that specifically represents a surface element of a tubular specimen. The results of the validity check for the IST in pure torsion are shown in Figure 5.3.

Results from symmetric strain-controlled incremental step tests performed under pure axial and pure torsional loading showed accurate reproduction with the calibrated material parameters. Consequently, reliable predictions can be expected for multiaxial proportional loading paths. However, under general multiaxial loading, the material's yielding and plastic flow behavior may deviate from that observed in uniaxial tests, particularly in complex non-proportional load cases. This is partly due to potential microstructural anisotropy, which may become evident in multiaxial tests, especially when evaluating responses in both axial and hoop directions.

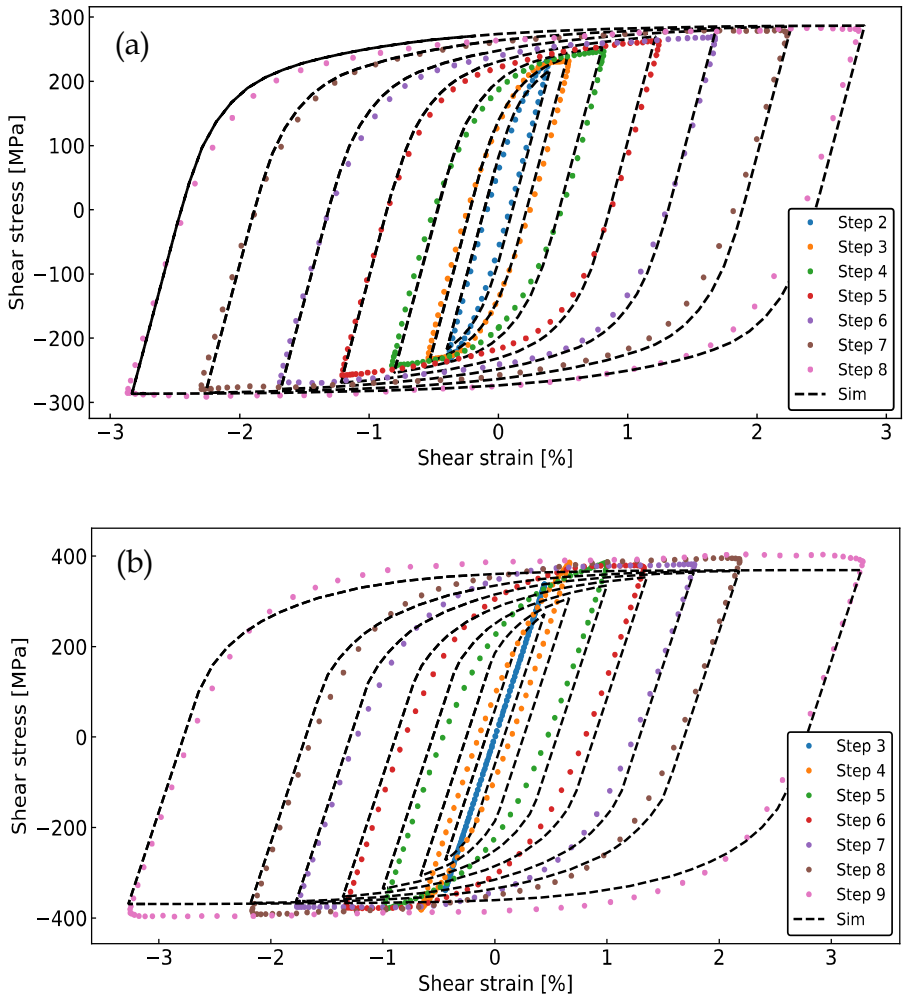

Figure 5.3 Torsional hysteresis loops for the BM (a) and HAZ (b) - experimental loops form IST are represented in colored symbols and simulated loops in dashed blacklines [128].

5.2.3 Validation of Hardening Parameters

The multiaxial IST involves a combination of tension-compression and torsion cycles. The test results were obtained using a similar methodology to uniaxial tests. First, the axial and torsional hysteresis loops are evaluated independently of each other. Figure 5.4 shows a comparison between the simulated and experimental loops for the BM. Due to the displacement- and angle-controlled setup, the axial and torsional signals do not exhibit perfect phase synchronization, as would be expected in an ideally proportional test. It is not expected that this marginal non-proportionality will result

in significant non-proportional hardening. Nevertheless, the asynchronous loading conditions could lead to a pronounced material reaction, which must be taken into account in the simulations.

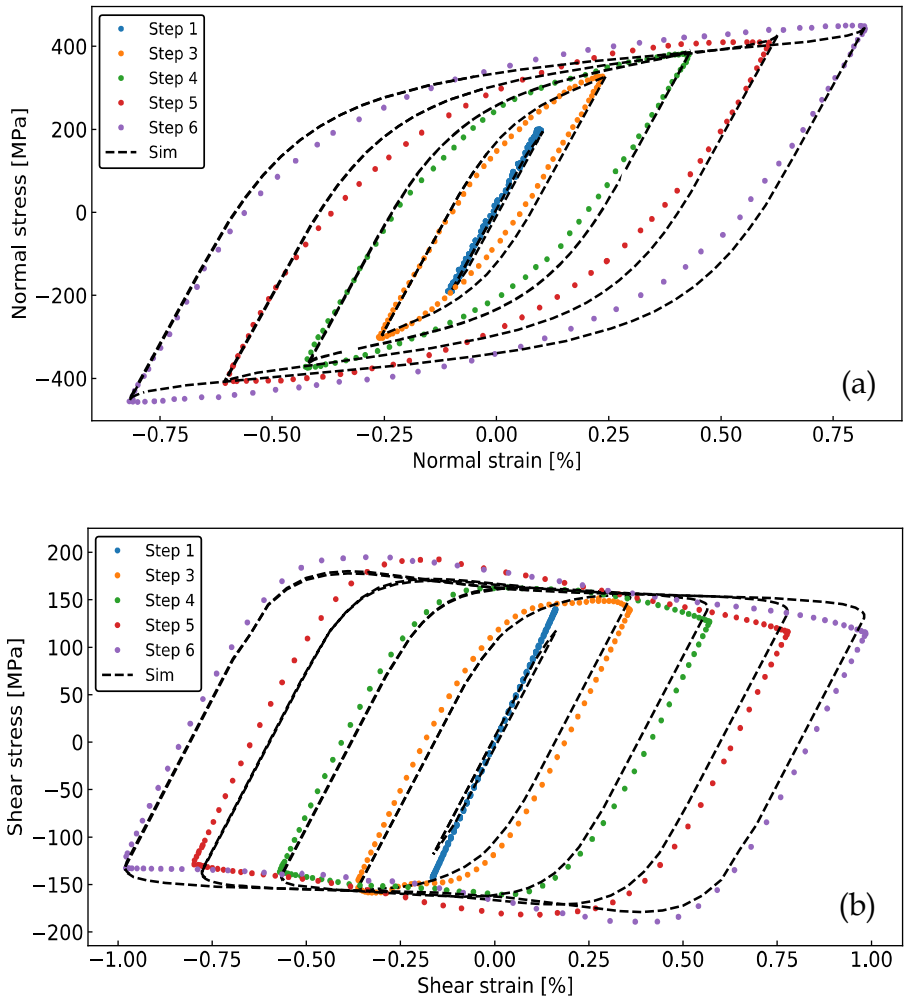

Figure 5.4 Experimental and simulated hysteresis loops for the BM from multiaxial proportional IST; normal (a) and shear (b) components - experimental loops are represented in colored symbols and simulated loops in dashed blacklines [128].

The observed phase shift between the normal and shear strain components is 9° for the BM and 18° for the HAZ. Figure 5.4 (a) illustrates the axial hysteresis loops for the test steps that exhibit significant plastic deformation. The loop shapes and the maximum stresses are accurately predicted for the two lowest strain amplitudes. With increasing strain amplitude, the peak stresses of the simulated axial hysteresis loops match well with the experimentally determined values, but the discrepancy in the loop shape between simulation and experiment increases, so that the simulated loops

show increased normal stresses at the transition from elastic to plastic deformation. For torsional cycles, as shown in Figure 5.4 (b), the model shows a slight underestimation of the stresses during the elastic-plastic transition. Conversely, the shear stress at maximum strain is consistently overestimated for all strain amplitudes.

In the HAZ, as shown in Figure 5.5, the axial loops show accurate prediction of both peak stress and hysteresis shape, with the exception of lower amplitudes, especially in step-3 (ε_a ~ 0.3 %), where the maximum stress is underestimated. A similar trend can be observed for the corresponding torsional loops, where the underestimation of the maximum stress in step-3 is even more pronounced.

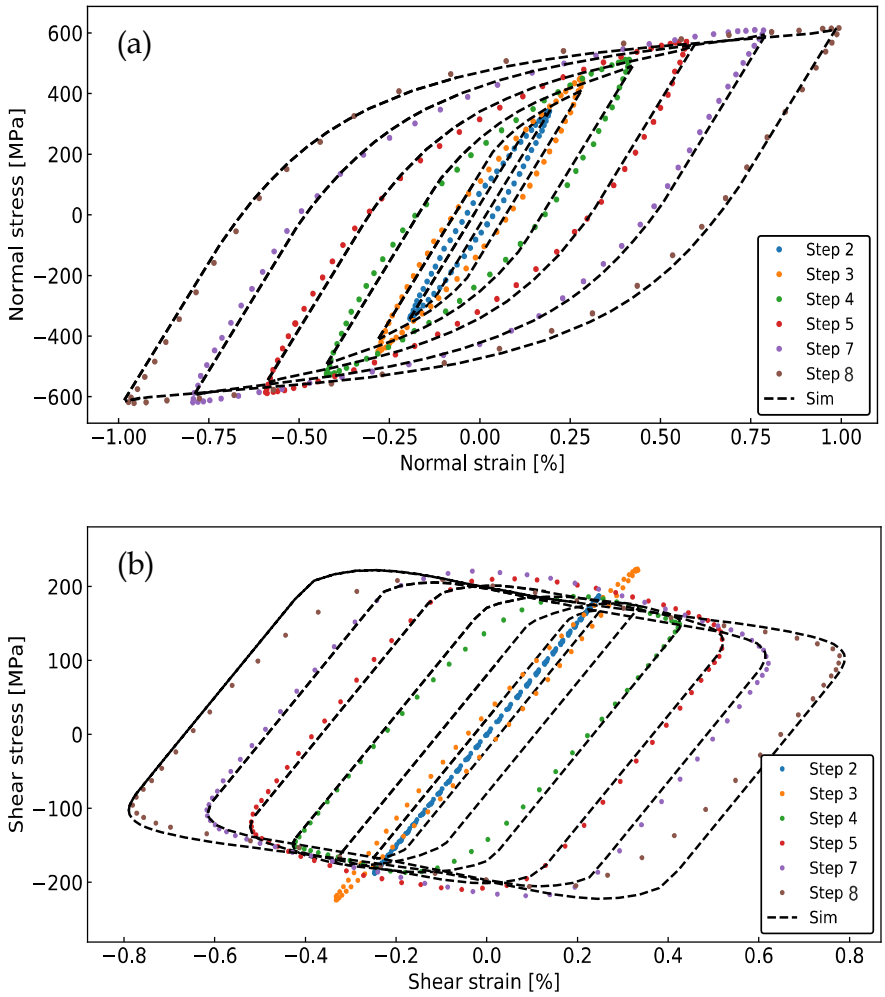

Figure 5.5 Experimental and simulated hysteresis loops for the HAZ from multiaxial proportional IST; normal (a) and shear (b) components - experimental loops are represented in colored symbols and simulated loops in dashed blacklines [128].

Non-proportional hardening (NPH) in the BM and HAZ was investigated in the context of symmetrical, displacement- and angle-controlled multiaxial ISTs with a 90° phase shift between the axial and torsional components. It was already known that the originally defined phase shift is not always maintained during a test. After checking the strain paths of the respective steps, the specific phase shift of 86.4° and 90° between the normal and shear components was found for the BM and the HAZ respectively. The simulations were performed using the kinematic and isotropic hardening model in ABAQUS together with the implemented UMAT subroutine to account for NPH, which integrates the constitutive non-proportional parameter of Tanaka [57]. The adjusted strain paths were incorporated into the simulations to accurately calibrate the non-proportional strain hardening parameter Φ. The modified isotropic strain hardening rate constant $\tilde{b}$ and the constant c_c, which determines the evolution of the components of C in Equation 2-39, were determined by trial and error. Table 5.3 shows the calibrated parameters for BM and HAZ. The effectiveness of the calibration is evaluated by plotting the hysteresis loops for the normal and shear components.

Table 5.3 Non-proportional (isotropic) hardening parameters for S355J2H - BM and HAZ [128].

Material	Q [MPa]	Φ [MPa]	$\tilde{b}$ [-]	c_c [-]
BM	13.37	106.25	10.0	1.0
HAZ	8.95	270	7.4	1.0

Figure 5.6 compares the simulated and experimental axial and torsional hysteresis loops for BM. This figure shows that the deviation between simulation and experiment is generally small for all steps. For the first step in particular, both the axial and torsional hysteresis loops are well represented by the simulation.

In the HAZ, similar to the uniaxial test, the simulation predicts the maximum and minimum normal stresses for all steps of the IST almost perfectly, with the exception of the higher strain ranges where the peak stresses are slightly underestimated. However, as far as the shape of the hysteresis loops is concerned, there is a consistent pattern across all steps. This pattern is characterized by a clear overestimation of the stress in the elastic-plastic transition, as shown in Figure 5.7. In order to eliminate this discrepancy, it seems essential to introduce an evolution law for kinematic hardening parameters that are dependent on A, beyond the simplified inclusion of non-

proportionality by the isotropic hardening law. However, more sophisticated calibration procedures are required for this adjustment.

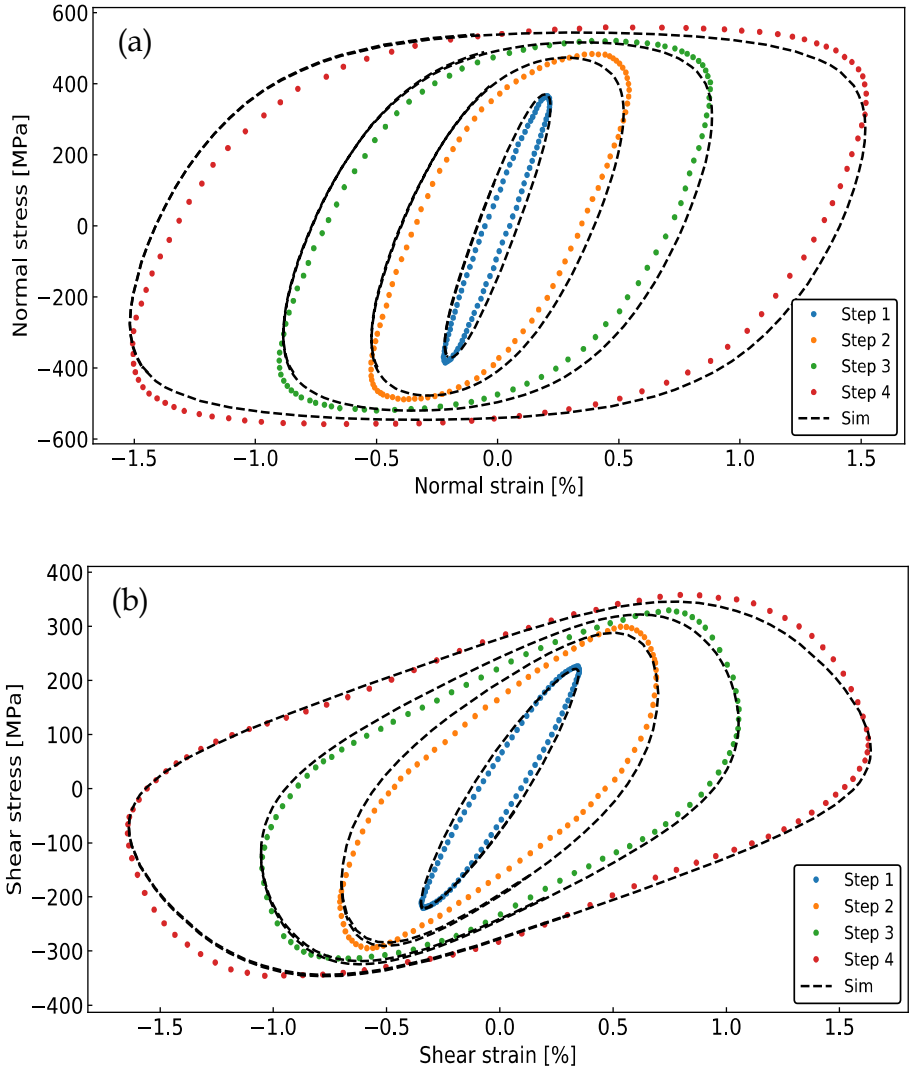

Figure 5.6 Experimental and simulated hysteresis loops for the BM from multiaxial non-proportional IST; normal (a) and shear (b) components - experimental loops are represented in colored symbols and simulated loops in dashed blacklines [128].

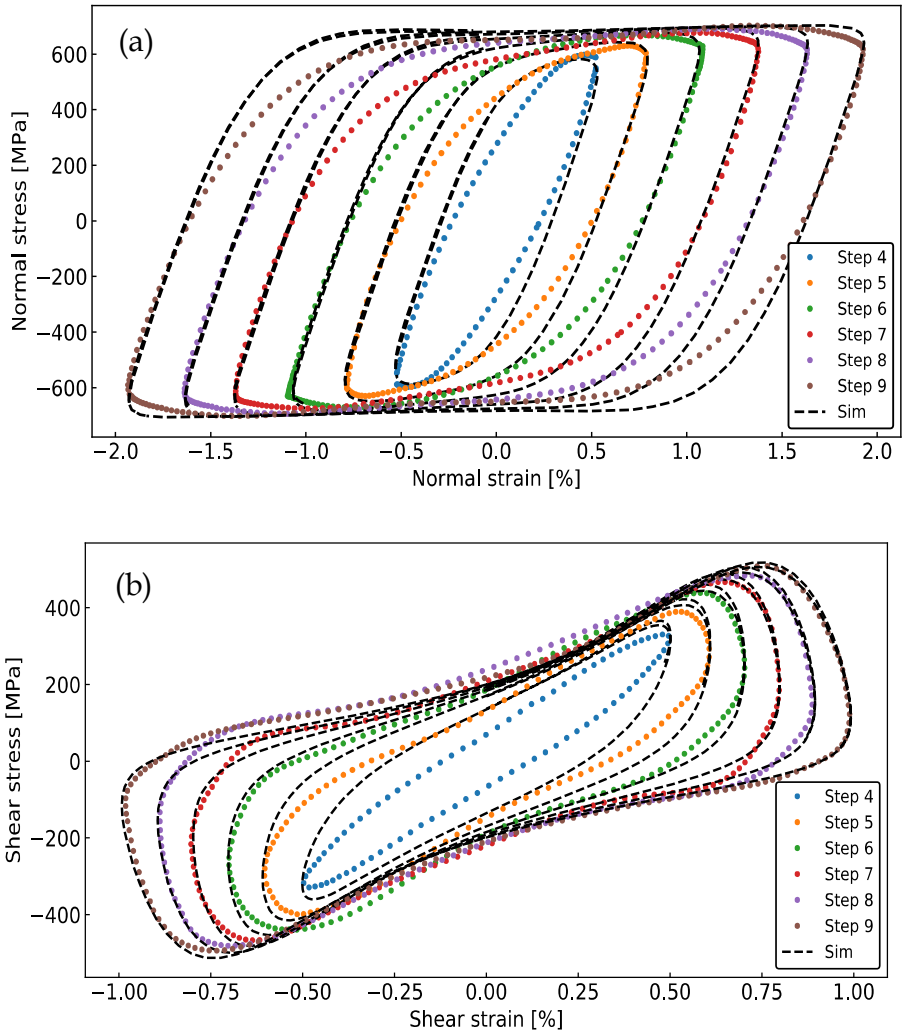

Figure 5.7 Experimental and simulated hysteresis loops for the HAZ from multiaxial non-proportional IST; normal (left) and shear (right) components - experimental loops are represented in colored symbols and simulated loops in dashed blacklines [128].

5.3 Summary and Conclusions

The isotropic hardening model appeared to be well-suited for predicting welding residual stresses in the single-pass bead-on-tube samples of S355J2H. Low-cycle fatigue tests conducted at three different strain ranges indicated that the isotropic component plays a significant role in the hardening behavior of S355J2H steel. As a result, the isotropic hardening model showed better consistency with the cyclic test results in predicting both the monotonic and cyclic responses of the material,

compared to kinematic or combined hardening models. In this context, cyclic hardening is of less importance, as the single-pass weld creates a relatively short plastic deformation path, thereby reducing the influence of material hardening.

The cyclic plasticity behavior of S355J2H steel under multiaxial loading conditions was also studied. Two different material states, the base material (BM) and the heat affected zone (HAZ), were investigated with regard to their significance for the fatigue assessment of welded joints. First, the calibration of the isotropic and kinematic hardening parameters was carried out using experimental data from uniaxial tests. The methodology for converting raw testing machine data into stress and strain was shown to produce accurate results. Relying on Nadai's solution [129], the approach successfully determined the true shear stress-strain curve in cyclic torsion tests for both solid and tubular specimens. Additionally, it performed well under complex multiaxial loading, including proportional and non-proportional tension-torsion. To validate the calibration under axial, torsional and combined axial-torsional loading, single element finite element simulations were performed using ABAQUS. The material responses under uniaxial and proportional multiaxial loading conditions were reliably predicted by the model after calibration. However, a common trend was observed in most tests, indicating a tendency for the simulation to consistently underestimate the peak stresses at lower equivalent strain amplitudes, e.g. at around 0.25% for the BM and 0.3% for the HAZ.

The plasticity model was extended to account for non-proportional hardening effects using Tanaka's non-proportionality parameter [57] based on internal constitutive variables. The non-proportional hardening term was integrated by modifying the isotropic hardening law and was manually calibrated using experimental data from the out-of-phase incremental step tests. The model incorporating non-proportional hardening improved the accuracy of prediction of experimental hysteresis loops obtained under non-proportional load paths. However, in the HAZ, the prediction of hysteresis loop shape was less accurate for both axial and torsional paths. In particular, the simulation tended to overestimate the transition stress between elastic and plastic slope. Consequently, there is room for optimization and further development of the model for the HAZ. The introduction of evolution equations for kinematic hardening parameters as a function of the non-proportionality parameter could be a possible improvement of the model.

Chapter 6 Simulation of Welding Residual Stresses and Relaxation

6.1 Finite Element Welding Simulation

Various assessment levels were examined alongside experimental results, considering the limitations and inconsistencies in the calculations. A tubular specimen of S355J2H construction steel, with a 56 mm outer diameter and 10 mm thickness, was used to assess welding residual stresses. After preliminary preparations, a single-pass dummy weld without filler material was produced using TIG welding with a total energy input of 7.2 kJ/cm. Details on the geometry of the specimens, welding parameters, specimen preparations and material characterization tests are given in [121]. A three-dimensional model for calculating welding residual stresses was developed using SYSWELD 8.5. The simulation employed an uncoupled procedure, where results from the initial thermo-metallurgical step—combining heat transfer and phase transformation analyses—served as input for the mechanical calculations. In the thermo-metallurgical step, the transient temperature history of the welding process was calibrated using the recorded thermocouple profiles. In addition, the fusion boundary of the weld bead was controlled according to the cross-section macrograph of the specimen. Once an accurate thermo-metallurgical solution is obtained, the mechanical part of the simulation can be performed. The required material properties for the mechanical simulations were obtained from the material characterization tests conducted on the BM. The accuracy of the calculated residual stresses was then validated using the measured data in order to optimize the selected variables. To characterize the surface and depth profiles of welding residual stresses, both x-ray and neutron diffraction methods were employed. These techniques are preferred for assessing through-thickness stress profiles, which are crucial for evaluating structural stability and defect tolerance.

6.1.1 Thermo-Metallurgical Simulation

To determine the heat source parameters, an iterative calibration process with combined thermal and metallurgical steps was performed. The optimal thermal simulation technique is to calibrate the welding efficiency by comparing the calculation results with the thermocouple responses, while keeping the welding parameters constant and consistent with those used to perform the welding process [139]. In this simulation, the position and speed of the migrating heat source depend on the movement of the real welding torch. In this sense, the Goldak parameters relevant to the weld pool geometry were kept constant as a function of the geometric features obtained from the weld macrographs. This analysis was continued until the most accurate temperature field was obtained. Within the scope of this work, the calibration of the heat source was carried out via the main three-dimensional finite element model using transient thermal analysis. This procedure requires a comparatively longer calculation time compared to a simple two-dimensional steady state fitting solution, but still provides the most accurate results. The shape and size of the heat source were then optimized by comparing the fusion boundary profile with a macrograph of the weld.

Heat diffusion is treated with an Enthalpic formulation by SYSWELD [20]. Both temperature history and phase fractions were mutually calculated in the coupled thermo-metallurgical calculations. The initial temperature of the model was set at 20°C, with the thermal-physical properties of the material defined by SYSWELD as a function of temperature and metallurgical phase fraction. Transient heat transfer calculations take into account the latent heat of fusion/solidification and metallurgical transformation. At the same time, for each point the different phase fractions depend on the temperature development.

Figure 6.1 (a) shows the variation of the temperature on the specimen at the thermocouple spots represented by Q1 to Q4, located at 4 positions on the specimen at the weld toe, each 90° apart around the weld circumference, starting with the weld start point. In this context, not only the peak temperatures but also the cooling rates at which the material solidifies and finally exhibits certain microstructures must be experimentally validated. Strong agreement was found for peak temperatures as well as heating and cooling rates by comparing the measured temperature history with the

calculation results of all thermocouples at each quadrant (Q1 to Q4). A welding efficiency of 75% corresponds to these results.

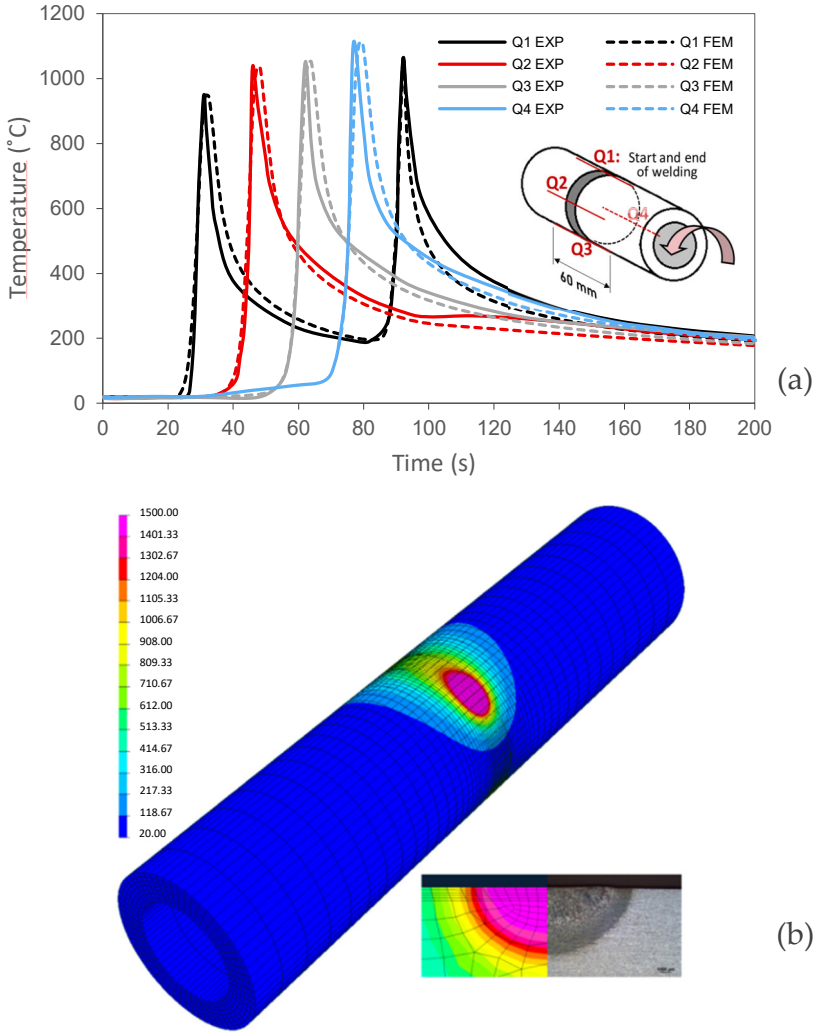

Figure 6.1 Experimental and numerical temperature history at every four quadrants (a) and temperature contour plot and fusion boundaries (b) [121].

The estimated boundary of the fusion zone with the expectation of being at temperatures equal to or above 1500°C (melting temperature) was compared with the experimentally defined weld cross-section, taking into account the calculated temperature contour plots. According to Figure 6.1 (b), the calculated fusion boundary agrees well with the actual cross-section of the weld in the macrograph.

6.1.2 Mechanical Simulation and Residual Stress Results

Assuming that the thermal and metallurgical results are sufficiently accurate, the emphasis is given to the mechanical aspects of the simulation in this section. Certain microstructure-dependent mechanical properties required for the mechanical analyses were defined using the CCT diagram for S355J2H, based on the cooling rate ($t_{8/5}$), which represents the time (in seconds) the material takes to cool from 800 °C to 500 °C during welding process. For S355J2H, the CCT diagram taken from [19] is shown in Figure 4.8. To determine the yield strength of distinct metallurgical phases at room temperature, different cooling rates were considered to identify cooling curves that produce microstructures with the highest fraction of each phase. Ideally, the mechanical properties at elevated temperatures should be determined experimentally; however, in this study, experimental data were only available at room temperature. High temperature mechanical properties for the initial material were obtained From the SYSWELD material database and [140][141]. In addition, an engineering method was used to derive the material properties of each phase at higher temperatures, where a proportional factor was determined at room temperature by dividing the yield stress of the initial material to that of a particular phase. Temperature dependent values for material phases were obtained by applying the proportional factor to the high temperature mechanical properties of the initial material. The properties and specifically, the yield strength of the mixture at each level, after determining the temperature-dependent material properties for each phase, were calculated by averaging the values of the individual phases. To eliminate the material's history at high temperatures, a value of 1300°C was set as the annealing temperature above which the stresses, total and plastic strains, and strain hardening of the material disappear.

The development of welding residual stresses was investigated across a variety of pathways inside the material. The comparison between the experimental and numerical surface residual stresses as the average of the values in quadrants Q2, Q3 and Q4 is shown in Figure 6.2. The overall agreement between the predicted and observed values is reasonably good as far as the area in the BM is considered. In the HAZ, and particularly in the weld zone, the predicted compressive residual stresses are higher than the measured values, which even tend to approach tensile levels.

From a fatigue perspective, the magnitude and location of residual stresses are decisive for the behavior of potential fatigue cracks, especially at the weld toe. The presence of compressive residual stresses can not only alter the stress and strain fields in the material but may also result in partial or complete crack closure under tensile loading. To fully understand the impact of weld-induced residual stresses on fatigue behavior, it is essential to thoroughly characterize both the magnitude and distribution of these stresses.

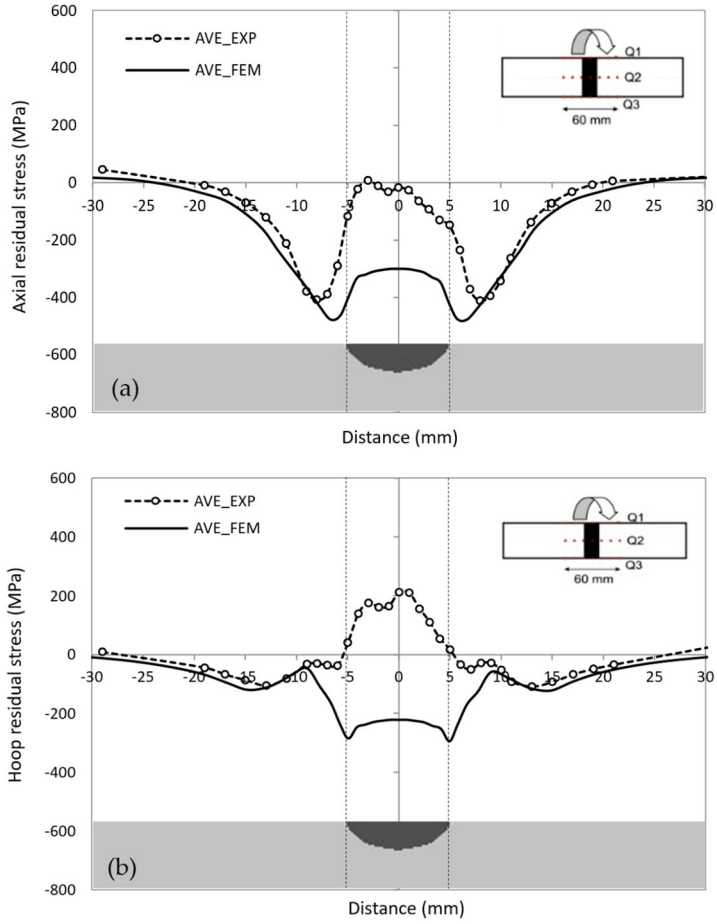

Figure 6.2 Experimental and numerical average values for (a) axial and (b) hoop residual stresses over Q2, Q3 and Q4 [121].

In addition to surface residual stresses, assessments were also devoted to the residual stress distribution in the bulk of the material. In relation to the ND measurements, typical contour plots of the residual stresses in the axial and hoop directions over the pipe thickness at 180° from the weld start point (Q3) are shown in Figure 6.3. Because of having the most possible steady state condition, quadrant Q3 is judged to be the most desirable place for residual stress comparisons. For both the axial and hoop

directions, the maximum residual stress is predicted to be near the inner surface of the pipe. According to Figure 6.3 the numerical results at first glance correspond very well to the experimentally calculated data.

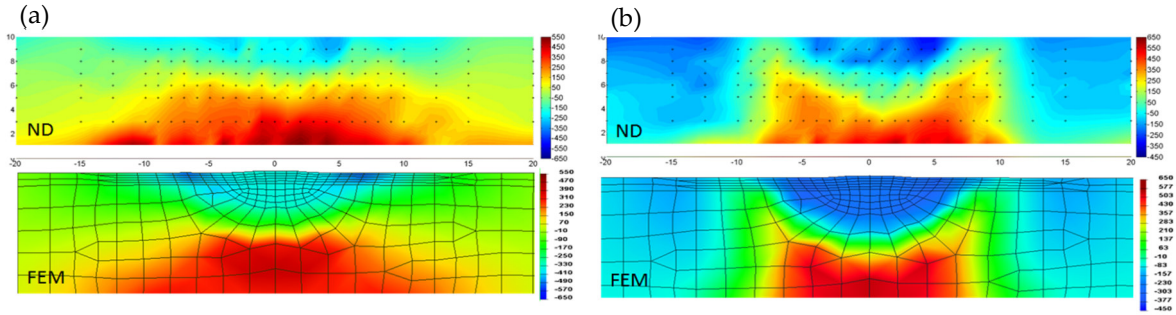

Figure 6.3 Comparison of the predicted and neutron-measured (a) axial and (b) hoop residual stress fields at Q3 [121].

For a more accurate assessment, residual stress values were derived from three lines across the same cross-sectional plane, representing depth profiles below the outer surface, beneath the melted zone, and near the inner surface, respectively. Figure 6.4 displays the residual stresses measured and calculated through the wall thickness at the above-mentioned levels (the error range for the measured data is noted to be around +/-50 MPa). According to Figure 6.4, the general agreement is good, although minor discrepancies exist between the measured and predicted residual stresses, particularly in the axial stresses within and beneath the weld region. However, outside the weld bead, the predicted results align closely with the measured values.

The variation of axial residual stress component along the centerline (A-A) over the thickness is shown in Figure 6.5. The residual stresses in the welded area are found to be compressive from the measurements, aside from the potential near-zero and tensile values of residual stresses on the surface of the weld bead. The FE simulations of residual stresses along the centerline match the measurements relatively well, particularly over a depth of 5 mm. The numerical estimates in the welded region indicate an almost uniform compressive residual stress profile without any noticeable deviation from the specimen surface. The predicted residual stresses in the weld region are higher than the experimental values. Both the surface and depth evaluations suggest that the FE calculations overestimate the compressive residual stresses in the welded area.

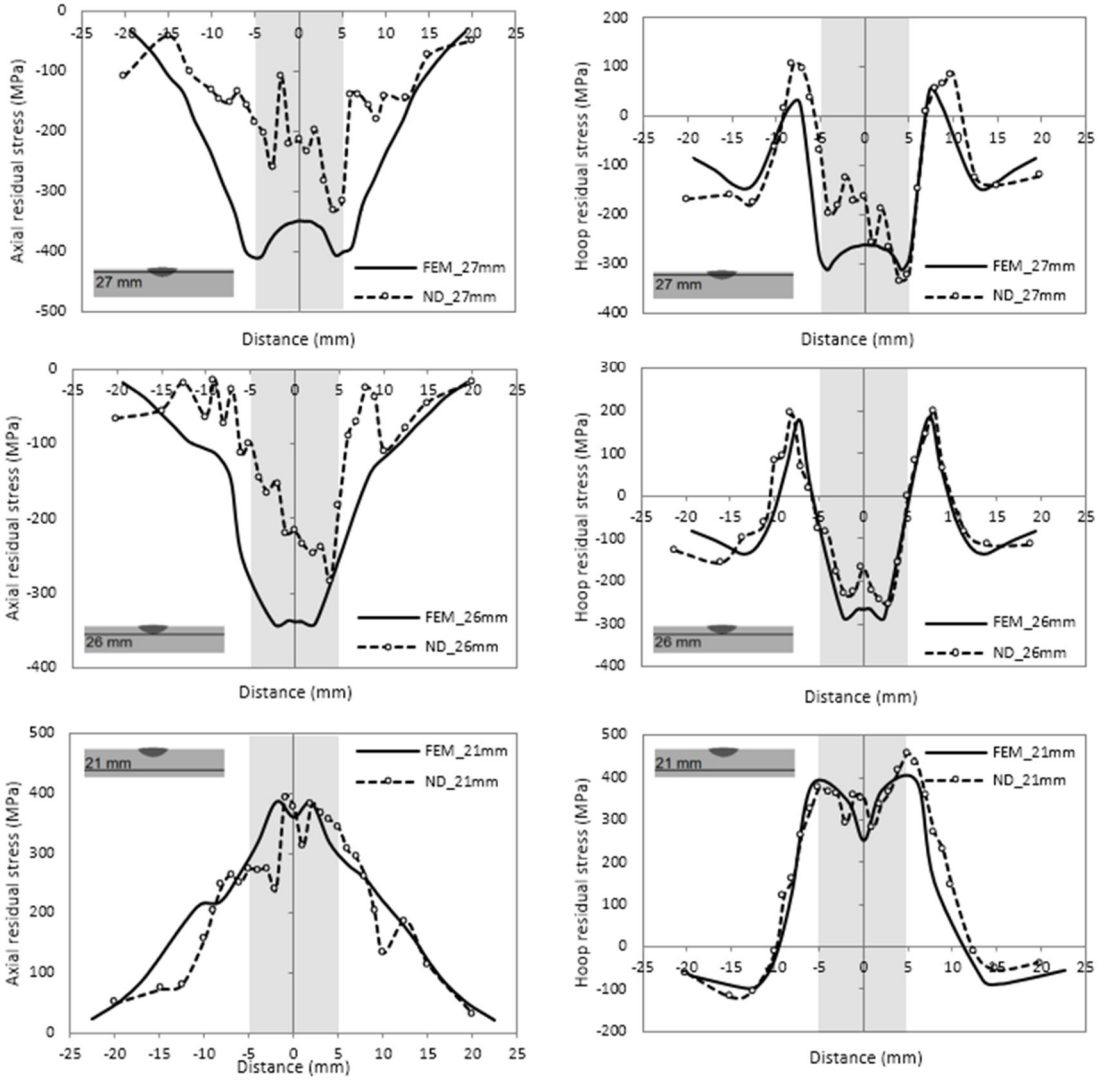

Figure 6.4 Measured vs. calculated axial and hoop residual stresses at the radius of 27 mm (below the outer surface), 26 mm (beneath the melted zone) and 21 mm (near the inner surface) [121].

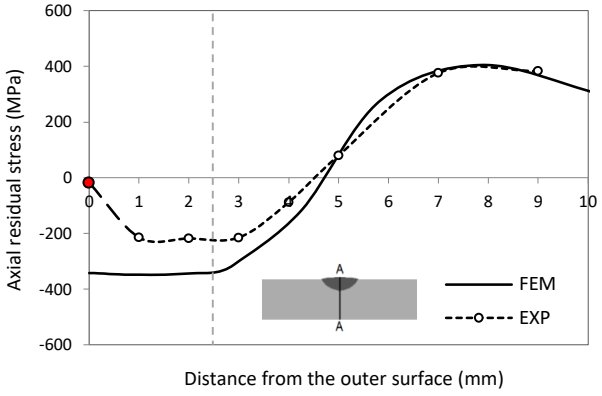

Figure 6.5 Through-thickness measured vs. calculated axial residual stresses along centerline A-A (Value on the surface belongs to x-ray measurement) [121].

The thermo-metallurgical and mechanical responses of the material during welding [142] need to be considered in order to further clarify the reasons for such overestimation. For this purpose, the evolution of thermal stresses, accumulated plastic strains and material phase changes during welding were studied at 4 nodes inside the cross-section of the weld at quadrant Q3. These nodes, which are located on the weld symmetry line, should be representative of the weld area, HAZ and base material (Figure 6.6). As shown in Figure 6.6, node-1 and node-2 are located in the weld and below the weld region, respectively, while node-3 and node-4 are located in the base material at different distances from the weld. Compared to Figure 6.4, node-1, node-2, and node-4 correspond to positions on the weld centerline at radii of 27 mm, 26 mm, and 21 mm, respectively

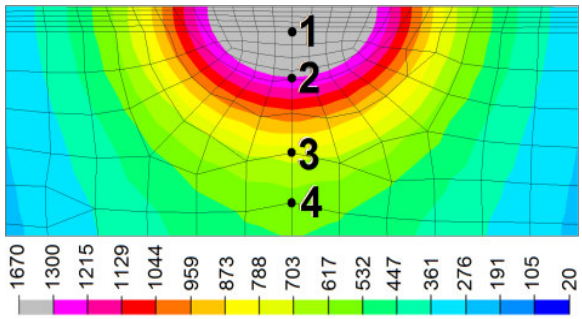

Figure 6.6 Different positions across the weld at Q3; node-1 and node-2 represent the weld area and HAZ, respectively. Node-3 and node-4 are in the BM at different distances from the weld [121].

Figure 6.7 indicates the development of the different material phases during welding as well as the evolution of the thermal stresses and the accumulated and equivalent plastic strains at node-1 and node-2 as a function of the welding temperature, all derived from the FE calculations. At node-1 the temperature approaches the melting point as this node is completely in the welding area. The peak temperature hits around 1290°C under the fusion boundary at node-2 which is very close but still lower than the temperature of the annealing. In these areas, thermal cycles are such that the material undergoes metallurgical phase transitions that create more difficulty in predicting the actual behavior of the material. The initial material within and below the weld region transforms completely into austenite during heating as the temperature goes above the temperature of the austenitization finish (Ac3).

Depending on the cooling rate, bainitic and martensitic transformations start to take place within certain temperature ranges during the cooling process.

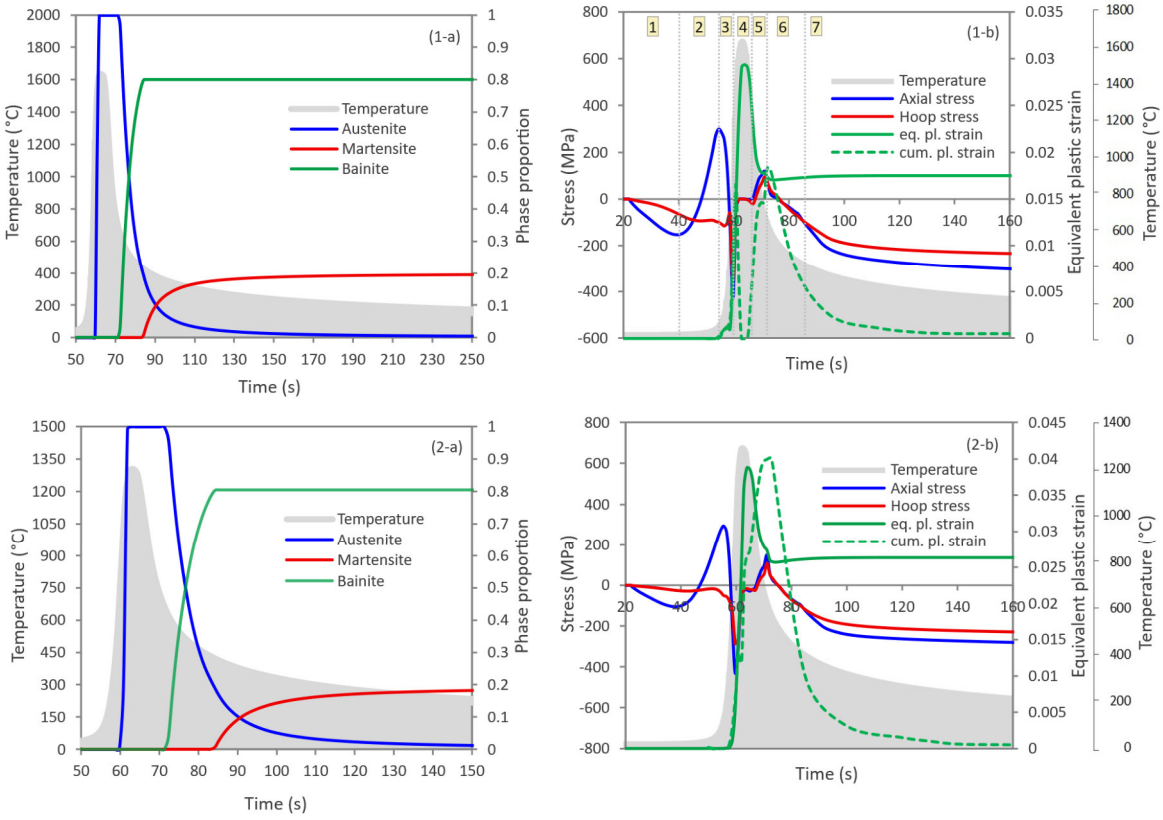

Figure 6.7 Evolution of (a) different material phases and (b) thermal stresses, cumulative and equivalent plastic strains in relation to welding temperature history at node-1 (top) and node-2 (bottom) [121].

As can be seen in Figure 6.7 (1-a) and (2-a), the final material comprises around 80 percent bainite and 20 percent martensite in both node-1 and node-2. The process time is broken into multiple ranges in order to analyze the evolution of expected material behavior at node-1, as shown in Figure 6.7 (1-b). The material at node-1 experiences complicated compressive and tensile load cycles during heating and cooling. During welding, due to the initial expansions and contractions, compressive and tensile stresses are elastically formed in the material before the torch reaches Q3 (shown as periods 1 and 2). Compressive stresses emerge in the material as soon as the local temperature rises at this point, followed by intensive yielding, which allows plastic strains to accumulate (period 3). The material's virgin condition, including stresses, total and plastic strains, and the strain hardening, is expected to be recovered once the annealing temperature is reached. It is noticeable in Figure 6.7 (1-b) that both the axial

and hoop stress components as well as the cumulative plastic strains (which shows the extent of isotropic hardening) have returned to zero in period 4 during which the temperature is above 1300°C. Yet the equivalent plastic strain is unexpectedly maintained. Monitoring the history of each component of the plastic strain suggests that no substantial plastic strain recovery is taken into account, except for a sharp discontinuity in the amount of strain at the annealing temperature. The strain hardening is anticipated to be recovered before annealing due to the austenitic transition, but due to the short time from the start of austenitization to the annealing temperature, it has a small impact covered by the annealing behavior. The cooling process from the temperature of annealing down to the temperature of bainitic transformation is defined as Time period 5. Tensile stresses are formed in this range and plastic strain accumulates in tension. During continuous cooling, austenite starts to turn into bainite once the bainitic transition temperature is reached and the volume increases, so the material undergoes compression as can be seen in period 6. In this case, the cooling rate is such that the bainitic transition ends at around 420°C and the remainder of the austenite turns into martensite, creating a larger increase in volume (period 7). The plastic strain no longer accumulates during the last two stages, and the strain hardening of the material diminishes due to the hardening recovery phenomenon associated with the $\gamma \rightarrow \alpha$ phase transformation.

This study assumes that both bainitic and martensitic transformations lead to a complete recovery of strain hardening. Apart from the absence of annealing, the thermal cycle experienced at node-2 is similar to that at node-1, as previously described. As shown in Figure 6.7 (2-b), at node-2, plastic strain accumulates under both tension and compression. However, strain hardening recovery occurs during austenitization while heating, followed by bainitic and martensitic transformations during cooling.

Figure 6.8 shows the evolution of thermal stresses, cumulative and equivalent plastic strains with respect to the welding temperature history at node-3 and node-4. Initial tensile stresses are induced elastically during welding until the moving heat source reaches quadrant Q3. At this point, the stresses change to negative values as soon as the local temperature begins to rise. According to Figure 6.8, plastic flow occurs significantly in compression during heating at both node-3 and node-4 , and then the compressive axial and hoop stresses reverse proportionally into tensile stresses on

cooling without substantial yielding, particularly at node-4, which is located at the furthest from the weld. The peak temperature at node-3 is around 800°C, which is higher than Ac1, but lower than Ac3. Thus, during heating, austenitization occurs partly, resulting in 35% austenite [121]. This volume of austenite is subsequently transformed at the end of the cooling process into 28% bainite and 7% martensite [121]. By contrast, node-4 only reaches 700°C, which is below the Ac1 temperature. Consequently, the material does not undergo any austenitic phase transformation in this region. Since the maximum temperature is below 1300°C at each of these nodes, there will be no annealing-related removal of strain history in these regions. At node-3, the cumulative plastic strain decreases during austenitization due to heating and slightly during bainitic and martensitic transformations during cooling, due to transformation-induced hardening recovery. In contrast, at node-4, the cumulative plastic strain is fully maintained throughout both the heating and cooling phases.

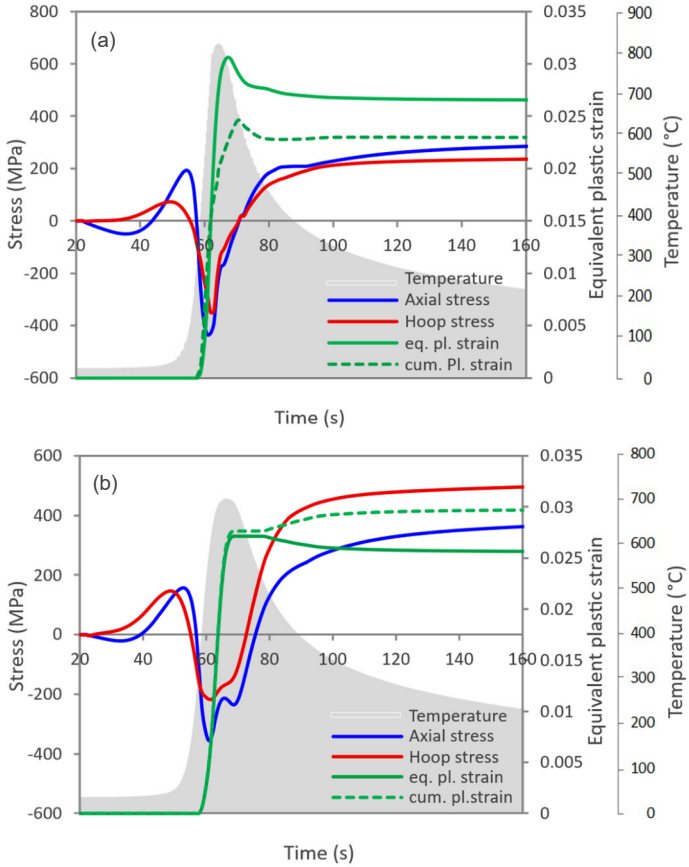

Figure 6.8 Evolution of thermal stresses, cumulative and equivalent plastic strains in relation to welding temperature history at node-3 (a) and node-4 (b) [121].

6.2 Residual Stress Redistribution/Relaxation

After characterizing the welding residual stress field, the focus is placed on how these residual stresses behave under mechanical loading. The reduction or redistribution of residual stresses depends on several factors, including the loading conditions, such as amplitude, direction and multiaxiality, and the static and cyclic properties of the material. In some cases, most of the residual stress relief occurs during the first loading cycle.

Numerical and experimental methods were combined to investigate the behavior of welding residual stresses under multiaxial mechanical loading in S355J2H tubular specimens. These specimens had a gauge section with an outer diameter of 21 mm and a thickness of 3.6 mm. A 5 mm-wide TIG bead-on-tube weld was made in the center of each specimen using filler material identical to the base material. Further details on the specimen geometry, preparation, and welding parameters are provided in [122]. In addition to the FE method, surface residual stresses in the as-welded condition were initially measured using x-ray diffraction along an axial line on the specimen surface, at an angle of 180° from the starting point of the weld [122]. The specimens were then subjected to various pure torsion and tension-torsion quasi-static loads. After each unloading, the surface residual stresses were measured again using the x-ray technique. The welding process was simulated with SYSWELD 12.5 software through three-dimensional thermomechanical analysis, and the resulting temperature profile and residual stress field were compared and calibrated with the experimental data.

In ABAQUS 6.14, a three-dimensional elastic-plastic FE model using the isotropic hardening model was developed alongside experimental measurements to numerically investigate the behavior of welding residual stresses under mechanical loading. For the relaxation analysis, the model was essentially identical to the one used for the welding simulation, with the residual stress field computed in SYSWELD incorporated into the relaxation model as a predefined field. By comparing experimental results with numerical simulations, the relaxation of welding residual stresses was analyzed.

6.2.1 Quasi-Static Pure Torsion Loading

The first specimen (Sample-1) was subjected to gradually increasing torsional loads and unloaded after each specific shear stress level to measure the residual stresses before reloading to the next level [122]. Figure 6.9 and Figure 6.10 show the differences in axial and hoop directions of welding residual stresses obtained from measurements compared to the predicted results under pure torsion loading conditions. In these figures, 'T' denotes Torsion, 'RSM' stands for Residual Stress Measurement, and 'FEM' represents the Finite Element Method. The experimental and numerical findings are in good agreement. It is evident that classical plasticity failure criteria can effectively describe the relaxation phenomena resulting from local plastic deformations. As the loading stress is applied in shear, the residual stresses in the region of interest begin to vary when the equivalent von Mises stress, which combines loading and residual stresses, exceeds the material's yield point at certain locations.

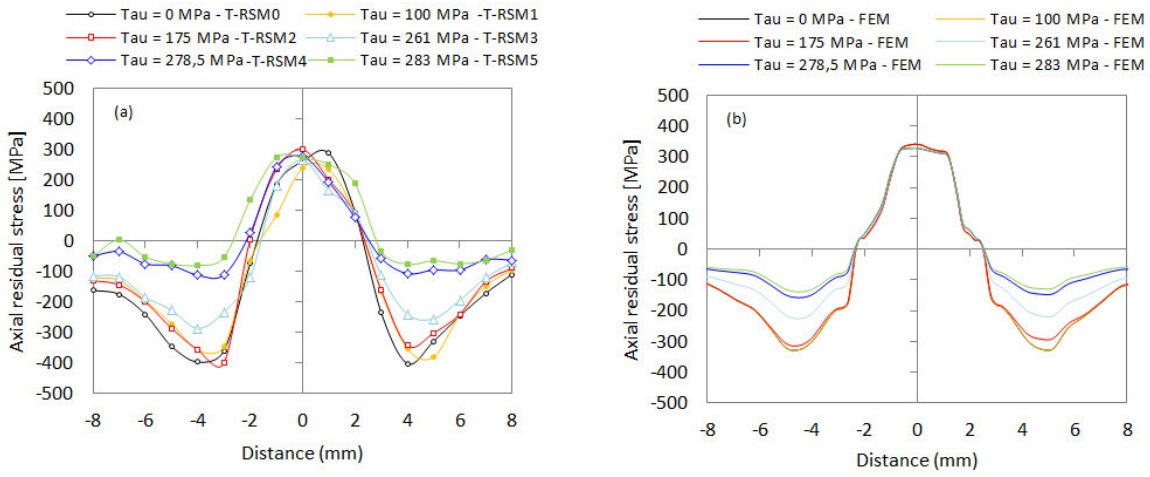

Figure 6.9 Measured – x-ray (a) and predicted (b) surface welding residual stress relaxation in the axial direction under pure torsion loading (Sample-1) [122].

According to Figure 6.9, the first significant change in residual stress occurs when the gradually increasing nominal shear stress reaches 261 MPa. At this point, the axial compressive residual stresses at the weld toe and in the HAZ begin to relax. However, no significant changes are observed in the weld area, where high tensile residual stresses persist. As the torque and nominal shear stress continue to increase, the relaxation progresses at the weld toe and its vicinity in the HAZ, while the tensile residual stresses in the weld bead remain largely unchanged. In the hoop direction,

as shown in Figure 6.10, some differences in residual stress profiles are observed, though these changes are less pronounced compared to the axial path relaxation. At higher load levels, the predicted relaxation in the axial direction is slightly underestimated compared to the experimental observations.

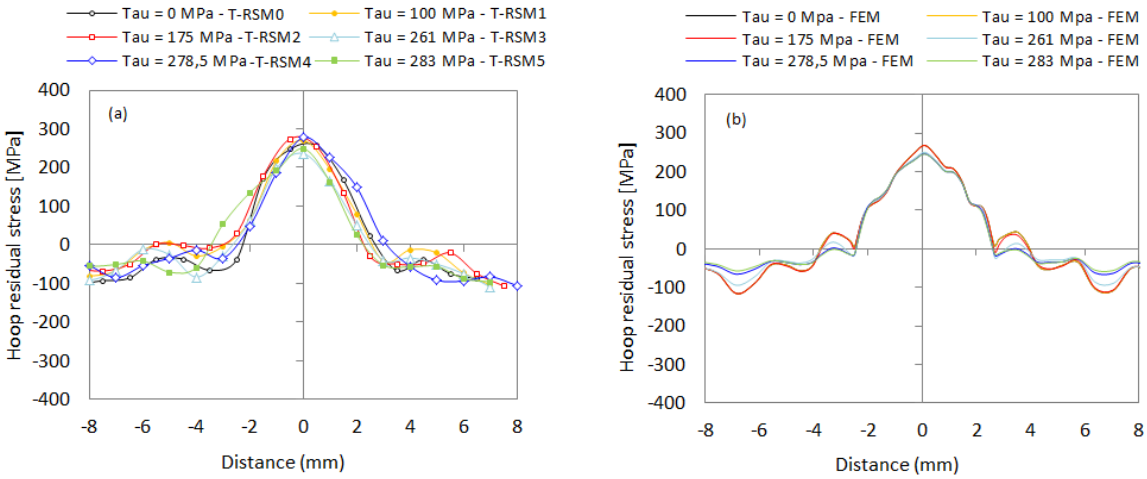

Figure 6.10 Measured – x-ray (a) and predicted (b) surface welding residual stress relaxation in the hoop direction under pure torsion loading (Sample-1) [122].

6.2.2 Quasi-Static Multiaxial Loading

The behavior of welding residual stresses under multiaxial loading was investigated in a subsequent test. Since a nominal shear stress of up to 175 MPa did not cause any relaxation in the previous test (Section 6.2.1), a lower nominal shear stress of 100 MPa was selected for the present test, combined with a progressively increasing tensile stress. In this setup, the specimen (Sample-2) was subjected to a constant torsional load corresponding to a nominal shear stress of 100 MPa, while the axial tensile load was incrementally increased during each loading session. After each combined tension-torsion loading and unloading cycle, Sample-2 was removed from the testing machine, and the residual stress changes were analyzed as described in [122]. Figure 6.11 and Figure 6.12 illustrate the comparison between predicted and measured residual stress relaxation in the axial and hoop directions under tension-torsion loading, with 'TT' denoting Tension-Torsion. The agreement between measurements and predictions is quite good. The observed relaxation is slightly greater than the FE

calculations, consistent with the trend seen under pure torsional conditions. Nevertheless, the yield criterion used remains effective even under complex multiaxial loading conditions. It is noted that the residual stresses in both the axial and hoop directions remain relatively stable unless the applied tensile stress exceeds the material's yield strength of 450 MPa. At this stress level, compressive residual stresses at the weld toe and HAZ are nearly eliminated, with no significant changes observed in the weld bead.

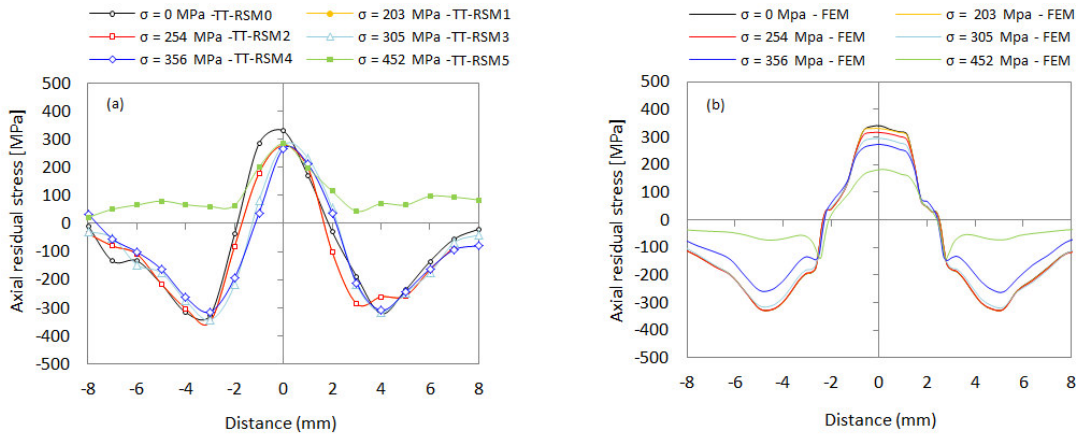

Figure 6.11 Measured – x-ray (a) and predicted (b) surface welding residual stress relaxation in the axial direction under tension-torsion loading (constant nominal shear stress = 100 MPa) (Sample-2) [122].

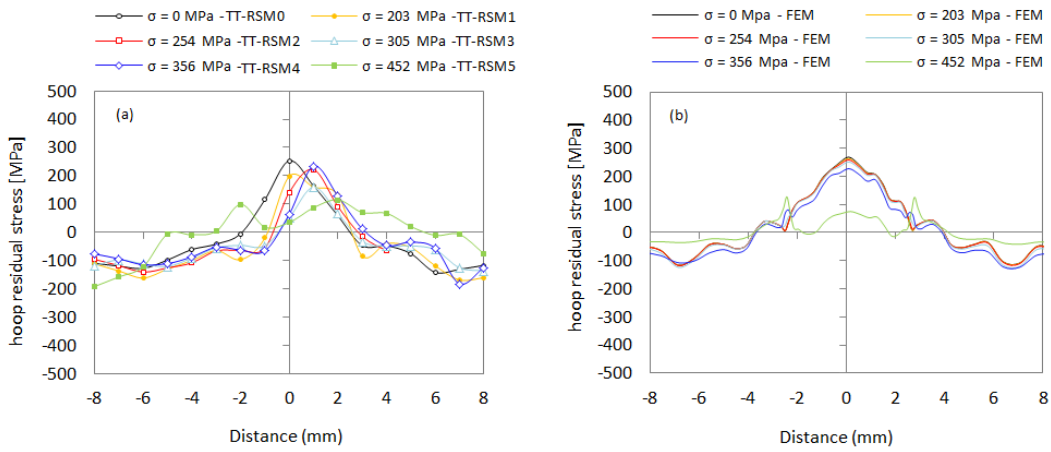

Figure 6.12 Measured – x-ray (a) and predicted (b) surface welding residual stress relaxation in the hoop direction under tension-torsion loading (constant nominal shear stress = 100 MPa) (Sample-2) [122].

As shown in Figure 6.11, there are some discrepancies between the measured and predicted results at a tensile stress level of 452 MPa. According to the x-ray measurements, the compressive residual stresses in the HAZ not only disappear but also partially transform into tensile stresses, with stress variations in the weld area being minimal. In contrast, the simulation results indicate that residual stresses in the HAZ remain somewhat compressive after relaxation, while tensile residual stresses in the weld area decrease only slightly. This discrepancy could be related to the initial simplifications in defining the material properties. For the simulation, the mechanical properties of the weld metal, HAZ, and base material were set to be identical to those of the HAZ. However, the weld metal is marginally harder, and the base metal is softer than the HAZ, which could lead to an overestimation of relaxation in the weld metal and an underestimation in the base metal. Another possible reason for this discrepancy could be related to the defined plasticity model [122].

6.3 Summary and Conclusions

Comprehensive numerical studies were conducted on welding residual stresses in single-pass bead-on-tube specimens made of S355J2H construction steel. X-ray and neutron diffraction measurements were used to experimentally determine the surface and depth profiles of residual stresses in both the axial and hoop directions. Comparing the computational results with experimental data, the overall agreement was generally good, although some inconsistencies were observed in the surface and subsurface stress results over the weld region. In the thermal-metallurgical analysis, the reliability of outputs, including temperature history and material phase fractions, depends on the accuracy of both the maximum temperature and cooling rate, which were experimentally calibrated. During weld fabrication, temperature data were collected using various thermocouples. Additionally, the predicted weld fusion boundary was compared with macrograph images of the weld cross-section, showing good alignment. Cooling curves from the weld-CCT diagram were used to define phase formation based on the calculated $t_{8/5}$. Mechanical simulations were influenced by the thermal history, which affected temperature- and phase-dependent mechanical properties, as well as thermal expansions and contractions. Additional factors such as strain hardening recovery during phase transformations and transformation-induced

plasticity were also considered. This study assessed the suitability of the applied material hardening model, the accuracy of predicted high-temperature annealing behaviors, the impact of microstructural transformations on the evolution of residual stresses, and the recovery of strain hardening during transformations. The key results and findings of this work are summarized below:

1) The FE analysis provided a fairly accurate calculation of the welding residual stresses in the base material within the tubular welded joint.
2) The combined measurement results from x-ray and neutron diffraction across the very thin surface layer revealed a sharp gradient in the welding residual stress profile extending into the material bulk.
3) The compressive residual stress field at the weld toe and its vicinity, beneficial for fatigue resistance, is attributed to low-temperature phase transformations. Simulations showed that compressive stresses in the weld area result from expansion associated with the $\gamma \rightarrow \alpha$ transformation during cooling.
4) In the present case, the isotropic hardening model was suitable for the prediction of welding residual stresses. In this context, cyclic hardening is less critical, as single-pass welding produces a relatively short plastic path despite the material's inherent hardening properties.
5) The used annealing function effectively eliminated the cumulative plastic strain once the temperature surpassed a certain threshold, though the strain history retained more than expected. In contrast, the strain hardening memory vanished during austenitic, bainitic and martensitic transformations. Nevertheless, the residual stress results in this study were not significantly affected by these factors.

The relaxation behavior of welding residual stresses under uniaxial and multiaxial loading conditions was investigated using numerical simulations and experimental studies. X-ray diffraction was used to measure surface residual stresses in the as-welded state and at various stages of relaxation. All experimental work was carried out under quasi-static loading conditions. The comparison between the experimental results and the FE calculations showed a strong agreement and confirmed that in the present case the FE approach using a nonlinear isotropic hardening model can effectively predict the relaxation of welding residual stresses under both uniaxial and multiaxial loading conditions. In addition, the von Mises yield criterion together with the local monotonic yield strength of the material proved to be effective in describing the relaxation phenomenon resulting from local plastic deformation.

Chapter 7 Fatigue Behavior and Life Predictions

To describe the multiaxial fatigue behavior of welds, a large number of constant amplitude fatigue tests were performed on un-notched specimens with different microstructures corresponding to different annealing conditions, as described in Section 3.7.1.2. Axial and torsional fatigue tests were performed on the smooth specimens to determine the fatigue baselines of the different materials, which are required for further multiaxial fatigue analyses. In addition, in-phase and out-of-phase tension-torsion fatigue tests were performed on the smooth specimens to verify the reliability of the obtained baselines for more complex loading conditions and to determine the probable non-proportional hardening parameter of the materials. The results for fatigue tests on un-notched specimens are presented in Section 4.5.1 based on the equivalent strain approach and the critical plane approach.

Fatigue tests were also conducted on welded specimens, incorporating various uniaxial and multiaxial loading conditions as detailed in Section 3.7.2. These tests aimed to investigate the possibility of correlating fatigue data, taking into account different weld-related aspects in the assessment of fatigue damage. The aspects considered include the non-uniform material structure in the weld and its surroundings, the notch effect of the weld, i.e., the local stress-strain state of the material and the stress gradient, the residual stresses in the weld and the non-proportionality of the load. This work primarily focuses on fatigue crack initiation. To assess the multiaxial fatigue life of the welds, both the equivalent stress/strain approach and the critical plane approach were used, with an elite damage model chosen for each based on an extensive literature review.

7.1 FE Calculation of Residual Stresses

Similar to the "residual stress specimens" in Chapter 6, FE welding simulation was also carried out for the "fatigue specimens", whose features are described in Section 3.2, in order to numerically determine the welding residual stress field prior to upcoming fatigue life analyses. The simulation was conducted using a three-dimensional FE model with the help of SYSWELD 12.5. The element size was kept as small as possible in order to achieve acceptable accuracy. In this context, the element size in the area of the weld notch was confined to 0.1 mm (Figure 7.1). A coupled thermo-metallurgical analysis followed by an uncoupled mechanical analysis was performed to describe the temperature distribution, microstructural transformations, and residual stresses and strains. The applied Goldak parameters as the heat source model were calibrated with respect to the observed fusion boundaries in the weld micrographs. The mechanical properties of the material at room temperature required for the simulations were obtained from the test results described in Section 4.3. The extrapolation-based methodology described in Section 6.1.2 was used to estimate the corresponding material properties at higher temperatures. The calculated surface and depth contours of residual stresses are given in Figure 7.2 in comparison with the experimental results with the x-ray and neutron diffraction measurements. The measured and predicted residual stress fields agree with each other considerably well.

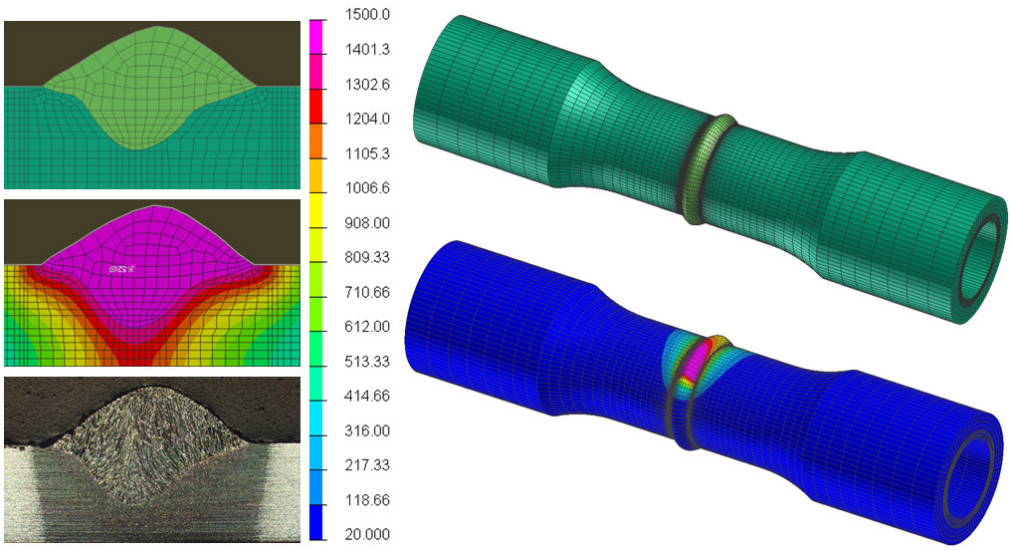

Figure 7.1 Three-dimensional FE model and welding simulation.

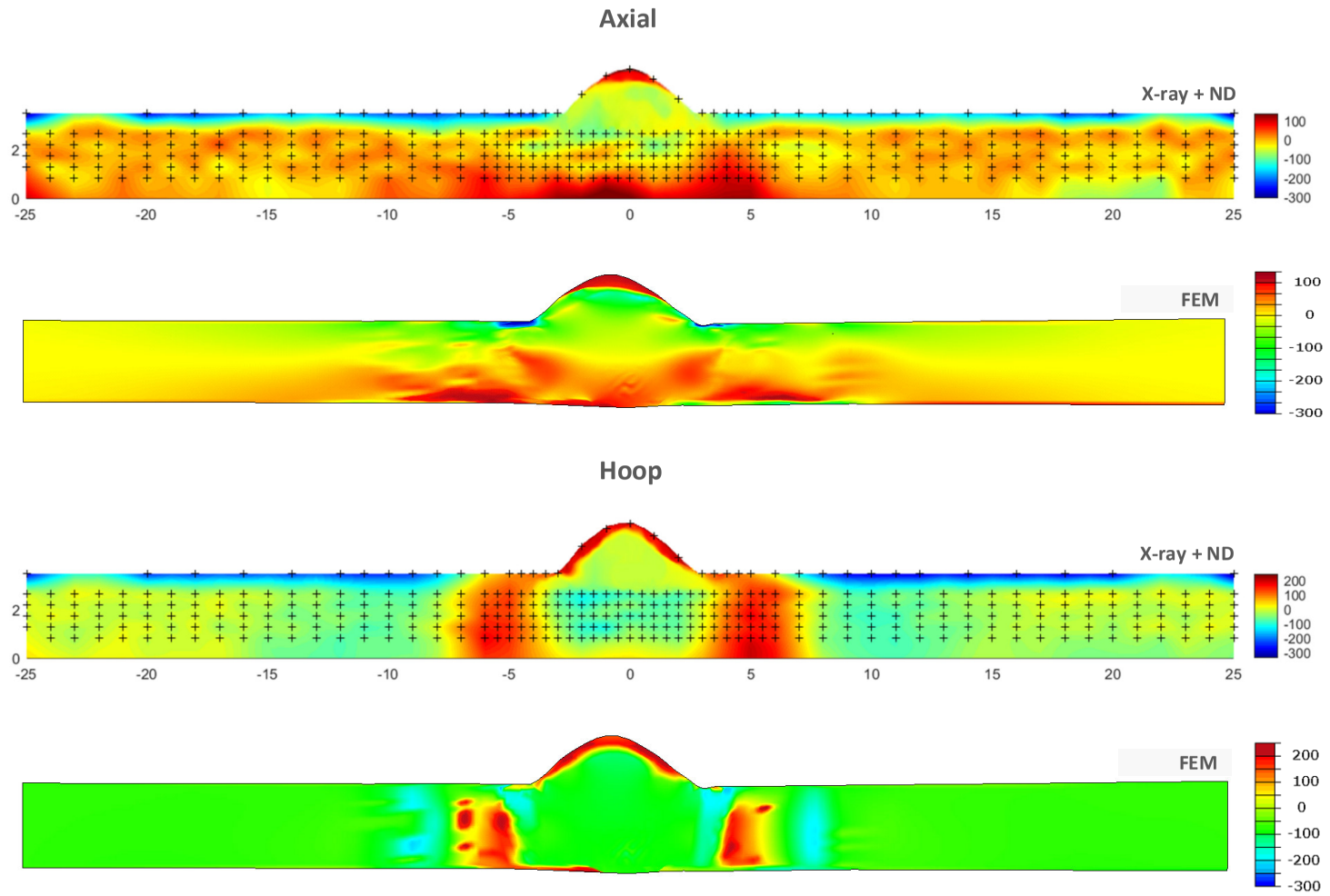

Figure 7.2 Experimental measurements vs. simulation results of the welding residual stresses at 180° from the weld start point.

7.2 FE Implementation for Fatigue Evaluations

A two-dimensional FE model was developed using ABAQUS 6.14 for the fatigue simulations and life evaluations with element type of CGAX4R. Since the weld specimens in this work have weld notches, determining the reliable local stress and strain state in the vicinity of the weld notch is one of the most important aspects. Therefore, in addition to the geometry effect, the material behavior in this area shall be described precisely. This requires that the weld-induced microstructural phase transformations are taken into account. Accordingly, the model was divided into four sections representing the base material, HAZ far field, HAZ near field and the weld area. Extensive material characterizations were performed for the BM and HAZ near field as described in Section 3.7.1. Properties of the weld material (WM) and HAZ far field were defined using a hardness-based interpolation as given in Figure 7.3.

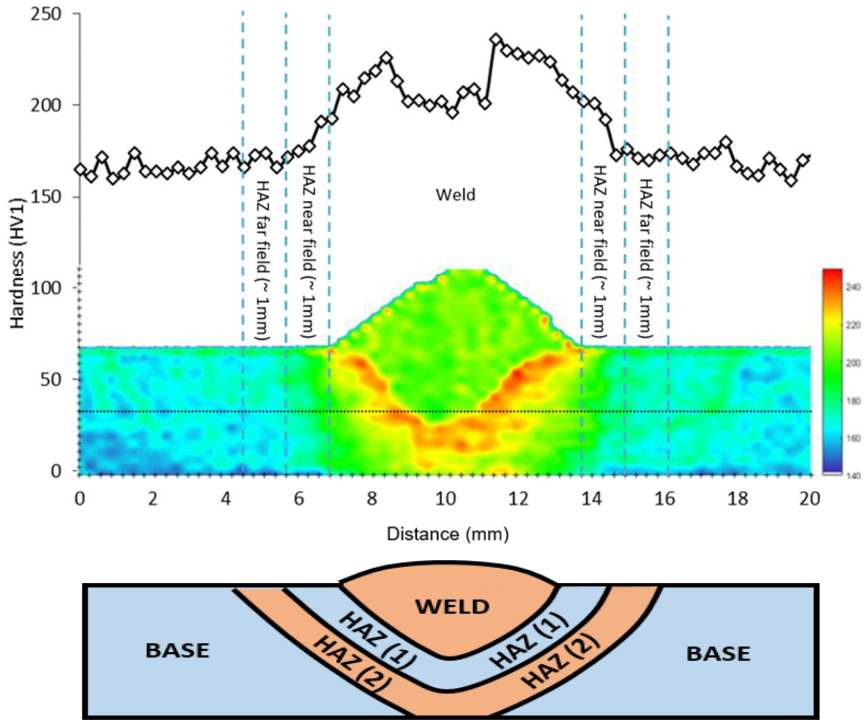

Region	HV	σ_y (MPa)	*C1*	*C2*	*C3*	*γ1*	*γ2*	*γ3*	*Q*	*b*	E (GPa)
HAZ (1)	226	415,33	78105	84330	34798	12808	1487,7	228,6	8,95	32,2	195
HAZ (2)	209	361,2	58618,9	257711,4	60535	8829	4435,1	579,62	10,34	30,5	196
WELD	203	342,07	51767	318904,9	69618,72	7924,68	5475,35	703,51	10,83	29,9	196,5
BASE	172	243,43	16268	635071	116551	168,9	10850	1343,6	13,37	26,81	197
	Measured	Interpolated									

Figure 7.3 Interpolation of the material properties based on the hardness distribution.

A sensitivity analysis was made to determine a suitable element size that would allow for accurate calculations as well as a reasonable calculation time. The plots of the sensitivity analyses based on the variation of axial stress and axial strain near the weld notch are shown in Figure 7.4 and Figure 7.5, respectively. For these analyses, the weld toe, which is believed to be the site of cracking, was modelled once as a sharp notch and second as a fillet that represents the real weld toe radius. The element sizes were set at 0.1 mm and then reduced to 0.01 mm and finally to 0.005 mm. The singularity effect caused by the sharp notch increases significantly with the reduction of the element size at a certain distance from the notch, which would lead to unrealistic stress and strain values and consequently affect the assessment of fatigue damage, as in reality there is likely to be a small radius at the weld notch. However, for the fillet weld toe, the peak stress and peak strain values increased when the element size was altered from 0.1 mm to 0.01 mm and tended to saturate when the element size was reduced to 0.005 mm, with the only visible change being the stress and strain gradient. After obtaining satisfactory results and a reasonable calculation time, the element size at the weld toe was set to 0.005 mm, while the model with a fillet corresponding to the actual radius of the weld toe was selected for damage assessment. The element size is gradually increased with increasing distance from the weld.

The calibrated FE model is now ready for the intended uniaxial and multiaxial fatigue analyses. The boundary conditions were designed to be as close as possible to the real conditions. To this aim, an axisymmetric constraint was applied to the two-dimensional model with one end fixed while loads were applied to the other end in the form of axial, torsional, in-phase and out-of-phase multiaxial loads as listed in Table 3.19 to Table 3.26. It is known that some of the fatigue specimens were stress-relieved while the other specimens remained in the as-welded condition. The same conditions were considered in the FE simulations, as the virgin two-dimensional model can represent the stress-relieved specimens, while for the as-welded condition, the residual stress field obtained from the three-dimensional welding simulations described in Section 7.1 was mapped onto the two-dimensional model using a Python script. For this purpose, the stress field from a section of the three-dimensional model located at an angle of 180° to the weld start point was selected for mapping. In such a case, the experimentally determined residual stress field could be mapped directly onto the two-dimensional model. However, the objective was mainly to evaluate the

ability of a fully FE-based approach to incorporate the multiple physical factors into the fatigue life assessment, especially where the experimental methods are not necessarily possible due to geometric complexity or cost constraints.

To account for residual stress relaxation under cyclic loading with multiple load cycles, a preloading step of 5 full cycles was considered in the simulation, after which a stable residual stress field was obtained. The main load cycle was applied to the model in the next step in the form of a single full cycle, based on the load information given in Table 3.19 and Table 3.26.

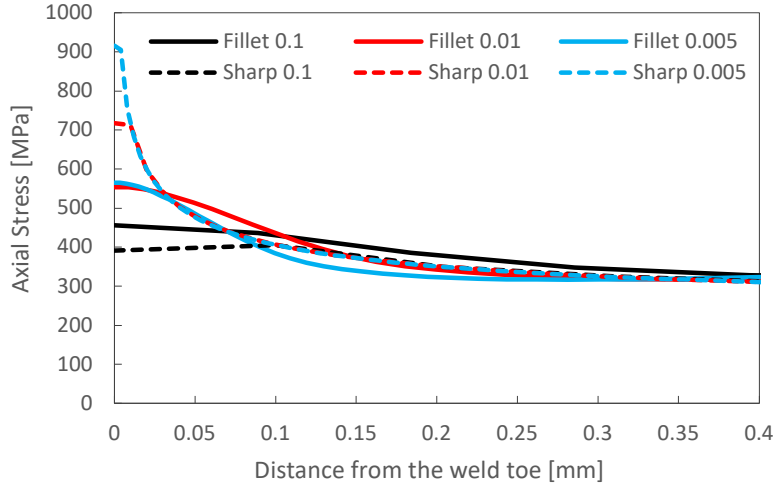

Figure 7.4 Mesh sensitivity and notch-geometry sensitivity analyses at the weld notch for the FE simulations based on the stress (Sharp: sharp notch, Fillet: realistic fillet notch – Mesh size: 0.1 mm, 0.01 mm and 0.005 mm).

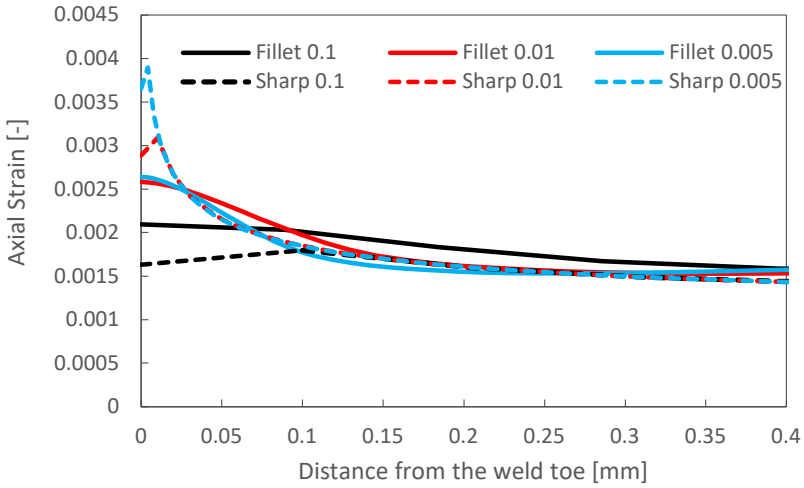

Figure 7.5 Mesh sensitivity and notch-geometry sensitivity analyses at the weld notch for the FE simulations based on the strain (Sharp: sharp notch, Fillet: realistic fillet notch – Mesh size: 0.1 mm, 0.01 mm and 0.005 mm).

7.3 Notch Effect in Fatigue Evaluations

A critical factor in fatigue assessment of notched specimens using local stress or strain methods is identifying the crack initiation site. For uniaxial or proportional load conditions, the location where the material experiences the maximum stress or strain amplitude is known as the fatigue failure site. However, under non-proportional loading, the location of maximum stress can vary within a single cycle. Therefore, fatigue evaluations may need to be conducted at multiple points to identify the maximum stress or strain amplitude. In this study, it was experimentally observed that fatigue cracks in welded specimens, regardless of the loading condition, consistently initiated on the tube surface, specifically at the weld toe.

Implementing nominal equivalent stress or strain approaches is particularly challenging for non-proportional loading. Determining the equivalent stress concentration factor is complicated when the location and magnitude of the maximum local stress amplitude continuously vary with changes in the nominal stress ratio. Therefore, the local analysis approach was favored over the nominal equivalent stress/strain approach in this study.

In addition to maximum stress or strain amplitude, the stress gradient is the other crucial factor in fatigue assessments. Since fatigue occurs within a process zone, considering the variation of stresses and strains within a finite volume is more effective than focusing solely on maximum values. Applying specific methods to account for the stress gradient effect is expected to significantly reduce conservatism in fatigue life predictions. Two common approaches, the fatigue notch factor (K_f) and the theory of critical distance (TCD), are discussed in Section 2.3.3.

To determine the notch factor, the stress concentration factor of the weld notch was first evaluated. The actual weld notch geometry was modeled using cross-sectional macrographs of the weld, specifically from a macrograph taken at 180° from the weld start of a randomly selected specimen (see Figure 7.1). A more accurate assessment can be achieved by statistically analyzing the notch geometry across multiple macrographs. The stress concentration factor of the notch under each loading condition, namely axial and torsional, was then determined by dividing the maximum stress at the notch by the nominal stress. A limitation of the fatigue notch factor method is that the characteristic length of the material is not always available. If this

length is unknown, it can be estimated using empirical methods, such as the methodology proposed by Kuhn and Hardrath [72] for steel alloys (see Section 2.3.3). A limitation of this method is that the material characteristic length cannot be defined for sharp notches with a notch root radius of zero. However, in practice, the notch radius at the weld toe is typically non-zero. Besides the approximation formula, the material characteristic length can be derived from grain size statistics [143][144]. Therefore, a correct definition of the effective grain size is essential. The average grain size, in terms of the grain diameter, can be obtained from experimental measurements [145][146] as described below:

$$d = \frac{1}{n}\sum_{i=1}^{n} n_i d_i \tag{7-1}$$

where n is the total number of measurements and n_i denotes the number of measurements corresponding to the grain size d_i.

For homogeneous microstructures, the average grain size can effectively represent the material's physical features. However, in heterogeneous microstructures, the average grain size may not be the best choice due to the large variation in grain sizes [147][148]. Typically, the lowest yield strengths are associated with the largest grains due to the longer slip planes [149][150]. Therefore, for heterogeneous microstructures, it is recommended to define material strength using a mixture rule that considers each grain's contribution to the overall strength based on its respective volume [151][152]. The volume-weighted average grain size is defined as follows:

$$d_v = \frac{1}{V_T}\sum_{i=1}^{n} V_i d_i \tag{7-2}$$

where V_T is the total material volume and V_i and d_i are the volume and size of the i^{th} grain. Based on this formulation, the volume-weighted average grain size should always be larger than the average grain size, unless all grains are the same size.

Since fatigue cracks often initiate in the weld notch area, the microstructure in this region, specifically the near-field HAZ, was analyzed with respect to grain size distribution. As previously mentioned, the microstructure in this region is more complex than the base material and exhibits greater variation in grain size. For this purpose, the optical micrographs presented in Section 4.2.2 were used for grain size measurements. Image processing was performed following the instructions in [153], converting the images to binary mode where grain boundaries were shown in black and grain interiors in white. The grain boundary map of the near-field HAZ is displayed in Figure 7.6.

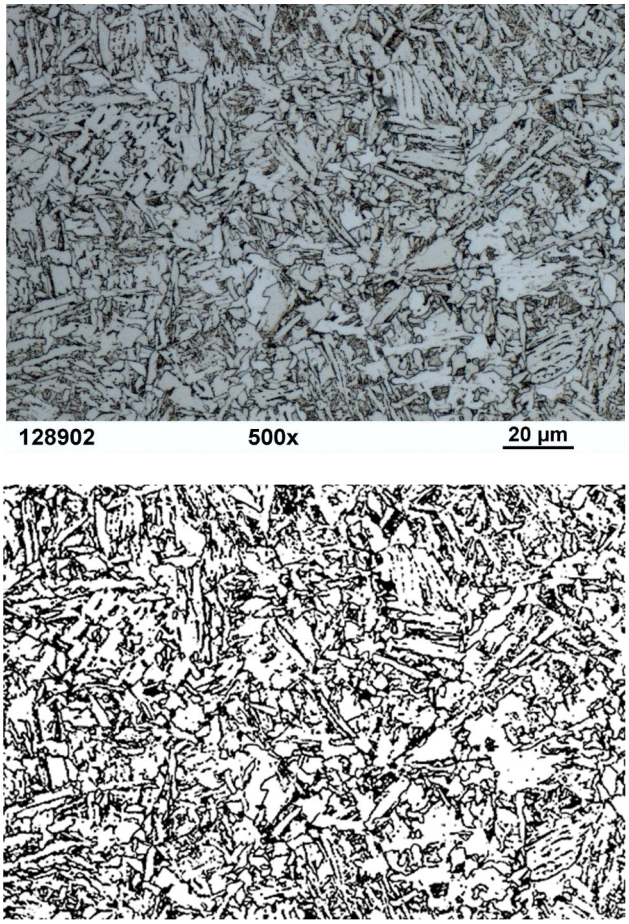

Figure 7.6 Grain distribution in the HAZ-near field and the binary mode micrograph.

The MathWorks MATLAB software generated by [153] was used to perform the grain size measurements. The linear intercept length method presented in ASTM E1382 [154] is a method for estimating the average grain size, where each direction is treated as a single distribution for analysis. In this study, a similar approach to the ASTM method was employed to measure the volume-weighted average grain size using the point-sampled intercept length method (Figure 7.7) [155][156], with the modification that random points were selected for the measurements.

A total of 1500 measurements were taken using the point-sampled intercept length method, surpassing the ASTM E1382 [154] recommended minimum of 500 measurements to ensure that the tails of the experimental data distribution are adequately captured.

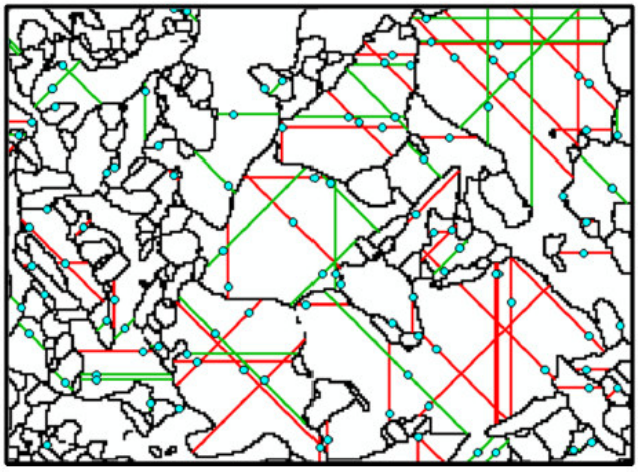

Figure 7.7 Point-sampled intercept length measurement [155][156].

The measured distributions were filtered to exclude measurements smaller than 3 pixels. To reduce measurement uncertainty, which is characterized by relative grain size dispersion, the method was adapted from Berbenni et al. [147]:

$$\frac{\Delta d}{d} = \frac{d_{max} - d_{min}}{d} = \frac{P_{99\%} - P_{1\%}}{d} \tag{7-3}$$

where the grain sizes corresponding to the 1% and 99% probability were respectively considered instead of the minimum and maximum grain sizes [153]. The volume fraction of individual grains was estimated in relation to the surface fractions, and the grain size was measured proportionally [157][158].

In addition to grain size distribution, defining a meaningful granular structure is crucial. For the base material, which has a ferritic-pearlitic microstructure, the grain characteristics are relatively straightforward. However, in the HAZ, where the microstructure is bainitic and partially martensitic, defining a specific grain structure is more challenging. The complex shape of the grains in this microstructure complicates the correlation between two-dimensional cross-sections and the three-dimensional grain configuration. To distinguish between the high-angle (>10°) interfaces and the packets consisting of blocks with low-angle (<10°) interfaces, the methodology outlined in [157] was employed. The values obtained for the parameters related to the grain size in the HAZ are listed in Table 7.1.

Table 7.1 Grain sizes of the test material (μm).

Microstructure	Image	d (μm)	d_v (μm)	$d_{99\%}$ (μm)
S355J2H-HAZ Nearfield	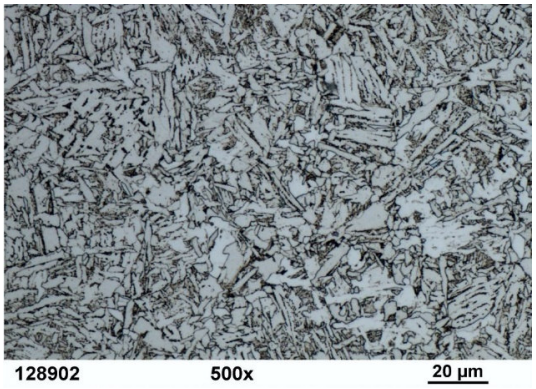	2.33	4.12	9.60

7.4 Equivalent Stress/Strain-Based Life Predictions

Conventionally it has been tried to relate the fatigue life of components under multiaxial loading conditions to the uniaxial fatigue damage criteria through defining equivalent stress or strain terms. Based on such approaches, the uniaxial fatigue baselines could be applied to conditions where multiaxial stress states exist. Stress-based equivalent approaches are the basic approaches suitable for purely elastic loading; with the introduction of plastic deformation, the strain-based equivalent approaches appear to be more suitable.

The simplest stress-based method assumes that there is a correlation between the alternating stress in the material and the fatigue life. When it comes to the multiaxial loading condition, to account for the multiaxial stress field an equivalent criterion such as von Mises or maximum principal stress would be essential to transform the multiaxial stress state into a single equivalent value which can be comparable with the uniaxial fatigue properties of the respective material. To account for the additional influencing factors, such as the surface quality of the material, size effect, temperature effect, environmental conditions etc., a number of empirical correction factors can be applied to the uniaxial S-N curve to adjust the respective fatigue strength. The other concern in the fatigue analyses is the presence of the mean stress. In such cases, several

models have been proposed to adjust the alternating stress in relation to the current mean stress.

The more comprehensive methodology which is analogous to its stress-based counterpart approach, is the equivalent strain approach in which the correlation is made between the strain quantity and the number of cycles to failure. This approach is known to be more commonly used due to its ability to better account for the plastic deformation of the material when such data are available.

In this section the equivalent von Mises stress and the equivalent von Mises strain approaches were applied to predict the fatigue life of welded specimens.

7.4.1 Equivalent Stress/Strain-Based Assessment Results

In the first step, the equivalent stress-based approach was applied as a basic methodology for predicting fatigue lives. Two approaches were considered in this regard to account for the localized plastic deformation at the notches in the lifetime evaluations. Initially, the local stress and strain states were estimated analytically from the theoretical elastic stress amplitudes using Neuber's rule [62]. For this purpose, the local von Mises pseudo stress along with the cyclic stress-strain curve were employed to derive the local stresses and strains. An equivalent stress concentration factor in terms of the ratio between the local elastic equivalent stress and the nominal equivalent stress was used to calculate the equivalent notch factor K_{fq}. Having the local equivalent stress amplitude $\Delta\sigma_q/2$, the stress-based fatigue damage evaluation can be performed. Besides the analytical approach, FE method in terms of elastic-plastic simulations was also used to describe the local stress and strain state in the notch area. The results of the fatigue life assessment, obtained from the analytical and FE methods, were compared based on local equivalent stresses. Figure 7.8 illustrates this comparison, displaying the experimentally measured fatigue life of individual HT weld specimens under uniaxial and in-phase multiaxial loading conditions in relation to the calculated amplitudes of the equivalent local stress.

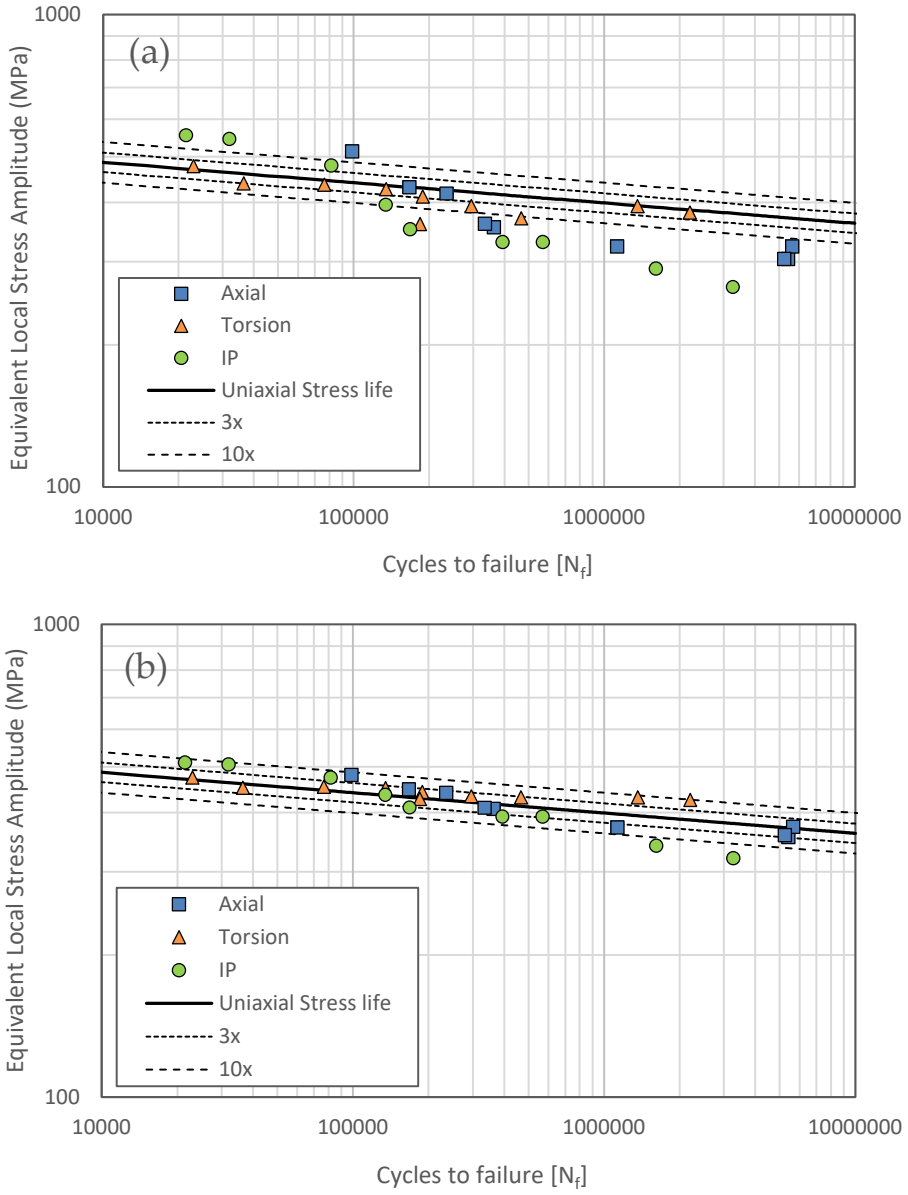

Figure 7.8 Fatigue life correlations for the HT specimens in terms of equivalent local stress amplitude vs. cycles to failure and based on von Mises equivalent stress-life approach and (a) Neuber's rule with fatigue notch factor, K_{fq} and (b) elastic-plastic FE analysis.

As the FE method provides more accurate correlations for the HT specimens, this method was used for the further lifetime evaluation of welded specimens. In addition, the use of the FE method offers the possibility to include residual stress as an initial stress field in the model. The equivalent stress based fatigue life assessment results

for HT and AW specimens under different loading conditions including out-of-phase multiaxial loading are shown in Figure 7.9 (a) and Figure 7.10 (a).

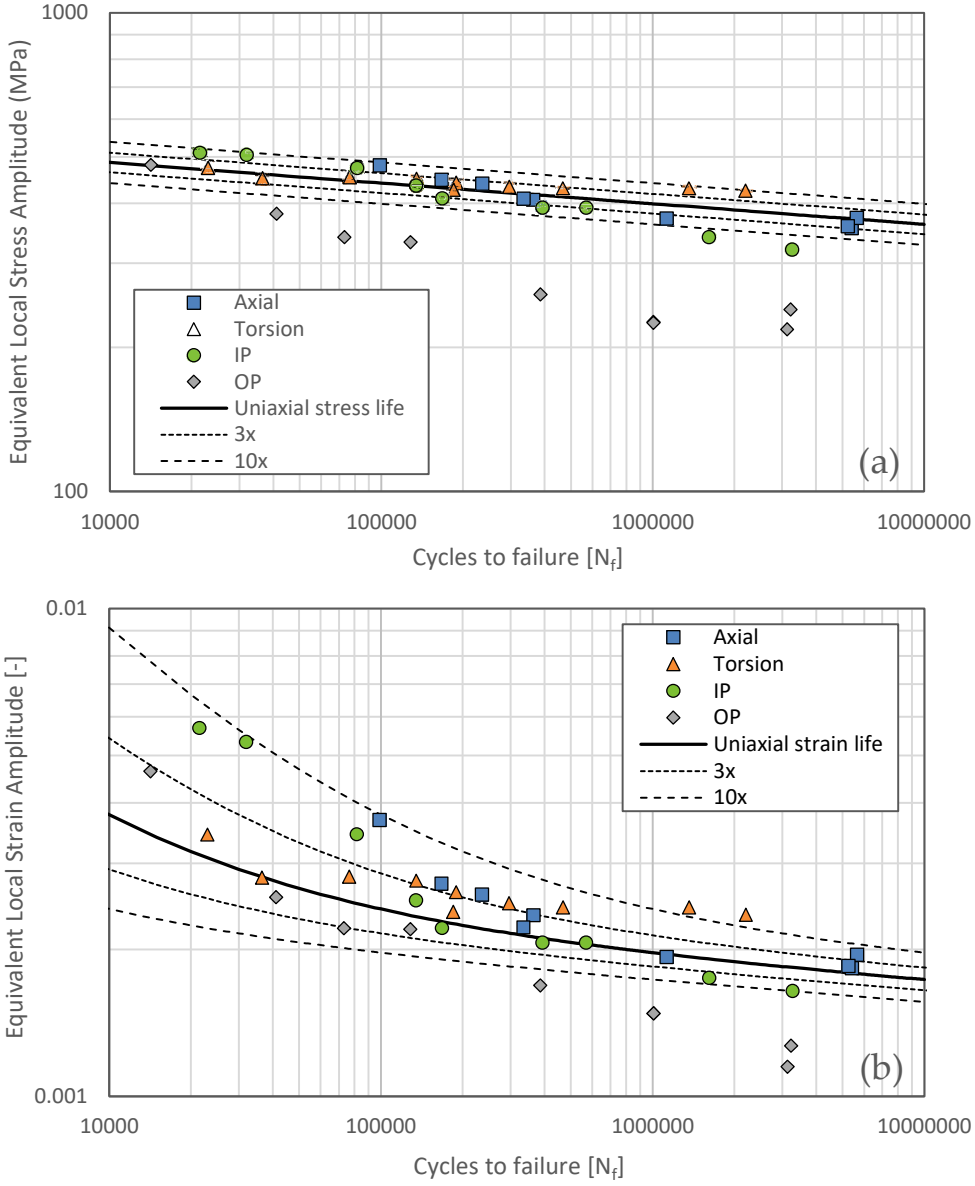

Figure 7.9 Fatigue life correlations for the HT specimens based on von Mises equivalent stress/strain-life approach and elastic-plastic FE analysis in terms of (a) equivalent local stress amplitude and (b) equivalent local strain amplitude vs. cycles to failure.

Similarly, the equivalent strain-based approach was also applied for the fatigue life assessment of welded specimens using the FE method to determine the local equivalent von Mises strains. The results of the fatigue life assessment based on local

equivalent strains using FE approach for the HT and AW specimens are shown in Figure 7.9 (b) and Figure 7.10 (b) respectively.

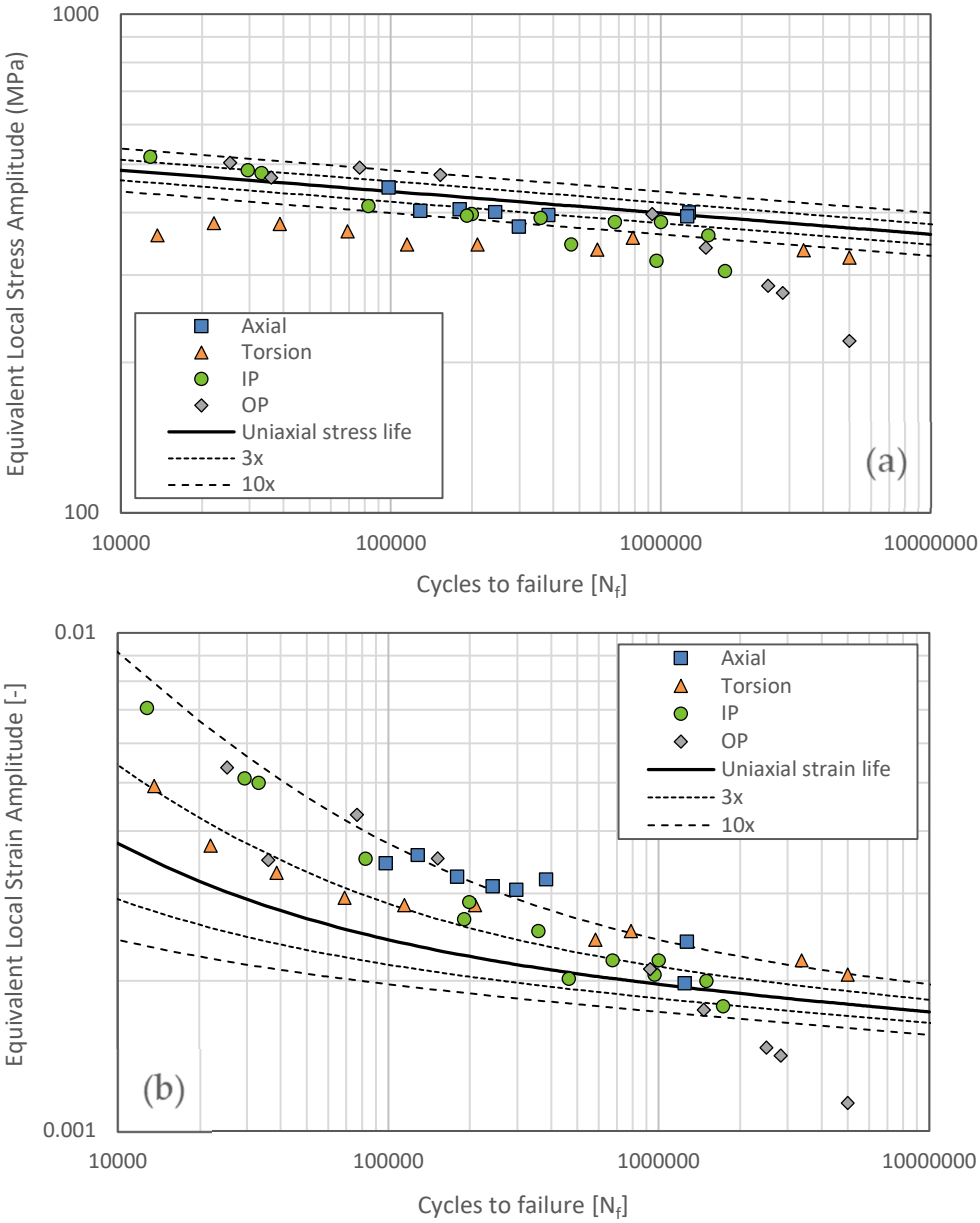

Figure 7.10 Fatigue life correlations for the AW specimens based on von Mises equivalent stress/strain-life approach and elastic-plastic FE analysis in terms of (a) equivalent local stress amplitude and (b) equivalent local strain amplitude vs. cycles to failure.

7.4.2 Discussion on Equivalent Stress/Strain-Based Life Assessments

This section provides a brief interpretation of the prediction results based on the conventional equivalent stress and strain approaches. Figure 7.9 and Figure 7.10 plot, based on the equivalent local stress and local strain approaches, the fatigue data of HT and AW specimens respectively. Based on these results, equivalent von Mises stress method can bring 92% and 55% of the fatigue data of uniaxial and proportional multiaxial loading conditions within scatter bands of ±10 for the HT and AW specimens respectively. And the equivalent von Mises strain method reached values of 92% and 77% for HT and AW specimens respectively. However, under 90° out-of-phase load condition the fatigue life predictions were significantly non-conservative.

Uniaxial fatigue data of HT specimens are correlated slightly better by the equivalent stress approach while the predictions based on the equivalent strain approach were mostly conservative. It can be observed that based on both stress-based and strain-based methods life predictions appear to be more accurate at shorter life for the case of pure torsion, and at longer life for the case of pure axial. For multiaxial tests however, the equivalent strain approach could provide slightly better predictions in comparison with its stress-based counterpart.

For the AW test data, the predictions are non-conservative by the stress-based approach while they are mostly conservative by the strain-based approach. However, since most of the fatigue tests in this study were designed to be in the HCF regime, consequently the accuracy of the prediction by these methods are not dramatically different, unless for those tests in LCF regime where the material undergoes local plastic deformation.

The capability of the equivalent stress/strain-based approaches in correlating the fatigue data for the AW specimens to fall into the desired scatter bands was lower than for the HT specimens. This observation could be related to the presence of welding residual stresses. Since equivalent stress/strain approaches typically represent the damage parameter as stress or strain ranges or amplitudes, they often do not adequately account for the influence of mean or residual stresses. This oversight limits their ability to accurately capture the complete stress state and its impact on material behavior.

To summarize, the conventional approaches based on equivalent stresses and strains show relatively remarkable efficiency in consolidating fatigue data from welded specimens into a single band, provided that non-proportional loading and welding residual stresses are not present. To improve the ability of these approaches to account for such complexities, complementary methodologies alongside damage calculations are recommended. Given the additional effort required to account for these nuances in conventional methods, the examination of more advanced damage parameters based on material physics seems better suited to achieve more accurate results.

7.5 Critical Plane-Based Life Predictions

To incorporate the stress gradient effect into lifetime evaluations using the critical plane approach, similar to equivalent stress/strain approaches, an additional methodology is needed. Implementing the fatigue notch factor method for non-proportional multiaxial loading is challenging due to the continuous variation of the stress concentration factor over a cycle. Therefore, the theory of critical distance (TCD) was used alongside the critical plane approach to consider the stress gradient effect using fracture mechanics principles. To implement this methodology, the critical distance L, as a material-dependent characteristic length, needs to be determined. Equation 2-49 can be used to determine this quantity, given that the fatigue limit stress $\Delta\sigma_o$ and the mode I threshold stress intensity factor range (ΔK_{th}) of the material are available. The fatigue limit stress can be determined from the uniaxial fatigue properties as the stress level corresponding to 10^7 cycles. To determine the threshold SIF for uniaxial crack growth, conducting crack growth tests is essential. However, due to the constraints imposed by the size and geometry of the material, particularly in the HAZ, producing and testing compact tension specimens proved challenging. Given the limited data on the stress intensity factor of the studied material, the microstructure-based characteristic length defined in Section 7.3 was used as a representative value for L. Consequently, a critical distance L of approximately 0.01 mm was selected (see Table 7.1). The critical distance under uniaxial loading is generally smaller than under pure torsion. For simplicity, however, it is often assumed to be the same as for pure axial loading. According to Susmel and Taylor [78], this assumption introduces an error margin of ±25%.

Figure 7.11 (a) and Figure 7.12 (a) present the correlation of fatigue data for HT and AW specimens, respectively, based on the original FS damage parameter and the point method TCD, under various uniaxial and multiaxial loading conditions.

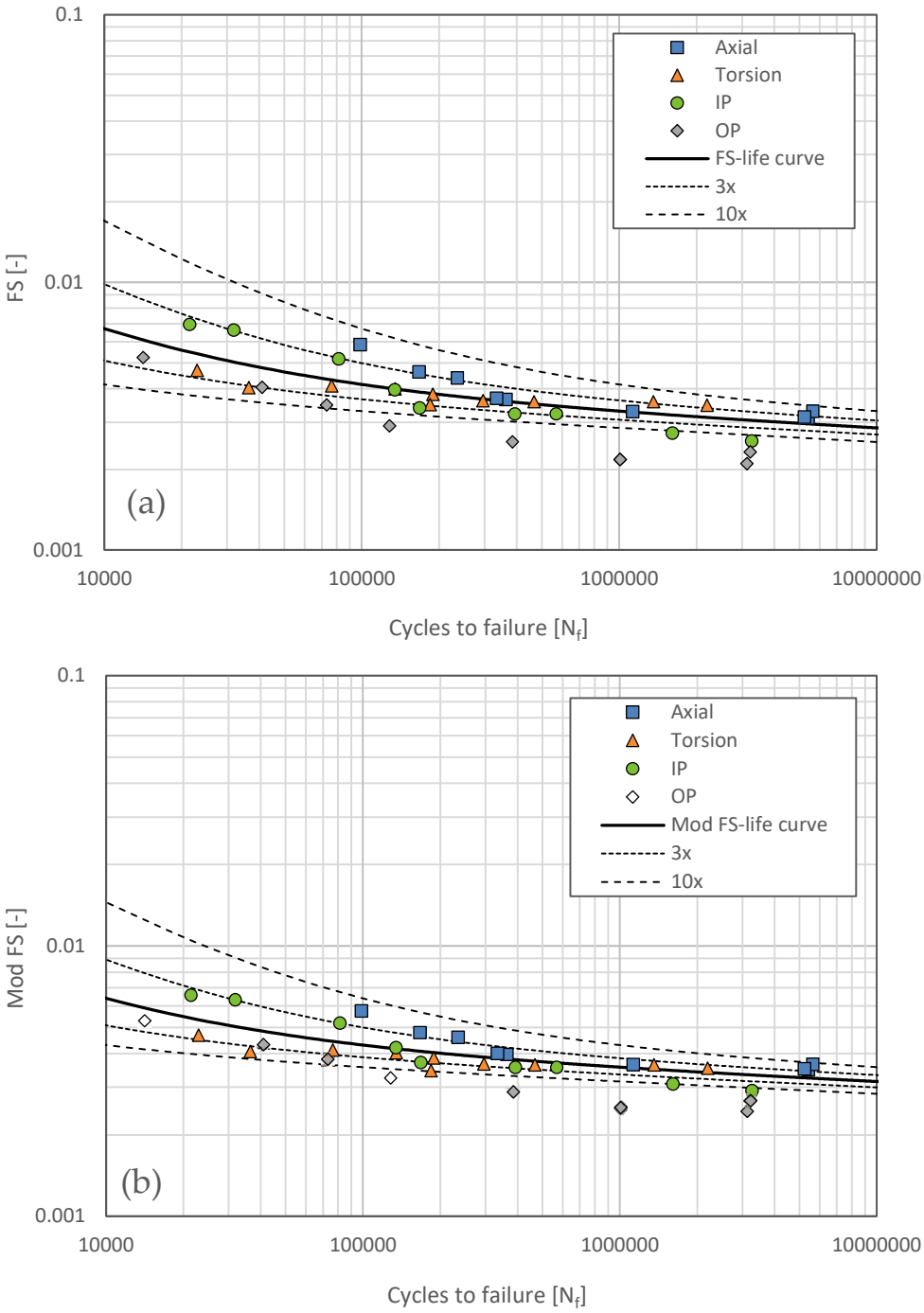

Figure 7.11 Fatigue life correlations for the HT specimens in terms of damage value vs. cycles to failure based on (a) FS and (b) mod-FS critical plane approaches and uniaxial strain-life properties.

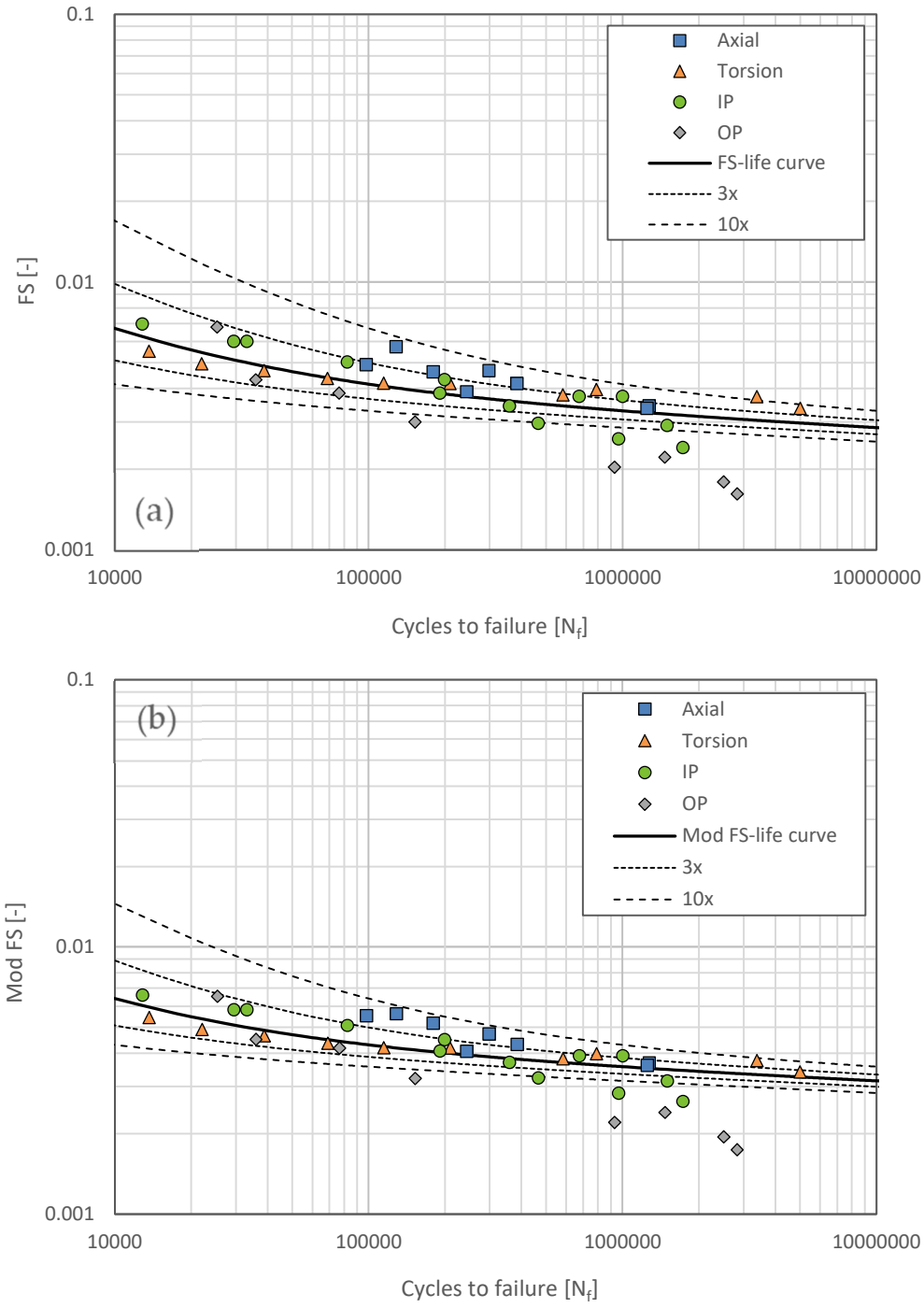

Figure 7.12 Fatigue life correlations for the AW specimens in terms of damage value vs. cycles to failure based on (a) FS and (b) mod-FS critical plane approaches and uniaxial strain-life properties.

According to these results, 54% of the fatigue data for HT specimens and 55% of the fatigue data for AW specimens fall within the ±3 scatter bands. Thus, the FS parameter, provided that accurate stress and strain data at crack-prone areas are available, correlates reasonably well with the constant amplitude multiaxial fatigue data.

7.5.1 Discussion on Critical Plane-Based Life Prediction Results

Using the shear-based FS parameter as a critical plane-based approach significantly improved the fatigue life correlation.

Predicted damage values within a factor of ±3 of experimental results were obtained for 48% of HT specimens and only 20% of AW specimens using the equivalent stress approach, and for 43% of HT specimens and 25% of AW specimens using the equivalent strain approach. These percentages increased to 54% for HT specimens and 55% for AW specimens when using the FS parameter. Although the predictions for HT fatigue data suggest that the FS parameter generally has potential to effectively predict fatigue damage for the loading conditions tested, the comparison of fatigue data under non-proportional loading conditions indicates that the parameter may be less effective in such cases. Additionally, predictions for AW specimens could be improved by better accounting for welding residual stresses.

High accuracy of results seems to be achieved using the TCD approach. This approach can provide a versatility in fatigue life evaluations as it can be used in combination with different life prediction methodologies. The reason is that TCD depends only on local stress distribution and a characteristic length derived from the material properties, allowing for greater flexibility in integrating different fatigue life assessment methods. However, it can be difficult to determine the correct L value and the methodological approach that provides the most accurate fatigue life predictions.

Given that the shear-based FS damage parameter was shown to correlate more strongly with fatigue data than the conventional approach, it was selected for further analyses.

7.6 Influence of Weld-Induced Residual Stresses on Fatigue Behavior of Welds

In the previous section, it was determined that the Fatemi-Socie critical plane-based damage parameter correlates relatively well with the fully reversed constant amplitude fatigue data of the weld specimens produced in this study. However, recent findings from the literature , e.g. [160] and [161], indicate that the FS parameter may provide non-conservative fatigue life predictions when large tensile mean stresses are present. Increasing the k value can improve the correlation with mean stresses by increasing the influence of the maximum normal stress term in the FS parameter. However, this adjustment may adversely affect the correlation with fatigue data for other multiaxial loading paths. Since one focus of this study is to consider the effects of residual stresses, it is crucial to ensure that the damage parameter adequately accounts for the effects of mean stresses.

7.6.1 Modified Fatemi-Socie Parameter

In an effort to enhance the accuracy of fatigue life predictions for AW specimens, a modified version of the FS parameter (mod-FS) [75] was examined, aligning with the objectives outlined in the previous section. Observations from fatigue tests indicated conservative predictions for AW specimens, suggesting the potential to increase the influence of the maximum normal stress in the FS model under conditions where welding residual stresses in the notch region are compressive. However, it is crucial to maintain fatigue life correlations for HT specimens, which requires a careful approach. This objective is addressed by the mod-FS parameter, where the yield strength in the FS equation is replaced by a stress amplitude/range-dependent term. The assumption that the ratio of normal stress to shear stress adequately captures the interactions between these stress types supports the beneficial use of a value dependent on the shear stress range rather than relying solely on the material yield strength. The correlation of the fatigue data based on the mod-FS parameter for the HT and AW specimens are shown in Figure 7.11 (b) and Figure 7.12 (b) respectively. The correlation of the fatigue data was improved, albeit only slightly, for the AW

specimens, where residual stresses are present, but also for the HT specimens, especially in the HCF range. In particular, the application of the mod-FS parameter resulted in an improved correlation of the out-of-phase fatigue data, favoring a more conservative approach compared to the significantly non-conservative correlation obtained with the conventional FS parameter.

To better assess the effectiveness of the mod-FS parameter in accounting for welding residual stresses when estimating fatigue damage, all fatigue simulations for the AW specimens except the out-of-phase load case were repeated without including the initial residual stress field in the FE model. As shown in Figure 7.13, the prediction of fatigue life significantly improves when the residual stress field is included in the FE analyses, especially beyond ~20,000 cycles, as would be expected in the HCF regime where residual stresses are less likely to relax. In addition, the approach that includes the residual stress field predicts generally longer fatigue lives than when the residual stresses are excluded from the fatigue life assessments. This is due to the fact that the axial welding residual stresses in the crack-prone region (weld notch) were compressive stresses that could have resisted cracking and increased the fatigue life.

7.7 Influence of Weld-Induced Microstructure Transformations on Fatigue Behavior of Welds

A wide range of material characterization studies were performed in the previous chapters to better clarify the role of weld-induced microstructural transformations on the deformation behavior and fatigue behavior of the material. Based on the results so far it seems that distinct differences exist between the behavior of the BM and HAZ. However, there may be concerns that accounting for the effects of transformations in both material elastic-plastic deformation properties and fatigue properties could lead to overlapping results. To reveal the intensity of material dependency of fatigue life predictions based on the critical plane approach, a sensitivity analysis was performed. This involved repeating fatigue life assessments for HT specimens (excluding the out-of-phase case) with a modified FE model. The key difference in this model was the uniform application of base material (BM) properties throughout, as opposed to defining separate properties for BM, weld material (WM), and heat-affected zone (HAZ) in the original model, as shown in Figure 7.3. Additionally, the damage-life

baseline of the BM was used for these assessments. The results, shown in Figure 7.14, clearly indicate that ignoring the specific properties of the material in the HAZ results in overly conservative fatigue life predictions.

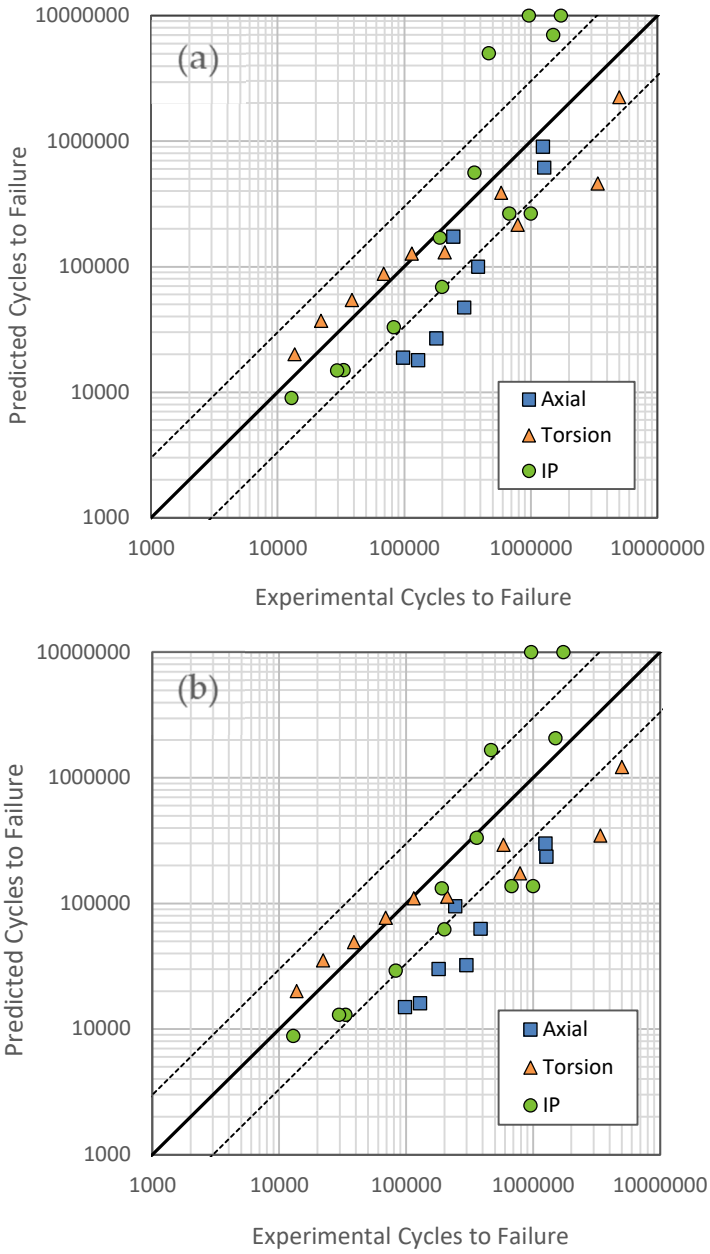

Figure 7.13 Experimental vs. predicted cycles to failure for the fatigue data of the AW specimens based on the mod-FS critical plane approach (a) with and (b) without considering the welding residual stress field into the FE model (OP test data are excluded).

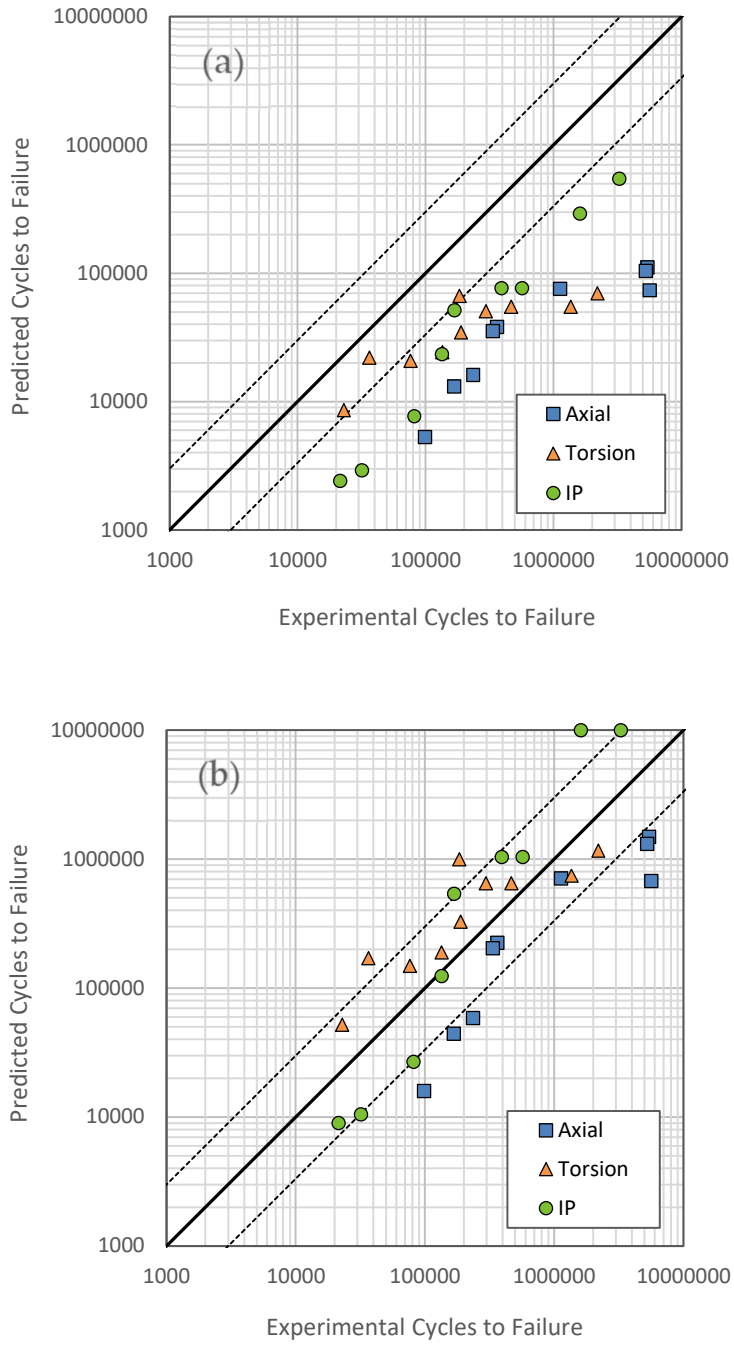

Figure 7.14 Experimental vs. predicted cycles to failure for the fatigue data of HT specimens based on the mod-FS critical plane approach using the (a) uniform material properties (BM only) and (b) combined material properties (HAZ+BM) (OP test data are excluded).

7.8 Integral Approach to Fatigue Damage Calculation at Non-Proportional Loading Condition

Although the fatigue life correlations for the out-of-phase loading condition improved with the use of the critical plane approach, particularly with the mod-FS parameter, the out-of-phase fatigue data for both HT and AW specimens still show significant deviations from the target band, especially at lower load levels. To achieve a better insight into the fatigue behavior of the material under out-of-phase loading, the calculated damage versus slip plane angles were plotted for two arbitrary tests, i.e., a pure torsion test and an out-of-phase test, as shown in Figure 7.15.

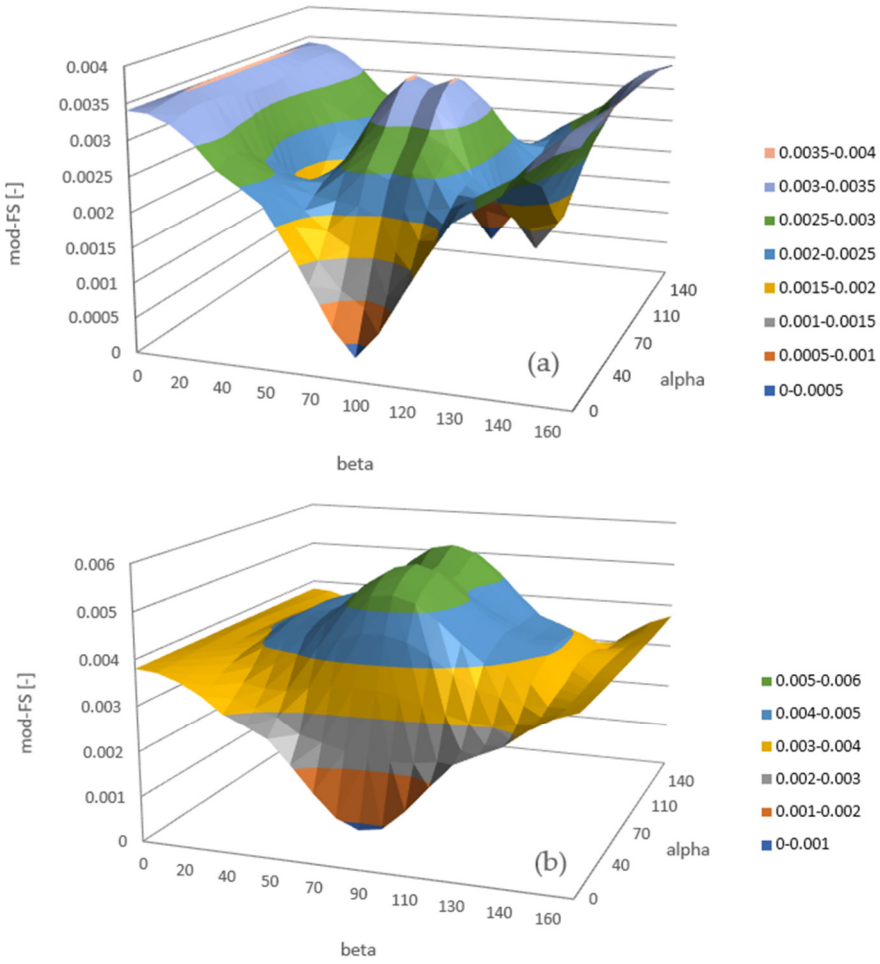

Figure 7.15 Damage vs. slip plane characteristic angles (alpha and beta) in a three-dimensional element for (a) pure torsion (HAZ-T-2) and (b) out-of-phase (HAZ-OP-1) cases.

The three-dimensional surface plots illustrate how the mod-FS damage parameter varies across different slip planes for both loading conditions. The plane characteristic angles represent the two coordinate transformations needed to define the normal vector to the respective plane. The smoother surface observed in the out-of-phase condition indicates a more uniform distribution of damage over a wider range of slip plane orientations compared to the pure torsion condition. From a scientific standpoint, this smoother surface indicates that a larger number of slip plane orientations contribute significantly to the overall damage of the material under out-of-phase loading. This phenomenon can be attributed to the fact that the out-of-phase loading introduces additional complexity to the stress and strain fields within the material, leading to a more heterogeneous distribution of damage across different slip planes. Therefore, the methodology proposed in Section 4.5.1.1, which is based on an integral approach, was implemented here in a three-dimensional sense.

Figure 7.16 presents the fatigue life predictions for the out-of-phase test data obtained through the integral approach in comparison with the pure mod-FS critical plane approach. It is noteworthy that the predictions are improved, especially in the HCF regime. The observed improvements in fatigue life predictions using the combined mod-FS approach with the integral approach, underscore the effectiveness of the proposed method in capturing the complexities of fatigue behavior under non-proportional loading conditions. By simultaneously considering the critical plane orientation and the multiaxial stress states, as well as the collective effect of damage occurring in different orientations, the combination of the mod-FS method with the proposed integral approach provides a scientifically robust method for fatigue life estimation.

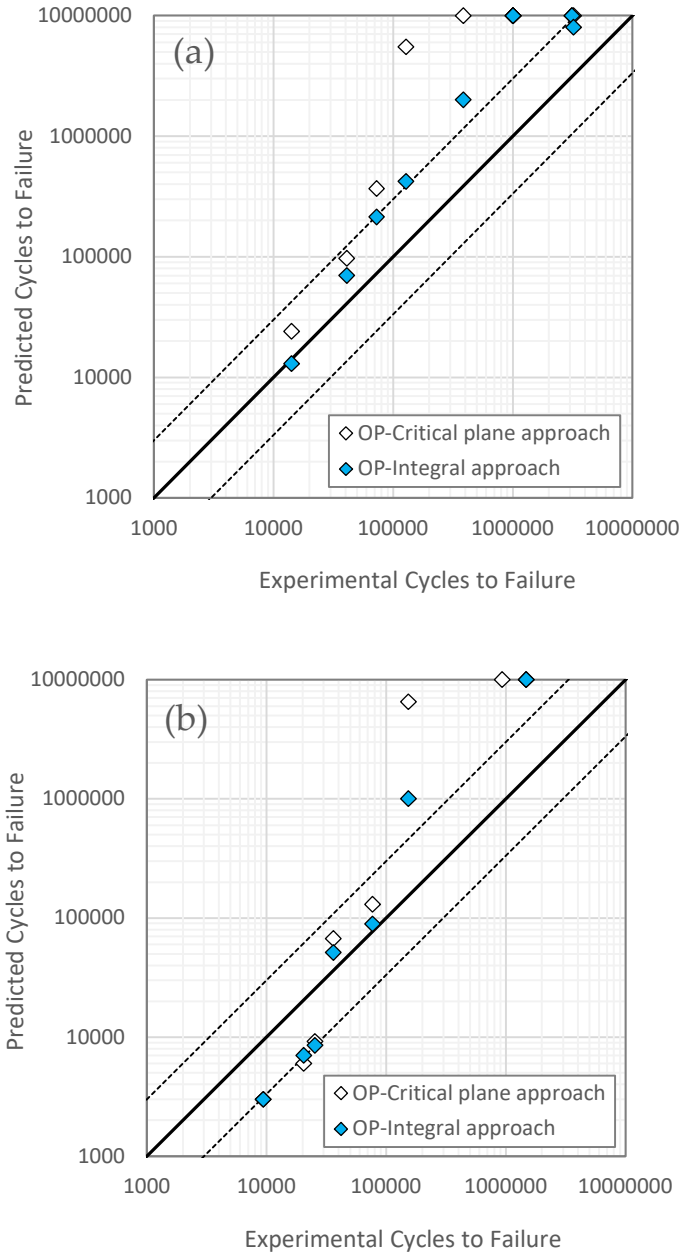

Figure 7.16 Experimental vs. predicted cycles to failure for the out-of-phase (OP) fatigue data of (a) HT and (b) AW specimens using the critical plane approach and the integral approach based on the mod-FS model.

7.9 Fatigue Analysis Considering Transient Cyclic Material Behavior

As shown in Figure 4.16 and Figure 4.17, both material states in this study, namely the BM and HAZ, exhibited cyclic transient softening below a certain equivalent strain range of 1% in both axial and torsion tests. However, the standard notch strain concept assumes that the stress-strain behavior of the material remains constant despite potential variations over the course of fatigue life.

Assuming a strain-controlled stress-strain path at the notch, transient softening behavior entails a gradual reduction of peak stress over fatigue life. For AW specimens in particular, this effect can lead to a gradual redistribution of welding residual stresses over several cycles. Typically, residual stress relaxation is most pronounced in the initial cycles, and material plasticity models are often calibrated based on this early behavior, under the assumption that it saturates quickly. This assumption generally holds for a broad range of metallic materials, where transient behavior in the initial cycles is negligible compared to overall fatigue life. However, for the materials studied here e.g., BM and HAZ, material behavior does not saturate until after a significant number of cycles, thus cannot be disregarded. For such materials, hysteresis shapes during LCF tests at specific strain ranges undergo significant changes with cycle number, indicating cyclic softening behavior.

One approach to account for the transient softening effect is to incorporate it through the cyclic hardening/softening term in the material's plasticity model. However, a major drawback of this method is the significant time and cost required to perform stress-strain analyses over numerous load cycles, which can be impractical. Alternatively, the transient softening effect can be directly integrated into damage calculations. In this context, a specific solution was implemented using a varying cyclic stress-strain curve (CSSC) as proposed by Kühne et al. [159]. This concept assumes that each load cycle induces unique damage to the material, that differs in magnitude from others. Consequently, a single, consistent damage parameter cannot be calculated for a specific test. With regard to the FS damage parameter, it can be assumed that the shear strain amplitude term of the FS model remains constant, as the state at the notch is likely to be strain-controlled. The only component of the FS damage parameter that varies with cycles due to transient softening is the normal

stress term. Given the specific local strain range, the cycle-dependent maximum stress component normal to the respective plane can be determined using the varying CSSC. To achieve this, the Python script for calculating the FS damage parameter was modified by adjusting the local stress and strain matrices derived from the FE results. In this context, the strain matrix was kept unchanged, while the normal and shear stress components of the stress matrix were updated using the damage-dependent Ramberg-Osgood formulae. After updating the peak stress values for each cycle, the damage contribution of the individual cycles can be determined. Consequently, the cumulative total damage, D, is calculated as the sum of the damage contributions of all cycles:

$$D = \sum_{i=1}^{N} \frac{1}{N_{f,i}} \tag{7-4}$$

where $\frac{1}{N_{f,i}}$ represents the contribution of the i-th cycle to the total damage, and $N_{f,i}$ values are determined according to the FS damage-life baseline. The cumulative damage D increases with each cycle, and once it reaches a value of one, the summation loop for damage accumulation ends. The corresponding N value at this point represents the total fatigue life of the material. To reduce calculation time, the damage assessment using the varying CSSC was performed only for specific elements within the area prone to cracking, rather than for the entire model. This approach is intended to enhance efficiency without compromising accuracy.

The flowchart in Figure 7.17 outlines the mentioned procedure for incorporating transient softening into damage calculations and lifetime predictions. To establish the damage-dependent CSSCs, LCF tests were conducted, during which the peaks of the hysteresis loops were recorded until final failure. This provided insight into the evolution of maximum stress throughout the material's lifespan. By plotting the peaks of symmetric hysteresis loops against the number of cycles, cyclic stress-strain curves as a function of damage can be derived. However, the limited number of LCF tests in this project, while adequate for establishing fatigue baselines, somewhat constrained the generation of damage-dependent CSSCs. Conducting additional tests would significantly improve the quality of the fit for this specific application.

The fitted CSSCs for the HAZ, corresponding to different levels of damage, are shown in Figure 7.18. For simplicity, the Ramberg-Osgood parameter K' was kept constant across all CSSCs, while the parameter n' was treated as variable. In addition to the

cycle (damage)-dependent CSSCs, the evolution of the n' parameter as a function of damage is also depicted in Figure 7.18. A polynomial fit was applied to express the variation of n' as a function of damage, making it suitable for implementation in the Python script. A similar procedure was used to generate the damage-dependent shear CSSCs, which were subsequently employed to calculate the damage-dependent shear stresses. As already known from Section 3.7.1.2, the torsional LCF tests were only available in torque-controlled mode.

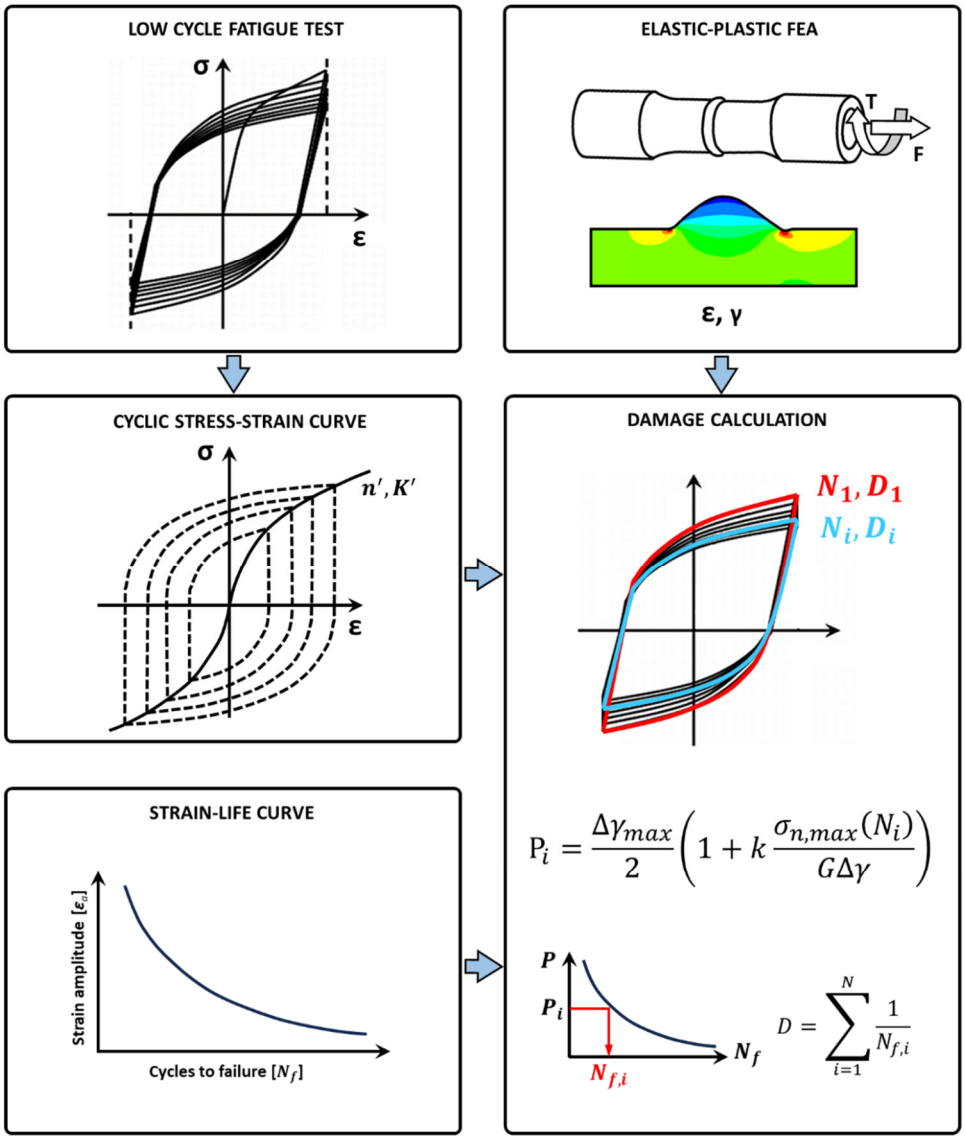

Figure 7.17 Schematic illustration of cycle-dependent damage calculation based on the concept of varying cyclic stress-strain curve.

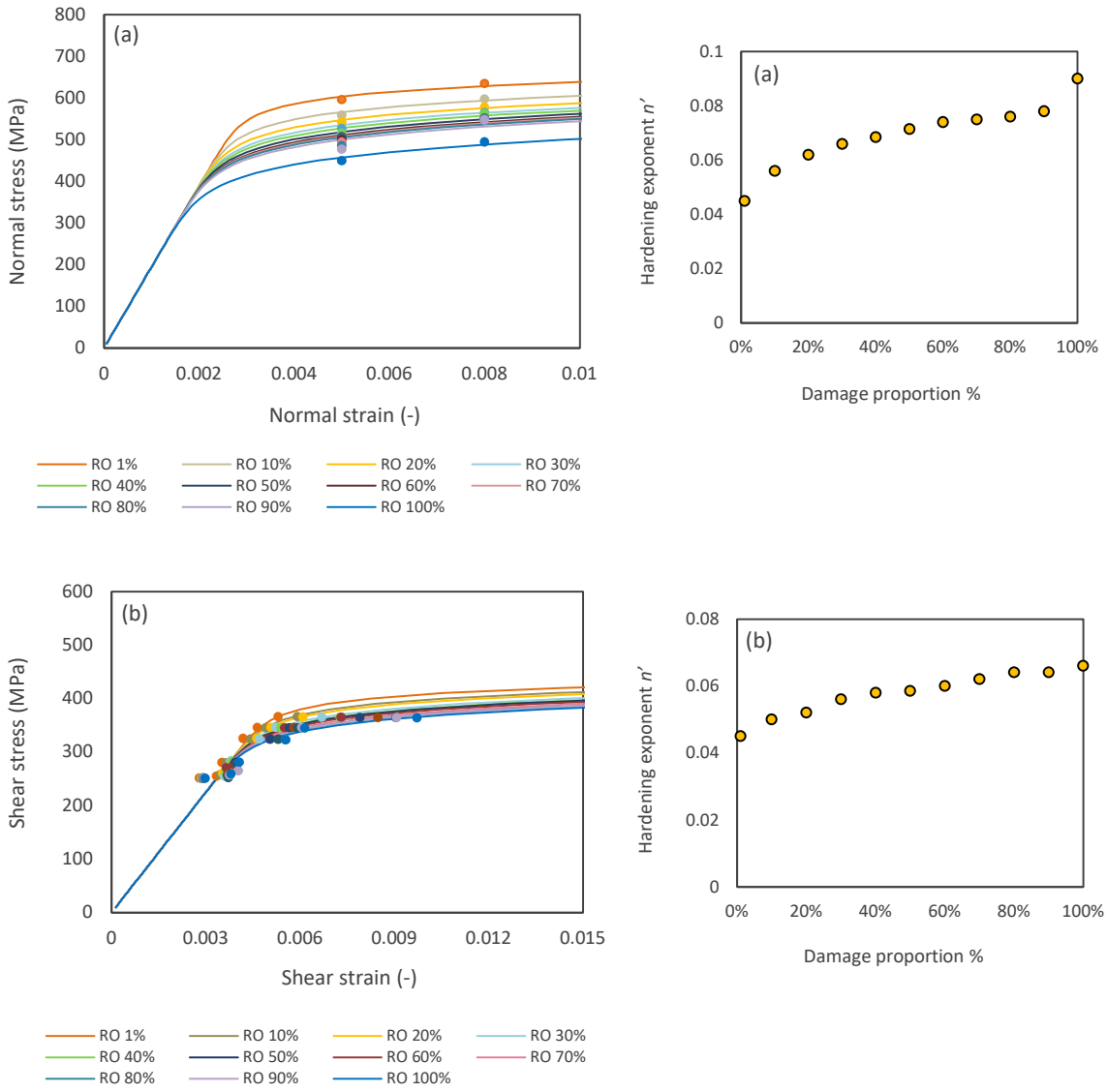

Figure 7.18 Evolution of the cyclic stress-strain curve (CSSC) and hardening exponent n' over the course of the (a) pure axial strain-controlled and (b) pure torsion torque-controlled cyclic loads (RO stands for the Ramberg-Osgood fit where K' assumed to be constant).

Based on the presented methodology, fatigue life estimates were re-evaluated using the mod-FS damage parameter for a subset of HT tests, including an axial test (HT-A-7), a pure torsion test (HT-T-11) and two in-phase tests (HT-IP-22, HT-IP-28) to account for cyclic softening effects. As can be seen in Table 7.2, the varying CSSC

method effectively incorporates the influence of cyclic softening into the fatigue life predictions and shows promising agreement with the expected trends.

Table 7.2 Impact of the consideration of transient softening based on the varying cyclic stress-strain curve (CSSC) concept on the results of the fatigue life prediction for the HT samples using the mod-FS approach of the critical plane.

Test ID	Load type	Applied strain amplitude $\bar{\varepsilon}_a$(%)	Improvement factor %
HT-T-11	Torsion	0.34	**15.2**
HT-A-7	Axial	0.37	**15.3**
HT-IP-22	In-phase	0.53	**18.7**
HT-IP-28	In-phase	0.57	**26.4**

7.10 Continuum Approach to Fatigue Crack Initiation and Propagation in Welded Steel Joints

In this section, the continuum-based discrete crack growth approach proposed by Remes et al. [143] was applied for the fatigue life analysis of welded tubes. This approach utilizes cumulative damage models incorporating material hardness and grain size statistics. As reported, fatigue tests and the experimentally determined fatigue crack growth rates have proven the validity of this approach [143]. There are generally two approaches to predicting fatigue life, namely damage mechanics and fracture mechanics. In many modern welding applications, advances in material quality and welding techniques and strict quality control measures have significantly reduced the occurrence of initial cracking. Consequently, the fracture mechanics requirement of having an initial crack is not always met. Alternative approaches are based on the concept of damage mechanics, which can be divided into coupled and uncoupled approaches. In contrast to the coupled damage approaches, the evolution of the stress and strain state at the crack tip as the result of the damage progress is not considered into the damage evaluation by uncoupled approaches however, they are simpler and more costly rather than the coupled techniques while keeping a reasonable accuracy. Therefore, the uncoupled approaches were chosen to be used in the current study by which only the notch geometry in the intact component is to be

considered. Therefore a few effects such as the stress gradient, crack propagation and the damage-induced redistribution of the stress and strain state at the cracked area is neglected. An ideal approach which considers both crack initiation and crack propagation may improve the prediction of fatigue life of the welds. In an attempt by Glinka et al. [162][163] and Wang et al. [164], the continuum-based approaches with uncoupled damage models were extended to the fatigue propagation that provided the fracture mechanics parameters such as the fatigue crack growth rate. With this concept, a finite material volume is considered whose size is equal to the material characteristic length described in Section 7.3. Within this characteristic volume which represents the fatigue damage process zone as a function of material microstructure, the material is assumed to be homogenous. As a result, the mean values of the continuum-based stresses and strains can be considered over this characteristic volume, which also contains the gradient effect. Thus, in addition to fatigue crack initiation, the approach can also predict fatigue crack propagation in the form of incremental crack growth. This means that the damage model is applied in each step of crack growth in the same way as in the previous steps.

7.10.1 Modelling of the Crack Growth

The discrete growth model accounts for incremental fatigue damage, where each growth step corresponds to the material characteristic length a_0, as illustrated in Figure 7.19. Once the density of microcracks within the damage process zone at the weld notch reaches the value required for the microcrack coalescence, a short macrocrack forms. Before this stage, the material at the notch is treated as intact and crack-free. Another zone of damage forms at the tip of this macrocrack and the growth process continues in the next stage. This process can be described as crack growth being replaced by multiple crack initiations. At each step the number of cycles needed for the formation of a crack with a length of a_0 is determined using the mod-FS parameter and utilizing the respective fatigue life baselines given in Section 4.5.1. To summarize, after the fracture of the first fatigue process zone, the fatigue crack grows stepwise with the a_0 crack length increments.

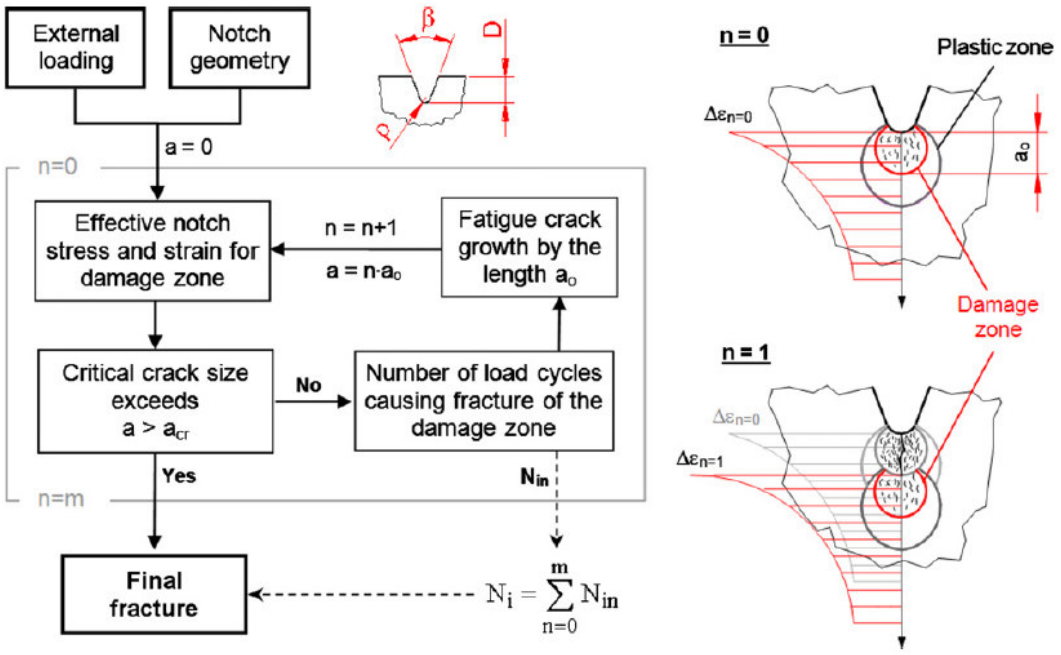

Figure 7.19 Flowchart of incremental fatigue crack growth approach [143].

7.10.2 Microstructure Homogenization and Material Characteristic Length

Under fatigue loading, microscopic cracks form within the grains due to the movement of dislocations and the consequent formation of slip bands [165]. Since the size, form, and distribution of the grains are not uniform, and the location/orientation of the grains is random, considering the mechanics of the single grains in fatigue evaluations may not necessarily be helpful. Instead, the collective effects of the grains on the behavior of the material continuum need to be considered. This procedure, which is called homogenization, is done based on the lowest strength concept. On this basis, the stress or strain gradient within a single grain is considered uniform, leading to fatigue strength being independent of the stress or strain gradient.

In this context, the Hall-Petch relationship [166][167] correlates the lowest strength to the largest grain size. Consequently, the minimum length for averaging stress or strain can be defined by the maximum grain size. The homogenization unit length is thus determined based on the upper bound of the grain size distribution, ensuring a uniform distribution even for smaller grains. Therefore, the material characteristic

length, a_0, is used as the homogenization length, considering the statistical variation in grain size. The averaging of stress and strain distribution over the material characteristic length was carried out using the Line Method [168][169]. The averaged stress, referred to as the effective stress, σ_e, is then calculated as follows:

$$\sigma_e = \frac{1}{a_0} \cdot \int_0^{a_0} \sigma \, dy \tag{7-5}$$

and the effective strain ε_e is calculated from this stress. The grain-based homogenization procedure is schematically shown in Figure 7.20.

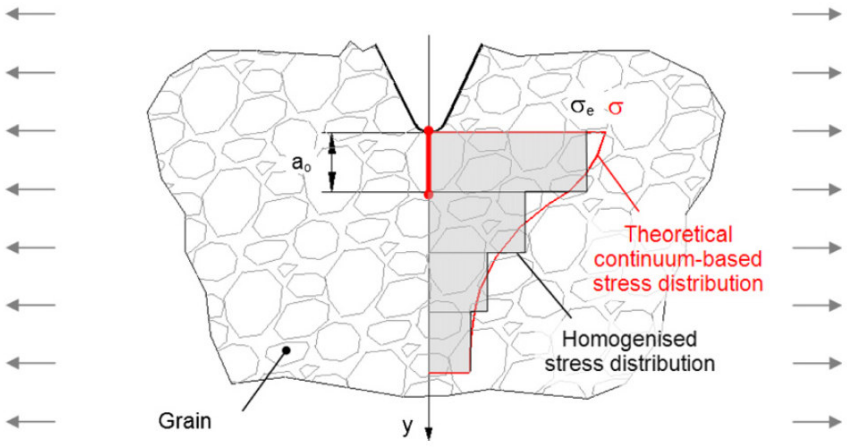

Figure 7.20 Grain-based homogenization of a theoretical stress distribution [143].

7.10.3 Results and Discussion

The fatigue lives of the pure axial tests for both HT and AW predicted by the incremental crack growth in conjunction with critical plane approach and the microstructural characteristics of HAZ are in good agreement with the experimental lifetime values as given in Figure 7.21. With this method the accuracy of the predictions of pure axial tests (except runouts) improved by 43% for HT and by 28% for AW. It appears that this microstructure-based approach to damage mechanics based on grain size statistics can predict both the lifetime of crack initiation and propagation and the orientation of crack growth without the need for fracture mechanics. However, no experimental evidence currently supports the accuracy of the predicted crack orientation in this study. In the present approach the criterion for

the size of the damage zone was the statistical 99% upper bound of the measured grain size. The average length of each grain is used as a measure of grain size. The ratio between the upper bound grain size to the average grain size for the HAZ is significantly higher than that of the BM.

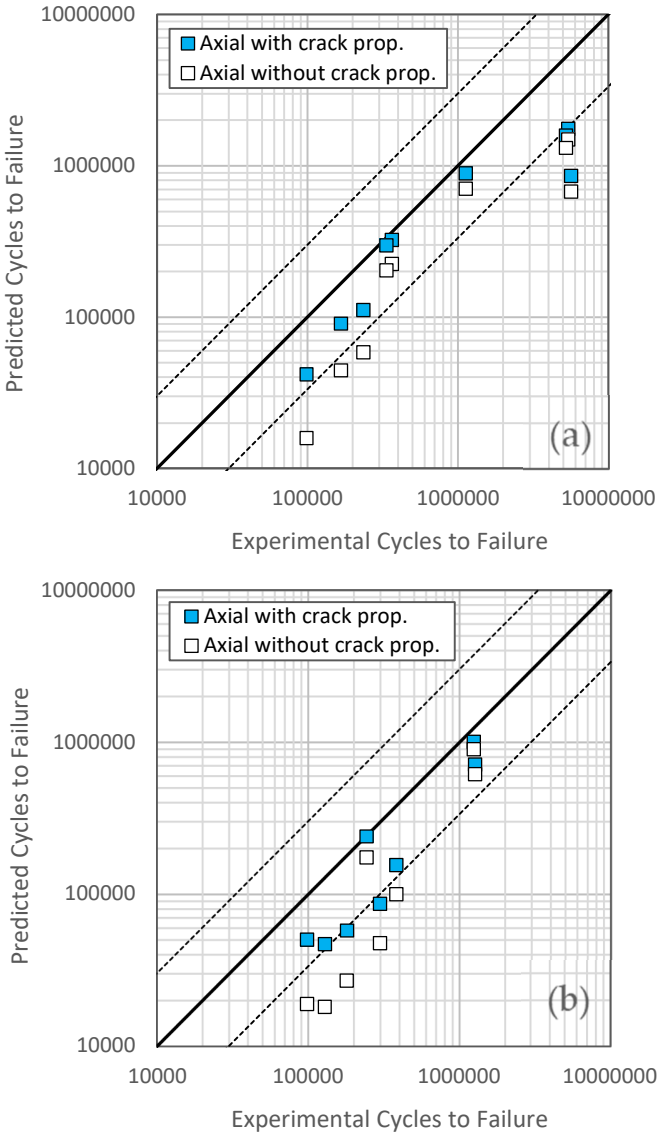

Figure 7.21 Experimental vs. predicted cycles to failure for the axial fatigue data of (a) HT and (b) AW specimens with and without crack propagation life based on mod-FS critical plane approach.

7.11 Summary and Conclusions

The accurate prediction of fatigue life for welds can be influenced by a multitude of factors. Neglecting any of these factors may lead to significant uncertainties in the predictions, especially under complex multiaxial loading conditions. These parameters include the notch effect and the effect of stress/strain gradient, load non-proportionality effect, weld-induced microstructural transformations, welding residual stresses and transient softening effect. Fatigue failure typically occurs when a crack grows to a critical length, with crack propagation constituting a non-negligible portion of the material's total fatigue life. However, depending on material properties, specimen geometry, and load type, crack initiation can account for a substantial or even dominant portion of the total fatigue life. Therefore, to accurately assess the fatigue life of a component, it is crucial to consider both crack initiation and propagation.

Although the fatigue life calculation method for the welds requires several different steps, the most basic aspect of any fatigue life study is to link the variation of stresses and strains to the fatigue damage that occurs within a material. Accurately predicting fatigue damage under multiaxial stress states is crucial, given the extensive use of engineering components subjected to such complex loading conditions. As a result, this chapter focused on determining the ability to correctly predict fatigue damage under a range of constant amplitude loading conditions from the best known conventional and advanced multiaxial fatigue life prediction methodologies. Evaluations were conducted using the equivalent stress/strain approach and critical plane-based damage parameters. The results were then compared to the experimental fatigue life data of heat-treated (HT) and as-welded (AW) specimens. Furthermore, complementary analyses were either conducted or developed to investigate the aforementioned influencing factors, including load non-proportionality, weld-induced microstructure, welding residual stresses, transient softening, and the proportion of crack growth.

Some key observations and findings on the analysis results based on the equivalent stress-strain and critical plane approaches can be summarized as follows:

1) Local equivalent stress- and strain-based analyses resulted in decent correlation of weld specimen fatigue data for all loading conditions except for the non-

proportional loading condition. The results for HT specimens were better than those for AW specimens, which can be attributed to the drawback of such methods to accommodate the residual stress effect in the evaluation.

2) While in some cases, equivalent stress- and strain-based approaches could work well, they lack general robustness. On the other hand, more sophisticated fatigue life analysis methods offer an ability to model different aspects of the fatigue failure process more precisely and under a wide range of loading conditions.

3) Fatigue life predictions based on the FS parameter were found to be more accurate in correlating the fatigue data of weld specimens.

4) Substituting the σ_y term with $G\Delta\gamma$ in the mod-FS parameter slightly improved the correlation of AW data without requiring new material constants for damage calculation. This adjustment also enhanced the correlation of fatigue data for HT specimens.

5) The FE-based methodology applied to account for the effect of welding residual stresses into the multiaxial fatigue assessment of welds, seems to work well. The main aspects of this methodology were the advanced simulation of welding process as well as the application of the advanced critical plane-based parameters. Although the residual stress fields in the AW specimens of the current study were relatively shallow, their influence could still be captured using the current methodology.

6) Welding thermal cycle induced intense microstructural transformations in the material in the weld region and the HAZ. Consideration of realistic transitions when defining the material properties in the FE simulations, along with using accurate fatigue properties of the material where fatigue cracks are likely to form, had a decisive impact on the accuracy of the fatigue life predictions.

7) Though the application of critical plane approach improved the fatigue life predictions under out-of-phase loading condition, however the level of improvement was not satisfactory enough. The proposed so-called integral approach in conjunction with the mod-FS parameter significantly improved the predictions for the out-of-phase fatigue data.

8) For the LCF tests, where local plastic deformation may occur to some extent at the notch, implementing material transient softening through the varying cyclic stress-strain curve (CSSC) led to the enhancement of fatigue life predictions in the

studied cases. The acceptable reliability and practicability of this method distinguish it from the complex method of considering the transient effect in the material constitutive equations.

9) Implementation of the discrete crack growth approach, based on microstructural characteristics, into the FE model effectively accounted for both crack initiation and crack growth in welded specimens. This approach significantly improved fatigue life predictions compared to the experimental results for the examined case study of pure axial loading condition.

Chapter 8 Overall Summary and Additional Research Recommendations

The main objective of this study was to better understand and predict the development of fatigue cracks in the weld notch as a stress concentrator subjected to complex multiaxial loading, with particular emphasis on the effects of weld-induced microstructural transformations and welding residual stresses on the fatigue performance of welds. Due to the variety of influencing parameters in welds, it is sometimes challenging to distinguish between different effects individually. The focus was on integrating various modeling approaches into a unified fatigue life analysis procedure that can be applied to each component of the fatigue failure process under general conditions. In this regard, the main focal points included understanding and modelling material deformation behavior, quantifying fatigue damage, notch effects, load non-proportionality effect, weld-induced microstructure transformation, welding residual stresses and transient softening effect. Besides crack initiation, crack propagation can also account for a significant proportion of the overall fatigue life, depending on the material properties and loading type. Therefore, neglecting crack propagation, especially when final fracture is used as the criterion for determining experimental lifetime, can increase uncertainties in the accuracy of fatigue damage quantification methodologies. With this background, part of the present work was dedicated to the crack growth behavior under multiaxial loading in the framework of a continuum-based discrete crack growth approach.

Experimental data and observations collected from material deformation and fatigue tests were used along with advanced computational techniques to gain insight into the damage mechanisms operating in a welded material under a specific set of loading

conditions. This allowed for testing and/or proposing different life prediction methods based on the real physics of fatigue failure.

The following sections summarize the key findings of this work concerning material deformation (Section 8.1), the formation, evolution, and relaxation of welding residual stresses (Section 8.2), and the processes of crack initiation and growth in fatigue failure (Section 8.3). Additionally, Section 8.4 discusses potential areas for future research to improve the accuracy and reliability of fatigue life analysis methods.

8.1 Summary of Cyclic Material Deformation Aspects

This study examined the cyclic plasticity behavior of constructional steel S355J2H under multiaxial loading conditions. With a focus on fatigue assessment of welded joints, both the base material (BM) and heat affected zone (HAZ) were analyzed. Isotropic and kinematic hardening parameters were primarily calibrated using experimental data from uniaxial tests. Nadai's solution [129] was employed to determine the true shear stress-strain curve and was successfully applied to cyclic torsion test data from both solid and tubular specimens. This method proves to be effective not only for pure torsion loading but also for complex multiaxial loading conditions, including both proportional and non-proportional cases.

The calibrated model proved to be well suited to predict the material behavior under uniaxial and proportional multiaxial loading. However, a common problem was observed in most of the tests: The model tended to underestimate the peak stress at lower equivalent strain amplitudes, in particular by 0.25% for the BM and 0.3% for the HAZ.

Tanaka's non-proportionality parameter [57], which uses constitutive internal variables, was also evaluated. Non-proportional hardening effects were integrated into a modified isotropic hardening model. The calibrated model incorporating the non-proportional hardening effects showed improved accuracy in predicting experimental hysteresis loops under non-proportional loading paths. However, for the HAZ, the model's predictions of the hysteresis loop shape were less accurate, particularly in overestimating the transition stress between the elastic and plastic regions for both axial and torsional loading scenarios.

Experimental results from LCF tests across various loading cases were analyzed to understand the transient cyclic behavior of the materials studied. For the BM, transient softening stabilizes after a certain number of cycles, which depends on the strain amplitude. In contrast, the HAZ exhibits transient softening until final failure. Similar cyclic softening effects were observed in torsional and proportional axial-torsional tests with comparable equivalent strain amplitudes, even under stress-controlled conditions. The transient softening effect is less pronounced under non-proportional load paths, likely due to the counteraction between cyclic softening and non-proportional hardening effects. These findings indicate that the transient softening behavior of BM and HAZ is significant for uniaxial and proportional loading conditions and must be included in the isotropic hardening law. This incorporation requires extensive calibration, suggesting a need for an additional testing program tailored to the material model.

8.2 Summary of Welding Residual Stress Formation and Relaxation

Numerical study of welding residual stresses was comprehensively carried out. X-ray and neutron diffraction measurements were used to experimentally validate the surface and depth profiles of computed residual stresses in the axial and hoop directions. Comparing the computational outcomes with the experimental one the overall agreement was found to be good except for some inconsistencies in the results of surface and subsurface stresses over the weld region. This problem was analyzed in detail by monitoring the most important aspects of the simulation process. In thermal-metallurgical solution the reliability of the output including temperature history and material solid state phase fractions was calibrated experimentally. In this respect, during weld fabrication, temperature data were collected using a variety of thermocouples placed in the heat affected region at every 90 degrees of the weld direction and very near to the weld toe. Since S355J2H construction steel undergoes metallurgical phase transformations during thermal cycles, both the maximum temperature and the cooling rate are critical factors. It was also found that the predicted weld fusion boundary aligns well with the macrograph images of the weld cross-section. The corresponding cooling curves in the weld-CCT diagram were used to define the formation of different phases based on the respective $t_{8/5}$, and then the

accuracy was monitored through metallographic observations of the resulting phases. Mechanical simulation is linked to thermal simulation through thermal expansions or contractions, as well as mechanical properties that vary with temperature and phase fraction. The accuracy of predicted residual stresses (or strains) depends not only on the precision of the defined temperature- and phase-dependent material properties but also on the simulation procedures and assumptions. In this regard, two important transformation-dependent variables that must be considered are strain hardening recovery during transformation and transformation plasticity. The suitability of the applied material strain hardening model, the reliability of the predicted high temperature annealing behavior, the effects of microstructural transformations on the evolution of residual stresses and the phenomenon of strain hardening recovery during transformation were the main factors discussed in this study. In the context of material constitutive modeling, the isotropic strain hardening model proved to be suitable for estimating the welding residual stresses. Given the significant isotropic component of strain hardening in S355J2H steel, this model provided a reasonable approximation of the monotonic and cyclic material responses compared to kinematic or combined strain hardening models, as evidenced by the LCF test results.

The high compressive residual stress field at the weld toe and its vicinity resulted from the effect of low temperature phase transformations, which is beneficial concerning fatigue performance. A sharp gradient in the welding residual stress profile from the surface towards the material bulk was detected by combining the measurement results from x-ray and neutron diffraction over the very thin top layer on the surface. This finding presents a challenge for achieving an accurate match between FE simulations and experimental results.

The relaxation behavior of welding residual stresses under uniaxial and multiaxial loading conditions was numerically analyzed using FE method. Compared to the measurements, the calculation results showed that the FE approach can effectively predict the relaxation behavior of the welding residual stresses under such conditions. The mechanisms of residual stress relaxation depend on the characteristics of the material. Therefore, using an appropriate constitutive model with accurate material properties in FE simulations can significantly improve the validity of the predictions. The nonlinear isotropic hardening model combined with von Mises yield criterion proved effective in capturing the relaxation phenomenon of residual stresses.

8.3 Summary of Fatigue Crack Initiation & Growth Aspects

After examining the material deformation behavior, the focus was on investigating fatigue behavior under constant amplitude loads. Initially, smooth specimen tests were conducted under pure axial and pure torsion loadings to establish fatigue baselines, including both stress-life and strain-life curves. These curves formed the basis for all subsequent fatigue life predictions. Additional tests were also conducted under in-phase and 90° out-of-phase loading conditions.

The shear-based FS parameter effectively correlated all multiaxial fatigue data, achieving up to 55% of fatigue life predictions within a factor of ±3 of the experimental results. An improved version of the parameter, which replaces yield strength on the maximum shear plane with the shear stress range (expressed as $G\Delta\gamma$), was utilized to better account for the effect of residual stresses. This modified FS parameter resulted in a slight enhancement in the correlation of fatigue data for both HT and AW specimens. Nevertheless, it was shown that the strain-based critical plane approach, which includes a term for the maximum normal stress, such as the FS or mod-FS parameters, can account reasonably well for the effects of welding residual stresses in the quantification of fatigue damage.

In the fatigue evaluations, neglecting the deformation and fatigue properties specific to the HAZ, where cracks are more likely to initiate due to the weld notch acting as a stress concentrator, can lead to significant errors in lifetime predictions. The material microstructure in the HAZ changes dramatically due to the intense thermal cycles imposed by the welding process, which affects its deformation and fatigue behavior.

To account for the stress/strain gradient effect at the notch, a microstructure-based method was applied to determine the characteristic length of the material structure at the crack initiation site. The characteristic length, obtained from grain size statistics, was used in conjunction with the theory of critical distance (TCD) to enhance the accuracy of fatigue predictions. Specifically, a critical distance of L=0.01 was employed in the TCD point method to better account for the effects of stress and strain gradients on crack initiation.

Life predictions based on the assumption of a stable material stress-strain response were found to be conservative for pure axial and in-phase load cases, but slightly non-

conservative for pure torsion cases when using the mod-FS parameter. Applying the varying cyclic stress-strain curve (CSSC), which incorporates a time-dependent evaluation of the FS parameter to account for transient softening, improved the accuracy of predictions across all studied cases. This method provides reliable results while being less complex than developing a detailed constitutive model to account for transient softening effects. Additionally, due to time and cost constraints, it is often impractical to simulate many cycles involving plastic deformation in the FE model.

Overall, the mod-FS parameter provided slightly more accurate fatigue life predictions for the weld specimens compared to the original parameter. However, the improvement for out-of-phase load cases was not sufficient. Even with the mod-FS model, predictions for out-of-phase conditions remained too non-conservative, especially at lower loads. The proposed integral approach significantly enhanced the prediction accuracy. This integral approach correlated the out-of-phase fatigue data of smooth specimens for both BM and HAZ with uniaxial and in-phase fatigue data more effectively than the critical plane models.

Life predictions for axial and combined axial-torsion loading conditions were consistently more conservative compared to those for pure torsion loading. This led to a less accurate correlation with the experimental fatigue data. This discrepancy can be attributed to the larger proportion of crack propagation in the experimentally determined total life under pure axial and combined axial-torsion loading conditions, due to the more pronounced stress gradient effect at the weld notch. In contrast, for pure torsion loading, the damage profile at the notch is more uniform, resulting in crack propagation contributing less significantly to the overall fatigue life.

To account for both crack initiation and crack growth in the fatigue life assessment of welded specimens, a discrete crack growth method was utilized, employing a strain-based approach that captures the continuum nature of material behavior. Grain size statistics were used to identify the largest grain size, which served as the basis for determining the material volume relevant to the damage process and the averaging length for stress and strain. The number of cycles required for the progression of fatigue damage and crack growth was estimated using the material's fatigue baseline and the mod-FS damage parameter. This method incorporates cumulative damage models with incremental growth steps. The approach was implemented in the FE analyses and validated through experimental case studies. The results indicated that

the method can accurately model crack initiation and growth in welded specimens, considering the effects of microstructure. The predicted fatigue lives were in good agreement with the experimental results.

8.4 Additional Research Recommendations

The analyses and discussions in this study have highlighted several areas where the implemented fatigue life prediction methods can be improved.

In the context of non-proportional hardening in the HAZ, the predicted hysteresis loop shapes were less accurate for both axial and torsional loops, with the simulation overestimating the transition stress between the elastic and plastic slopes. This shows that the model for the HAZ needs to be optimized and further developed. Integrating the non-proportionality parameter into evolution equations for kinematic hardening parameters could enhance the accuracy of the model.

Constitutive modelling remains challenging even for mass-produced steel, especially in complex situations such as weld seams. Developing multiscale material models that incorporate microscale physical mechanisms and link them to macroscopic properties could significantly progress the field. The integration of extensive experimental data with machine learning algorithms has the potential to revolutionize traditional constitutive material modelling in the coming years.

In the framework of accurate welding simulation, the non-negligible differences in the measured and calculated residual stress on the surface and subsurface result in the welding area need to be investigated in the sense of a specific subject, particularly for those materials that sustain metallurgical phase transformations.

In the context of discrete fatigue crack growth, determining the actual strain within the damage zone and capturing short crack propagation are not feasible with current approaches, which mainly address large stress and strain gradients. Crystal plasticity-based analyses could provide a more detailed understanding of these factors in weld materials. Additionally, crystal plasticity modeling offers the potential advantage of capturing a more realistic residual stress relaxation driven by micro-mechanisms during cyclic loading.

To improve the accuracy of fatigue life prediction for welds made of construction steel under uniaxial and multiaxial loading, it is recommended to simultaneously

incorporate the combined effects of transient softening, crack propagation, and non-proportionality (in the case of non-proportional loading). As a case study in the present work, the absolute percentage error in fatigue life prediction for a heat-treated specimen under axial loading (HT-A-7) decreases by 45% when both transient softening and the concept of incremental crack growth are included in the fatigue life assessment. While considering all these aspects requires more evaluation time, the significant improvement in fatigue life prediction justifies this effort.

Last but not least, the current study was carried out under constant amplitude loading conditions, so that the influence of load sequence was excluded. Therefore, the methodology used should be extended to model variable amplitude loads to better reflect real conditions. However, it should be taken into account that regular load profiles with variable amplitude are not frequently encountered in practice. Therefore, for a more realistic analysis, multiaxial variable amplitude load profiles extracted from real operational conditions are required. For this purpose, variable amplitude fatigue tests must be performed based on axial, torsional and combined axial and torsional loading conditions that reflect the recorded operating loads.

References

[1] R6, Assessment of the Integrity of Structures Containing Defects, Br. Energy, Revision 4, 2013.

[2] Goldak J., Web Based Simulation of Welding and Welded Structures, CWA Conference, 2013.

[3] Erker A., Dehnungsmessungen an geschweißten Bauteilen, Schweißen u. Schneiden, Jahrgang 6, Heft 2, pp. 66-69, 1954.

[4] Erker A., Einfluß der Eigenspannungen und des Werkstoffzustandes und die Betriebssicherheit, Schweißen u. Schneiden, Jahrgang 8, Heft 11, pp. 436-442, 1956.

[5] Kunz H. G., Eigenspannungen, Verwerfungen und Maßhaltigkeit beim Schweißen, Schweißen u. Schneiden, Jahrgang 11, pp. 84-92, 1959.

[6] Koch H., Beitrag zur Ermittlung der Schweißeigenspannungen in Schmelzgeschweißten Stumpfnähten (Auffederungsmethode), Schweißen u. Schneiden, Jahrgang 18, pp. 263-268, 1966.

[7] Bratt J. F., Berme N., Residual Stresses and Strain Energy in Butt Welds, Brit. Weld. J, vol. 13, pp. 707-710, 1966.

[8] Leblond J. B., Mottet G., Devaux C. J., A Theoretical und Numerical Approach to the Plastic Behaviour of Steels During Phase Transformations, J. Mech. Phys. Solids, vol. 34, pp. 395-409, 1986.

[9] Joens W. K. C., Alberry P. J., Ferritic Steels for Fast Reactor Steam Generators, Br. Nucl. Eng. Soc., pp. 1-4, 1977.

[10] Joens W. K. C., Alberry P. J., Residual Stresses in Welded Constructions, Weld. Inst., Cambridge, 1977.

[11] Leblond J. B., Mathematical Modelling of Transformation Plasticity in Steels II: Coupling with Strain Hardening Phenomena, Int. J. Plast. Vol. 5, pp. 573–591, 1989.

[12] Wohlfahrt H., Die Bedeutung der Austenitumwandlung für die Eigenspannungsentstehung beim Schweißen, Härterei-Technische-Mitteilung, vol. 41, pp. 248-257, 1986.

[13] Hauk V., Structural and Residual Stress Analysis by Non-Destructive Methods, Elsevier, 1997.

[14] Wohlfahrt H., Schweißeigenspannungen, Härterei-Technische-Mitteilungen, Jahrgang 31, pp. 56-71, 1976.

[15] Noyan I. C., Cohen J. B., Residual Stress Measurements by Diffraction and Interpretation, Mater. Res. Eng., Springer-Verlag, 1987.

[16] Goldak J., Chakravarti A., Bibby M., A New Finite Element Model for Welding Heat Sources, Metall. Trans. B. vol. 15, pp. 299-305. 1984.

[17] Leblond J. B., Devaux J., A New Kinetic Model for An-Isothermal Metallurgical Transformations in Steels Including the Effect of Austenite Grain Size, Acta Metall., vol. 32, pp. 137-146, 1984.

[18] Koistinen D. P., Marburger R. E., A General Equation Prescribing the Extent of the Austenite-Martensite Transformation in Pure Fe-C Alloys and Plain Carbon Steels, Acta Metall., vol. 7, pp. 59-60, 1959.

[19] Seyffarth P., Meyer B., Scharff A., Großer Atlas Schweiß-ZTU-Schaubilder, Deutscher Verlag für Schweißtechnik, DVS-Verlag, 1992.

[20] SYSWELD, Reference Manual, ESI Group, 2011.

[21] Vöhringer O., Wohlfahrt H., Abbau von Eigenspannungen, HTM, Zeitschrift für Wärmebehandlung und Werkstofftechnik, Carl Hanser Verlag, pp. 144-156.

[22] Holzapfel H., Schulze V., Vöhringer O., Macherauch E., Residual Stress Relaxation in an AISI 4140 Steel Due to Quasistatic and Cyclic Loading at Higher Temperatures, Mater. Sci. Eng. A, vol. 248, pp. 9-18, 1998.

[23] Morrow J., Ross A. S., Sinclair G. M., Relaxation of Residual Stresses Due to Fatigue Loading, SAE Trans., vol. 68, pp. 40-48, 1960.

[24] McClung R. C., A Literature Survey on the Stability and Significance of Residual Stresses During Fatigue, Fatigue Fract. Eng. Mater. Struct., vol. 30, pp. 173-205, 2007.

[25] Zaroog O. S., Aidy A., Sahari B. B., Zahari R., Modeling of Residual Stress Relaxation: A Review, J. Sci. Technol., vol. 17, pp. 211-218, 2009.

[26] Walker C. A., Waddell A. J., Johnston D. J., Vibratory Stress Relief: An Investigation of the Underlying Processes, Proc. Inst. Mech. Eng., vol. 209, pp. 51-58, 1995.

[27] James M. R., Relaxation of Residual Stresses: An Overview, Advances in Surface Treatments: Technology, Applications, and Effects, Pergamon Press, pp. 349-65, 1987.

[28] Farajian M., Stability and Relaxation of Welding Residual Stresses, PhD Diss., Shaker Verlag, 2011.
[29] Xie X. F., Jiang W., Luo Y., Xu S., Gong J. M., Tu S. T., A Model to Predict the Relaxation of Weld Residual Stress by Cyclic Load: Experimental and Finite Element Modeling, Int. J. Fatigue, vol. 95, pp. 293-301, 2017.
[30] Zhuang W. Z., Halford G. R., Investigation of Residual Stress Relaxation under Cyclic Load, Int. J. Fatigue, vol. 23, pp. 31-37, 2001.
[31] Seungho H., Lee T., Shin B., Residual Stress Relaxation of Welded Steel Components under Cyclic Load, Mater. Technol. (Steel Res.), vol. 73, pp. 414-420, 2002.
[32] Maximov J. T., Duncheva G. V., Mitev I. N., Modeling of Residual Stress Relaxation Around Cold Expanded Holes in Carbon Steel, J. Constr. Steel Res., vol. 65, pp. 909-17, 2009.
[33] Morrow J., Sinclair G. M., Cycle-Dependent Stress Relaxation, Symposium on Basic Mechanisms of Fatigue, ASTM STP237, Am. Soc. Test. Mater., 1958.
[34] Kodama S., The Behavior of Residual Stress During Fatigue Stress Cycles, Proc. Int. Conf. Mech. Behav. Metals II, Soc. Mater. Sci., Kyoto, pp. 111-118, 1972.
[35] Jhansale H. R., Topper T. H., Engineering Analysis of the Inelastic Stress Response of a Structural Metal under Variable Cyclic Strains, Cyclic Stress-Strain Behavior_Analysis, Experimentation, and Failure Prediction, Am. Soc. Test. Mater., pp. 246-270, 1973.
[36] Landgraf R. W., Chernenkoff R. A., Residual Stress Effects on Fatigue of Surface Processed Steels, Analytical and Experimental Methods for Residual Stress Effects in Fatigue (ASTM STP 1004), Am. Soc. Test. Mater., West Conshohocken, pp. 1-12, 1988.
[37] Lindgren M., Lepistö T., Effect of Mean Stress on Residual Stress Relaxation in Steel Specimens, Materials Science and Technology, vol. 18, pp. 845-849, 2002.
[38] Valluri S. R., Some Recent Developments at "GALCIT" concerning a Theory of Metal Fatigue, Acta Metall., vol. 11, pp. 759-775, 1963.
[39] Qian Z., Chumbley L. S., Karakulak T., Johnson E., The Residual Stress Relaxation Behavior of Weldments During Cyclic Loading, Metall. Mater. Trans., vol. A 44, pp. 3147-3156, 2013.
[40] Dattoma V., Giorgi M. D., Nobile R., Numerical Evaluation of Residual Stress Relaxation by Cyclic Load, J. Strain Anal. Eng., vol. 39, pp. 663-672, 2004.
[41] Lee C. H., Chang K. H., Van Do V. N., Finite Element Modeling of Residual Stress Relaxation in Steel Butt Welds under Cyclic Loading, Eng. Struct., vol. 103, pp. 63-71, 2015.
[42] Cho J., Lee C. H., FE Analysis of Residual Stress Relaxation in a Girth-Welded Duplex Stainless Steel Pipe under Cyclic Loading, Int. J. Fatigue, vol. 82, pp. 462-473, 2016.
[43] Hill R., A Theory of the Yielding and Plastic Flow of Anisotropic Metals, Proc. Roy. Soc. Lond. A: Math. Phys. Sci., vol. 193, pp. 281-297, 1948.
[44] Drucker D. C., A More Fundamental Approach to Plastic Stress-Strain Relations, Proc. 1st US Natl. Congr. Appl. Mech., pp. 487-491, 1951.
[45] Prager W., Recent Developments in the Mathematical Theory of Plasticity, J. Appl. Phys., vol. 20, pp. 235-241, 1949.
[46] Bauschinger J., Über die Veränderung der Elastizitätsgrenze und der Festigkeit des Eisens und Stahls durch Strecken und Quetschen, durch Erwärmen und Abkühlen und durch oftmals wiederholte Beanspruchung, Mitteilungen des mechanisch-technischen Laboratoriums der Königlich Technischen Hochschule München, vol. 13, 1886.
[47] Armstrong P. J., Frederick C., A Mathematical Representation of the Multiaxial Bauschinger Effect, Cent. Electr. Gen. Bd. & Berkeley Nucl. Lab., vol. 731, 1966.
[48] Chaboche J., Viscoplastic Constitutive Equations for the Description of Cyclic and Anisotropic Behaviour of Metals, Bull. Pol. Acad. Sci., Tech. Sci., vol. 25, pp. 33-41, 1977.
[49] Chaboche J., Dang-Van K., Cordier G., Modelization on the Strain Memory Effect on the Cyclic Hardening of 316 Stainless Steel, In Trans. of the 5th Int. Conf. on SMiRT, vol. 11, 1979.
[50] Chaboche J., Rousselier G., On the Plastic and Viscoplastic Constitutive Equations-Part 1: Rules Developed with Internal Variable Concept, J. Press. Vessel Technol., vol. 105, pp. 153-158, 1983.

[51] Taira S., Inoue T., Yoshida T., Low-Cycle Fatigue under Multiaxial Thermal Stresses (in the Case of Combined Cyclic-Torsion-Compression and Cyclic Torsion out of Phase at Elevated Temperature), Proc. 11th Japan Congr., Testing and Materials, pp. 60-65, 1968.
[52] Tanaka E., Murakami S., Ooka M., Effects of Plastic Strain Amplitudes on Non-Proportional Cyclic Plasticity, Acta Mech., vol. 57, pp. 167-182, 1985.
[53] Benallal A., Le Gallo P., Marquis D., An Experimental Investigation of Cyclic Hardening of 316 Stainless Steel and of 2024 Aluminium Alloy under Multiaxial Loadings, Nucl. Eng. Des., vol. 114, pp. 345-353, 1989.
[54] Lamba H., Sidebottom O., Cyclic Plasticity for Non-Proportional Paths-Part 1: Cyclic Hardening, Erasure of Memory and Subsequent Strain Hardening Experiments, J. Eng. Mater. Technol., vol. 100, pp. 96-103, 1978.
[55] Kanazawa K., Miller K., Brown M., Cyclic Deformation of 1% Cr-Mo-V Steel under Out-of-Phase Loads, Fatigue Fract. Eng. Mater. Struct., vol. 2, pp. 217-228, 1979.
[56] Doong S. H., Socie D. F., Robertson I. M., Dislocation Substructures and Non-proportional Hardening, J. Eng. Mater. Technol., vol. 112, pp. 456-464, 1990.
[57] Tanaka E., A Non-Proportionality Parameter and a Cyclic Viscoplastic Constitutive Model Taking into Account Amplitude Dependences and Memory Effects of Isotropic Hardening, Euro. J. Mech. A: Solids, vol. 13, pp. 155-173, 1994.
[58] Jiang Y., Kurath P., Non-Proportional Cyclic Deformation: Critical Experiments and Analytical Modeling, Int. J. Plast., vol. 13, pp. 743-763, 1997.
[59] Zhang J., Jiang Y., Constitutive Modeling of Cyclic Plasticity Deformation of a Pure Polycrystalline Copper, Int. J. Plast., vol. 24, pp. 1890-1915, 2008.
[60] Prager W., Recent Developments in the Mathematical Theory of Plasticity, J. Appl. Phys., vol. 20, pp. 235-241, 1949.
[61] Ohno N., A Constitutive Model of Cyclic Plasticity with a Nonhardening Strain Region, J. Appl. Mech., vol. 49, pp. 721-727, 1982.
[62] Neuber H., Theory of Stress Concentration for Shear Strained Prismatic Bodies with Arbitrary Non-Linear Stress-Strain Law, J. Appl. Mech., vol. 28, pp. 544-550, 1961.
[63] Glinka G., Energy Density Approach to Calculation of Inelastic Strain-Stress near Notches and Cracks, Eng. Fract. Mech., vol. 22, pp. 485-508, 1985.
[64] Sharpe W. N., Yang Jr. C. H., Tregoning R. L., An Evaluation of the Neuber and Glinka Relations for Monotonic Loading, J. Appl. Mech, vol. 59, pp. 50-56, 1992.
[65] Hoffmann M., Seeger T., Stress-Strain Analysis and Life Predictions of a Notched Shaft under Multiaxial Loading, in: Leese, G. E., Socie, D. F. (Eds.), Multiaxial Fatigue: Analysis and Experiment, Advances in Engineering Series, AE-14. Soc. Automot. Eng., Inc., Warrendale, PA, pp. 81-99, 1989.
[66] Moftakhar A. A., Buczynski A., Glinka G., Calculation of Elasto-Plastic Strains and Stresses in Notches under Multiaxial Loading, Int. J. Fract., vol. 70, pp. 357-373, 1995.
[67] Barkey M. E., Socie D. F., Hsia K. J., A Yield Surface Approach to the Estimation of Notch Strains for Proportional and Nonproportional Cyclic Loading, J. Eng. Mater. Technol., vol. 116, pp. 173-180, 1994.
[68] Mroz Z., On the Description of Anisotropic Work Hardening, J. Mech. Phys. Solids, vol. 15, pp. 163-175, 1967.
[69] Tipton S. M., Nelson D. V., Advances in Multiaxial Fatigue Life Prediction for Components with Stress Concentrations, Int. J. Fatigue, vol. 19, pp. 503-515, 1997.
[70] Topper T. H., Wetzel R. M., Morrow J. D., Neuber's Rule Applied to Fatigue of Notched Specimens, J. Mater. JMSLA 4, pp. 200-209, 1969.
[71] Neuber H., Kerbspannungslehre. Springer, Berlin, 1958.
[72] Kuhn P., Hardrath H. F., An Engineering Method for Estimating Notch Size Effect in Fatigue, NASA Tech. Note No. 2805, 1952.
[73] Susmel L., The Theory of Critical Distances: A Review of its Applications in Fatigue, Eng. Fract. Mech., vol. 75, pp. 1706-1724. 2008.
[74] Taylor D., The Theory of Critical Distances, Eng. Fract. Mech., vol. 75, pp. 1696-1705, 2008.
[75] Gates N., Fatemi A., Multiaxial Variable Amplitude Fatigue Life Analysis Including Notch Effects, Int. J. Fatigue, vol. 91, pp. 337-351, 2016.

[76] Susmel L., Taylor D., The Theory of Critical Distances to Estimate Lifetime of Notched Components Subjected to Variable Amplitude Uniaxial Fatigue Loading, Int. J. Fatigue, vol. 33, pp. 900-911, 2011.
[77] Susmel L., Taylor D., An Elasto-Plastic Reformulation of the Theory of Critical Distances to Estimate Lifetime of Notched Components Failing in the Low/Medium-Cycle Fatigue Regime, J. Eng. Mater. Technol., vol. 132, Art. 021002, 2010.
[78] Susmel L., Taylor D., A Simplified Approach to Apply the Theory of Critical Distances to Notched Components under Torsional Fatigue Loading, Int. J. Fatigue, vol. 28, pp. 417-430, 2006.
[79] Sonsino C. M., Multiaxial Fatigue of Welded Joints under In-Phase and Out-of-Phase Local Strain and Stresses, Int. J. Fatigue, vol. 17, pp. 55-70, 1995.
[80] Lee Y., Tjhung Tana., Jordan A., A Life Prediction Model for Welded Joints under Multiaxial Variable Amplitude Loading Histories, Int. J. Fatigue, vol. 29, pp. 1162-1173, 2007.
[81] Fatemi A., Socie D. F., Damage Mechanisms and Life Predictions, in: Branco C. M., Rosa L. G. (Eds.), Adv. Fatigue Sci. Technol., E: Appl. Sci., Klumer Academic Publishers, NATO Adv. Stud. Inst., Alvor, Portugal, pp. 877-890, 1989.
[82] Lopez-Crespo P., Moreno B., Lopez-Moreno A., Zapatero J., Study of Crack Orientation and Fatigue Life Prediction in Biaxial Fatigue with Critical Plane Models, Eng. Fract. Mech., vol. 136, pp. 115-130, 2015.
[83] Sonsino C. M., Multiaxial Fatigue of Welded Joints under In-Phase and Out-of-Phase Local Strains and Stresses, Int. J. Fatigue, vol. 17, pp. 55-70, 1995.
[84] Ellyin F., Fatigue Damage, Crack Growth and Life Prediction, Chapman and Hall, London, 1997.
[85] Park J., Nelson D. V., Evaluation of an Energy-Based Approach and a Critical Plane Approach for Predicting Multiaxial Fatigue Life, Int. J. Fatigue, vol. 22, pp. 23-39, 2000.
[86] Fatemi A., Shamsaei N., Multiaxial Fatigue: An Overview and Some Approximation Models for Life Estimation, Int. J. Fatigue, vol. 33, pp. 948-958, 2011.
[87] Socie D. F., Marquis G. B., Multiaxial Fatigue, Soc. Automot. Eng., Inc., Warrendale, PA, 2000.
[88] Esderts A., Betriebsfestigkeit bei mehrachsiger Biege- und Torsionbeanspruchung, PhD Diss., TU Clausthal, 1995.
[89] Socie D. F., Marquis G. B., Multiaxial Fatigue, Soc. Automot. Eng., PA 15096-0001, USA, 2000.
[90] Papadopoulos I., Critical Plane Approaches in High-Cycle Fatigue: On the Definition of the Amplitude and Mean Value of the Shear Stress Acting on the Critical Plane, Fatigue Fract. Eng. Mater. Struct., vol. 21, pp. 269-285, 1998.
[91] Findley W. N., Modified Theory of Fatigue Failure under Combined Stress, Proc. Soc. Exp. Stress Anal., vol. 14, pp. 35-46, 1956.
[92] McDiarmid D. L., A General Criterion for High Cycle Multiaxial Fatigue Failure, Fatigue Fract. Eng. Mater. Struct., vol. 14, pp. 429-453, 1991.
[93] Brown M. W., Miller K. J., A Theory for Fatigue under Multiaxial Stress-Strain Conditions, Proc. Inst. Mech. Eng., vol. 187, pp. 745-756, 1973.
[94] Fatemi A., Socie D. F., A Critical Plane Approach to Multiaxial Fatigue Damage Including Out-of-Phase Loading, Fatigue Fract. Eng. Mater. Struct., vol. 11, pp. 149-165, 1988.
[95] Stephens R. I., Fatemi A., Stephens R. R., Fuchs H. O., Metal Fatigue in Engineering, 2nd ed. Wiley Interscience, 2000.
[96] Socie D. F., Schield T. W., Mean Stress Effects in Biaxial Fatigue of Inconel 718, ASME J. Eng. Mater. Technol., vol. 106, pp. 227-232, 1984.
[97] Kaufman R. P., Topper T., The Influence of Static Mean Stresses Applied Normal to the Maximum Shear Planes in Multiaxial Fatigue, in: Carpinteri A., de Freitas M., Spagnoli A. (Eds.), Biax./Multiax. Fatigue Fract., pp. 123-143, 2003.
[98] Fatemi A., Kurath P., Multiaxial Fatigue Life Predictions under the Influence of Mean Stresses, J. Eng. Mater. Technol., vol. 110, pp. 380-388, 1988.
[99] Smith R. N., Watson P., Topper T. H., A Stress-Strain Parameter for the Fatigue of Metals, J. Mater. JMSLA, vol. 5, pp. 767-778, 1970.
[100] Firat M., A Numerical Analysis of Combined Bending-Torsion Fatigue of SAE Notched Shaft, Finite Elem. Anal. Des., vol. 54, pp. 16-27, 2012.

[101] Gao Z., Qiu B., Wang X., Jiang Y., An Investigation of Fatigue of a Notched Member, Int. J. Fatigue, vol. 32, pp. 1960-1969, 2010.
[102] Kujawski D., A Deviatoric Version of the SWT Parameter, Int. J. Fatigue, vol. 67, pp. 95-102, 2014.
[103] Liu K. C., A Method Based on Virtual Strain-Energy Parameters for Multiaxial Fatigue Life Prediction, in: McDowell D. L., Ellis R. (Eds.), Advances in Multiaxial Fatigue, ASTM STP 1191, Am. Soc. Test. Mater., Philadelphia, pp. 67-84, 1993.
[104] Chu C. -C., Fatigue Damage Calculation Using the Critical Plane Approach, J. Eng. Mater. Technol., vol. 117, pp. 41-49, 1995.
[105] Glinka G., Wang G., Plumtree A., Mean Stress Effects in Multiaxial Fatigue, Fatigue Fract. Eng. Mater. Struct., vol. 18, pp. 755-764, 1995.
[106] Han C., Chen X., Kim K. S., Evaluation of Multiaxial Fatigue Criteria under Irregular Loading, Int. J. Fatigue, vol. 24, pp. 913-922, 2002.
[107] Kim K. S., Park J. C., Shear Strain Based Multiaxial Fatigue Parameters Applied to Variable Amplitude Loading, Int. J. Fatigue, vol. 21, pp. 475-483, 1999.
[108] Morrow D. L., Biaxial-Tension Fatigue of Inconel 718, PhD Diss., University of Illinois at Urbana-Champaign, 1988.
[109] Thomas A., Durmaz A. R., Alam M., Gumbsch P., Sack H., Eberl C., Materials fatigue prediction using graph neural networks on microstructure representations, Sci. Rep., vol. 13, Art. no. 12562, 2023.
[110] Durmaz A. R., Natkowski E., Arnaudov N., Sonnweber-Ribic P., Weihe S., Münstermann S., Eberl C., Gumbsch P., Micromechanical fatigue experiments for validation of microstructure-sensitive fatigue simulation models, Int. J. Fatigue, vol. 160, Art. no. 106824, 2022.
[111] Ferro P., Berto F., James M. N., Borsato T., Review of Recent Advances in Local Approaches Applied to Prestressed Components under Fatigue Loading, Procedia Struct. Integr., vol. 2, pp. 3467-3474, 2016.
[112] Ferro P., The Local Strain Energy Density Approach Applied to Pre-Stressed Components Subjected to Cyclic Load, Fatigue Fract. Eng. Mater. Struct., vol. 37, pp. 1268-1280, 2014.
[113] Ferro P., Berto F., Lazzarin P., Generalized Stress Intensity Factors Due to Steady and Transient Thermal Loads with Applications to Welded Joints, Fatigue Fract. Eng. Mater. Struct., vol. 29, pp. 440-453, 2006.
[114] Lazzarin P., Tovo R., A Notch Stress Intensity Factor Approach to the Stress Analysis of Welds, Fatigue Fract. Eng. Mater. Struct., vol. 21, pp. 1089-1104, 1998.
[115] Wang D., Zhang H., Gong B., Deng C., Residual Stress Effects on Fatigue Behavior of Welded T-Joint: A Finite Fracture Mechanics Approach, Mater. Des., vol. 91, pp. 211-217, 2016.
[116] Hobbacher A., Recommendations for Fatigue Design of Welded Joints and Components, IIW Doc., XIII-2151-07 / XV-1254-07, 2013.
[117] Bäckström M., Marquis G., A Review of Multiaxial Fatigue of Weldments: Experimental Results, Design Code and Critical Plane Approaches, Fatigue Fract. Eng. Mater. Struct., vol. 24, pp. 279-291, 2001.
[118] Lopez-Jauregi A., Esnaola J. A., Ulacia I., Urrutibeascoa I., Madariaga A., Fatigue Analysis of Multipass Welded Joints Considering Residual Stresses, Int. J. Fatigue, vol. 79, pp. 75-85, 2015.
[119] Carpinteri A., Spagnoli A., Vantadori S., Multiaxial Fatigue Life Estimation in Welded Joints Using the Critical Plane Approach, Int. J. Fatigue, vol. 31, pp.188-196, 2009.
[120] DIN EN 10210-2:2016.
[121] Hemmesi K., Farajian M., Boin M., Numerical Studies of Welding Residual Stresses in Tubular Joints and Experimental Validations by Means of X-ray and Neutron Diffraction Analysis, Mater. Des., vol. 15, pp. 339-350, 2017.
[122] Hemmesi K., Mallet P., Farajian M., Numerical Evaluation of Surface Welding Residual Stress Behaviour under Multiaxial Mechanical Loading and Experimental Validations, Int. J. Mech. Sci., vol. 168, Art. 105127, 2020.
[123] Macherauch E., Müller P., Das $\sin^2\psi$-Verfahren der Röntgenographischen Spannungsmessung, Z. angew. Physik, vol. 13, pp. 305-312, 1961.
[124] Hutchings M. T., Withers P. J., Holden T. M., Lorentzen T., Introduction to the Characterization of Residual Stresses by Neutron Diffraction, Boca Raton London New York Singapore: Taylor & Francis, ISBN 0-415-31000-8, 2005.
[125] Bragg W. L., The Diffraction of Short Electromagnetic Waves by a Crystal, Proc. Camb. Philos. Soc., vol. 17, pp. 43-57, 1913.

[126] IS0/TTA3, Polycrystalline Materials – Determination of Residual Stresses by Neutron Diffraction, in: Technology Trends Assessment, Int. Stand. Organ., 2001.
[127] https://www.nde-ed.org/EducationResources/CommunityCollege/Materials/Mechanical/Hardness.php, [Online].
[128] Hemmesi K., Holey H., Elmoghazy A., Böhm R., Farajian M., Schulze V., Modelling and Experimental Validation of Material Deformation at Different Zones of Welded Structural-Steel under Multiaxial Loading, Mater. Sci. Eng. A, vol. 824, Art. 140826, 2021.
[129] Nadai A., Wahl A. M., Plasticity, McGraw-Hill Book Company, inc., 1931.
[130] Wu H. C., Xu Z., Wang P. T., Determination of Shear Stress-Strain Curve from Torsion Tests for Loading-Unloading and Cyclic Loading, J. Eng. Mater. Technol., vol. 119, pp. 113-115, 1997.
[131] Brown M., Torsional Stresses in Tubular Specimens, J. Strain Anal. Eng. Des., vol. 13, pp. 23-28, 1978.
[132] GOM GmbH. Aramis user manual, 2009.
[133] Manson S. S., Behavior of Materials under Conditions of Thermal Stress, Proc. Heat Transfer Symp., pp. 9-75, 1953.
[134] Coffin L. F., A Study of the Effects of Cyclic Thermal Stresses on a Ductile Metal, Trans. ASME, vol. 76, pp. 931-950, 1954.
[135] Morrow J. D., Cyclic Plastic Strain Energy and Fatigue of Metals, ASTM STP 378, pp. 45-87, 1965.
[136] Basquin O. H., The Exponential Law of Endurance Test, Proc. ASME, vol. 10, pp. 625-630, 1910.
[137] Bhadeshia H. K. D. H., Honeycombe R. W. K., Steels: Microstructure and Properties, Oxford, UK: Elsevier, 2006.
[138] Abson D. J., Acicular Ferrite and Bainite in C-Mn and Low-Alloy Steel Arc Weld Metals, Sci. Technol. Weld. Joining, vol. 23, pp. 1-14, 2018.
[139] Smith M. C., Smith A. C., Wimpory R., Ohms C., A Review of the NeT Task Group 1 Residual Stress Measurement and Analysis Round Robin on a Single Weld Bead-on-Plate Specimen, Int. J. Press. Vessels Piping, vol. 120-121, pp. 93-140, 2014.
[140] Outinen J., Kesti J., Mäkeläinen P., Fire Design Model for Structural Steel S355 Based upon Transient State Tensile Test Results, J. Constr. Steel Res., vol. 42, pp. 161-169, 1997.
[141] Richter F., Physikalische Eigenschaften von Stählen und Ihre Temperaturabhängigkeit, Verlag Stahleisen M. B. H, Düsseldorf, 1983.
[142] Muránsky O., Smith M. C., Bendeich P. J., Holden T. M., Luzin V., Martins R. V., Edwards L., Comprehensive Numerical Analysis of a Three-Pass Bead-in-Slot Weld and its Critical Validation Using Neutron and Synchrotron Diffraction Residual Stress Measurements, Int. J. Solids Struct., vol. 49, pp. 1045-1062, 2012.
[143] Remes H., Varsta P., Romanoff J., Continuum Approach to Fatigue Crack Initiation and Propagation in Welded Steel Joints, Int. J. Fatigue, vol. 40, pp. 16-26, 2012.
[144] Remes H., Strain-Based Approach to Fatigue Crack Initiation and Propagation in Welded Steel Joints with Arbitrary Notch Shape, Int. J. Fatigue, vol. 52, pp. 114-123, 2013.
[145] Ramtani S., Bui H. Q., Dirras G., A Revisited Generalized Self-Consistent Polycrystal Model Following an Incremental Small Strain Formulation and Including Grain-Size Distribution Effect, Int. J. Eng. Sci., vol. 47, pp. 537-553, 2009.
[146] Zhu B., Asaro R. J., Krysl P., Bailey R., Transition of Deformation Mechanisms and Its Connection to Grain Size Distribution in Nanocrystalline Metals, Acta Mater., vol. 53, pp. 4825-4838, 2005.
[147] Berbenni S., Favier V., Berveiller M., Micro-Macro Modelling of the Effects of the Grain Size Distribution on the Plastic Flow Stress of Heterogeneous Materials, Comput. Mater. Sci., vol. 39, pp. 96-105, 2007.
[148] Raeisinia B., Sinclair C. W., Poole W. J., Tomé C. N., On the Impact of Grain Size Distribution on the Plastic Behaviour of Polycrystalline Metals, Model. Simul. Mater. Sci. Eng., vol. 16, Art. 025001, 2008.
[149] Takaki S., Review on the Hall-Petch Relation in Ferritic Steel, Mater. Sci. Forum, vol. 654-656, pp. 11-16, 2010.
[150] Raeisinia B., Poole W. J., Modelling the Elastic-Plastic Transition of Polycrystalline Metals with a Distribution of Grain Sizes, Model. Simul. Mater. Sci. Eng., vol. 20, Art. 015015, 2012.

[151] Kurzydlowski K. J., Bucki J. J., Flow Stress Dependence on the Distribution of Grain Size in Polycrystals, Acta Metall. Mater., vol. 41, pp. 3141-3146, 1993.
[152] Kurzydlowski K. J., A Model for the Flow Stress Dependence on the Distribution of Grain Size in Polycrystals, Scr. Metall. Mater., vol. 24, pp. 879-883, 1990.
[153] Lehto P., Remes H., Saukkonen T., Hänninen H., Romanoff J., Influence of Grain Size Distribution on the Hall–Petch Relationship of Welded Structural Steel, Mater. Sci. Eng. A, vol. 592, pp. 28-39, 2014.
[154] ASTM E1382-97, Standard Test Methods for Determining Average Grain Size Using Semiautomatic and Automatic Image Analysis, ASTM Int., West Conshohocken, PA, 2004.
[155] Gundersen H. J. G., Jensen E. B., Particle Sizes and Their Distributions Estimated from Line- and Point-Sampled Intercepts. Including Graphical Unfolding, J. Microsc., vol. 131, pp. 291-310, 1983.
[156] Gundersen H. J. G., Jensen E. B., Stereological Estimation of the Volume-Weighted Mean Volume of Arbitrary Particles Observed on Random Sections, J. Microsc., vol. 138, pp. 127-142, 1985.
[157] Underwood E. E., Quantitative Stereology, Addison-Wesley Publishing Co., Reading, MA, 1970.
[158] ASTM E1245 - 03, Standard Practice for Determining the Inclusion or Second-Phase Constituent Content of Metals by Automatic Image Analysis, ASTM Int., West Conshohocken, PA, 2003.
[159] Kühne D., Guilleaume C., Seiler M, Hantschke P., Ellmer F., Linse T., Brosius A., Kästner M., Fatigue Analysis of Rolled Components Considering Transient Cyclic Material Behaviour and Residual Stresses, Prod. Eng., vol. 13, pp. 189-200, 2018.
[160] Meyer N., Effects of Mean Stress and Stress Concentration on Fatigue Behaviour of Ductile Iron, MS Thesis, University of Toledo, 2014.
[161] Jiang Y., Zhang J., Benchmark Experiments and Characteristic Cyclic Plasticity Deformation, Int. J. Plast., vol. 24, pp. 1481-1515, 2008.
[162] Noroozi A. H., Glinka G., Lambert S., A Two Parameter Driving Force for Fatigue Crack Growth Analysis, Int. J. Fatigue, vol. 27, pp. 1277-1296, 2005.
[163] Mikheevskiy S., Glinka G., Elastic–Plastic Fatigue Crack Growth Analysis under Variable Amplitude Loading Spectra, Int. J. Fatigue, vol. 31, pp. 1828-1836, 2009.
[164] Wang X., Yin D., Xu F., Qiu B., Gao Z., Fatigue Crack Initiation and Growth of 16MnR Steel with Stress Ratio Effects, Int. J. Fatigue, vol. 35, pp. 10-15, 2012.
[165] McDowell D. L., Dunne F. P. E., Microstructure-Sensitive Computational Modelling of Fatigue Crack Formation, Int. J. Fatigue, vol. 32, pp. 1521-1542, 2010.
[166] Hall E. O., The Deformation and Ageing of Mild Steel: III Discussion of Results, Proc. Phys. Soc. Sect. B, vol. 64, pp. 747-753, 1951.
[167] Petch N. J., The Cleavage Strength of Polycrystals, J Iron Steel Inst., vol. 174, pp. 25-28, 1953.
[168] Taylor D., Geometrical Effects in Fatigue: A Unifying Theoretical Model, Int. J. Fatigue, vol. 21, pp. 413-420, 1999.
[169] Neuber H., Über die Berücksichtigung der Spannungskonzentration bei Festigkeitsberechnungen, Konstruktion, vol. 20, pp. 245-251, 1968.

List of Publications

Hemmesi K., Holey H., Elmoghazy A., Böhm R., Farajian M., Schulze V., Modelling and Experimental Validation of Material Deformation at Different Zones of Welded Structural-Steel under Multiaxial Loading, Mater. Sci. Eng. A, vol. 824, pp. 1-15, 2021.

Hemmesi K., Mallet P., Farajian M., Numerical Evaluation of Surface Welding Residual Stress Behavior under Multiaxial Mechanical Loading and Experimental Validations, Int. J. Mech. Sci., vol. 168, Art. 105127, 2020.

Hemmesi K., Farajian M., Numerical Welding Simulation as a Basis for Structural Integrity Assessment of Structures: Microstructure and Residual Stresses, In book: Residual Stress Analysis on Welded Joints by Means of Numerical Simulation and Experiments, 2018.

Hemmesi K., Farajian M., Boin M., Numerical Studies of Welding Residual Stresses in Tubular Joints and Experimental Validations by Means of X-ray and Neutron Diffraction Analysis, Mater. Des., vol. 15, pp. 339-350, 2017.

Hemmesi K., Farajian M., Fatemi A., Application of the Critical Plane Approach to the Torsional Fatigue Assessment of Welds Considering the Effect of Residual Stresses, Int. J. Fatigue, vol. 101, pp. 271-281, 2017.

Hemmesi K., Farajian M., Siegele D., Numerical and Experimental Description of the Welding Residual Stress Filed in Tubular Joints for Fatigue Assessment, Int. J. Mater. Joining, Welding in the World, vol. 60, pp. 741-748, 2016.

Hemmesi K., Farajian M., Siegele D., Numerical Investigation of Welding Residual Stress Field and its Behavior under Multiaxial Loading in Tubular Joints, Adv. Mater. Res., vol. 996, pp. 788-793, 2014.